

University of St Andrews



Full metadata for this thesis is available in
St Andrews Research Repository
at:

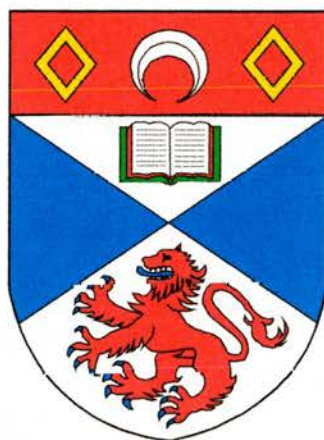
<http://research-repository.st-andrews.ac.uk/>

This thesis is protected by original copyright

Ultrashort pulse generation using quasi-phasematched crystals

Thesis submitted for the degree of Doctor of Philosophy
to the University of St. Andrews
by

Pablo Loza Alvarez



The J. F. Allen Physics Research Laboratories
School of Physics and Astronomy
University of St. Andrews
North Haugh
St. Andrews
Fife, KY16 9SS
Scotland.



June 2000

TL

D 688 .

Declarations

I, Pablo Loza Alvarez, hereby certify that this thesis, which is approximately 50,000 words in length, has been written by me, that is the record of work carried out by me and that it has not been submitted in any previous application for a higher degree.

date 21-06-00 signature of candidate

I was admitted as a research student and as a candidate for the degree of Doctor of Philosophy in September, 1996; the higher study for which this is a record was carried out in the University of St. Andrews between 1996 and 2000.

date 21-06-00 signature of candidate

I hereby certify that the candidate has fulfilled the conditions of the Resolution and Regulations appropriate for the degree of Doctor of Philosophy in the University of St. Andrews and that the candidate is qualified to submit this thesis in application for that degree.

date 21-06-00 signature of supervisor

Copyright

In submitting this thesis to the University of St. Andrews I understand that I am giving permission for it to be made available for use in accordance with the regulations of the University Library for the time being in force, subject to any copyright vested in the work not being affected thereby. I also understand that the title and abstract will be published, and that a copy of the work may be made and supplied to any bona fide library or research worker.

date 21-06-00 signature of candidate

To my parents



Abstract

In this thesis several nonlinear frequency-conversion systems based on quasi-phases-matched (QPM) crystals, that produce high-repetition rate, femtosecond pulses are investigated. These systems are based on synchronously pumped optical parametric oscillation (OPO) and second-harmonic generation (SHG). Nonlinear crystals such as RbTiOAsO₄ (RTA), KTiOPO₄ (KTP) and LiNbO₄ are used in this work.

Ultrashort pulse characterisation techniques are investigated and used to study these systems. Relevant theory and complete details for the implementation of a real-time SHG-based frequency-resolved optical gating (FROG) system are described. Preliminary results of a cross-correlation-based FROG (X-FROG) technique for the simultaneous characterisation of two femtosecond pulses, at different frequencies, are included. Also, the two-photon response of a GaN laser diode is investigated to measure real-time intensity and interferometric autocorrelations of femtosecond pulses in wavelength regions from 415 – 630 nm.

Several OPO systems based on periodically-poled RTA (PPRTA) or periodically-poled LiNbO₄ (PPLN) are presented. With these OPO's, high peak power, femtosecond pulses that are tunable from 910 nm to 6.8 μm are produced. Depending on the material, and/or on the OPO cavity, pulse durations ranging from 100 - 400 fs and average output powers from $\sim 200 \mu\text{W}$ to 600 mW are obtained.

Detailed experimental results of simultaneous frequency-doubling and pulse compression of chirped femtosecond OPO pulses using aperiodically-poled crystals of KTP (APP-KTP) and lithium niobate (APPLN) are given. In both cases linearly frequency chirped femtosecond pulses of ~ 300 fs duration were temporally compressed and frequency-doubled to obtain transform limited pulses of ~ 130 fs duration. Experimental results are compared with a numerical model in which the complex pulse amplitude of the second-harmonic pulses are calculated using data obtained by FROG characterisation of the input pulses. The results of this model have been used to analyse several aspects of the pulse generation process.

By combining several of the techniques mentioned above, an experimental system is proposed for the study of the coherent control of electrical currents in bulk semiconductor materials.

Preface

In Chapter I, a brief review of conventional sources delivering femtosecond pulses, with high average output powers and at high-repetition rate are described. Nonlinear frequency-conversion systems such as synchronously pumped optical parametric oscillators (OPOs) are then presented as alternative ways to expand the current spectral coverage of femtosecond sources. A complete review of synchronously pumped femtosecond OPO systems is included here. Some of the advantages of using quasi-phasematched (QPM) materials, as opposed to birefringent phasematched (BPM), as active media in OPO's are discussed. Finally, a review of the use of aperiodically-poled crystals to frequency-double and compress chirped pulses is given.

In the second part of this chapter, the self-modelocked Ti:sapphire laser is presented as the pump source for the OPO systems. Here, the concepts relative to modelocking operation are studied. Finally the theory of linear and nonlinear ultrashort pulse propagation is presented.

In Chapter 2 a review of the theory of nonlinear optics is provided. The coupled wave equations for the general case of three-frequency mixing process are presented and the concepts of phasematching using birefringent materials are explained. The theory of quasi-phasematching is then introduced and a review of the periodically poling technique to achieve QPM in ferroelectric crystals is given. Finally, some of the physical properties of the nonlinear optical materials used in this work are outlined.

Ultrashort pulse characterisation techniques are described in Chapter 3. The chapter starts by reviewing some of the basic concepts of second-order autocorrelation. Then, the linear and nonlinear response of a GaN-based laser diode are presented and used to construct a two-photon absorption based autocorrelator for characterising femtosecond pulses in the 410 – 730 nm spectral range. In the second part of the chapter, the concepts of frequency-resolved frequency gating technique (FROG) are studied. Here, a detailed description to implement the FROG technique, based on second-harmonic generation, is presented. Finally, preliminary results are included for the cross-correlation based FROG (X-FROG) technique which provided for simultaneous characterisation of two different femtosecond pulse sequences.

In Chapter 4, several OPO systems are described and characterised. These are based either on periodically poled RbTiOAsO₄ (PPRTA) or lithium niobate (PPLN). The different characteristics such as tunability, pulse durations and output powers obtained, are described for each system. Thus the first section highlights the large tunability range and constant pulse duration of a PRTA OPO in the 1.375 to 1.575 μm spectral range. In the next section, an all-solid-state PPLN OPO that is tunable up to 4.88 μm is described. In the third section, a PPLN OPO that tunes in the signal wavelengths from 1.06 to 1.55 μm , using three different set of mirrors, is described and some dispersive effects arising at the extremes of the tuning range of each operating set of mirrors, are studied. This chapter concludes by describing a PPLN-based OPO as a source of idler wavelengths as long as 6.8 μm and with a 4 μm tunability range.

In Chapter 5 simultaneous SHG and femtosecond pulse compression using aperiodically poled crystals of KTiOPO_4 (APP-KTP) or lithium niobate (APPLN) is studied. In the first part of the chapter, a chirped grating in a crystal of APP-KTP that would produce optimal SHG pulse compression is designed after full characterisation of the fundamental pulses of a RTA-based OPO. In the second part, an APPLN crystal with 8 different linearly chirped gratings is used to frequency-doubled and compress arbitrary chirped femtosecond pulses from a PPRTA-based OPO. In both cases, experimental results are compared with a numerical model that incorporates the complex pulse amplitude retrieved from SHG-FROG characterisation of the fundamental pulses.

In Chapter 6, the principles of coherent control of ultrafast electrical currents is described. Initially, a brief review of the coherent control mechanisms, together with some of the possible applications that coherent control offers are presented. This is followed by a resume of previous works that use the coherent control technique to generate electrical currents. Finally, I propose a system, based on several of the techniques presented in this work, that will enable the coherent control of ultrafast electrical currents to be assessed quantitatively.

CONTENTS

Declarations	<i>ii</i>
Abstract	<i>iv</i>
Preface	<i>v</i>
Contents	<i>viii</i>
1 Introduction	1
1.1 Introduction:	1
1.1.1 Conventional sources of ultrashort pulses	4
1.1.2. Synchronously pumped optical parametric oscillators	8
1.1.3. Quasi-phasematched femtosecond optical parametric oscillation and second harmonic generation	12
1.2 The Ti:sapphire laser and modelocking	17
1.2.1 The Ti:sapphire gain medium	18
1.2.2 Modelocking	21
1.3 Linear and nonlinear pulse propagation	25
1.4 Conclusions	32
1.5 References	34
2 Nonlinear optics and materials	42
2.1 Nonlinear Optics	42
2.1.1 The nonlinear susceptibility tensor	43
2.1.2 The coupled wave equations	46
2.1.3 Phasematching	49
2.2 Quasi-phasematching	56
2.2.1 Theory of quasi-phasematching	56
2.2.2 The periodic-poling technique	60
2.3. Nonlinear optical materials	63
2.3.1 The KTP family of nonlinear crystals	64
2.3.2 The lithium niobate crystals	68

2.4 Conclusions	73
2.5 References	74
3 Ultrashort pulse characterisation techniques	77
3.1 Autocorrelation	77
3.2 Two-photon absorption autocorrelator	82
3.2.1 Two-photon autocorrelation of visible femtosecond pulses	83
3.3 Frequency-Resolved Optical Gating	90
3.3.1. Time-frequency domain methods	91
3.3.2. The frequency-resolved optical gating technique	92
3.3.3. Implementation of a real-time SHG-FROG scheme	95
3.3.4. The crosscorrelation-FROG technique	99
3.4 Conclusions	102
3.5 References	103
4 OPO based on periodically-poled crystals.	105
4.1 The periodically-poled RbTiOAsO ₄ OPO	106
4.2 All-solid-state PPLN-based optical parametric oscillator	113
4.3 Characterisation of a PPLN-based OPO in the 1.26 to 1.58 μm range	117
4.4 Optical parametric oscillator with continuous tunability from 2.8 to 6.8 μm	123
4.4.1 Introduction	123
4.4.2 The experimental setup and results	124
45 Conclusions	132
4.6 References	134
5 Simultaneous second harmonic generation and pulse compression	136
5.1 Simultaneous SHG and pulse compression in AP-KTP	137
5.1.1 The RTA-based OPO	137

5.1.2 Extracavity SHG and pulse compression	140
5.1.3. Intracavity SHG and pulse compression	142
5.1.4 The numerical model	144
5.1.5 Experimental results and discussion	145
5.1.6 Efficiency calculations	152
5.2 Simultaneous SHG and pulse compression in APPLN	154
5.2.1 The PPRTA-based OPO	154
5.2.2. The aperiodically poled lithium niobate crystal	156
5.2.3. The numerical model	158
5.2.4. Experimental results and discussion	159
5.3 Conclusions	167
5.4 References	169
6 Applications: coherent control	171
6.1 Some applications using coherent control	172
6.2 Coherent control of electrical currents in semiconductors	179
6.2.1 Coherent control of photocurrents. Review	180
6.3. Electrical pulse generation by coherent control. My approach	185
6.3.1 The OPO source	186
6.3.2 The experimental setup	189
6.3.3 The collaboration with NPL	191
6.4 Conclusions	192
6.5 References	193
7 General conclusions	196
7.1 References	204
Publications	205
Aknowledgements	209

CHAPTER 1

INTRODUCTION

1.1 Introduction

High average output power sources delivering femtosecond pulses at high-repetition rates are of great interest for many applications ranging from spectroscopy to biological imaging. The impact of “femtosecond technology” has been so huge that the 1999 Nobel Prize for chemistry was awarded for the development of a technique for ultrafast spectroscopy in which a femtosecond laser pulse excites the vibrational and rotational states of motion of molecules. A second pulse, tens of femtosecond later then probes the resulting relaxation behaviour allowing the observation of these vibrational and electronic changes in a chemical reaction as they occur.^{1,2} The awarded prize not only acknowledged the pioneering work in femtochemistry, but also represented an outstanding recognition of the entire field of ultrafast optics and femtosecond laser applications.

In Zewail’s work, the intrinsic high pulse-repetition-rate of the source was of primary importance as it allowed to achieve high signal-to-noise ratios in the measurement of the data. For other applications, however, other characteristics apart from the high pulse-repetition rate may also be desirable. The importance of developing new high-repetition-rate femtosecond-pulse sources delivering high average output power and broad wavelength tuning in different regions of the optical

spectrum is crucial for the emergence or success of such applications. Other fields such as multiphoton spectroscopy, materials processing and coherent control of carrier populations in semiconductors will benefit from these new sources. Some of these novel applications are explained below.

Multi-photon microscopy

Due to the high peak powers (P_{pk}) generated by a femtosecond pulse, biological imaging using multi-photon microscopy has enabled researchers to examine microstructures inside individual cells and track, for example, the flow of calcium ions in a system. This form of imaging relies on a simultaneous absorption of two (or more) pump photons rather than a single photon by a molecule before it emits a fluorescence photon. The process enables excitation to be limited to a very small volume near the focus of the beam, where the photon flux density is high enough for the nonlinear process to occur, and therefore, high-resolution 3-D images can be constructed.³

The same principle can be applied to two-photon absorption microscopy. In this case, the ultrashort pulses in the infrared ($\sim 1.2 \mu\text{m}$) are directed to the back of a polished microchip. An optical beam induced current is generated by two-photon absorption of the ultrashort pulse. By recording the electrical current generated by the different features of the circuitry as a function of the beam position, it is possible to obtain a map of the integrated circuit inside the microchip.⁴

Material processing

The extreme concentration of energy in femtosecond pulses has also been exploited for materials processing due to the absence of thermal interactions caused by longer pulses. Carbon dioxide, Nd:YAG and copper vapour lasers which have

been used as the workhorses of cutting tools in industry, present several drawbacks such as thermal load, limited strut size, and limited choice of materials. In contrast, femtosecond lasers can machine materials with very high precision, maintaining the integrity of surrounding material. When machining to a micron-scale, precision is achieved because removal of material occurs faster than heat can be conducted into it.⁵ Therefore, minimal or no thermal damage occurs, strut sizes in the range of a few microns can be achieved and materials such as ceramics, glass, and polymers can be machined without creating large heat-affected zones and burr due to resolidification of the material.⁶

Metrology and coherent control

Femtosecond pulses have also found an application in electrical metrology for the calibration of fast oscilloscopes.⁷ Such an application is based on electro-optic sampling⁸ and uses a femtosecond laser together with an ultrafast photoconductive switch to generate and measure electric pulses as short as 650 fs. Coherent control of currents in semiconductors have also been demonstrated by varying the phase between a fundamental beam and its frequency doubled beam.⁹ In Chapter 6, we will exploit this idea and an experimental set up will be proposed that permits the generation of ultrafast electrical currents in a sample of low-temperature-grown GaAs.

From these examples it is clear that there are many applications which demand reliable high-repetition-rate femtosecond sources delivering high peak powers and broad tunability. In the next section, a review of the main sources of femtosecond pulses is presented.

1.1.1 Conventional sources of ultrashort pulses

Existing sources delivering high repetition rate, high average power, femtosecond pulses may be classified in one of the following main categories: Colliding-pulse-modelocked (CPM) dye lasers, coupled-cavity modelocked (CCM) colour-centre lasers, Kerr-lens modelocked (KLM) lasers, fibre lasers and semiconductor absorber (saturable-Bragg-reflectors (SBR) and semiconductor saturable absorber mirror (SESAM)) modelocked lasers. These will be briefly explained.

Colliding-pulse-modelocked dye laser

The first demonstration of a modelocked laser capable of producing pulses with duration less than 100 fs at a high repetition rate (~100 MHz), was made using a CPM dye laser.¹⁰ This laser consisted of two or more counterpropagating pulses resonant in a ring cavity containing an absorber jet of 3,3'-diethyloxadicarbocyanide iodide (DODCI) in solution and a gain jet of rhodamine 6-G (Rh6G). When the counterpropagating pulses met in the thin DODCI jet, the bleaching action of the absorber sharpened the leading edges of the pulses. Then, gain saturation of the Rh6G jet reduced the pulse duration further by sharpening the trailing edge of the pulses. Because of the inclusion of the saturable absorber, operation was limited to \leq 10 mW of output power and gave rise to a threshold of several Watts. Another important drawback was that CPM dye lasers were only tunable over a narrow spectral range since the net bandwidth of the gain and absorber dyes was of the order of the bandwidth of the resonant pulses. Using different gain/absorber combinations could result in a limited spectral coverage across the visible, but complete tuning has never been convincingly demonstrated for femtosecond pulses.

Coupled-cavity modelocked colour-centre lasers

The coupled-cavity modelocking (or additive-pulse modelocking) is an alternative technique to produce modelocked femtosecond pulses in the near infrared. It was first demonstrated with a synchronously-modelocked KCl:Ti colour centre laser in 1984.¹¹ In this technique, self-phase modulation (SPM) is successfully employed to obtain passive modelocking by constructing the laser as an interferometer with the nonlinear element placed in one arm. An intense noise feature will experience an intensity-dependent phase shift on propagating through the nonlinear element (often a single-mode optical fibre). When the two arms are suitably aligned it is possible after recombining the nonlinear arm and the main cavity pulses, for constructive interference to occur at the centre of the noise feature thus enhancing the peak intensity, while destructive interference suppresses the wings of the noise feature. After many round trips, a modelocked pulse sequence is obtained.¹² The need to maintain the colour-centre crystal at cryogenic temperatures restricted the availability of these lasers to research centres with access to sources of liquid nitrogen. Furthermore, the limited tuning range (1.4 – 1.6 μm) restricted their operation to the near-infrared.

Kerr-lens modelocked lasers.

Solid-state vibronic materials are amongst the most recent laser media to have supported femtosecond modelocking. Vibronic media such as Ti:sapphire have vibrational sublevels which spread the electronic energy levels into broad bands, allowing laser transitions over a range of energies. This broad emission bandwidth is the feature of vibronic media which makes them attractive materials for femtosecond pulse generation.

In 1990 it was observed by Spence et al.¹³ that passive modelocking could be established in a Ti:sapphire laser cavity with no apparent modelocking element and pulses as short as 60 fs were demonstrated. In these lasers, modelocking operation is favoured over CW through the self-amplitude modulation (SAM) that is provided by self-focusing (via the optical Kerr-effect) in the gain medium. This then induces beam shaping in the laser cavity. By configuring the laser cavity in a suitable fashion, the laser field experiences greater gain for stronger self-focusing. This effect enhances the high intensity noise components of the circulating field at the expense of the low intensity CW background. Incorporating a pair of prisms¹⁴ into the laser cavity compensates for normal dispersion due to the Ti:sapphire crystal and for the SPM induced by the high intensities in the gain medium. After many round trips a modelocked pulse train develops (in Section 1.3, these concepts will be studied in detail). Using this method, self-modelocked Ti:sapphire lasers (and indeed other vibronic lasers such as $\text{Cr}^{3+}:\text{LiSrAlF}_6$) have produced ultrafast pulses with unprecedented qualities such as pulse duration, robustness and stability, however, its tunability is restricted to the 700 – 1050 nm spectral region.

Although other vibronic gain media such as Cr:forsterite, $\text{Cr}^{4+}:\text{YAG}$, alexandrite and $\text{Co}:\text{MgF}_2$ may cover different spectral regions, a complete coverage can only be achieved by using a variety of pump sources and laser media.

Saturable absorber modelocking lasers

Passive modelocking resulting in femtosecond pulse operation has been successfully demonstrated in solid state lasers using semiconductor saturable absorbers.^{15,16} The most common of these are semiconductor saturable absorber mirrors (SESAM)¹⁷ and saturable Bragg reflectors (SBR).¹⁸ Typically a

semiconductor saturable absorber is integrated directly into a mirror structure, resulting in a self-amplitude modulating device whose reflectivity increases as the incident power intensity increases. If the response time of the absorber is sufficiently fast, an optical pulse travelling through a saturable absorber is shortened by the SAM. In a SBR/SESAM modelocked laser as well as in a KLM laser, pulse formation should start from normal noise fluctuation in the laser to initiate modelocking, however, cavity stability adjustments are less critical compared to KLM lasers. Modelocked lasers using saturable absorber mirrors are becoming commercially available and a variety of lasers has been demonstrated using Nd:glass, Yb:YAG, $\text{Cr}^{3+}:\text{LiSrAlF}_6$ and $\text{Cr}^{3+}:\text{LiSrGaF}_6$ ^[19] but practical tuning operation finds similar difficulties as in the case of KLM lasers.

Fibre lasers

Modelocked diode-pumped Erbium-doped fibre lasers (EDFL) have started to gain place as alternative sources of femtosecond pulses. These lasers typically produce sub-100 femtosecond pulses at 1.55 μm with average output powers of more than 50 mW. This laser consists of a ring cavity with two sections. In one section the fibre is doped with erbium, constituting the gain medium of the laser, and an ultrashort pulse travelling in here will acquire positive group velocity dispersion. The other section is a standard communication fibre and therefore has (for the pulses at 1.55 μm) negative dispersion. Thus, a pulse travelling in the laser will be chirped before passing through the gain medium, and then it is compressed as it passes through the standard fibre²⁰. The cavity is assembled so it acquire a near zero (slightly positive) dispersion in order to avoid spectral sidebands but shorter pulse duration can be achieved for slightly negative dispersion.²¹ EDFL have a large

drawback and is that direct tunability of the laser is poor and operation is limited to the transmission windows of the fibres (1.3 and 1.55 μm). however, the high peak power provided by the output pulses of EDFL can be exploited to frequency doubled the femtosecond pulses and operation at 775 nm can be achieved. This frequency doubled pulses are typically used to seed Ti:sapphire regenerative amplifiers which are commonly employed to pump optical parametric amplifiers and/or generators.

Analogously to the EDFL, the high peak output powers already available from all these previously explained ultrashort pulse lasers, can be efficiently used to generate new wavelengths using nonlinear frequency conversion techniques such as optical parametric oscillation (OPO). In the next section, a general overview of femtosecond pulse OPO will be presented.

1.1.2 Synchronously pumped optical parametric oscillators

To generate ultrashort pulses beyond the tuning range reached by the lasers described in the previous section, optical parametric oscillators (OPO) offer an attractive alternative²². The first demonstration of an ultrashort pulse OPO was made by Burneika and co-workers in 1972. They proposed a synchronously pumped OPO configured so that the cavity length of the OPO was equal to the cavity length of the modelocked pump laser²³. In this technique, many consecutive pulses from the pump laser sequentially pump one circulating pulse within the cavity of the OPO. The interval between the arrival of adjacent pump pulses (equal to the round-trip time of the pump laser cavity) is arranged to match the round-trip time of the down-converted pulses within the OPO cavity, so that the two pulses always meet in the nonlinear medium; i.e. the cavities are synchronous. Since this early work on OPOs,

which never became practical due to the lack of suitable pump sources and nonlinear crystals, there have been considerable efforts on optical parametric amplifiers²⁴ and oscillators.²⁵ The basic requirements for such parametric generators are very different from those for high-repetition rate oscillators in the picosecond and femtosecond time domain. Factors such as group velocity walk-off (GVW) put restrictions on crystal lengths, and as a result, extended gain bandwidth is required to support the shorter duration pulses. The nonlinear material's resistance to optical damage also becomes an important issue. Nevertheless, these earlier efforts were the precursors of the advances in the latter devices.

OPOs based on birefringent crystals

Since these early developments, many OPOs, synchronously pumped by Q-switched mode-locked lasers, have been demonstrated. These systems generated ultrashort pulses in the near- and mid-infrared by using of a variety of nonlinear crystals, including LiNbO_3 ,²⁶ $\text{MgO}:\text{LiNbO}_3$, $\text{Ba}_2\text{NaNb}_5\text{O}_{15}$,^{27,28} $\beta\text{-BaB}_2\text{O}_4$ (BBO),²⁹ LiB_3O_5 (LBO)³⁰ and KTiOPO_4 (KTP).³¹ Although the high peak power of Q-switched modelocked pulses produces ample gain to overcome oscillation threshold, the output from these OPOs consists of only the finite trains of mode-locked pulses during the burst of the Q-switched output. Furthermore, both the time-durations and the amplitudes of the mode-locked pulses are not constant during a single Q-switched envelope. Because of these characteristics, Q-switched mode-locked OPOs are not useful for applications in which steady trains of identical pulses at a high repetition rate are required. Doubly resonant CW mode-locked OPOs were also studied using materials such as $\text{Ba}_2\text{NaNb}_5\text{O}_{15}$ ^[32] and KTP.³³ Although the doubly resonant OPO (DRO) offers the benefit of the relatively low oscillation threshold,

stringent control of the OPO cavity length and extremely good frequency stability of the pump laser are required to maintain the proper phase relationship between the pump, signal and idler in parametric processes. For ultrashort pulses, this requirement is difficult to satisfy in practice due to the dispersion and birefringence of a nonlinear crystal. Consequently, a mode-locked DRO usually suffers from poor output stability in both amplitude and frequency and from serious cluster effects.^{34,35} In a singly resonant OPO (SRO), on the other hand, only the signal is oscillating in the cavity, and the idler adjusts its phase automatically such that the energy transfer from the pump to the signal is maximised. As a result more tolerance is permitted in both the cavity-length adjustment and the pump-laser stability, resulting in stable output pulses applicable to practical experiments. This is, however, at the expense of an increase in the oscillation threshold typically by two orders of magnitude, but the advantage of the relaxed tolerance more than offsets this drawback.

The first practical realisation of a CW high-repetition rate femtosecond single resonant OPO were demonstrated by Eldestein *et al.*³⁶ and Wachman *et al.*³⁷ This OPO was based on a crystal of KTP, and to obtain sufficient peak power, the crystal was intracavity pumped by a Rh 6G femtosecond dye laser. Shortly after that, the first externally pumped CW mode-locked OPO was reported by Mak *et al.*³⁸ This OPO was based on a KTP crystal and was pumped by the output of a hybridly mode-locked dye laser to produce 220 fs pulses tunable from 1.20 to 1.34 μm with an output power of a few tens of milliwatts. Following to that, McCarthy and Hanna³⁹ developed an all-solid-state KTP OPO synchronously pumped by the second harmonic of a diode-pumped additive-pulse mode-locked Nd:YLF laser, generating 1.5 ps pulses that were tunable from 1.002 μm to 1.096 μm with 42 mW of average power. Since then, and due to the development of the femtosecond Ti:sapphire

laser¹³ which allowed the femtosecond OPO to be pumped externally, a great variety of ultrashort pulse OPOs, operating in the near and mid-infrared, have been demonstrated. These were based on a variety of birefringent nonlinear materials such as KTP,^{40,41} BBO,^{42,43,44} LBO,⁴⁵ KTiOAsO₄ (KTA),^{46,47} KNbO₃,^[48] CsTiOAsO₄ (CTA),⁴⁹ In:KTiOAsO₄ (In:KTA),⁵⁰ RbTiOAsO₄ (RTA)⁵¹⁻⁵⁴ and AgGaSe₂.⁵⁵ With exception of the AgGaSe₂ OPO, the typical spectral coverage of these OPOs is from 1 to 5 μm (signal and idler). As the AgGaSe₂ OPO was pumped by another OPO which was based on a CTA crystal, the total tunability range of this system expanded from 2 to 8 μm . In all the above systems, average output powers up to 500 mW, pulse repetition rates of 80 to 350 MHz and pulse durations of 30 to 300 fs are obtained. The roles of self phase-modulation and group velocity dispersion, which lead to both pulse broadening and frequency chirping, have been widely studied⁵⁶, including solitonic effects⁵⁷. Furthermore, cascaded intracavity frequency doubling within the OPO cavity itself allowed an extension of the tuning ranges in the visible region^{58,59}.

All these OPO implementations proved to be very efficient and reliable. In each system, the crystals were designed to phase-match the interacting wavelengths either in a noncritical (i.e., all the waves propagate parallel to a crystal axis) or a critical (the waves propagate non-parallel to a crystal axis) geometries. The practicability of these systems has, therefore, been limited by several difficulties associated with conventional birefringent phase matching (BPM) such as Poynting-vector walk-off, low effective nonlinear coefficient and narrow tolerances in phase-matching temperatures and angles. For example, critically cut crystals offer small values of pump-signal pulse walkaway, but this is at the expense of spatial walk-off effects. On the other hand, noncritical-cut geometries permit collinear pumping and

therefore, are characterised by ease of alignment, operational simplicity and the consequent elimination of spatial walk-off effects, but at expense of large pump-signal (and in some cases pump-idler) walkaway. Along with these problems, the tuning of noncritical crystals is often dependent on the wavelength range of the pump source and may cover a smaller range than that provided by a critically phase-matched OPO.

1.1.3 Quasi-phase-matched femtosecond OPOs and SHG

Quasi-phase-matching (QPM) makes it possible to combine the convenience of noncritical phase-matching with the wavelength coverage of a critical geometry. QPM is a technique for phase matching nonlinear optical interactions in which the relative phase of the interacting waves is corrected at regular intervals using a structural periodicity (grating period) built into the nonlinear medium⁶⁰. This technique offers the advantage that the interacting waves can be chosen so that coupling occurs through the largest element of the $\chi^{(2)}$ tensor. Moreover, phase-matching can be obtained using a single polarisation along the crystal axis for all interacting waves. This yields a noncritical configuration, which eliminates the problem of spatial walk-off. Most important is the possibility to tailor the material to phase match arbitrary processes within the transparency range of the material by simply choosing an appropriate period of the modulation. Thus, QPM has been used to up- and down-convert a wide range of wavelengths at high conversion efficiencies within CW, nanoseconds, picosecond and femtosecond regimes^{61,62}.

OPOs based on quasi-phasematched crystals

QPM has been demonstrated in a wide variety of structures produced by stacking of polished plates,⁶³ diffusion bonding,⁶⁴ periodic poling of nonlinear crystals,⁶⁵ integrated-optic technology⁶⁶ and poled-polymer films^{67,68}. These structures have been implemented in a wide variety of devices where the exploitation of the novel phase matching characteristics have been successful.^{69,70} Thus, second-harmonic generation (SHG)⁷¹ and sum-⁷² and difference-frequency mixing⁷³ have been achieved over an extensive range of wavelengths. In addition to these, parametric processes have received much attention with generators,⁷⁴ amplifiers,⁷⁵ and oscillators.^{76,77} The first demonstration of a femtosecond OPO based on a QPM material was reported simultaneously by K. C. Burr *et al.*⁷⁸ and C. McGowan *et al.*⁷⁹ and was based on a periodically-poled crystal of lithium niobate (PPLN). This achievement was closely followed by other groups.⁸⁰⁻⁸² Since then femtosecond OPO systems have been demonstrated with materials such as periodically poled RTA (PPRTA)^{83,84} and periodically-poled KTP (PPKTP).⁸⁵ In all these cases broad spectral coverage has been successfully achieved by means of tuning the pump wavelength, changing the OPO cavity-length, using different quasi-phase-matched periods in a crystal, or changing the crystal temperature. Particular interest was then placed on PPLN because it proved to be a useful crystal to generate wavelengths as long as $5.3\ \mu\text{m}$,^[78,86] or deeper into the mid-infrared (mid-IR). Work using picosecond pump pulses showed OPO oscillation resulting in an idler wavelength of $5.41\ \mu\text{m}$ ^[87] and evidence (inferred from signal tuning data) of idler emission at $6.3\ \mu\text{m}$. After that, demonstration of a PPLN-based picosecond OPO operating at the wavelengths of 6 , 6.2 and $6.57\ \mu\text{m}$ was reported.⁸⁸ More recent work (described in this thesis) demonstrated complete access to the whole transparency range of a

crystal of PPLN, which for the extraordinary polarisation extends up to 7 μm . Femtosecond pulse oscillation that was continuously tunable in a 4 μm range and up to 6.8 μm (in the idler wavelengths) was obtained with significant output powers.⁸⁹ In this way, it has then been demonstrated that femtosecond pulses that are tunable from 2.8 to 6.8 μm can be obtained using single crystal of PPLN in an femtosecond Ti:sapphire-pumped OPO. Finally, as an effort to go further into the mid-IR, Marzenell *et al.* demonstrated an OPO system which showed tunability up to 7.9 μm . However, the extended tunability came at a price since the system had to use a more complicated cascaded approach where a CsTiOAsO₄ - (CTA) based OPO was used to pump another OPO based on a crystal of AgGaSe₂.

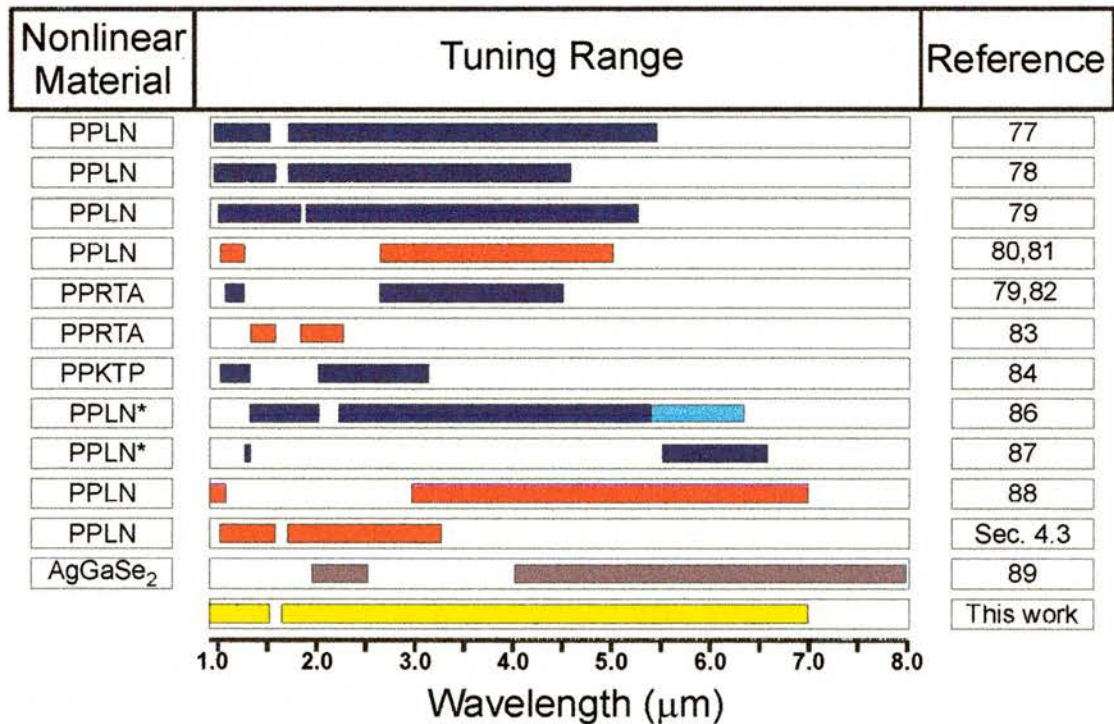


Figure 1. Tuning range of femtosecond OPO based on QPM crystals reported by other groups (blue) and in this work (red/yellow). Included in the figure for comparison purposes: an asterisk (*) indicates OPO working in the picosecond regime; brown indicates that BPM crystals were used; light blue indicates wavelengths inferred from signal measurements.

The next table resume the working characteristics of the OPO systems mentioned in Figure 1.

Pump	Pump Power/ Threshold (W)	Nonlinear Material	Beam	Tuning Range (μm)	Output Power (mW)	$\Delta\tau$ (fs)	Ref.
Millennia + Ti:sapphire (790-815nm)	0.85/ 0.065	PPLN	S	0.925 - 1.56	--	100	77
			I	1.7 - 5.4	20 (5.4 μm)	125	
Ar ⁺ + Ti:sapphire (800nm)	1.5/ 0.045	PPLN	S	0.975 - 1.54	90 (1.35 μm)	140	78
			I	1.67 - 4.55	70 (--)	-	
Millennia + Ti:sapphire (800nm)	1.5/ 0.045	PPLN	S	0.975 - 1.54	240 (1.16 μm)	210	79
			I	1.67 - 5.3	106 (2.6 μm)	190	
Millennia + Ti:sapphire (830nm)	0.90/ --	PPLN	S	0.966 - 1.22	240 (1.16 μm)	210	80,81
			I	2.6 - 4.98	25 (4.88 μm)	190	
Ar ⁺ + Ti:sapphire (830-850nm)	1.2/ --	PPRTA	S	1.06 - 1.225	120 (1.2 μm)	125	79, 82
			I	2.67 - 4.5	105 (2.8 μm)	115	
Ar ⁺ + Ti:sapphire (850nm)	1.0/ 0.090	PPRTA	S	1.375 - 1.575	110 (1.46 μm)	215	83
			I	2.67 - 4.5	60 (2.1 μm)	150	
Ar ⁺ + Ti:sapphire (758nm)	0.65/ 0.15	PPKTP	S	1.0 - 1.235	140 (1.2 μm)	330	84
			I	2.0 - 3.0	--	--	
Ar ⁺ + Ti:sapphire (780-810nm)	1.6/ 1.1-1.5	PPLN	S	0.91 - 1.08	--	--	89
			I	2.8 - 6.8	0.2 (6.5 μm)	150	

Table 1. Working characteristics of reported high-repetition-rate femtosecond OPO based on QPM crystals (Ar⁺ + = argon ion laser as primary pump; Millennia + = Frequency-doubled, diode-pumped NdYVO₄ laser (Spectra Physics), S=signal, I=idler).

SHG with aperiodically-poled nonlinear crystals.

Femtosecond pulses created by periodically poled materials have been successfully used to generate ultrashort pulses covering a spectral range from the visible to the mid-infrared. In the case of SHG of ultrashort pulses using a QPM device, the frequency-doubled generated femtosecond pulses are not always transform-limited because of several factors such as group velocity mismatch, phase mismatch and linear absorption.⁹⁰ In order to reduce the pulse duration for the second harmonic pulses, discrete compression schemes such as pairs of prisms¹⁴ or diffraction gratings⁹¹ have been used.⁹² Also, long interaction lengths that introduce large material dispersion should be avoided and the only alternative to obtain high efficiencies is to use a crystal with the largest nonlinear coefficient available. Although this is partially satisfied by the QPM technique, it was not until recently that the inherent material properties have been used to reduce the duration of second-harmonic pulses. Self-compression of the SHG pulses is made possible by designing crystals with gratings that are not strictly periodic.⁹³ In particular, by fabricating frequency-doubling crystals with a linearly varying grating period one can define the position in the crystal at which any given frequency is converted to its second harmonic. When a broad-bandwidth chirped pulse is used as the input to such a crystal, the variation of its frequency with time can be arranged so that all the converted frequency components exit the crystal simultaneously, in the form of a transform-limited pulse. Compression occurs because of the difference between the group-velocity delay of the fundamental and second harmonic wavelengths and the wavelength dependence of the conversion position. This technique was first demonstrated in aperiodically-poled lithium niobate (AP-LN) to recompress temporally stretched pulses in the picosecond regime from an erbium-doped fibre

laser^{94,95} and a theoretical study of the compression process in AP-LN has been published⁹⁶. Practical limitations on the current technology to engineer small grating periods ($<5 \mu\text{m}$) in periodically-poled crystals have prevented the use of more conventional sources, such as Ti:sapphire lasers, to produce simultaneous SHG and pulse compression in the femtosecond regime. More recently, a synchronously pumped OPO, which was operated without any dispersion compensation elements, was used as a source of chirped femtosecond pulses at longer wavelengths. In this work, femtosecond pulse compression was successfully demonstrated using an aperiodically poled crystal of KTP (AP-KTP)^{97,98} and AP-LN⁹⁹. In both cases, ~ 300 fs chirped pulses from an OPO were frequency doubled and compressed to obtain pulses of 120 and 80 fs respectively.

1.2 The Ti:sapphire laser and modelocking

The Kerr-lens modelocked Ti:sapphire laser has become one of the most important sources of femtosecond pulses. The high gain of the active medium, its tunability and ability to produce stable and reliable ultrashort pulses, serve to explain the success of this laser as a source to synchronously pump OPOs. This section is, therefore, dedicated to the study of this pump source. The pulses emitted by this laser and their subsequent propagation in linear and nonlinear media will also be considered.

1.2.1 The Ti:sapphire gain medium

Ti:sapphire ($\text{Ti}:\text{Al}_2\text{O}_3$) is a uniaxial crystal consisting of a sapphire (Al_2O_3) host doped with a small percentage ($\sim 0.1\%$) of impurity ions (Ti^{3+}). Its molecular structure consists of either a Ti^{3+} ion or an Al^{3+} ion surrounded by an octahedral arrangement of six O^{2-} ions, as shown in Figure 2.

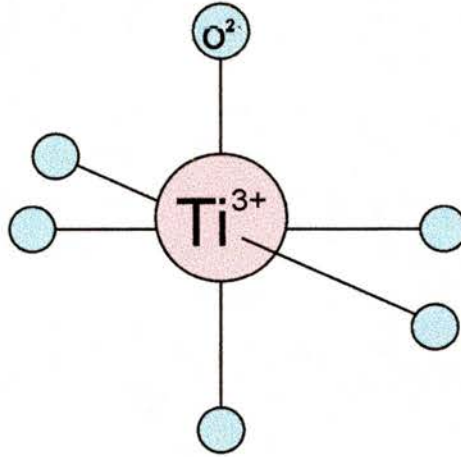


Figure 2. Molecular structure of Ti:sapphire.

Ti:sapphire is a vibronic gain medium, a characteristic of which is that electronic vibrations within the crystal cause laser transitions between broad bands and it is this property which allows the laser output to be both widely and continuously tunable.¹⁰⁰ The Ti^{3+} ion has an electronic configuration of $1s^2 2s^2 2p^6 3s^2 3p^6 3d^1$ and so, it has a closed shell plus one outer $3d^1$ valence electron. This single electron has a 2D ground state, but within the sapphire lattice, the cubic field from the O^{2-} ions splits the energy levels into a triply degenerate 2T_2 ground state and a doubly degenerate 2E excited state. The 2T_2 ground level is split, due to the trigonal arrangement of the Al^{3+} ions, into two levels and the lower of this is split into a two levels by the spin orbit interaction.¹⁰¹ The energy level diagram is shown in Figure 3.

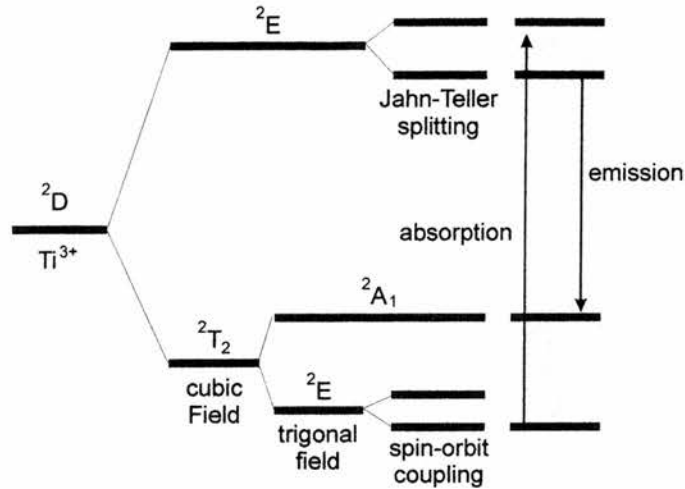


Figure 3. Energy levels in *Ti:sapphire* (from ref. 101)

The peak absorption from the ground 2T_2 state, to the excited 2E state occurs in the visible at around 500 nm and is characterised by a dual peak spectrum caused by the Jahn-Teller splitting. Emission from the excited to the ground states occurs from 600 – 1100 nm with a peak at around 790 nm. Typical absorption and fluorescence spectra are presented in Figure 4^[100].

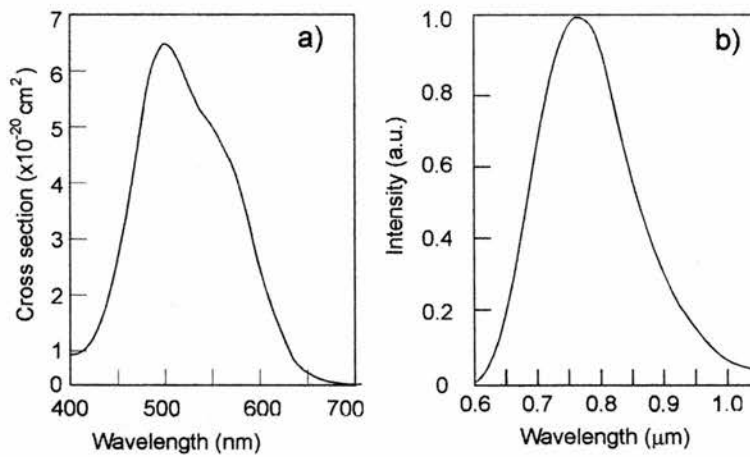


Figure 4. a) Absorption and b) fluorescence spectra of *Ti:sapphire* (from ref. 100)

The short excited state lifetime of 3.15 μs (at 300 K) of a crystal of *Ti:sapphire* limits the type of pump sources to continuous wave (cw), short-pulse or Q-switched. At higher temperatures, the upper-state lifetime falls, but undesirable

non-radiative decay processes occur. At room temperature these nonradiative processes are less significant and it is sufficient to cool the Ti:sapphire crystal using a simple low-pressure water-cooling system. A further advantage is that Ti:sapphire as a laser gain medium, has a relatively large stimulated emission cross-section of $3 \times 10^{-19} \text{ cm}^2$, which allows crystal lengths as short as a few millimetres to be used. Some other spectroscopic and material properties are given in Table 2.¹⁰²

Traditionally, Ti:sapphire lasers are pumped by mainframe argon-ion lasers that produce the appropriate wavelengths of 488 and 514.5 nm to excite the ground state of the crystal. These lasers can produce high output powers ($>10 \text{ W}$), but they require three-phase mains electricity and high pressure water cooling. More recently the all-solid-state diode pumped frequency-doubled ($\lambda = 532 \text{ nm}$) Nd:YVO₄ lasers have gained acceptance and are progressively replacing the argon-ion pump lasers because they are more compact, powered with a single-phase mains electricity and cooled with a closed-loop water cooling system.¹⁰³ However, these lasers are restricted to operation at powers levels up to 10 W.

Property	Value ^[100,102]
Refractive index, n	1.760
Nonlinear refractive index, n_2 .	$3 \times 10^{-16} \text{ cm}^2 \text{ W}^{-1}$
Fluorescence lifetime	3.15 μs
Absorption coefficient	0.7 - 3 cm^{-1}
Gain cross-section	$3 - 4 \times 10^{-19} \text{ cm}^2$
Thermal conductivity	0.33 $\text{Wcm}^{-1}\text{K}^{-1}$
Peak absorption λ	490 nm
Peak emission λ	790 nm
Ti ⁺³ concentration	$1 - 5 \times 10^{19} \text{ cm}^{-3}$

Table 2. Material and spectroscopic properties of Ti:sapphire.

1.2.2 Modelocking

The technique of modelocking has resulted in one of the most important ways in which lasers are employed. With this technique, it is possible to generate pulses of the order of $\sim 10^{-15}$ s. We will briefly consider the phenomenon of mode locking in the next section.

It is well known that in a standing-wave laser cavity of length l (or in a travelling-wave ring cavity of perimeter $p = 2l$), oscillation will take place for those longitudinal modes (or oscillating frequencies) that experience enough gain to overcome the losses inside the cavity. These modes are separated in frequency by:

$$\Delta\nu = \frac{c}{2nl} \quad (1.1)$$

where n is the index of refraction of the gain medium, and c , is the speed of the light in the vacuum. Now we consider the total electrical field resulting from such multimode oscillation at some arbitrary point in the optical resonator:

$$E(t) = \sum_m E_m e^{i[(\omega_0 + m\omega)t + \phi_m]} \quad (1.2)$$

where ϕ_m is the phase of the m th mode and ω_0 is chosen arbitrarily as a reference frequency. In the previous equation, summation is extended over all the oscillating modes. In typical lasers, the phases, ϕ_m , are likely to vary with time. This causes the intensity of the laser output to fluctuate randomly. However, if the phases, ϕ_m , are forced to maintain their relative values, the oscillation intensity will consist of a periodic train with a period $T = 2nl/c$.¹⁰⁴

From this analysis we see that modelocking causes the oscillation energy of the laser to be condensed into a *packet* that travels back and forth between the mirrors with velocity of the light c and period T . A direct consequence of this, is that the

individual pulse width will be smaller and the peak power of these pulses will increase if the number of modes that are locked together increase. In this respect, the high gain and broad bandwidth of the Ti:sapphire gain medium, make this crystal an ideal candidate to construct a modelocked laser as it will be able to support a large number of longitudinal modes simultaneously. There are two main mechanisms to achieve modelocking in a laser, namely active and passive modelocking¹⁰⁵. In the following sections, a brief review of these mechanisms is presented.

Active modelocking

In active modelocking, an amplitude or phase modulator can be used to generate ultrashort pulses. In the case of amplitude modulation, a loss (or gain for diode lasers) modulator is placed inside the laser cavity and driven at a modulation frequency ω_m , that exactly matches the axial-mode spacing, or one of its integer multiples. The axial modes in the laser cavity at frequency ω_q , will acquire modulation sidebands at frequencies $\omega_q \pm n \times \omega_m$, as a result of the active modulator. The modulation sidebands from each axial-mode will fall on top of one of the other axial-modes in the cavity. Each of these sidebands will tend to injection lock with the frequency which it is in resonance and so the intracavity modulator will tend to couple together, or mode-lock, each axial mode the neighbouring modes.

Modelocking can be induced by internal phase, rather than loss, modulation. Typically this is done by placing an electrooptic crystal so that a passing wave will undergo a phase delay proportional to the instantaneous electric field across the crystal. If the frequency of the modulation signal is chosen, to match the longitudinal intermode frequency separation, then, it is possible to show that the distribution of the energy of the modulated electric beam will form sidebands as a function of the

frequency of the modulation.¹⁰⁴ As in the loss modulation case, the modes will become coupled with locked phases.

Passive modelocking

In the previous discussion, modelocking was caused by incorporating a modulator and an external signal is required to activate the modulation mechanism. In contrast to active modelocking, in some other laser systems the effect of periodic gating occurs spontaneously and relies only on the circulating laser field. In this case, a nonlinear element is included in the laser resonator which possess an intensity-dependent loss in a such way that the high power components (e.g. noise features) of the circulating laser field experiences the least loss. The phases of the individual modes adjust themselves to maximise the rate of stimulated emission inside the gain medium. Thus, modelocking operation is favoured over free running cw operation.¹⁰⁶ Because pulse shortening in passive modelocking is driven by the circulating laser field, significantly shorter pulse durations can be obtained compared to active modelocking schemes. Exploitation and optimisation of passive modelocking in a Ti:sapphire laser has allowed the generation of pulses as short as 6 fs.^[107]

Passive modelocking can be achieved by several mechanisms. Some are based on the insertion of a slow or a fast saturable absorber inside the cavity.^{108,109} Others use a regenerative modelocking technique to initiate a high intensity modelocked pulse to initiate self-modelocking.¹¹⁰ Perhaps, the most important modelocking technique (and more relevant to the purposes of this work), is based on passive modelocking using an effective fast saturable absorber and is called self-modelocking or Kerr-lens modelocking.¹³

Kerr-lens modelocking

In a typical Ti:sapphire system, the transverse cavity mode is focused into the gain medium. The high power density produces a nonlinear component at the frequency of the exciting wave which is induced inside the dielectric medium, giving rise to an instantaneous change of the refractive index n_0 proportional to the intensity as follows:

$$n(x, y, z, t) = n_0 + n_2 I(x, y, z, t) \quad (1.3)$$

where n_2 is the nonlinear refractive index. This is called the optical Kerr effect,¹¹¹ and causes self-phase modulation (SPM) in its longitudinal form, and a self-focussing (or Kerr lens) in the transversal form. SPM will also add spectral components to the pulse, and therefore, much shorter pulses can be created with suitable phase correction. SPM will be discussed later and for the moment we will centre our attention to self-focusing which is a dramatic consequence of the nonlinear refractive index. The result of this nonlinear response (in a Gaussian beam) is that the refractive index of the material is larger at the centre of the beam, where the intensity is higher, than at the periphery. Consequently, the medium is turned into a positive lens that focuses the high intensity part of the beam more strongly than the low intensity part. If the Kerr-lens is then combined with an intracavity aperture, the arrangement will produce less loss for high intensities and will form an effective saturable absorber. In this way, the cavity losses are intensity dependent and the system sees a higher gain with increasing intensity. In a suitable cavity, such passive

“self-amplitude” modulation (SAM) can favour modelocked operation over cw operation.¹³ Also, it was demonstrated that the required SAM to self-modelocked a laser could be achieved without the insertion of an intracavity aperture.¹¹²

Although a self-starting self-modelocking laser has been reported,¹¹³ in most instances, a mechanism is usually required to introduce a noise feature inside the laser cavity. There are several techniques to initiate modelocking, the most widely used being an extracavity moving mirror,¹¹⁴ a semiconductor saturable absorber mirror structure (SESAM),¹⁰⁷ or physically translating or tapping a cavity end mirror or prism.¹³

To exploit the full broad bandwidth for generating shorter pulses, the cavity has to have the same effective length for all of the frequencies, simultaneously. Since the refractive index of Ti:sapphire changes as a function of frequency, the pulse becomes dispersed and modelocking could not be achieved. The different dispersion mechanisms and methods to compensate them for, are studied in the following sections.

1.3 Linear and nonlinear pulse propagation

When a polarised electric field, E , interacts with an atomic medium, a corresponding polarisation, P , is induced. The frequency response of the system is characterised by the atomic susceptibility $\chi(\omega)$, which relates the electric and polarisations fields by:

$$P(\omega) = \chi(\omega)\epsilon_0 E(\omega) \quad (1.4)$$

where ϵ_0 is the dielectric permeability of the free space. The refractive index is defined in terms of the atomic susceptibility by:

$$n(\omega) = \sqrt{1 + \chi'(\omega)} \quad (1.5)$$

where $\chi'(\omega) = \text{Re}(\chi(\omega))$. The frequency dependence of the refractive index is known as dispersion and is usually represented in terms of the propagation constant $\beta(\omega)$ as:

$$\beta(\omega) = \frac{\omega}{c} n(\omega) \quad (1.6)$$

The propagation constant $\beta(\omega)$ can be rewritten by a Taylor expansion around a central carrier frequency ω_0 as:

$$\begin{aligned} \beta(\omega) = & \beta(\omega_0) + \frac{d}{d\omega} \beta(\omega_0)(\omega - \omega_0) + \frac{1}{2!} \frac{d^2}{d\omega^2} \beta(\omega_0)(\omega - \omega_0)^2 + \\ & \frac{1}{3!} \frac{d^3}{d\omega^3} \beta(\omega_0)(\omega - \omega_0)^3 + \dots \end{aligned} \quad (1.7)$$

In a pulse, the central carrier frequency, ω_0 , propagates at the phase velocity, v_ϕ . However, the different frequencies within the pulse travel with different velocities. In a normal (positive) dispersion system, the longer wavelength components of a pulse travel faster than shorter wavelengths. Thus, the pulse envelope propagates with an instantaneous group velocity v_g . Broad bandwidth ultrashort pulses propagating inside a dispersive medium, the dispersion of the group velocity (GVD) is important, causing a distortion of the pulse envelope shape. Third order dispersion (TOD) effects become significant when generating pulses of tens of femtoseconds. The various terms of Equation (1.7) are associated with these physical concepts as follows:

$\left[\frac{\beta(\omega_0)}{\omega_0} \right]^{-1}$	is the phase velocity, v_ϕ	$\left[\frac{m}{s} \right]$
$\left[\frac{d}{d\omega} \beta(\omega_0) \right]^{-1}$	is the group velocity, v_g .	$\left[\frac{m}{s} \right]$
$D = \frac{d^2}{d\omega^2} \beta(\omega_0)$	is the group velocity dispersion (GVD).	$\left[\frac{s^2}{m} \right]$
$\frac{d^3}{d\omega^3} \beta(\omega_0)$	is the third order dispersion (TOD).	$\left[\frac{s^3}{m} \right]$

Table 3. Significance of the various terms of Equation (1.7).

In the context of ultrashort pulse propagation, a number of important temporal effects have to be taken into account. Relevant to this work is the temporal walkaway, or group velocity walkaway (GVWA), which determines the degree of temporal overlap between the interacting pulses being generated in a nonlinear medium. Pump-signal and pump-idler GVWA introduce shaping of the OPO pulses by affecting the temporal overlap of the three waves. Because of the absence of gain outside of the temporal window of the pump pulse conversion efficiency is severely restricted. This effect can limit the useful length of nonlinear crystal over which efficient interaction can occur. The effects of temporal walkaway can be estimated by evaluation the difference in pulse arrival times after propagation through 1 mm of material. Expressed in femtoseconds per millimetre this difference is given by :

$$\Delta t = \left(\frac{1}{v_{g1}} - \frac{1}{v_{g2}} \right) * 1\text{mm} \quad (1.8)$$

where the subscripts refer to the two wavelengths being involved in the process.

The majority of pulse broadening in ultrashort pulse lasers occurs by the group-velocity dispersion, which originates in the gain medium. Group velocity dispersion is a linear, temporal effect. As explained before, there exist other pulse-shaping effects in the laser gain medium such as self-phase modulation (SPM). For applied optical signals having strong electric fields, the susceptibility tensor $\chi(\omega)$ shows high order terms (see Equation 2.1) giving rise to a number of nonlinear effects, including SPM through the Kerr effect.

Self-phase modulation

Self-phase modulation is the change in the phase of an optical pulse due to an intensity induced nonlinearity in the refractive index of the material medium and is characterised by equation (1.3). For a pulse propagating in a dielectric medium (with $n_2 > 0$), the refractive index of the material increases with intensity, reaching a maximum at the peak of the pulse and then returning to its original value after the trailing edge of the pulse. Due to this change in the refractive index, the leading edge of the pulse will be shifted to lower frequencies (the arrival of longer wavelengths is advance), and the trailing edge to higher frequencies (the arrival of shorter wavelengths is delayed). Thus, using Equation (1.3), the net phase shift can be written as

$$\phi(t) = \frac{2\pi}{\lambda} (n_0 + n_2 I(t)) z = \phi_0 + \phi_{NL}(t) \quad (1.9)$$

and therefore, the instantaneous frequency will be given by:

$$\omega(t) = \frac{d}{dt} \phi_0 + \frac{d}{dt} \phi_{NL}(t) = \omega_0 + \frac{d}{dt} (Q |E(t)|^2) \quad (1.10)$$

where Q is a negative (to be consistent with this analysis) proportionality constant that depends on the linear and nonlinear properties of the Kerr-medium.

The frequency shift across the middle part of a pulse produced by a self-modelocked Ti:sapphire laser, is approximately linear and is similar to the frequency shift produced by propagation through a positive dispersive material. Therefore, the spectral distortion effect of SPM can also be minimised using a mechanism to compensate for material dispersion.

Pulse chirping

As mentioned before, GVD (and SPM in the middle part of a smooth pulse) in a positively dispersive material, produce a linearly time-varying instantaneous frequency. Such a signal is often said to have positive linear frequency *chirp*. A convenient way to express the linear chirp of a pulse is by adding to the instantaneous frequency a linearly varying function so that Equation (1.10) (in absence of SPM) can be rewritten as:

$$\frac{d}{dt}\phi = \omega(t) = \omega_0 + 2bt \quad (1.11)$$

Thus, an optical pulse with a carrier frequency, ω_0 , will be:

$$E(t) \propto \exp\left[-j(\omega_0 t + bt^2)\right] \quad (1.12)$$

with the parameter b as a measure of this chirp. From Equation (1.12), it can be seen that a positive linear chirp ($b > 0$), produces a quadratic dependence on the temporal phase of the pulse (examples of pulses with positive linear chirp will be presented in detail in Chapter 5).

In the frequency domain, a signal with frequency chirp will also have a phase shift of the Fourier spectrum in frequency, but most important, it can be shown that the presence of frequency chirp increases the spectral bandwidth, $\Delta\nu_{ch}$, compared to an unchirped pulse, $\Delta\nu$, with the same pulsewidth in time.¹⁰⁵ In the case of a

Gaussian pulse with duration, τ_p (measured at full width at half maximum,(FWHM)), and with linear frequency chirp, the ratio of increment of spectral bandwidth is given by:

$$\frac{\Delta v_{ch}}{\Delta v} = \sqrt{1 + \left(\frac{b}{a}\right)^2} \quad (1.13)$$

where the parameter a is related to the duration of an unchirped pulse as $\tau_p = \sqrt{2 \ln 2 / a}$.

From the general Fourier theorem we know that the time-bandwidth product, $\Delta v \Delta \tau$, of the shortest pulse which can be supported by a particular frequency bandwidth pulse is constrained by the uncertainty principle. In the case of Gaussian pulses $\Delta v_p \Delta \tau_p \geq 0.44$, where Δv_p and $\Delta \tau_p$ are measured at FWHM. The exact value of the time-bandwidth product $\Delta v \Delta t$ of an arbitrary pulse shape depends, however, on the exact temporal intensity profile, the definition used to measure Δv_p and $\Delta \tau_p$ and the amount of chirp within the pulse. For chirped pulses, the time-bandwidth product is, therefore, not minimum, and it can be shown that for linear frequency chirp, a Gaussian pulse is related to the time-bandwidth product as:

$$\Delta v_p \Delta \tau_p = 0.44 \times \sqrt{1 + \left(\frac{b}{a}\right)^2} \quad (1.14)$$

For pulses with no chirp, ($b = 0$, in Equation (1.14)) the pulse is said to be *transform limited*. In the next section, a technique to reduce the amount of chirp on a pulse to obtain pulses with a minimum time-bandwidth product, will be studied.

Dispersion compensation

Different compression schemes, to compensate for GVD, have been proposed. These are based on pairs of prisms,¹⁴ pairs of diffraction gratings⁹¹ and

chirped mirrors.¹¹⁵ In this section the use of pairs of prisms to compensate for GVD will be considered. The experimental arrangement is illustrated in Figure 5.

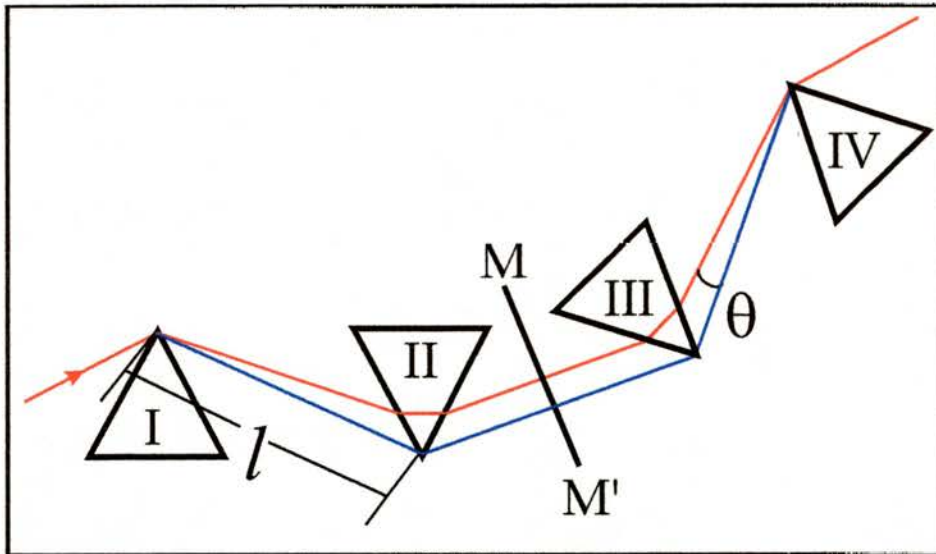


Figure 5. Prisms sequence to compensate for dispersion.

The experimental set up consists, typically, of a sequence of four identical prisms. These are cut in such a way that the angle of incidence is both the Brewster angle and the minimum deviation angle in order to minimise displacement and losses. In this arrangement, the output face of prism I is parallel to the input face of prism II. The plane MM' is normal to the exit rays and defines a symmetry plane for the other two prisms. Due to this symmetry, a similar arrangement can be obtained by using only the prisms I and II and placing a mirror in the plane MM'.

To calculate total dispersion of the prism sequence we rewrite the expression for the dispersion, D , (the third term on Equation (1.7)) in terms of the optical path length, P , as

$$D = \frac{\lambda}{cL} \frac{d^2 P}{d\lambda^2} \quad (1.15)$$

where L is the physical length of the light path. The derivative $d^2P/d\lambda^2$ is a function of the angular divergence θ , the refractive index of the prism material n , and the apex separation, l , of the prisms. Equation (1.15) can be rewritten as:

$$\frac{d^2P}{d\lambda^2} = 4l \left\{ \left[\frac{d^2n}{d\lambda^2} + \left(2n - \frac{1}{n^3} \right) \left(\frac{dn}{d\lambda} \right)^2 \right] \sin(\theta) - 2 \left(\frac{dn}{d\lambda} \right)^2 \cos(\theta) \right\} \quad (1.16)$$

It can be shown that by changing the prism positions l , it is possible to vary the total dispersion of the cavity from positive to negative.

The use of prism pairs has been successfully used to compensate for group velocity dispersion systems such as Ti:sapphire lasers. However, if pulses in the sub-100 fs regime are required, third-order dispersion effects become important and have to be compensated. In this case, a careful selection of the prism material should be made and the amount of material inside the cavity should be kept to a minimum.¹¹⁶ Alternatively, by using chirped dielectric mirrors as the source of broadband negative GVD, TOD effects are minimised as no intracavity glass is present inside the cavity. With these mirrors, generation of 5–6 fs laser pulses have been generated.^{107,117,118}

1.4 Conclusions

In this chapter, it can be seen that femtosecond lasers can be used as versatile sources for several applications. These applications rely, mainly, on the high peak powers and high repetition rates that conventional sources of femtosecond pulses can provide. In some applications it is also desirable to extend the spectral range of such optical sources. One way to do this, is by taking advantage of their high pump

intensities to exploit nonlinear frequency generation techniques, notably optical parametric oscillation and harmonic generation. With these two techniques, it has been possible to extend the tunability range of ultrashort pulses, while keeping, at the same time, high average output powers and high repetition rates. Thus, in the first half of this chapter, a general overview of the progress, of these two techniques has been presented.

The Ti:sapphire laser as a pump source for an OPO has been studied in the second part of this chapter. The physical properties of the Ti:sapphire gain medium, and the mechanisms involved to achieve Kerr-lens modelocking have been described. The consequent behaviour of the output pulses and the characteristics of ultrashort pulses under propagation through linear and nonlinear media have also been studied.

The short pulse durations and consequent high peak powers obtained from Ti:sapphire lasers have been successfully exploited to pump OPOs. However, to achieve efficient nonlinear frequency-conversion, a proper choice of the nonlinear crystal must also be considered. In Chapter 2, the nonlinear crystals that have been used in this work and the mechanisms under which efficient frequency-conversion takes place is described.

1.5 References

1. A. H. Zewail, "Laser femtochemistry," *Science*, **242**, 1645 – 1653 (1988).
2. M. Dantus, R. M. Bowman, A. H. Zewail, "Femtosecond laser observations of molecular vibration and rotation," *Nature*, **343**, 737 – 739 (1990).
3. S. Maiti, "Measuring serotonin distribution in live cells with three photon excitation," *Science*, **275**, 530 – 532 (1997).
4. C. Xu, W. Denk, "Two-photon optical beam induced current imaging through the backside of integrated circuits," *Appl. Phys. Lett.*, **71**, 2578 – 2580 (1997).
5. A. P. Kanavin, I. V. Smetanin, V. A. Isakov, Y. V. Afanasiev, B. N. Chichkov, B. Wellegehausen, S. Nolte, C. Momma, A. Tunnermann, "Heat transport in metals irradiated by ultrashort laser pulses," *Phys. Rev. B*, **57**, 14698 – 14703 (1998).
6. H. K. Tonshoff, C. Momma, A. Ostendorf, S. Nolte, G. Kamlage, "Microdrilling of metals with ultrashort laser pulses," *J. Laser Appl.*, **12**, 23 – 27 (2000).
7. A. J. A. Smith, A. G. Roddie, D. Henderson, "Electrooptic sampling of low temperature GaAs pulse generators for oscilloscope calibration," *Opt. Quantum. Electron.*, **28**, 933 – 943 (1996).
8. J. A. Valdmanis, "1-THz-bandwidth probe for high-speed devices and integrated-circuits," *Electron. Lett.*, **23**, 1308 – 1310 (1987).
9. A. Hache, J. E. Sipe, H. M. van Driel, "Quantum interference control of electrical currents in GaAs," *IEEE J. Quantum Electron.*, **34**, 1144 – 1154 (1998).
10. R. L. Fork, B. I. Greene, C. V. Shank, "Generation of optical pulses shorter than 0.1 psec by colliding pulse mode-locking," *Appl. Phys. Lett.*, **38**, 671 – 672 (1981).
11. L. F. Mollenauer, R. H. Stolen, "The soliton laser," *Opt. Lett.*, **9**, 13 – 15 (1984).
12. K. J. Blow, D. Wood, "Mode-locked lasers with nonlinear external cavities," *J. Opt. Soc. Am. B*, **5**, 629 – 632 (1988).
13. D. E. Spence, P. N. Kean, W. Sibbett, "60-femtosecond pulse generation from a self-mode-locked Ti:sapphire laser," *Opt. Lett.*, **16**, 42 – 44 (1991).
14. R. L. Fork, O. E. Martinez, J. P. Gordon. "Negative dispersion using a pair of prisms," *Opt. Lett.*, **9**, 150 – 152 (1984).
15. U. Keller, D. A. B. Miller, G. D. Boyd, T. H. Chiu, J. F. Ferguson, M. T. Asom, "Solid-state low-loss intracavity saturable absorber for Nd:YLF lasers - an antiresonant semiconductor fabry-perot saturable absorber," *Opt. Lett.*, **17**, 505 – 507 (1992).
16. R. Mellish, P. M. W. French, J. R. Taylor, P. J. Delfyett, L. T. Florez, "Self-starting femtosecond Ti:sapphire laser with intracavity multiquantum-well absorber," *Electron. Lett.*, **29**, 894 – 896 (1993).
17. U. Keller, K. J. Weingarten, F. X. Kartner, D. Kopf, B. Braun, I. D. Jung, R. Fluck, C. Honninger, N. Matuschek, J. A. derAu, "Semiconductor saturable absorber mirrors (SESAM's) for femtosecond to

- nanosecond pulse generation in solid-state lasers," *IEEE J. Sel. Top. Quantum Electron.*, **2**, 435 – 453 (1996).
18. S. Tsuda, W. H. Knox, S. T. Cundiff, W. Y. Jan, J. E. Cunningham, "Mode-locking ultrafast solid-state lasers with saturable Bragg reflectors," *IEEE J. Sel. Top. Quantum Electron.*, **2**, 454 – 464 (1996).
 19. D. M. Finlayson, B. D. Sinclair, "*Advances in lasers and applications*," Proceedings of the fifty second Scottish Universities Summer School in Physics, St. Andrews, (Institute of Physics publishing) Sep. 1998 ISBN 07503-0631-9.
 20. K. Tamura, E. P. Ippen, H. A. Hauss, L. E. Nelson, "77-fs pulse generation from a stretched-pulse mode-locked all-fiber ring laser," *Opt. Lett.*, **18**, 1080 – 1082 (1993).
 21. L. E. Nelson, D. J. Jones, K. Tamura, H. A. Hauss, E. P. Ippen, "Ultrashort-pulse fiber ring lasers," *Appl. Phys. B*, **65**, 277 – 294 (1997).
 22. M. Ebrahimzadeh, R. Eckardt, M. H. Dunn, Editors of special issue on "Optical parametric processes and their applications," *J. Opt. Soc. Am. B*, **16**, 1475 – 1597 (1999).
 23. K. Burneika, M. Ignatavichyus, V. Kabelka, A. Piskarskas, A. Stabinis, "Parametric light amplification and oscillation in KDP with mode-locked pump," *IEEE J. Quantum Electron.*, **8**, 574 (1972).
 24. A. Laubereau, L. Greiter, W. Kaiser, "Intense tunable picosecond pulses in the infrared," *Appl. Phys. Lett.*, **25**, 87 – 89 (1974).
 25. B. Bareika, R. Danielius, G. Dikchius, R. Gadonas, A. Piskarskas, V. Sirutkaitis, "Subpicosecond tunable IR pulses - synchronously pumped OPO with color-center amplifier," *Appl. Phys. B*, **29**, 176 – 176 (1982).
 26. T. Kushida, Y. Tanaka, M. Ojima, "Tunable picosecond pulse generation by optical parametric oscillator," *Jpn. J. Appl. Phys.*, **16**, 2227 – 2235 (1977).
 27. A. S. Piskarskas, V. J. Smilgevicius, A. P. Umbrasas, J. P. Judisius, A. S. L. Gomes, J. R. Taylor, "Picosecond optical parametric oscillator pumped by temporally compressed pulses from a Q-switched, mode-locked, cw-pumped Nd:YAG laser," *Opt. Lett.*, **14**, 557 – 559 (1989).
 28. A. S. Piskarskas, V. J. Smilgevicius, A. P. Umbrasas. "The parametric generation of bandwidth-limited picosecond light pulses," *Opt. Commun.*, **73**, 322 – 324 (1989).
 29. L. J. Bromley, A. Guy, D. C. Hanna, "Synchronously pumped optical parametric oscillation in beta-barium borate," *Opt. Commun.*, **67**, 316 – 320 (1988).
 30. M. Ebrahimzadeh, G. J. Hall, A. I. Ferguson, "Singly resonant, all-solid-state, mode-locked LiB₃O₅ optical parametric oscillator tunable from 652 nm to 2.65 μ m," *Opt. Lett.*, **17**, 652 – 654 (1992).
 31. L. J. Bromley, A. Guy, D. C. Hanna, "Synchronously pumped optical parametric oscillation in KTP," *Opt. Commun.*, **70**, 350 – 354 (1989).
 32. A. S. Piskarskas, V. I. Smil'gyavichyus, A. P. Umbrasas, "Continuous parametric generation of picosecond light pulses," *Sov. J. Quantum. Electron.*, **18**, 155 – 156 (1988).
 33. M. Ebrahimzadeh, G. P. A. Malcolm, A. I. Ferguson, "Continuous-wave mode-locked optical parametric oscillator synchronously pumped by a diode-laser-pumped solid-state laser," *Opt. Lett.*, **17**, 183 – 185 (1992).

34. J. E. Bjorkholm, "Some spectral properties of doubly and singly resonant pulsed optical parametric oscillators," *Appl. Phys. Lett.*, **13**, 399 – 401 (1968).
35. J. Falk, "Instabilities in the doubly resonant parametric oscillator: a theoretical analysis," *IEEE J. Quantum Electron.*, **7**, 230 – 235 (1971).
36. D. C. Edelstein, E. S. Wachman, C. L. Tang, "Broadly tunable high repetition rate femtosecond optical parametric oscillator," *Appl. Phys. Lett.*, **54**, 1728 – 1730 (1989).
37. E. S. Wachman, D. C. Edelstein, C. L. Tang, "Continuous-wave mode-locked and dispersion-compensated femtosecond optical parametric oscillator," *Opt. Lett.*, **15**, 136 – 138 (1990).
38. G. Mak, Q. Fu, H. M. van Driel, "Externally pumped high repetition rate femtosecond infrared optical parametric oscillator," *Appl. Phys. Lett.*, **60**, 542 – 544 (1991).
39. M. J. McCarthy, D. C. Hanna, "Continuous-wave mode-locked singly resonant optical parametric oscillator synchronously pumped by a laser-diode-pumped Nd:YLF laser," *Opt. Lett.*, **17**, 402 – 404 (1992).
40. W. S. Pelouch, P. E. Powers, C. L. Tang, "Ti:sapphire-pumped high-repetition-rate optical parametric oscillator," *Opt. Lett.*, **17**, 1070 – 1072 (1992).
41. Q. Fu, G. Mak, H. M. van Driel, "High power 62-fs infrared optical parametric oscillator pumped by a 76-MHz Ti:sapphire laser," *Opt. Lett.*, **17**, 1006 – 1008 (1992).
42. G. M. Gale, F. Hache, L. I. Pavlov: *Ultrafast Phenomena VII*, ed. by C. B. Harris, E. P. Ippen, G. A. Mourou, A. H. Zewail, Berlin, Heidelberg **53** Springer, 1990.
43. G. M. Gale, F. Hache, M. Cavallari, "Broad-bandwidth parametric amplification in the visible: Femtosecond experiments and simulations," *IEEE J. Sel. Top. Quantum. Electron.*, **4**, 224 – 229 (1998).
44. G. M. Gale, M. Cavallari, F. Hache, "Femtosecond visible optical parametric oscillator," *J. Opt. Soc. Am. B*, **15**, 702 – 714 (1998).
45. J. D. Kafka, M. L. Watts, J. Pieterse, "A synchronously pumped parametric oscillator producing 40 fs pulses," In *Conference on Lasers and Electro-Optics*, OSA Technical Digest (Optical Society of America, Washington DC, 1993), **11**, Postdeadline paper CPD32, p. 736.
46. P. E. Powers, S. Ramakrishna, C. L. Tang, "Optical parametric oscillation with KTiOAsO_4 ," *Opt. Lett.*, **18**, 1171 – 1173 (1993).
47. D. T. Reid, C. McGowan, M. Ebrahimzadeh, W. Sibbett, "Characterization and modeling of a noncollinearly phase-matched femtosecond optical parametric oscillator based on KTA and operating to beyond 4 μm ," *IEEE J. Quantum Electron.*, **33**, 1 – 9 (1997).
48. D. E. Spence. S. Wielandy, C. L. Tang, "High-repetition-rate femtosecond optical parametric oscillator based on KNbO_3 ," *Opt. Lett.*, **19**, 680 – 682 (1994).
49. P. E. Powers, C. L. Tang, L. K. Cheng, "High-repetition-rate optical parametric oscillator based on CsTiOAsO_4 ," *Opt. Lett.*, **19**, 37 – 39 (1994).
50. P. E. Powers, R. J. Ellingson, W. S. Pelouch. C. L. Tang, "Recent advances of the Ti-sapphire-pumped high-repetition-rate femtosecond optical parametric oscillator," *J. Opt. Soc. Am. B*, **10**, 2162 – 2167 (1993).

51. P. E. Powers, C. L. Tang, L. K. Cheng, "High-repetition-rate optical parametric oscillator based on RbTiOAsO₄," *Opt. Lett.*, **19**, 1439 – 1441 (1994).
52. D. T. Reid, M. Ebrahimzadeh, W. Sibbett, "Noncritically phase-matched Ti:sapphire-pumped femtosecond optical parametric oscillator based on RbTiOAsO₄," *Opt. Lett.*, **20**, 55 – 57 (1995)
53. D. T. Reid, C. McGowan, W. Sleat, M. Ebrahimzadeh, and W. Sibbett, "Characterization and modeling of a noncollinearly phase-matched femtosecond optical parametric oscillators," *IEEE J. Quantum. Electron.*, **33**, 1 – 9 (1997).
54. D. T. Reid, M. Ebrahimzadeh, and W. Sibbett, "Design criteria and comparison of femtosecond optical parametric oscillators based on KTiOPO₄ and RbTiOAsO₄," *J. Opt. Soc. Am. B*, **12**, 2168 – 2179 (1995).
55. S. Marzenell, R. Beigang and R. Wallenstein, "Synchronously pumped femtosecond optical parametric oscillator based on AgGaSe₂ tunable from 2 μm to 8 μm," *Appl. Phys. B*, **60**, 423 – 428 (1999).
56. J. M. Dudley, D. T. Reid, M. Ebrahimzadeh, and W. Sibbett, "Characteristics of a noncritically phase-matched Ti:sapphire-pumped femtosecond optical parametric oscillator," *Opt. Commun.*, **104**, 419 – 430 (1994).
57. D. T. Reid, J. M. Dudley, M. Ebrahimzadeh, W. Sibbett, "Soliton formation in a femtosecond optical parametric oscillator," *Opt. Lett.*, **19**, 825 – 827 (1994).
58. R. J. Elligston, C. L. Tang, "High-power high-repetition-rate femtosecond pulses tunable in the visible," *Opt. Lett.*, **18**, 438 – 440 (1994).
59. D. T. Reid, M. Ebrahimzadeh, W. Sibbett, "Efficient femtosecond pulse generation in the visible in a frequency-doubled optical parametric oscillator based on RbTiOAsO₄," *J. Opt. Soc. Am. B*, **12**, 1157 – 1163 (1995).
60. J. A. Armstrong, N. Bloembergen, J. Ducuing, P. S. Peshan, "Interactions between light waves in a nonlinear dielectric," *Phys. Rev.*, **127**, 1918 – 1939 (1962).
61. J. C. Diels and W. Rudolph, "Ultrashort Laser Pulse Phenomena," Academic Press, New York, (1996).
62. M. H. Dunn, M. Ebrahimzadeh, "Parametric generation of tunable light from continuous-wave to femtosecond pulses." *Science*, **286**, 1513 – 1517 (1999).
63. D. E. Thompson, J. D. McMullen, D. B. Anderson, "Second harmonic generation in GaAs 'stack of plates' using high power CO₂ laser radiation," *Appl. Phys. Lett.*, **29**, 113 – 115 (1976).
64. E. Lallier, M. Brevignon, J. Lehoux, "Efficient second-harmonic generation of CO₂ lasers with a quasi-phase-matched GaAs Crystal," *Opt. Lett.*, **23**, 1511 – 1513 (1998).
65. H. Karlsson, F. Laurell, P. Henriksson and G. Arvidsson, "Frequency doubling in periodically poled RbTiOAsO₄," *Electron Lett.*, **32**, 556 – 557 (1996).
66. E. J. Lim, M. M. Fejer, R. L. Byer, "Second-harmonic generation of green light in periodically poled planar lithium niobate waveguide," *Electron. Lett.*, **25**, 174 – 175 (1989).
67. G. Khanarian, M. A. Mortazavi, A. J. East, "Phase-matched second-harmonic generation from free standing periodically stacked polymer films," *Appl. Phys. Lett.*, **63**, 1462 – 1464 (1993).

68. M. A. Mortazavi, G. Khanarian, "Quasi-phase-matched frequency doubling in bulk periodic polymeric structures," *Opt Lett.*, **19**, 1290 – 1292 (1994).
69. M. M. Fejer, G. A. Magel, D. H. Jundt, R. L. Byer, "Quasi-phase-matched second-harmonic generation: tuning and tolerances," *IEEE J. Quantum Electron.*, **28**, 2631 – 2654 (1992).
70. L. E. Myers, R. C. Eckardt, M. M. Fejer, R. L. Byer, W. R. Bosenberg, J. W. Pierce, "Quasi-phase-matched optical parametric oscillators in bulk periodically poled LiNbO₃," *J. Opt. Soc. Am. B*, **12**, 2102 – 2116 (1995).
71. A. Feiss, P. Koidl, "Current induced periodic ferroelectric domain structures in LiNbO₃ applied for efficient nonlinear optical frequency mixing," *Appl. Phys. Lett.*, **47**, 1125 – 1127 (1985).
72. M. Asobe, I. Yokohama, H. Itoh, T. Kaino, "All-optical switching by use of cascading of phase-matched sum-frequency-generation and difference-frequency-generation processes in periodically poled LiNbO₃," *Opt. Lett.*, **47**, 1125 – 1127 (1997).
73. L. Goldberg, W. K. Burns, R. W. McElhanon, "Difference frequency generation of tunable mid-infrared radiation in bulk periodically poled LiNbO₃," *Opt. Lett.*, **22**, 274 – 276 (1995).
74. A. Galvanaskus, M. A. Arbore, M. M. Fejer, M. E. Fermann, D. Harter, "Fiber-laser-based femtosecond parametric generation in bulk periodically poled LiNbO₃," *Opt. Lett.*, **22**, 105 – 107 (1997).
75. J. J. Zayhowski, "Periodically poled lithium niobate optical parametric amplifiers pumped by high-power passively Q-switched microchip lasers," *Opt. Lett.*, **22**, 105 – 107 (1997).
76. S. D. Butterworth, V. Pruneri, D. C. Hanna, "Optical parametric oscillation in periodically poled lithium niobate based on continuous-wave synchronous pumping at 1.047 μm ," *Opt. Lett.*, **21**, 1345 – 1347 (1996).
77. S. D. Butterworth, P. G. R. Smith, D. C. Hanna, "Picosecond Ti:sapphire pumped optical parametric oscillator based on periodically poled LiNbO₃," *Opt. Lett.*, **22**, 618 – 620 (1997).
78. K. C. Burr, C. L. Tang, M. A. Arbore, M. M. Fejer, "Broadly tunable mid-infrared femtosecond optical parametric oscillator using all-solid-state-pumped periodically poled lithium niobate," *Opt. Lett.*, **22**, 1458 - 1460 (1997).
79. C. McGowan, D. T. Reid, Z. E. Penman, M. Ebrahimzadeh, W. Sibbett, D. H. Jundt, "Femtosecond optical parametric oscillator based on periodically poled lithium niobate," *J. Opt. Soc. Am. B*, **15**, 694 – 701 (1998).
80. D. T. Reid, G. T. Kennedy, A. Miller, W. Sibbett, M. Ebrahimzadeh, "Widely tunable, near- to mid-infrared femtosecond and picosecond optical parametric oscillators using periodically poled LiNbO₃ and RbTiOAsO₄," *IEEE J. Quantum Electron.*, **4**, 238 – 248 (1998).
81. Z. E. Penman, P. Loza-Alvarez, D. T. Reid, M. Ebrahimzadeh, W. Sibbett, D. H. Jundt, "All-solid-state mid-infrared femtosecond optical parametric oscillator based on periodically-poled lithium niobate," *Opt. Comm.*, **146**, 147 - 150 (1998).
82. Z. E. Penman, C. McGowan, P. Loza-Alvarez, D. T. Reid, M. Ebrahimzadeh, W. Sibbett, D. H. Jundt, "Femtosecond optical parametric oscillators based on periodically poled lithium niobate," *J. Mod. Opt.*, **45**, 1285 – 1294 (1998).

83. D. T. Reid, Z. Penman, M. Ebrahimzadeh, W. Sibbett, H. Karlsson, F. Laurell, "Broadly-tunable infrared femtosecond optical parametric oscillator based on periodically-poled RbTiOAsO₄," *Opt. Lett.*, **22**, 1397 – 1399 (1997).
84. P. Loza-Alvarez, D. T. Reid, M. Ebrahimzadeh, W. Sibbett, H. Karlsson, P. Henriksson, G. Arvidsson, F. Laurell, "Periodically poled RbTiOAsO₄ femtosecond optical parametric oscillator tunable from 1.38 to 1.58 μm " *Appl. Phys. B*, **68**, 177 – 180 (1999).
85. T. Kartaloglu, K. G. Koprulu, O. Aytur, M. Sundheimer, W. P. Risk, "Femtosecond optical parametric oscillator based on periodically poled KTiOPO₄," *Opt. Lett.*, **23**, 61 – 63 (1998).
86. L. Lefort, K. Puech, S. D. Butterworth, G.W. Ross, P. G. R. Smith, D.C. Hanna, D. H.Jundt, "Efficient, low-threshold synchronously-pumped parametric oscillation in periodically-poled lithium niobate over the 1.3 μm to 5.3 μm range," *Opt. Com.*, **152**, 55 – 58 (1998).
87. L. Lefort, K. Puech, G.W. Ross, Y.P. Svirko and D.C. Hanna, "Optical parametric oscillation out to 6.3 μm in periodically poled lithium niobate under strong idler absorption," *Appl. Phys. Letts.*, **73**, 1610 – 1612 (1998).
88. M. Sato, T. Hatanaka, S. Izumi, T. Taniuchi, H. Ito. "Generation of 6.6- μm optical parametric oscillation with periodically poled LiNbO₃," *Appl. Opt.*, **38**, 2560 – 2563 (1999).
89. P. Loza-Alvarez, C. T. A. Brown, D. T. Reid, W. Sibbett, M. Missey, "High repetition rate ultrashort-pulse optical parametric oscillator continuously tunable from 2.8 to 6.8 μm ," *Opt. Lett.*, **24**, 1523 – 1525 (1999).
90. E. Sidick, A. Knoesen, A. Dienes, "Ultrashort-pulse second-harmonic generation in quasi-phase-matched dispersive media," *Opt Lett.*, **19**, 266 – 268 (1994).
91. E. B. Treacy, "Optical pulse compression with diffraction gratings," *IEEE J. Quantum Electron.*, **5**, 454 – 458 (1969).
92. M. A. Arbore, M. M. Fejer, M. E. Fermann, A. Hariharan, A. Galvanauskas, D. Harter, "Frequency doubling of femtosecond erbium-fiber soliton laser in periodically poled lithium niobate," *Opt. Lett.*, **22**, 13 – 15 (1997).
93. M. A. Arbore, A. Galvanauskas, D. Harter, M. H. Chou, M. M. Fejer, "Compression of ultrashort pulses using second-harmonic generation in aperiodically poled lithium niobate," In *Conference on Lasers and Electro-Optics*, OSA Technical Digest (Optical Society of America, Washington DC, 1997), **6**, p. 736. Postdeadline paper CPD6-2.
94. M. A. Arbore, A. Galvanauskas, D. Harter, M. H. Chou, M. M. Fejer, "Engineerable compression of ultrashort pulses by use of second-harmonic generation in chirped-period-poled lithium niobate," *Opt. Lett.*, **22**, 1341 – 1343 (1997).
95. A. Galvanauskas, D. Harter, M. A. Arbore, M. H. Chou, M. M. Fejer, "Chirped-pulse amplification circuits for fiber amplifiers, based on chirped-period quasi-phase-matching gratings," *Opt. Lett.*, **23**, 1695 – 1697 (1998).
96. M. A. Arbore, O. Marco, M. M. Fejer, "Pulse compression during second-harmonic generation in aperiodic quasi-phase-matching gratings," *Opt. Lett.*, **22**, 865 – 867 (1997).
97. P. Loza-Alvarez, D. T. Reid, P. Faller, M. Ebrahimzadeh, W. Sibbett, H. Karlsson, F. Laurell, "Simultaneous femtosecond-pulse compression and second-harmonic generation in aperiodically poled KTiOPO₄," *Opt. Lett.*, **24**, 1071 – 1073 (1999).

98. P. Loza-Alvarez, D. T. Reid, P. Faller, M. Ebrahimzadeh, W. Sibbett, "Simultaneous second-harmonic generation and femtosecond-pulse compression in aperiodically poled KTiOPO_4 with a RbTiOAsO_4 -based optical parametric oscillator," *J. Opt. Soc. Am. B*, **16**, 1553 – 1560 (1999).
99. P. Loza-Alvarez, D. T. Reid, P. Faller, M. Ebrahimzadeh, W. Sibbett, D. Artigas, M. Missey, "Frequency-doubling and compression of chirped femtosecond pulses using aperiodically-poled lithium niobate," In *Conference on Lasers and Electro-Optics*, OSA Technical Digest (Optical Society of America, Washington DC, 2000), pp. 476, paper CThM38.
100. P. F. Moulton, "Spectroscopic and laser characteristics of $\text{Ti:Al}_2\text{O}_3$," *J. Opt. Soc. Am. B*, **3**, 125 – 133 (1986).
101. E. D. Nelson, J. Y. Wong, A. L. Shawlow, "Far infrared spectra of $\text{Al}_2\text{O}_3:\text{Cr}^{3+}$ and $\text{Al}_2\text{O}_3:\text{Ti}^{3+}$," *Phys. Rev.*, **156**, 298 – 308 (1967).
102. K. Oppo, *Tunable femtosecond lasers with low pump thresholds*, Doctoral thesis, School of Physics and Astronomy, University of St. Andrews, Scotland (1996)
103. W. L. Nigham, Jr. S. B. Hutchinson, D. Dudley, M. S. Keirstead, "Highly efficient, diode-bar-end-pumped Q-switched Nd:YAG laser with 11 W TEM_{00} output," in *Conference on Lasers and Electro-Optics*, OSA Technical Digest (Optical Society of America, Washington DC, 1996) pp. 320, paper CWN2.
104. A. Yariv, "Internal modulation in multimode laser oscillators," *J. Appl. Phys.*, **36**, 388 (1965).
105. A. E. Siegman, "Lasers", University Science Books, (California, USA 1986).
106. S. E. Shwarz, T. Y. Tan, "Wave interactions in saturable absorbers," *Appl. Phys. Lett.*, **10**, 4 (1967).
107. I. D. Jung, F. X. Kärtner, N. Matuscheck, D. H. Sutter, F. Morier-Genoud, Z. Shi, V. Scheuer, M. Tisch, T. Tschudi, U. Keller, "Semiconductor saturable absorber mirrors supporting sub-10-fs pulses," *Appl. Phys. B*, **65**, 137 – 150 (1997).
108. H. Mocker, R. J. Collins, "Mode competition and self-locking effects in a Q-switched ruby laser," *Appl. Phys. Lett.*, **7**, 270 (1965).
109. A. J. DeMaria, D. A. Stetser, H. Heynau, "Self mode-locking of laser with saturable absorbers," *Appl. Phys. Lett.*, **8**, 174 (1966).
110. D. E. Spence, J. M. Evans, W. E. Sleat, W. Sibbett, *Opt. Lett.*, "Regeneratively initiated self-mode-locked Ti:sapphire laser," **17**, 1762 – 1764 (1991).
111. R. W. Boyd, "Nonlinear optics," Academic Press Inc., (California, USA, 1992).
112. J. Herrmann, "Theory of Kerr-lens mode-locking - role of self-focusing and radially varying gain," *J. Opt. Soc. Am. B*, **11**, 498 – 512 (1994).
113. G. Cerullo, S. De Silvestri, V. Magni, "Self-starting Kerr-lens mode-locking of a Ti:sapphire laser," *Opt. Lett.*, **19**, 1040 – 1042 (1994).
114. N. H. Rizvi, P. M. W. French, J. R. Taylor, "Continuously self-mode-locked Ti:sapphire laser that produces sub-50-fs pulses," *Opt. Lett.*, **17**, 279 – 281 (1992).
115. R. Szipocs, K. Ferencz, C. Spielmann & F. Krausz, "Chirped multilayer coatings for broadband dispersion control in femtosecond lasers," *Opt. Lett.*, **19**, 204 – 206 (1994).

116. C. Huang, M. T. Asaki, S. Backus, M. M. Murnane, H. C. Kapteyn, "17-fs pulses from a self-mode-locked Ti:sapphire laser," *Opt. Lett.*, **17**, 1289 – 1291 (1992).
117. M. Nisoli, S. de Silvestri, O. Svelto, R. Szipocz, K. Ferencz, Ch. Spielmann, S. Sartania, F. Krausz, "Compression of high-energy laser pulses below 5 fs," *Opt. Lett.*, **22**, 522 – 524 (1997).
118. G. Steinmeyer, D. H. Sutter, L. Gallmann, N. Matuschek, U. Keller, "Frontiers in ultrashort pulse generation: pushing the limits in linear and nonlinear optics," *Science*, **286**, 1507 – 1512 (1999).

CHAPTER 2

NONLINEAR OPTICS AND MATERIALS

In this chapter, the basic concepts of nonlinear optics will be presented. A set of coupled equations, which establish the rate of growth and decay of the generated fields under a three-wave mixing interaction of electromagnetic waves, will be established. These will allow the phasematching conditions to be found for the achievement of efficient frequency conversion of light in birefringent nonlinear materials. This review will be followed by an analysis of quasi-phasematching and the implementation of this technique using periodically-poled ferroelectrical crystals. The chapter will conclude by presenting some of the physical properties of the nonlinear crystals that were used in this work.

2.1 Nonlinear Optics

As mentioned in Chapter 1, the interaction between an electromagnetic field and a dielectric material results in an induced polarisation field in the material. We have seen that principally this polarisation is linearly proportional to the applied field (see Equation (1.4)) having the linear optical susceptibility, $\chi^{(1)}(\omega)$, as the proportionality constant. We have also seen that the linear susceptibility is related to the index of refraction, $n(\omega)$, of the medium. In a crystal, the linear susceptibility is a tensor, which obeys the symmetry properties of the medium.

2.1.1 The nonlinear susceptibility tensor

The induced polarisation will be linear only for limited values of the field strength. When the crystal is illuminated with a sufficiently intense electromagnetic field (comparable to the field strength within the dielectric), the induced polarisation exhibits nonlinear properties. A general Taylor series expansion of the polarisation includes higher-order terms of the electromagnetic field:

$$\tilde{P}(t) = \varepsilon_0 \left(\chi^{(1)} \tilde{E}(t) + \chi^{(2)} \tilde{E}^2(t) + \chi^{(3)} \tilde{E}^3(t) + \dots \right) \quad (2.1)$$

where ε_0 is the electric permittivity, $\chi^{(2)}$ and $\chi^{(3)}$ are the second- and third-order nonlinear susceptibility tensors respectively, and \tilde{P} and \tilde{E} are the polarisation and electric field vectors.

A number of interesting optical phenomena arise from these susceptibilities. For example, $\chi^{(2)}$ gives rise to SHG, DC rectification, parametric oscillation and in general any three-wave frequency mixing processes. The third-order susceptibility is responsible for third-harmonic generation, self-phase modulation, self-focussing (the optical Kerr-effect was discussed in Chapter 1). Like the linear susceptibility, the tensor coefficients of the second order nonlinear susceptibility must reflect the symmetry properties of the crystal medium. An immediate consequence of this fact is that in *centrosymmetric* media the second-order nonlinear coefficient must vanish. Thus, $\chi^{(2)}$ -based nonlinear optical effects are restricted to *non-centrosymmetric* materials.¹

The susceptibility coefficients $\chi^{(n)}$ are tensors of rank (n+1). Thus the second order nonlinear components of the polarisation field can be expressed as:

$$\tilde{P}_i^{NL}(t) = \sum_{i,j,k} \varepsilon_0 \chi_{ijk}^{(2)} \tilde{E}_j(t) \tilde{E}_k(t) \quad (2.2)$$

In addition to crystal symmetry restrictions, $\chi_{ijk}^{(2)}$ satisfies two additional symmetry relations. The first is an intrinsic symmetry relation which can be derived for a lossless medium from general energy considerations. This consideration states that $\chi_{ijk}^{(2)}(-\omega_3, \omega_2, \omega_1)$ is invariant under any permutation of the j and k indices.² The second symmetry relation is based on a conjecture by Kleinman³ that in a lossless medium the order of the frequencies is irrelevant and therefore $\chi_{ijk}^{(2)}$ is symmetric under any permutation of its indices.

Now, if we define the field component at frequency ω by the Fourier relation:

$$\tilde{E}(r, t) = \frac{1}{2} \left[E(r, \omega) e^{i(k \cdot r - \omega t)} + c.c \right] \quad (2.3)$$

and substitute in Equation (2.2) we find that,

$$P_i^{NL}(-\omega_3) = \varepsilon_0 \sum_{i,j,k} d_{ijk}(-\omega_3, \omega_2, \omega_1) E_j(\omega_2) E_k(\omega_1) \exp[i(k_2 + k_1 - k_3) \cdot r] \quad (2.4)$$

where the coefficient

$$d_{ijk}(-\omega_3, \omega_2, \omega_1) = \frac{\chi_{ijk}^{(2)}(-\omega_3, \omega_2, \omega_1)}{2} \quad (2.5)$$

is often referred as the nonlinear coefficient.

Because interchanging E_j and E_k in Equation (2.4) has no physical meaning, the nonlinear coefficient can be written in reduced notation (known as the piezoelectric contraction) as $d_{i(jk)} = d_{im}$ to form a 3 x 6 element matrix where m runs from 1 to 6 with the following correspondence:

jk	11	22	33	23 = 32	13 = 31	12 = 21
m	1	2	3	4	5	6

Table 1. Correspondence between expanded and piezoelectric contraction of the subindices of the nonlinear coefficients.

The resulting matrix has the same form for all members of a particular crystal class, and relates the polarisation and electric field such that:

$$\begin{pmatrix} P_x(\omega_3) \\ P_y(\omega_3) \\ P_z(\omega_3) \end{pmatrix} = 2\epsilon_0 \begin{pmatrix} d_{11} & d_{12} & d_{13} & d_{14} & d_{15} & d_{16} \\ d_{21} & d_{22} & d_{23} & d_{24} & d_{25} & d_{26} \\ d_{31} & d_{32} & d_{33} & d_{34} & d_{35} & d_{36} \end{pmatrix} \begin{pmatrix} E_x(\omega_1)E_x(\omega_2) \\ E_y(\omega_1)E_y(\omega_2) \\ E_z(\omega_1)E_z(\omega_2) \\ E_y(\omega_1)E_z(\omega_2) + E_y(\omega_2)E_z(\omega_1) \\ E_x(\omega_1)E_z(\omega_2) + E_x(\omega_2)E_z(\omega_1) \\ E_x(\omega_1)E_y(\omega_2) + E_x(\omega_2)E_y(\omega_1) \end{pmatrix} \quad (2.6)$$

For the 21 out of 32 crystal classes that lack a centre of inversion, the contracted form of the d_{im} tensor, and the respective values of the different components can be found in a number of references.^{1,4,5}

In the foregoing discussion we have restricted the number of components to 18 in the most general case but in practice it is possible to have fewer. If in a crystal class with a given susceptibility matrix, we perform a symmetry operation that does not physically alter the crystal, then the same operation should leave the matrix unchanged. As a result of this certain components of the matrix must be zero and others numerically equal but opposite in sign. However, even with all these reductions, Equation (2.4) involves summations over all non-zero matrix elements and the directions of polarisation of the interacting fields. To simplify notation yet further it is possible to define the *effective nonlinear coefficient*, d_{eff} , and write a new expression for only one frequency component of the polarisation:

$$P(\omega_3) = 2\varepsilon_0 d_{eff} E(\omega_1) E(\omega_2) \quad (2.7)$$

Explicit expression of the effective nonlinear coefficient, d_{eff} , for a variety of nonlinear crystal can be found in the literature.^{1,4-6}

2.1.2 The coupled wave equations

We are now in position to derive a set of coupled wave equations for the electromagnetic field amplitudes generated by the nonlinear driving polarisation. Clearly, at any point, the decrease or increase of the amplitude of a wave at a particular frequency depends on the amplitudes of the other waves. For three interacting waves, then, we must seek three coupled amplitude equations, each giving the rate of growth, or decay, of the field at one frequency as a function of the fields at the two other frequencies. In addition, we should expect in each of these equations some measure of the phase difference between the polarisation wave and the electromagnetic wave.

Starting from Maxwell's equations and the constitutive relations of the matter (which relates the electric field, flux density and induced polarisation), and considering an anisotropic, non-magnetic, non-conducting, homogeneous dielectric, it is possible to obtain the following form of the wave equation:

$$\nabla^2 \vec{E} - \mu_0 \varepsilon_0 \frac{\partial^2}{\partial t^2} \vec{E} = \mu_0 \frac{\partial^2}{\partial t^2} \vec{P}, \quad (2.8)$$

where ε_0 and μ_0 are the electric permittivity and the magnetic permeability in the vacuum, respectively. In what follows, we will consider the direction of propagation parallel to the z axis and limit the analysis to the general three wave mixing at frequencies ω_1 , ω_2 and ω_3 in a such a way that energy is conserved, i.e. $\omega_3 = \omega_1 + \omega_2$.

We now use the definition of the electric field, Equation (2.3), and introduce it together with the nonlinear polarisation, Equation (2.7), into Equation (2.8). Then after assuming that the variation of the complex field amplitude varies very slowly with respect to the frequency carrier, it is possible to derive a set of expressions for the coupling between the interacting waves in a nonlinear process:

$$\begin{aligned}\frac{dE_1}{dz} &= -\frac{i\omega_1}{2n_1c}d_{eff}E_3E_2^*\exp[-i(\Delta k)z] \\ \frac{dE_2}{dz} &= -\frac{i\omega_2}{2n_2c}d_{eff}E_3E_1^*\exp[-i(\Delta k)z] \\ \frac{dE_3}{dz} &= -\frac{i\omega_3}{2n_3c}d_{eff}E_1E_2\exp[+i(\Delta k)z]\end{aligned}\quad (2.9)$$

where Δk is called the *wave vector mismatch* and is given by:

$$\Delta k = k_3 - k_2 - k_1 \quad (2.10)$$

The effective nonlinear coefficient, d_{eff} , here is derived from the nonlinear matrix (Equation (2.6)) and depends on the polarisation directions of the incident fields.

When plane waves propagate through the nonlinear medium, the coupled wave equations can be solved to give the value of the generated power P_3 inside the crystal at a distance L from the input plane:

$$P_3 = \frac{2\pi^2\omega_1\omega_2\mu_0d_{eff}^2L^2}{n_1n_2n_3c}P_1P_2 \operatorname{sinc}^2\left(\frac{\Delta kL}{2}\right). \quad (2.11)$$

From the previous equation, it is possible to see that the optical power generated has a $\operatorname{sinc}^2(x)$ dependence on ΔkL , and that the conversion efficiency is proportional to d_{eff} and L^2 . Thus we should like to carry out the process in a nonlinear crystal to maximise these factors.

Further examination to the three coupled Equations (2.9) shows that the second equation can be obtained from first interchanging E_1 and E_2 but the third equation can not be obtained in a similar way. A consequence of this statement becomes clearer if we look at the power flow in the interaction. If we assume perfect phasematch ($\Delta k = 0$), and after some algebraic manipulation it is possible to equate the three relations to find that¹

$$\frac{1}{\omega_1} \frac{dI_1}{dz} = \frac{1}{\omega_2} \frac{dI_2}{dz} = -\frac{1}{\omega_3} \frac{dI_3}{dz}. \quad (2.12)$$

where the derivatives dI_i/dz should be interpreted as the change of power of the source at ω_i . Equation (2.12) is known as the Manley-Rowe relation and has far-reaching consequences. For the case of sum-frequency generation ($\omega_3 = \omega_1 + \omega_2$) the Manley-Rowe relations state that the sources at ω_1 and ω_2 will lose power which is gained at the source at ω_3 . But for difference-frequency generation, $\omega_3 - \omega_2 = \omega_1$, we find that the source at ω_3 loses power not only to the generated frequency ω_1 , but also to the source ω_2 . Because the source of ω_2 in the difference frequency generation gains power, this opens the possibility of generating the difference frequency between a strong source at ω_3 (the pump) and a very weak source at ω_2 . If the weak signal at ω_2 is passed through the crystal again and again, it will gain power with every pass and will build up; as a consequence, the signal at ω_1 will also build up. A strong consequence of this fact is that the frequency ω_2 (or ω_1) does not have to be introduced from outside, it can be a frequency in the noise radiation, and the many passes can be obtained by placing the nonlinear crystal in a mirror cavity that is resonant at ω_2 (or ω_1). If the gain per pass is higher than the loss per pass, such a

system will reach an oscillation threshold. A system like this is called an *optical parametric oscillator*.

2.1.3 Phasematching

An important characteristic of nonlinear properties is that the several different electromagnetic waves that can interact with each other in the material, have to satisfy the condition of energy conservation.

$$\omega_3 = \omega_1 + \omega_2 . \quad (2.13)$$

Therefore, different frequencies can be created by modulating the parameters of the crystal. To find out which one of these frequencies will be radiated we have to examine the phases of the different waves involved. In nonlinear interactions, *phasematching* selects the process of interest to the exclusion of the other possible processes. It involves precise control of the refractive indices at the frequencies involved in the mixing process, to match the velocities of propagation of the polarisation wave and the electromagnetic wave which it radiates. Optimum conversion efficiency is met when $\Delta k = 0$ (see Equation (2.10)). This condition can be expressed in terms of the refractive indices as:

$$\frac{1}{c}(n_3\omega_3 - n_1\omega_1 - n_2\omega_2) = 0 \quad (2.14)$$

Equation (2.14) effectively expresses the phasematching condition in terms of the conservation of the momentum, which in the most general case can be expressed as:

$$\vec{k}_3 = \vec{k}_1 + \vec{k}_2 \quad (2.15)$$

Equations (2.13) and (2.15) must be simultaneously satisfied for light amplification to occur in any three-wave mixing process. A consequence of Equation (2.15) is that phasematching can be achieved either collinearly or noncollinearly, where the wave vectors are arranged as shown in Figure 1:

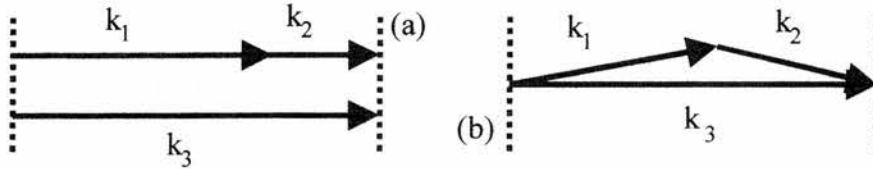


Figure 1. (a) Collinear and (b) non collinear phase matching.

Due to material dispersion, $n(\omega)$, in Equation (2.10), the phasematching condition $\Delta k = 0$ is not always fulfilled and the different waves being generated travel at different velocities. If these waves propagate collinearly, there is still an interaction between them as they propagate through the crystal. The waves convert to other wavelengths and then they are converted back, until such time that the phase relation favours forward conversion once again, and the process repeats itself. The overall conversion to new wavelengths, over the length of the crystal is negligible, and no useful light is generated. The distance over which the relative phases of the waves change by π is called the *coherence length*, L_c , and is given by

$$L_c = \frac{\pi}{\Delta k} \quad (2.16)$$

which is also the half period of the growth and decay cycle of the interaction. For typical non-birefringent crystals, this coherence length is of the order of 10-100 μm , which severely limits the useful crystal length and, hence, the output power. Note that in the optical transparency region in isotropic crystals, the conditions given by

equations (2.13) and (2.15), are never fulfilled because of normal dispersion. If the refractive index can be matched by some means, for example, by using the birefringence of an anisotropic material, high conversion efficiencies can be obtained.

Birefringent phasematching.

A popular method for achieving phasematching involves using a nonlinear material that is birefringent. When light consisting of orthogonal polarisation propagates in an arbitrary direction through a birefringent material, each polarisation experiences a different value of the refractive index. With a suitable combination of wavelengths, polarisations and propagation directions, a phasematched configuration can be obtained for the nonlinear process.

There are two kinds of optically anisotropic crystals. If all three axes of the indicatrix are unequal, the crystal is called biaxial, because in that case, two optical axes can be defined. If two of the axes are equal, the crystal is uniaxial and the *optic axis* (z axis) is perpendicular to the plane of the two equal axes. The plane containing the z axis and the wave vector, \mathbf{k} , of the light wave is termed the *principal plane*. The light beam whose polarisation is normal to the principal plane is called *ordinary beam* or an *o-beam*. The beam polarised in the principal plane is called *extraordinary beam* or *e-beam*. The refractive index of the o-beam does not depend on the propagation direction, whereas for the e-beam it does. The difference between the refractive indices of the ordinary and extraordinary beams is known as *birefringence*. The refractive index of ordinary and extraordinary beams are denoted by n_o and n_e , respectively. If $n_e > n_o$ the crystal is positive and if $n_e < n_o$ the crystal is negative. The

refractive index of the extraordinary wave is a function of the polar angle θ between the z axis and the vector k . It is determined by the equation:

$$\frac{1}{n_{oe}^2(\theta)} = \frac{\cos^2(\theta)}{n_o^2} + \frac{\sin^2(\theta)}{n_e^2} \quad (2.17)$$

where $n_{oe}(90) = n_e$, and $n_{oe}(0) = n_o$. This angular variation of the refractive index of the extraordinary wave means that it may be possible, for a particular propagation of the light within the crystal, to achieve phasematching of the waves that are involved in the process.

For a general three-wave mixing interaction, if the pair of input or output waves in the process have the same polarisation the phasematching is Type-I, otherwise it is Type-II. In parametric generation, the expressions given above can be used to determine the unique wavelengths that are phasematched for a chosen propagation direction and pump wavelength. The type of phase matching in both positive and negative uniaxial crystals, involves the combination of waves polarisations shown in Table 2.

	Type I ($\lambda_3 \rightarrow \lambda_1 + \lambda_2$)	Type II ($\lambda_3 \rightarrow \lambda_1 + \lambda_2$)
Positive	$o \rightarrow e + e$	$o \rightarrow e + o$ $o \rightarrow o + e$
Negative	$e \rightarrow o + o$	$e \rightarrow o + e$ $e \rightarrow e + o$

Table 2. Type of phase matching in negative and positive uniaxial crystals where $\lambda_3 < \lambda_2 < \lambda_1$.

When a plane wave propagates in uniaxial crystals, the direction of propagation of the wave phase (vector \mathbf{k}) generally does not coincide with that of the wave energy vector (vector \mathbf{S}). As the extraordinary wave propagates in a crystal, its power flow direction differs by the *double refraction angle* ρ from its phase velocity direction. The effect referred as a *Poynting vector walk-off*, leads to walk-off of the beam energy at an angle ρ . The double refraction angle is given by:

$$\rho(\theta) = \pm \arctan \left[\left(\frac{n_o}{n_e} \right)^2 \tan(\theta) \right] \mp \theta \quad (2.18)$$

where the upper sign refers to a negative crystal and the lower sign to a positive one. Note that in the $\lim_{\gamma \rightarrow \infty} \tan^{-1}(\gamma) = 90^\circ$, therefore at $\theta = 90^\circ$, $\rho(\theta) \rightarrow 0$. And there is no Poynting vector walk-off.

Generally a birefringent crystal has three different optical axes, defined independently of the crystallographic axis and designated x , y and z . The refractive indices associated with each axis are n_x , n_y and n_z . For biaxial crystals, the dependence of refractive indices on the light propagation direction and its polarisation correspond to a much more complex surface than that for uniaxial crystals. The surface has a bilayer structure with four points of interlayer contact through which two optic axes pass.

For simplicity we confine ourselves to the case of light propagating in the principal planes xz , xy , and yz . In these planes, the dependencies of the refractive index on the propagation direction of two waves with orthogonal polarisations represent a combination of an ellipse and a circle. We shall relate optical (x, y, z) and *crystallographic* (a, b, c) axes in a biaxial crystal in a such a way that the optic axes,

whose directions are given by the intersection points of ellipses and circle will always be in the plane xz .

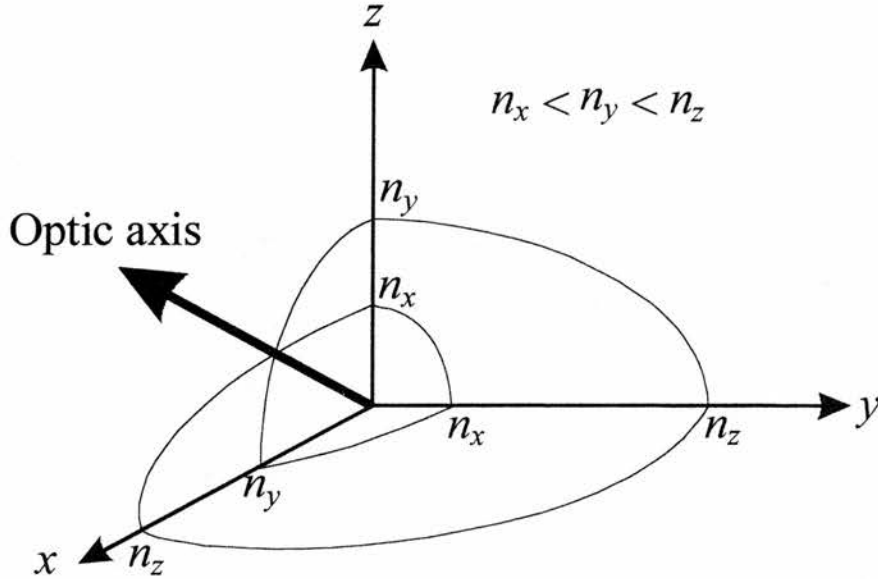


Figure 2. Indicatrices of refractive indices in a biaxial crystal.

The calculation of the crystal directions which support phasematching therefore requires the active index associated with a given direction to be computed. In a biaxial crystal, the refractive index experienced by a wave polarised along (θ, ϕ) is described by an ellipse known as the index ellipsoid which, in its general form is given by the transcendental equation:

$$\frac{\sin^2(\theta)\cos^2(\phi)}{n_i^{-2} - n_{1i}^{-2}} + \frac{\sin^2(\theta)\sin^2(\phi)}{n_i^{-2} - n_{2i}^{-2}} + \frac{\cos^2(\phi)}{n_i^{-2} - n_{3i}^{-2}} = 0 \quad (2.19)$$

The general solution of Equation (2.19) requires an iterative method, so is often more convenient restrict the calculation of phase matching to principal planes formed by the optical axes. This not only simplifies the mathematics but is useful since the effective nonlinear coefficient always maximises in at least one principal plane. The equations for calculating phasematching angles upon collinear propagation of interacting waves in the principal planes of a biaxial crystal can be

found in the literature.⁶ A more general approach to calculation of the phase matching angles is given by Hobden⁷ and Stepanov *et al.*⁸

Birefringent phasematching can be achieved for two geometries for an optical parametric oscillator cavity. The phasematching can be either critical or noncritical. For noncritical phasematching, all the waves propagate along a crystal axis, and consequently see the refractive index of one of the other axes ($\theta = 90^\circ$ in Equation (2.19)). One advantage of this configuration is that there is no walk-off between the interacting waves and all remain collinear over the length of the crystal; therefore, they interact over the entire length of the crystal. The output can be tuned by tuning the pump wavelength or varying the temperature of the crystal. Rapid angle tuning is not possible and thus the tuning range can be limited. To obtain a particular wave from the OPO it is sometimes necessary to propagate the incident light at an angle to a crystal optical axis. This geometry is called critical phasematching. In this configuration, Poynting vector walk-off, means that the extraordinary and ordinary waves interact with each other over a short distance only, and the interaction may be far less efficient than in the case of noncritical phasematching.

The general disadvantage of birefringent phasematching is the dependence on inherent material parameters. Only a certain pair of wavelengths can be phasematched for a certain propagation direction and the range of wavelengths that can be generated from one single material is limited. Moreover, the value of the nonlinear coefficient depends on both propagation direction and the polarisation directions that are used in the interaction.

2.2 Quasi-phasematching

Quasi-phase-matching (QPM) makes it possible to combine the convenience of noncritical phase-matching with the wavelength coverage of a critical geometry. For this purpose, QPM was devised independently by Armstrong *et al.*² and Franken and Ward.⁹ QPM is a technique for phase matching nonlinear optical interactions in which the relative phase of the interacting waves is corrected at regular intervals using a structural periodicity (grating period) built into the nonlinear medium. Such a spatial modulation can be obtained by periodically altering the crystal orientation so that the effective nonlinearity alters between $-d_{eff}$ and $+d_{eff}$. Thus, the first demonstration of QPM was achieved by stacking thin plates of GaAs that were successively rotated by 180° with respect to each other.¹⁰ Since then, other QPM structures have also been demonstrated such as crystal growth,¹¹ integrated optic technology,¹² diffusion bonding¹³, poled-polymer films^{14,15}, and periodic electric field poling (or periodic-poling) of ferroelectric nonlinear crystals¹⁶ which represents the most successful implementation of QPM.

2.2.1 Theory of quasi-phasematching

In all the above cases, the interacting waves still propagate with different phase velocities, but when the accumulated phase mismatch (ΔkL) reaches π , the sign of the driving nonlinear susceptibility is also reversed so that the phase difference is “reset” to zero. This creates a step-wise growth in the output power along the crystal length, as can be seen in Figure 3.

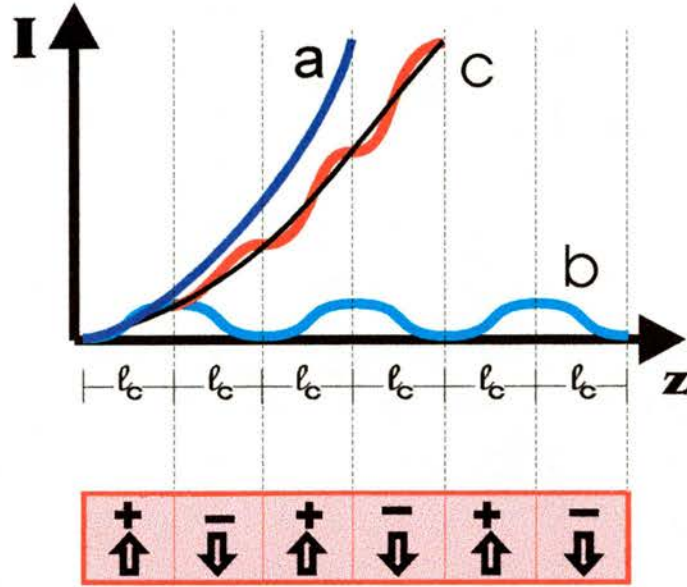


Figure 3. Comparison of the output power versus crystal length. (a) Perfect phase matching. (b) Non-phase matched interaction. (c) First-order QPM.

As mentioned in section 2.1.2, the distance over which the relative phase of the two waves changes by π is the coherence length L_c , which is also the half period of the growth and decay cycle of the generated interaction. Thus QPM involves repeated inversion of the relative phase between the interacting waves after an odd number of coherent lengths. The phase is thus reset periodically so that, on average (black line on Figure 3), the proper phase relationship is maintained for growth of the generated interaction. In QPM the highest conversion efficiency is obtained when the periodicity of the modulation, Λ , corresponds to $2L_c$. This represents the first-order QPM, but also higher-order QPM (eg. in a third-order QPM in which the sign of d_{eff} is switched every three L_c) gives continuous frequency conversion, but with lower effective nonlinearity.

The wave vector mismatch (Equation 2.10) for the QPM interaction has, therefore, a term including the periodicity modulation, and is given by:

$$\Delta k_Q = k_3 - k_2 - k_1 - k_g \quad (2.18)$$

where k_g is the grating vector and is given by:

$$k_g = \frac{2\pi m}{\Lambda} \quad (2.19)$$

where $m = 1, 3, 5\dots$, is the order of the quasi-phasematched process. The wave vectors are, therefore arranged as follows:

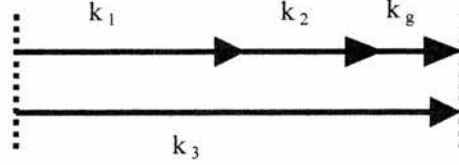


Figure 4. Collinear quasi-phasematching via a three-wave interaction.

Much of the theory of conventional birefringent phasematched three-wave mixing processes carries over to QPM bulk interactions with only a few simple substitutions. To introduce the periodic modulation, the nonlinear coefficient, d_{eff} , has to be expressed by a Fourier expansion of its spatial harmonics along the direction of propagation as follows:

$$d_{eff}(x) \cdot e^{-i\Delta kx} \rightarrow d_{eff} \left[\sum_{m=-\infty}^{\infty} c_m e^{im \frac{2\pi}{\Lambda} x} \right] \cdot e^{-i\Delta kx} \quad (2.20)$$

where c_m are the Fourier coefficients. From the previous equation we see that quasi-phasematching is obtained when the period is chosen such that one of the spatial harmonics $im(2\pi/\Lambda)x$ compensates for the phase mismatch $-i\Delta kx$, and the grating period is, therefore

$$\Lambda = m \frac{2\pi}{\Delta k}, \quad (2.21)$$

in accordance with Equation (2.19).

By assuming $d_{eff}(x)$ to be a rectangular function with a duty cycle of $D \equiv l/\Lambda$, where l is the length of a section over which the sign of the nonlinear coefficient

remains constant (*i.e.* $l \equiv \Lambda/2$ yields a duty cycle of 50%), the Fourier coefficients can be written as:

$$c_m = \frac{2}{m\pi} \sin(m\pi D) \quad (2.22)$$

As the conversion efficiency in a nonlinear process varies as the square of the nonlinear coefficient, there exists a $1/m^2$ factor dependence on the order of the QPM. The largest value of the c_m is $2/\pi$ and is obtained for first order QPM ($m = 1$) and with a duty cycle of 50%. Therefore, there is $(2/\pi)^2$ factor reduction on the conversion efficiency of a first order QPM process compared with birefringent phasematching, as illustrated in Figure 3. Consequently, the nonlinear coefficient in a QPM process should be expressed as:

$$d_{\text{eff}}^{\text{QPM}} = \frac{2}{m\pi} d_{\text{eff}}. \quad (2.23)$$

The use of QPM configurations in nonlinear processes has a number of advantages over conventional birefringent phasematching. Most important is the ability to tailor the material to phasematch arbitrary parametric processes by simply choosing an appropriate period of the modulation according to Equations (2.18) and (2.21). This allows generation of any desired wavelength within the transparency range of the material. Moreover, phasematching can be obtained using one single polarisation along one crystal axis for all interacting waves. This yields a noncritical type-I QPM which eliminates the problem of walk-off. However, if the crystal is angle tuned, walk-off can be present in a QPM material. Therefore, temperature tuning, pump wavelength tuning or the use of different crystal grating periods are commonly used to achieve broad spectral tunability.

The use of parallel polarisations together with the free choice of propagation direction gives access to diagonal elements of the nonlinear tensor. Therefore, the

largest nonlinear coefficient can be accessed. This may result in conversion efficiencies substantially higher than in the case of birefringent phasematching or even, to phasematch interactions that can not be accessed by conventional birefringent phase matching.

2.2.2 The Periodic-poling technique

All of these advantages make QPM a very desirable technique to produce nonlinear frequency conversion. However, implementation of QPM requires a fabrication method that can achieve uniform micrometer scale periodic structures while preserving the materials transparency and nonlinearity. It was not until the introduction of periodically-poling of ferroelectric nonlinear optical crystals that the popularity of QPM increased over birefringent phasematching.¹² Ferroelectric materials have important characteristics that makes them ideal candidates to produce a QPM device by means of periodic-poling, as we will see in the next section.

Ferroelectric materials

All ferroelectric materials have an asymmetric structure that is due to a built-in polarisation, termed spontaneous polarisation, P_s , created in the medium. In a ferroelectric crystal, regions of spontaneous polarisations (called domains), with opposite values may be found. Therefore, ions inside a ferroelectric material have two equilibrium positions. This is illustrated schematically in Figure 5. The essential feature of a ferroelectric is not the fact that it has a spontaneous polarisation, but rather the fact that it can be reversed by means of an electric field. Domain reversal can be obtained if an external field exceeding the internal field which has been set up

by the spontaneous polarisation is applied. This critical value of the external field at which domain reversal occurs is called coercive field, E_c . One important characteristic of the ferroelectric crystal structures is that they have the highest degree of non-symmetry that is susceptible to being reversed. This noncentrosymmetric structure is the one which determines the nonlinear optical properties of these materials.

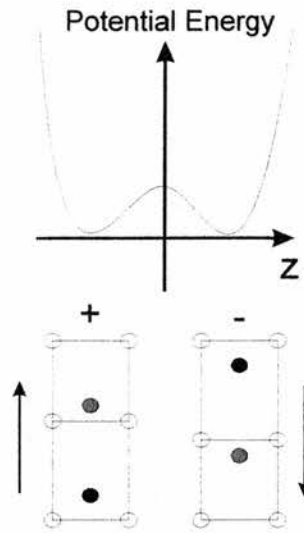


Figure 5. Qualitative picture of potential wells in ferroelectrics. Domain polarity can be reversed by application of a field sufficiently intense to move the ions from the one stable location to the other.

The amount of charge, Q , needed to reverse a single domain crystal of a certain area, A is related to the spontaneous polarisation as¹⁷

$$Q = 2AP_s \quad (2.24)$$

At this condition the energy needed to invert the crystal lattice is reached and a small displacement current flows through the crystal corresponding to the charge transfer during inversion. Table 3 lists the coercive fields and spontaneous polarisations that have been reported for the three materials used in this work.

	E_c ^[30] (kV/mm for 1 mm)	P_s ^[4] (C/m ²)
LiNbO ₃	~20.7	0.78
RbTiOAsO ₄	2.1 – 2.3	–
KTiOPO ₄	2.0 – 2.1	0.14

Table 3. Coercive field, E_c , and the spontaneous polarisation, P_s , for LiNbO₃ RTA and KTP (from ref. 30).

Periodic-poling

The periodic-poling technique in ferroelectric materials makes it possible to manufacture high quality QPM crystals because a periodic reversal of the electric domains produces antiparallel domains that correspond to a sign reversal of the nonlinear coefficient. With this technique several QPM devices based on a number of ferroelectric crystals, such as LiNbO₃,^[16] LiTaO₃,^[18] RbTiOAsO₄,^[19] KTiOPO₄,^[20] RbTiOPO₄,^[21] and KTiOAsO₄,^[22] have been demonstrated.

To periodically-poled ferroelectric materials, several approaches have been implemented. Chemical in-diffusion in LiNbO₃ has been used to produce QPM structures in waveguides, however, the pattern is limited to shallow layers.²³ Bulk devices in ferroelectrics have been made by periodic modulation of the sign of the nonlinearity during growth of the crystal, but, this technique suffers from axial variation in domain periodicity.¹¹ Periodic poling of ferroelectrics using electron-beam writing can produce good periodicity in bulk crystals, but reproducibility is poor and the process is expensive.²⁴ An efficient method for ferroelectric domain reversal consists of applying an external electric field that exceeds the coercive field of the material. Here domain periodicity is defined by a lithographic mask by standard microfabrication techniques. This creates a regular multi-domain structure into the material.¹⁶

To prepare the samples, the initial crystal wafers are Z-cut with polished Z-faces. The wafers have to be single-domain poled, prior to patterning of periodic electrodes. After this procedure, the wafers are cut into samples and polished for propagation along the x-axis. The samples are then patterned with periodic electrodes on one of the polar faces (usually c^+) using standard lithography methods. The mask consists of a layer of insulator in the form of a photoresist, and a layer of conductor, which is often aluminium. These layers can be applied in either order to form the mask. In both cases, contact is made to the exposed metal with a liquid electrolyte such as LiCl or KCl in deionised water. For the negative electrode, liquid electrolyte is applied directly in the opposite (usually c^-) bare face. An electric field, that can be continuous or as a series of short pulses, is then applied along the material to reverse the polarity. Significant domain reversal occurs when the applied field exceeds the value of the coercive field of the material.

With this technique, domains typically grow beyond the width of the metal electrode defined by the grating lithography as a result of the remaining fringing fields along the edges. Thus, electrode widths are normally a few micrometers (3 to 4 μm) narrower than the desired width of the domains.

2.3 Nonlinear optical materials

The optical parametric oscillators described in Chapter 3 and frequency doubling materials used in Chapter 4 are based on three different periodically-poled ferroelectric materials: RTA (RbTiOAsO_4), KTP (KTiOAsO_4) and lithium niobate (LiNbO_3). In this section, a review of the physical properties of these crystals will be presented.

2.3.1 The KTP family of nonlinear crystals

The isomorphic KTP family compounds are characterised by the formula unit $MTiOXO_4$, where M can be K, Rb or Cs and X can be P or As^[25]. Available family members are KTP, RTP, KTA, RTA and CTA. All of these positively birefringent materials are orthorhombic and belong to the noncentrosymmetric point group $mm2$, with only slight different parameters. The structure is characterised by chains of TiO_6 octahedra, which are linked at two corners and separated by XO_4 tetrahedra. Alternating long and short Ti-O bonds occur along these chains, which result in a net z-directed polarisation and are the major contributors to the material's nonlinear and electro-optic coefficients. These bonds are also responsible for the ferroelectric properties. The M -ion is weakly bonded to the Ti octahedra and the X tetrahedra. Channels exist in the crystal lattice along the z-axis whereby M -ions can move through a vacancy mechanism with diffusion constants several orders of magnitude larger in the x-y plane.

Most members of the KTP family can be grown using a high temperature (850-950 °C) solution growth process in which the material crystallises out of a molten self-flux composition (i.e. the solvent contains no other elements than those of the final crystalline material) when cooled. The flux growth operates at atmospheric pressure and the growth time is about 5-8 weeks^{26,27}.

KTP can also be grown by the hydrothermal technique (Ht-KTP), in which the crystals are grown at constant high pressure and lower temperature.²⁸ This technique yields crystals of very good uniformity and optical quality. However, the process is more complicated and takes longer time, making it less available and more expensive

Flux grown KTP has higher conductivity than RTA (approximately two orders of magnitude) and therefore, is more difficult to pole periodically. When poling a ferroelectric material, a small displacement current flows through the crystal that corresponds to the charge transfer during domain inversion. However, the relatively high ionic conductivity of flux KTP leads to a high current through the sample when the high voltage is applied. This current, besides screening the displacement current, affects the poling process in a way that is difficult to predict. To overcome this problem a method based on ion-exchange has been developed. It consists on immersing the KTP crystal in a bath of 100% melted RbNO_3 . This results in an exchange of K and Rb ions and forming a low conductive layer of $\text{Rb}_x\text{K}_{1-x}\text{TiOPO}_4$ (Rb:KTP) at the two c-faces²⁹. Such exchanged crystals produce a reduction of the total conductivity of up to 50% which indicates that there is a substantial difference in conductivity between the exchanged layer and the bulk. After this procedure, periodic-poling carries on as described before. The ion exchanged method has been successfully applied to pole crystals of KTP up to 3 mm thick.³⁰

Optical properties of the KTP family

The optical transmission characteristics for KTP and RTA are presented in Figure 6. In both cases, the propagation transmission is in the x-axis and the polarisation along the z-axis. The absorption bands at $2.8 \mu\text{m}$ most likely represent OH stretching bands which indicates that H_2O was incorporated during growth. Because the arsenate compounds have an extended transmission in the infrared, these should be selected for applications in the $3\text{-}5 \mu\text{m}$ spectral range.

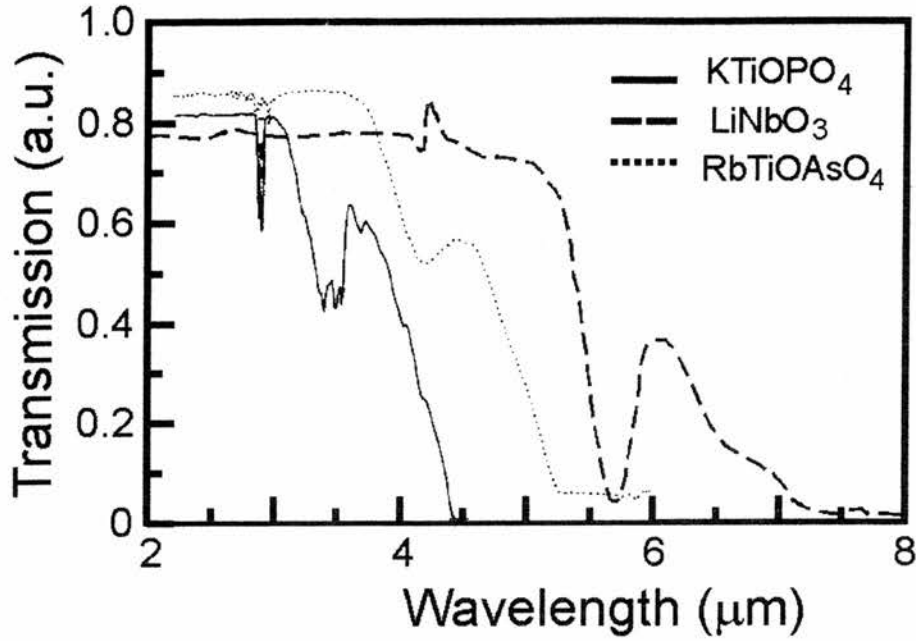


Figure 6. Transmission curves for KTP and RTA (9.5 mm and 10 mm crystal lengths respectively).³⁰ Also included for comparison purposes the transmission of LiNbO₃ [1 mm crystal length (see sec. 2.3.2)].

There are several dispersion data for the KTP materials available in the literature in the form of Sellmeier equations^{6,30-35}. Table 4 shows the dispersion data for the crystals used in this work as a Sellmeier equation (λ in μm):

$$n(\lambda) = \sqrt{A + \frac{B}{1 - C/\lambda^2} - D\lambda^2} \quad (0.25)$$

	Index	A	B	C	D
KTP ^[32]	n_x	2.16747	0.83733	0.04611	0.01713
	n_y	2.19229	0.83547	0.04970	0.01621
	n_z	2.25411	1.06543	0.05486	0.02140
RTA ^[34]	n_x	2.04207	1.17785	0.04063	0.01035
	n_y	2.14941	1.09267	0.04606	0.01067
	n_z	2.18962	1.30103	0.05203	0.01390

Table 4. Dispersion data for KTP (flux-grown) and RTA.

The following temperature dependence can be used to calculate the temperature tuning characteristics of KTP³⁶ and RTA³⁷ through the following equation (λ in μm):

$$\frac{dn_z}{dT} = \frac{a}{\lambda^3} + \frac{b}{\lambda^2} + \frac{c}{\lambda} + d \quad (0.26)$$

	a (10 ⁶)	b (10 ⁶)	c (10 ⁶)	d (10 ⁶)	α (10 ⁻⁶)
KTP ^[36]	12.415	-44.414	59.129	-12.101	11
RTA ^[37]	-76.34	257.19	-237.97	0	15.1

Table 5. Temperature dependence of the index of refraction for KTP and RTA. α is the expansion coefficient (/°C).

The crystal symmetry of the KTP materials result in the following nonlinear matrices:

$$d_{i,m} = \begin{pmatrix} 0 & 0 & 0 & 0 & d_{15} & 0 \\ 0 & 0 & 0 & d_{24} & 0 & 0 \\ d_{31} & d_{32} & d_{33} & 0 & 0 & 0 \end{pmatrix} \quad (0.27)$$

and the respective values for these coefficients (in pm/V) are:

	d_{31}	d_{32}	d_{33}	d_{24}	d_{15}	$d_{\text{eff}} = (2/\pi)d_{33}$
KTP ^[6]	2.5	4.4	16.9	7.6	6.1	~10.8
RTA ^[37]	2.3	3.8	15.8	0	0	~10.0

Table 6. Effective QPM ($m=1$) and birefringent nonlinear coefficients for KTP and RTA.

It should be noted that for PPKTP a $(2d_{33}/\pi d_{24})^2 = 2$ -fold increase in conversion efficiency can be obtained by using the d_{33} coefficient in a first-order

QPM process compared with using d_{24} in a birefringently phasematched process. An analogous situation occurs for the PPRTA crystals in which the d_{33} nonlinear coefficient can be only accessed by a QPM process and nonlinear effective coefficient as large as $d_{eff} = 10$ pm/V (or a ~ 7 -fold increase in the conversion efficiency) is obtained. The QPM effective nonlinear coefficients for KTP and RTA are listed in Table 6.

Optically induced damage in the crystals put fundamental limitations on their performance on practical applications. Damage threshold depends strongly on parameters such as average intensities, pulse peak intensities, pulse energy, pulse duration, wavelength and absorption. The next table lists the observed damage threshold ($\lambda = 1.064\mu\text{m}$, $\tau_p = 10\text{ns}$) for RTA, KTP and Lithium niobate.³⁸

Crystal	Damage Threshold ³⁸ (GW/cm ²)
KTiOPO ₄	~ 0.5
RbTiOAsO ₄	~ 0.5
LiNbO ₃	0.3

Table 7. Observed damage threshold for KTP, RTA (from ref. 38). Lithium niobate is included for comparison (see section 2.3.2).

2.3.2 Lithium niobate crystals

Lithium niobate has played a very important role in the development of new nonlinear sources. The success of this material relies mainly in its very large transparency and high nonlinearity. We will discuss these and other physical properties of this crystal in the following sections.

The negative uniaxial crystal class of LiNbO_3 is has a rhombohedral $R3c$, trigonal structure and belongs to the point group $3m$.^[6] The crystal is composed of distorted oxygen octahedra that are slightly rotated, stacked one above the other, and with one face in common.³⁹ The oxygen ions are arranged in a hexagonally close-packed arrangement, in planes perpendicular to the crystal z-axis. The planes are separated by lithium and niobium along the crystallographic axis and as shown in the figure 7.

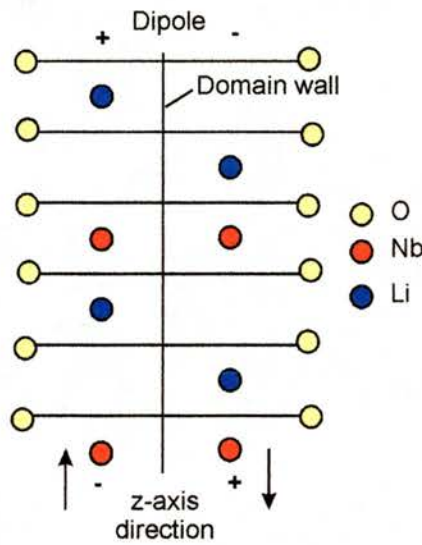


Figure 7. Schematic diagram of the structure of a crystal of lithium niobate.

The spontaneous polarisation, P_s , that is present with in the crystalline structure means that each ion can take more than one equilibrium position. The polarity of a ferroelectric domain in LiNbO_3 , is determined by the displacement of the metal ions from the oxygen layers. Inversion of the poling direction in lithium niobate results if the lithium ions can be induced to move through the oxygen ions into the adjacent space,³⁹ as shown in figure 7. In a QPM crystal of LiNbO_3 , a grating period, Λ , is composed of two consecutive inverted domain periods of width $\Lambda/2$.

Generally speaking, lithium niobate crystals are pulled with the c (z) axis as the pulling direction and they are made single domain during the poling process by passing a small poling current through the rod. This action will align all the electric domains in the same direction. This can only be achieved by holding the crystal at sufficiently high temperature (above 1150°C) for the domain direction to be reversible. Subsequently the crystal is cooled until the domains are no longer reversible, and the field is removed.

Optical properties of LN.

One of the most important characteristics of lithium niobate is its large transparency. Lithium niobate has an extra transmission window that expands the transparency range well into the mid-infrared, and up to 7 μm . The optical transmission characteristics for an extraordinary wave propagating along the x -axis are presented in Figure 6 (for a comparison in the transmission characteristics between extraordinary and ordinary waves, see chapter 4 figure 17). In chapter 4 (section 4.4), we will illustrate a means of exploiting this transmission window and an OPO operating at wavelengths as long as 6.8 μm , will be presented.

There are several dispersion data for the LiNbO_3 that can be found in the literature in the form of Sellmeier equations^{6,40-43}. Table 8 shows the dispersion data for the crystals used in this work that fits into the Sellmeier equation (λ in μm and T in K):

$$n_e(\lambda, T) = \sqrt{a_1 + b_1 T^2 + \frac{a_2 + b_2 T^2}{\lambda^2 - (a_3 + b_3 T^2)^2} + \frac{a_4 + b_4 T^2}{\lambda^2 - a_5^2} - a_6 \lambda^2} \quad (0.28)$$

Coefficient	Value	
	Ref. [40]	Ref. [43]
a ₁	4.5567	5.35583
a ₂	0.097	0.100473
a ₃	0.201	0.20692
a ₄	0	100
a ₅	0	11.34927
a ₆	2.24×10 ⁻²	1.5334×10 ⁻²
b ₁	2.605×10 ⁻⁷	4.629×10 ⁻⁷
b ₂	2.7×10 ⁻⁸	3.862×10 ⁻⁸
b ₃	5.4×10 ⁻⁸	-0.89×10 ⁻⁸
b ₄	0	2.657×10 ⁻⁵

Table 8. Sellmeier data for lithium niobate.

The Sellmeier data from Reference 40 have better agreement for wavelengths in the mid-infrared region than the data from Reference 43, which have better agreement at shorter wavelengths (visible).

At elevated temperatures (~150°C), the crystal expands in the propagation direction, and the grating periods increases correspondingly. The thermal expansion of a crystal of length l at a temperature T normalised to the length of 25°C, $l_{25^\circ\text{C}}$ is given by⁴⁴:

$$l = l_{25^\circ\text{C}} \left[1 + \alpha(T - 25^\circ\text{C}) + \beta(T - 25^\circ\text{C})^2 \right], \quad (0.29)$$

where $\alpha = 1.54 \times 10^{-5} \text{ K}^{-1}$ and $\beta = 5.3 \times 10^{-9} \text{ K}^{-2}$.

The crystal symmetry of lithium niobate result in the following nonlinear matrices:

$$d_{i,m} = \begin{pmatrix} 0 & 0 & 0 & 0 & d_{31} & -d_{22} \\ -d_{22} & d_{22} & 0 & d_{31} & 0 & 0 \\ d_{31} & d_{31} & d_{33} & 0 & 0 & 0 \end{pmatrix} \quad (0.30)$$

and the respective values for these coefficients (in pm/V) are

Coefficient	Value ¹⁶
d_{22}	2.1
d_{31}	4.3
d_{33}	27
$d_{\text{eff}(QPM)} = (2/\pi)d_{33}$	17

Table 9. Birefringent and QPM effective ($m=1$) nonlinear coefficients for LiNbO_3 .

As previously explained, the coefficient d_{33} can only be accessed by a QPM process. Thus, quasi-phasematching with all the waves polarised parallel to the z-axis yields a gain enhancement over the birefringently phasematched process of a factor of ~ 20 -fold increase in conversion efficiency.

Despite the large transparency range and the high nonlinear coefficient, LiNbO_3 has a very important drawback in that it suffers from a damage mechanism called photorefractive damage.⁴⁵ This effect is caused by optically excited free charges in the crystal which diffuse in the electromagnetic field of the light beam. They scatter through the material towards lower light intensities (outside the beam) and set up an internal field, which distorts the beam via the electro-optic effect. Photorefractive damage is particularly a limiting factor when trying to use this crystal for high power and short wavelength generation. Photorefractive damage can be minimised by heating the crystal at temperatures above 100 °C for applications in the infrared or at 180 °C for applications in the visible.^{2,46}

2.4 Conclusions

In this chapter the basic concepts of nonlinear optical theory were presented. The material requirements and characteristics to achieve efficient wavelength conversion in birefringent nonlinear crystals and in the frame of a three-wave process was studied.

Quasi-phasematching was then presented as an alternative and powerful technique to achieve efficient wavelength conversion. The general theory of QPM was discussed and emphasis was made to the implementation of QPM devices by the periodic-poling technique in ferroelectric materials.

The chapter finished by giving a review of some of the physical properties of the nonlinear crystals, KTP, RTA and lithium niobate, that were used in this work. The optical transmission, dispersion data and relations and nonlinear coefficients, together with some other physical properties, were presented. We have seen that for frequency conversion processes, periodically-poling these materials offer several advantages compared to the bulk materials. One of these advantages is that it is possible to access the largest nonlinear coefficients that are available in the crystal and therefore to obtain more efficient frequency conversion processes.

2.5 References

1. F. Zernike, J. E. Midwinter, *Applied nonlinear optics*, Academic Press, New York (1973).
2. J. A. Armstrong, N. Bloembergen, J. Ducuing, P. S. Pershan, "Interactions between light waves in nonlinear dielectrics," *Phys. Rev. Lett.*, **127**, 1918 – 1939 (1962).
3. D. A. Kleinman, "Nonlinear dielectric polarization in optical media," *Phys. Rev.*, **126**, 1977 (1962).
4. P. G. Harper, B. S. Wherrett, *Nonlinear optics*. Proceedings of the fifty second Scottish Universities Summer School in Physics, 1975 (Academic Press, New York 1977).
5. R. W. Boyd, *Nonlinear optics*, Academic Press Inc., (California, USA, 1992)
6. V. G. Dimitriev, G. G. Gurzadyan, D. N. Nikogosyan, *Handbook of nonlinear optical crystals*, Springer series in optical science **64**, Springer-Verlag, Berlin Heidelberg 1991.
7. M. V. Hobden, *J. Appl. Phys.*, **38**, 4365 (1967)
8. D. Yu. Stepanov, V. D. Shigorin, G. P. Shipulo, "Phase-matching directions under optical mixing in biaxial crystals with quadratic susceptibility," *Kvantovaya elektron* **11**, 1957 – 1964 (1984).
9. P. A. Franken, J. F. Ward, "Optical harmonics and nonlinear phenomena," *Rev. Mod. Phys.*, **35**, 23 – 39 (1963).
10. D. E. Thompson, J. D. McMullen, D. B. Anderson, "Second harmonic generation in GaAs 'stack of plates' using high power CO₂ laser radiation," *Appl. Phys. Lett.*, **29**, 113 – 115 (1976).
11. Y. Lu, L. Mao, N. B. Ming, "Blue light generation by frequency doubling of an 810-nm cw GaAlAs diode laser in a quasi-phase-matched LiNbO₃ crystal," *Opt. Lett.*, **19**, 1037 – 1039 (1994).
12. M. Yamada, N. Nada, M. Saitoh, K. Watanabe, "First-order quasi-phase matched LiNbO₃ waveguide periodically poled by applying an external field for efficient blue second-harmonic generation," *Appl. Phys. Lett.*, **62**, 435 – 436 (1993).
13. E. Lallier, M. Brevignon, J. Lehoux, "Efficient second-harmonic generation of CO₂ lasers with a quasi-phase-matched GaAs Crystal," *Opt. Lett.*, **23**, 1511 – 1513 (1998).
14. G. Khanarian, M. A. Mortazavi, A. J. East, "Phase-matched second-harmonic generation from free standing periodically stacked polymer films," *Appl. Phys. Lett.*, **63**, 1462 – 1464 (1993).
15. M. A. Mortazavi, G. Khanarian, "Quasi-phase-matched frequency doubling in bulk periodic polymeric structures," *Opt Lett.*, **19**, 1290 – 1292 (1994).
16. L. E. Myers, R. C. Eckardt, M. M. Fejer, R. L. Byer, W. R. Bosenberg, J. W. Pierce, "Quasi-phase-matched optical parametric oscillators in bulk periodically poled LiNbO₃," *J. Opt. Soc. Am. B*, **12**, 2102 – 2116 (1995).
17. I. Camlibel, *J. Appl. Phys.*, **40**, 1690 (1969).
18. S. N. Zhu, Y. Y. Zhu, Z. Y. Zhang, H. Shu, H. F. Wang, J. F. Hong, C. Z. Ge, N. B. Ming, "LiTaO₃ crystal periodically poled by applying an external pulsed field," *J. Appl. Phys.*, **77**, 5481 – 5483 (1995).

19. H. Karlsson, F. Laurell, P. Henriksson, G. Arvidsson, "Frequency doubling in periodically poled RbTiOAsO₄," *Electron. Lett.*, **32**, 556 – 557 (1996).
20. H. Karlsson, F. Laurell, "Electric field poling of flux grown KTiOPO₄," *Appl. Phys. Lett.*, **71**, 3474 – 3476 (1997).
21. H. Karlsson, F. Laurell, L. K. Cheng, "Periodic poling of RbTiOPO₄ for quasi-phase matched blue light generation," *Appl. Phys. Lett.*, **74**, 1519 – 1521 (1999).
22. G. Rosenman, A. Skliar, Y. Findling, P. Urenski, A. Englander, P. A. Thomas, Z. W. Hu, "Periodically poled KTiOAsO₄ crystals for optical parametric oscillation," *J. Phys. D Appl. Phys.*, **32**, 49 – 52 (1999).
23. E. J. Lim, M. M. Fejer, R. L. Beyer, "Second harmonic generation of green light in periodically poled planar lithium niobate waveguide," *Electron. Lett.*, **25**, 174 – 175 (1989).
24. H. Ito, C. Takyu, H. Inaba, "Fabrication of periodic domain grating in LiNbO₃ by electron beam writing for application of nonlinear optical processes," *Electron. Lett.*, **27**, 1221 – 1222 (1991).
25. J. D. Bierlein, H. Vanherzeele, "Potassium titanyl phosphate - properties and new applications," *J. Opt. Soc. Am. B*, **6**, 622 – 633 (1989).
26. L. K. Cheng, L. T. Cheng, J. Galperin, P. A. Morris, Hotsenpiller, J. D. Bierlein, "Crystal-growth and characterization of KTiOPO₄ isomorphs from the self-fluxes," *J. Crystal Growth*, **137**, 107 – 115 (1994).
27. G. M. Loiacono, D. N. Loiacono, R. A. Stolzenberger, "Crystal-growth and characterization of ferroelectric CsTiOAs₄," *J. Crystal Growth*, **131**, 323 – 330 (1993).
28. P. F. Bordoui, M. M. Fejer, "Inorganic crystal for nonlinear frequency conversion," *Annu. Rev. Mater. Sci.*, **23**, 321 (1993).
29. K. Daneshvar, E. A. Giess, A. M. Bacon, D. G. Dawes, L. A. Gea, L. A. Boatner, "Ion exchange in potassium titanyl phosphate," *Appl. Phys. Lett.*, **71**, 756 – 758 (1997).
30. H. Karlsson, *Fabrication of periodically poled crystals from the KTP family and their applications in nonlinear optics*, Doctoral thesis. Department of laser physics and quantum optics. The Royal Institute of technology, Stockholm. ISSN 0280-316X (1999).
31. T. Y. Fan, C. E. Huang, B. Q. Hu, R. C. Eckardt, Y. X. Fan, R. L. Byer, R. S. Feigelson, "2nd harmonic-generation and accurate index of refraction measurements in flux-grown KTiOPO₄," *Appl. Opt.*, **26**, 2390 – 2394 (1987).
32. V. A. Dyakov, V. V. Krasnikov, V. I. Pryalkin, M. S. Pshenichnikov, T. B. Razumikhina, V. S. Solomatin, A. I. Kholodnykh, "The Sellmeier equation and tuning characteristics of KTP-crystal frequency-converters in the range from 0.4 to 4.0 μm," *Kvantovaya elektronika*, **15**, 1703 – 1704 (1988).
33. K. Kato, "Parametric oscillation at 3.2 μm in KTP pumped at 1.064 μm," *IEEE J. Quantum Electron.*, **27**, 1137 – 1140 (1991).
34. D. L. Fenimore, K. L. Shepler, D. Zelmon, S. Kuck, U. B. Ramabadran, P. Von Richter, "Rubidium titanyl arsenate difference-frequency generation and validation of new Sellmeier coefficients," *J. Opt. Soc. Am. B*, **13**, 1935 – 1940 (1996).

35. K. Fradkin, A. Arie, A. Skliar, G. Rosenman, "Tunable mid-infrared source by difference frequency generation in bulk periodically poled KTiOPO_4 ," *Appl. Phys. Lett.*, **74**, 914 – 916 (1999).
36. W. Wiechmann, S. Kubota, T. Fukui, H. Masuda, "Refractive-index temperature derivatives of potassium titanyl phosphate," *Opt. Lett.*, **18**, 1208 – 1210 (1993).
37. H. Karlsson, M. Olson, G. Arvidsson, F. Laurell, U. Bäder, A. Borsutzky, R. Wallenstein, S. Wickström, M. Gustafsson, "Nanosecond optical parametric oscillator based on large-aperture periodically poled RbTiOAsO_4 ," *Opt. Lett.*, **24**, 330 – 332 (1999).
38. D. M. Finlayson, B. D. Sinclair, "*Advances in lasers and applications*," Proceedings of the fifty second Scottish Universities Summer School in Physics, St. Andrews, (Institute of Physics publishing) Sep. 1998 ISBN 07503-0631-9.
39. M. Houé, P. D. Townsend, "An introduction to methods of periodic poling for 2nd-harmonic generation," *J. Appl. Phys.*, **28**, 1747 – 1763 (1995).
40. M. V. Hobden, J. Warner, *Phys. Lett.*, **22**, 243 (1966).
41. R. A. Andrews, *IEEE J. Quantum. Electron.*, **6**, 68 (1970).
42. G. J. Edwards, M. Lawrence, "A temperature-dependent dispersion-equation for congruently grown lithium-niobate," *Opt. Quantum Electron.*, **16**, 373 – 375 (1984).
43. D. H. Jundt, "Temperature-dependent Sellmeier equation for the index of refraction, $n(e)$, in congruent lithium niobate *Opt. Lett.*, **22**, 1553 – 1555 (1997).
44. Y. S. Kim, R. T. Smith, *J. Appl. Phys.* **40**, 4637 (1969).
45. G. E. Peterson, A. M. Glass, T. J. Negran, "Control of the susceptibility of lithium niobate to laser induced refractive index changing," *Appl. Phys. Lett.*, **19**, 130 (1971).
46. L. E. Myers, W. R. Bosenberg, "Periodically poled lithium niobate and quasi-phase-matched optical parametric oscillators," *IEEE J. Quantum Electron.*, **33**, 1663 – 1672 (1997).

CHAPTER 3

ULTRASHORT PULSE CHARACTERISATION TECHNIQUES

In this chapter, I will review key features of the techniques that were used in the laboratory for measuring femtosecond pulses. I will start by describing the typical SHG-autocorrelation, followed by the use of two-photon absorption in a photodiode as the nonlinear element in an autocorrelator which will be described in the next section. Special emphasis will be made in the use of these devices to autocorrelate pulses in the visible spectral region. I will then introduce the frequency-resolved optical gating (FROG) technique and present our experimental setup and some results. Finally, I will briefly describe preliminary results using a new and improved pulse characterisation technique, cross-FROG (X-FROG), for measuring mid-infrared femtosecond pulses.

3.1 Autocorrelation

Early on, it was realised that the only event fast enough to measure an ultrashort pulse was the pulse itself by means of an autocorrelation. An autocorrelation is made by mixing the pulse, $E(t)$ and a replica, in a nonlinear medium such as a second-harmonic generation crystal¹ or a two-photon absorber^{2,3} (e.g a photodiode) and detecting the signal that is being produced by the device as a function of the time delay, τ between the pulse and its replica. The mixing signal is

maximised when the two pulses are temporally coincident, so that the range of delays over which the signal is detected, is comparable with the pulse duration. Mathematically the autocorrelation is given by:

$$g_2(\tau) = \frac{\int_{-\infty}^{\infty} \left| [E(t) + E(t + \tau)] \right|^2 dt}{\int_{-\infty}^{\infty} |E(t)|^4 dt} \quad (3.1)$$

This interferometric (or fringe resolved) autocorrelation can provide quantitative information about the pulse duration. Information about the phase $\phi(t)$ can be partially obtained and therefore, just a qualitative measure of the amount of chirp present can be made.

The laboratory arrangement typically used in the measurement of ultrashort pulses is illustrated in Figure 1. It consists of a Michelson interferometer in which one of the mirrors is stationary and the other one is on a moving loudspeaker. The loudspeaker provides the necessary variable delay driven by a large amplitude low frequency signal, which is also used for triggering purposes. The two beams are then recombined in the nonlinear crystal and the second-harmonic signal is detected and displayed on an oscilloscope. This output displays the interferometric autocorrelation or, by using a suitable smoothing capacitance, the time-averaged intensity autocorrelation $G_2(\tau) = \langle g_2(\tau) \rangle$.

Now, if we substitute the expression for the electric field, with its temporal dependence explicitly expressed into Equation (3.1), it is possible to obtain:

$$g_2(t) \propto AK \int_{-\infty}^{\infty} \{ E_0^4(\omega, t) + E_0^4(\omega, t + \tau) + 4E_0^2(\omega, t)E_0^2(\omega, t + \tau) + 2E_0^2(\omega, t)E_0^2(\omega, t + \tau)\cos(2\omega t) + [4E_0^3(\omega, t)E_0(\omega, t + \tau) + 4E_0(\omega, t)E_0^3(\omega, t + \tau)]\cos(\omega t) \} dt. \quad (3.2)$$

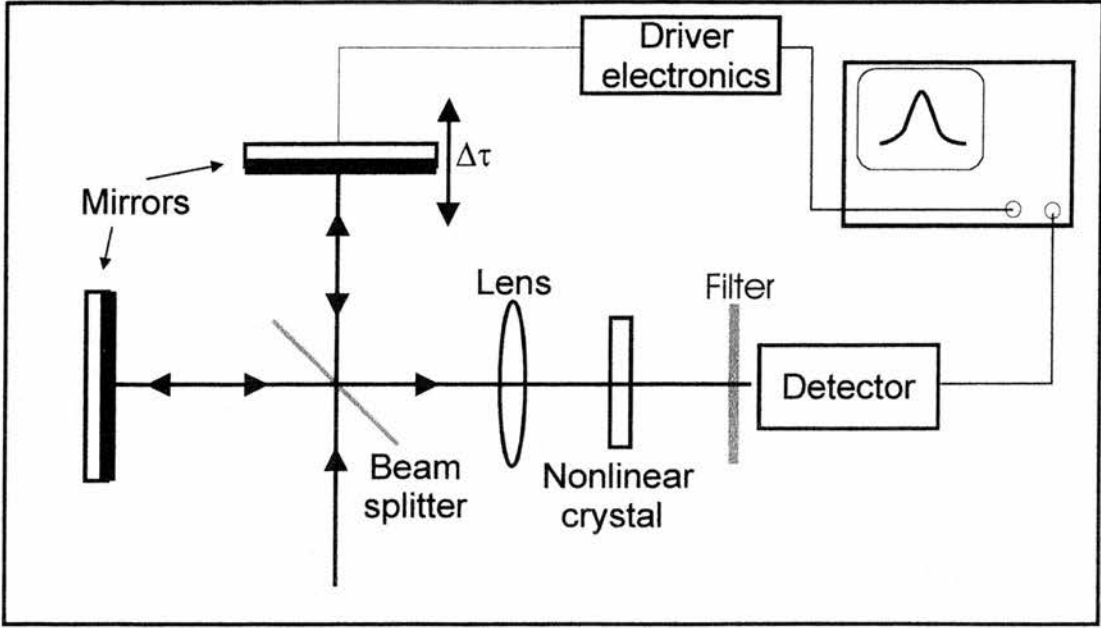


Figure 1. Experimental set up for pulse autocorrelation.

At time delay $\tau = \pm \pi/\omega$, where $\cos(\omega\tau) = -1$, and $\cos(2\omega\tau) = +1$ we have

$$g_2(t = \pm \frac{\pi}{\omega}) \propto AK \int_{-\infty}^{\infty} \{2E_0^4(\omega, t) + 6E_0^4(\omega, t) - 8E_0^4(\omega, t)\} dt = 0. \quad (3.3)$$

Thus for values of the delay where pulses overlap, the interference terms will cause oscillation of the signal. The signal goes from maximum to minimum values for a delay change of $\Delta\tau = \pm \pi/\omega$. This means that the interferometric autocorrelation is self calibrating: the fringe separation corresponds to one optical cycle at the centre wavelength of the pulse.

As $\tau \rightarrow \infty$ (large delay or no overlap) only the background terms will be present. Since the pulses are identical we have:

$$g_2(\infty) \propto 2KA \int_{-\infty}^{\infty} E_0^4(\omega, t) dt \quad (3.4)$$

At zero delay we have

$$g_2(0) \propto 16KA \int_{-\infty}^{\infty} E_0^4(\omega, t) dt \quad (3.5)$$

Therefore, the fringes in any interferometric autocorrelation will have a peak-to-background contrast ratio given by

$$\frac{g_2(0)}{g_2(\infty)} = \frac{16KA \int_{-\infty}^{\infty} E_0^4(\omega, t) dt}{2KA \int_{-\infty}^{\infty} E_0^4(\omega, t) dt} = 8:1 \quad (3.6)$$

This contrast ratio conveys additional information regarding the frequency chirp present on a pulse. This is because a variation of the instantaneous phase over the duration of the pulse will reduce interference of the delayed pulses and hence reduce fringe visibility.

If the detection electronics used can not resolve fringes (because the mirror scans through one fringe faster than the detection response time) then the cosine terms in Equation (3.2) will average to zero giving:

$$g_2(t) \propto AK \int_{-\infty}^{\infty} \{E_0^4(\omega, t) + E_0^4(\omega, t + \tau) + 4E_0^2(\omega, t)E_0^2(\omega, t + \tau)\} dt \quad (3.7)$$

Then we find that the intensity autocorrelation have a peak-to-background ratio of

$$\frac{g_2(0)}{g_2(\infty)} = \frac{6KA \int_{-\infty}^{\infty} E_0^4(\omega, t) dt}{2KA \int_{-\infty}^{\infty} E_0^4(\omega, t) dt} = 3:1 \quad (3.8)$$

The full width at half maximum (FWHM) of the pulse intensity is related to the FWHM of the pulse autocorrelation by a conversion factor that depends on the pulse shape and the type of autocorrelation recorded. Table 1 shows these conversion factors for pulses with $\text{sech}^2(t)$ and Gaussian (e^{-t^2}) intensity profiles, together with their respective pulse duration-bandwidth product, $\Delta\nu\Delta\tau_p$, of the transformed-limited pulse shape.

Intensity Profile	$\frac{\Delta\tau_{g_2(t)}}{\Delta\tau_p}$	$\frac{\Delta\tau_{\langle g_2(t) \rangle}}{\Delta\tau_p}$	$\Delta\nu_p\Delta\tau_p$
e^{-t^2}	1.697	1.414	0.441
$\text{sech}^2(t)$	1.897	1.543	0.315

Table 1. Theoretical conversion factors for interferometric and intensity autocorrelations, together with the pulse duration-bandwidth products for Gaussian and sech^2 pulse shapes.

SHG interferometric and intensity autocorrelations of the output of a $\text{Cr}^{3+}:\text{LiSrGaF}_6$ (Cr:LiSGaF) laser⁴ pumped with a self-injection-locked AlGaInP diode laser are shown in Figure 2(a) and 2(b), respectively. The laser was operating at a wavelength of 850 nm and delivering transform-limited pulses of 100 fs pulses when pumped with 45 mW. The interferometric autocorrelation shows an 8:1 peak-to-background ratio which indicates complete modelocking in the absence of an intense cw background or spike components. For the same reason, the intensity autocorrelation also shows the 3:1 peak-to-background ratio.

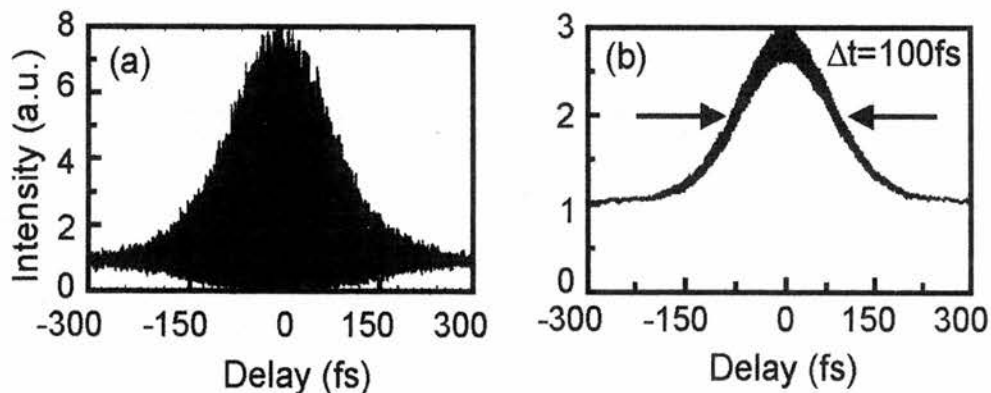


Figure 2. Interferometric (a) and intensity (b) autocorrelations of the output of a Cr:LiSGaF laser pumped with an self-injection-locked AlGaInP diode laser.

In the previous analysis, chirp-free pulses were assumed. However, if the calculated value of the pulse duration-bandwidth product, $\Delta\nu\Delta\tau_p$, is larger than expected, then the pulses are likely to be frequency-chirped. In this case, care should be taken when measuring them. As explained before, in the interferometric autocorrelation, the individual optical cycles within the pulse envelope are resolved. However, in frequency chirped pulses, the leading and trailing edges are not coherent and thus do not interfere⁵. Consequently, the interferometric autocorrelation function collapses over this part of the pulse.

3.2 Two-photon absorption autocorrelator

Although in widespread use, the SHG-autocorrelator does have several drawbacks. The main limitation is that appropriate nonlinear crystals for SHG in the UV and MIR are not available. Even at wavelengths where SHG crystals are available, systematic error associated with the finite phasematching bandwidth of the nonlinear crystal can arise when measuring particular short pulses. In this case, the SHG crystal must be kept to a minimum thickness to ensure conversion of the whole phasematching bandwidth, at the expense of a reduced extraction of power. Also for longer pulses, the thickness of the crystal may introduce undesirable effects such as temporal walk-away and Pointing vector walk-off. Additionally, due to its phasematching properties and finite spectral bandwidth, several doubling crystals may be needed when characterising large spectral ranges.

Sensitive second-order optical autocorrelation measurements of femtosecond pulses have been demonstrated using the two-photon response of semiconductor devices to produce the necessary quadratic dependence of photocurrent on incident

peak intensity. The basic requirement is that the bandgap energy of the semiconductor is greater than the wavelength of the light to be characterised. This involves exciting the valence band electrons to a virtual energy level with one photon. A second photon is required to promote this electron into the conduction band. The response of this effect has a quadratic dependence on the intensity of the incident light⁶, therefore, two-photon absorption devices can replace the SHG crystal and the photodetector (such as photomultipliers) in a second-order autocorrelator.

A number of devices able to perform second-order autocorrelations in the near- and mid-IR have already been demonstrated. Autocorrelation of near-IR wavelengths from approximately 800 - 1300 nm has been achieved using semiconductor devices such as AlGaAs light-emitting diodes (LEDs)⁷, GaAsP photodiodes⁸ and ZnSe photoconductors⁹. Ultrashort pulses at longer wavelengths have been measured using Si photodiodes¹⁰, GaAs LEDs^{11,12} and InGaAsP laser-diodes⁶ and mid-infrared wavelengths have been accessed by using InGaAs¹³ or InAs¹⁴ photodiodes to cover the 2 - 5 μm wavelength region.

3.2.1 Two-photon autocorrelation of visible femtosecond pulses

The spectral region which had until now remained difficult to access using two-photon measurement techniques was the visible, principally because of the lack of suitable detectors in which the two-photon response dominated the residual linear response at wavelengths above the bandgap wavelength. Recent results using a custom-made gallium-nitride (GaN) photodiode structure demonstrated two-photon

autocorrelation of low repetition-rate amplified femtosecond pulses with energies of 20 nJ at a wavelength of 410 nm¹⁵. Inferior material quality in commercially-available GaN photodiodes prevented a similar measurement from being made using off-the-shelf devices or femtosecond sources with a smaller peak:average power ratio. Improvements in the quality of GaN semiconductors have resulted recently in the successful fabrication of laser diodes from this material¹⁶ which are now available on a commercial basis. Using one such laser diode with a nominal emission wavelength of 393 nm (Nichia NLHV500) we have found a strong two-photon response across a range of visible wavelengths which has enabled sensitive measurement of intensity and interferometric second-order autocorrelations.

In order to consistently characterise the single-photon and two-photon response of the laser diode we selected three wavelengths, 440, 540 and 630 nm, which could be approximately accessed both by the CW and modelocked laser sources available to us. The CW sources used were HeNe, frequency-doubled Nd:YVO₄ and HeCd lasers which produced outputs at 633, 532 and 442 nm. To generate red femtosecond pulses we used an optical parametric oscillator (OPO) based on periodically-poled lithium niobate (PPLN) and synchronously-pumped by a self-modelocked Ti:sapphire laser with a repetition rate of 85 MHz. The OPO was operated near 1250 nm and was dispersion-compensated using an intracavity pair of Brewster-cut SF10 prisms. The average output power of the OPO was 350 mW and we were able to produce around 10 mW of red light tunable from 600 - 630 nm by using single-pass frequency-doubling in a 2-mm long BBO crystal. The PPLN crystal used in the OPO had a number of different grating periods and by selecting a shorter period and changing the cavity mirrors of the OPO we

were able to operate at a wavelength of 1080 nm and obtain average output powers of around 300 mW at this wavelength. Frequency doubling enabled us to generate up to 5 mW of green output at 540 nm. Blue light at 440 nm was produced by tuning the Ti:sapphire laser to operate at 880 nm then frequency doubling its output to produce up to 20 mW of average power. In all the experiments we focused the light into the diode using a standard 20 × microscope objective with a numerical aperture of 0.4. The laser diode was mounted in a standard 5.6 mm package and the generated photocurrent (no applied bias) was measured by connecting the diode output across the terminals of a 1 MΩ oscilloscope.

Figure 3 shows the diode response at red (triangles), green (squares) and blue (circles) wavelengths to incident modelocked (filled symbols) and CW (open symbols) laser radiation. The dashed lines are best fits through the data of lines with slopes of 1 (CW measurement) and the solid lines are best-fits with slope 2 (modelocked measurement). The results show that we were able to observe a dominant nonlinear response even for incident powers of around 100 μW which correspond to pulse energies of approximately 1 pJ. The nonlinear sensitivity could be easily extended to include pulses with only femtojoule energies by using a simple amplifier. Modelocked measurements made at 440 nm required more power to be incident on the diode because residual linear absorption at this wavelength meant that the linear response dominated the two-photon response at low powers. To avoid saturation of the diode while still allowing it to generate an appreciable photocurrent we used a 10 kΩ resistor in parallel with the diode outputs which enabled us to measure the nonlinear response at 440 nm shown in Figure 3 (filled circles). The differences in the absolute nonlinear responsivity

measured at the individual test wavelengths are attributed to differences in the coupling efficiency into the laser diode. The decrease in linear responsivity as the wavelength is increased is expected as the incident photon energy falls below the device bandgap energy.

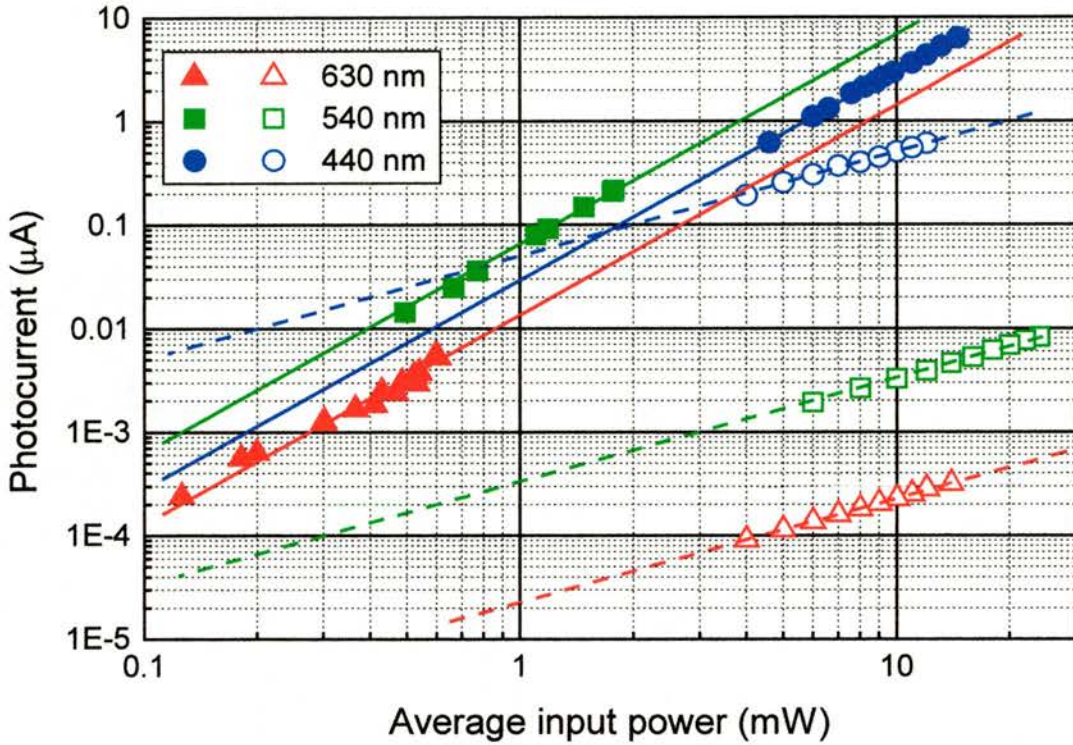


Figure 3. Photocurrent produced by the GaN laser diode for illumination by modelocked (filled symbols) and CW (open symbols) sources at red (triangles), green (squares) and blue (circles) wavelengths. For details of exact wavelengths used see text. Modelocked data is shown together with a best-fit line of slope = 2 (solid lines) and CW data with a best-fit line of slope = 1 (dashed lines).

It is clear from the nonlinear responsivity measurements that a true quadratic response to incident peak intensity is accessible across the visible wavelength range for modest average powers and therefore the diode is a suitable nonlinear detector for autocorrelation purposes. We recorded intensity and fringe-resolved interferometric autocorrelations at all three test wavelengths using a scanning Michelson interferometer

comprising a plane mirror in each arm and a broadband 50:50 visible beamsplitter. Inspection of the measured profiles shown in Figure 4 shows that the expected 8:1 contrast ratio is obtained for the interferometric results, which confirms that the measurements are true second order autocorrelations. Interferometric measurements were possible for incident average powers on the laser diode as low as 0.7 mW, corresponding to pulse energies of around 8 pJ.

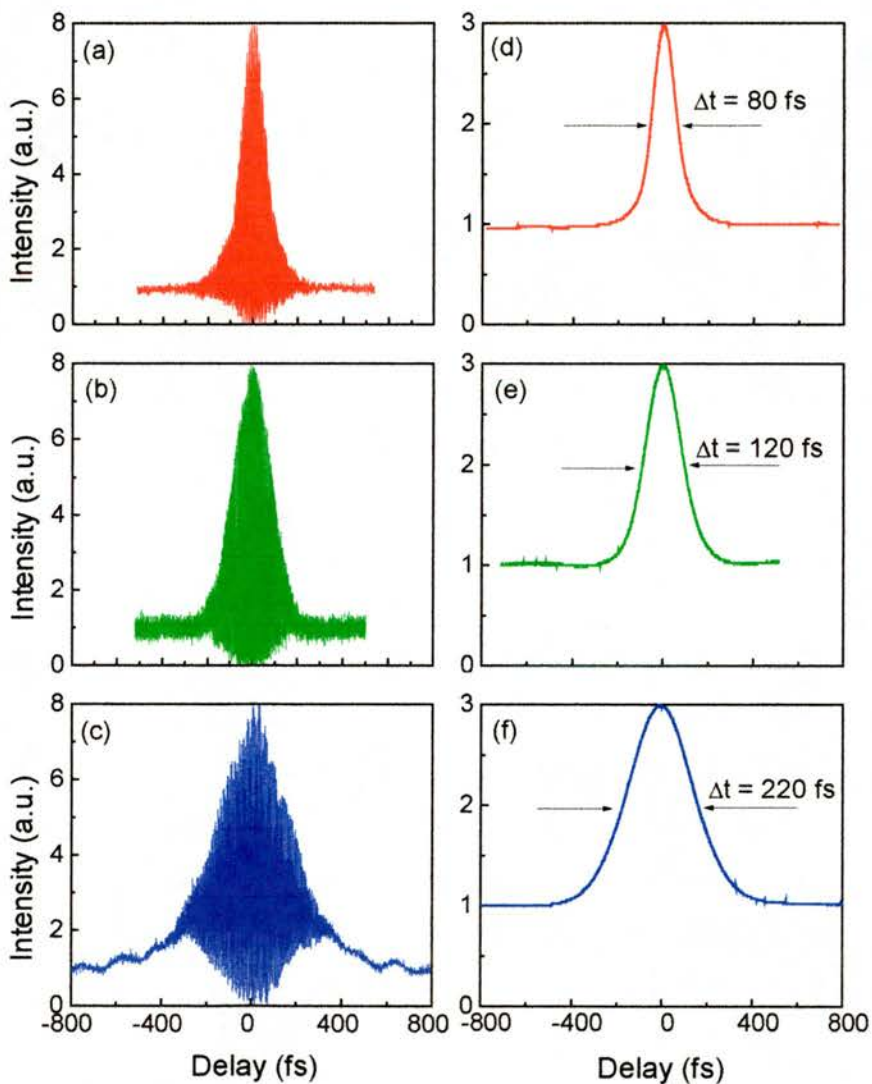


Figure 4. Fringe-resolved interferometric (left column) and intensity (right column) autocorrelations of femtosecond pulses with centre wavelengths at 630 (a, d), 540 (b, e) and 440 nm (c, f), measured using the GaN laser diode as the nonlinear element in a Michelson autocorrelator.

As an additional check of the integrity of our measurements we compared an autocorrelation recorded at 630 nm using the laser diode with one made using a phasematched KDP crystal and a photomultiplier tube and found excellent agreement (see Figure 5). The cut of the KDP crystal available to us prevented similar measurements from being made at shorter wavelengths.

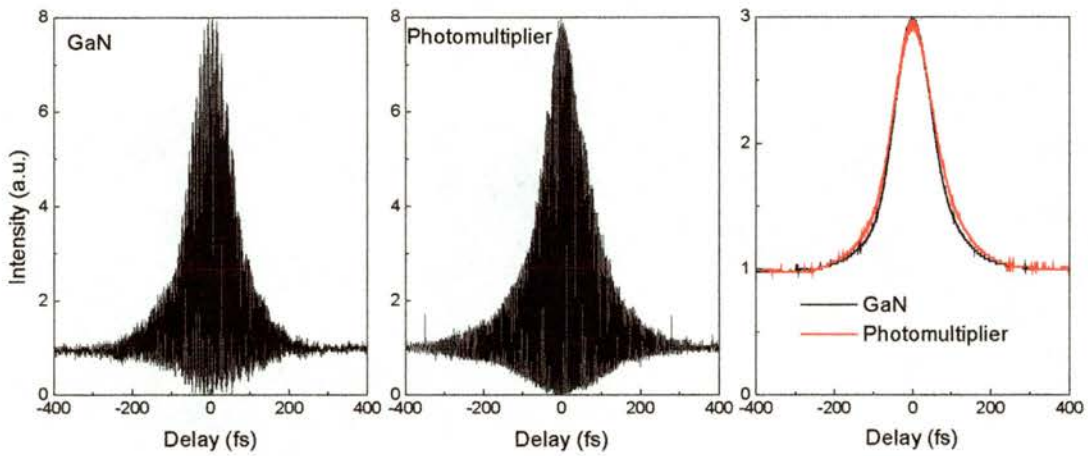


Figure 5. Comparison between the interferometric and intensity autocorrelations obtained by two-photon absorption using a GaN diode laser and SHG using a KDP crystal and a photomultiplier tube.

To identify the shortest useful measurement wavelength accessible using the diode we tuned the Ti:sapphire laser to generate second harmonic wavelengths as low as 415 nm. We were able to record good quality fringe-resolved and intensity autocorrelations at 425 nm (Figure 6a and 6b). Strong linear absorption at 415 nm prevented us from measuring an interferometric autocorrelation here but the fringes produced by the linear response averaged to zero at high scan speeds, allowing us to record an intensity autocorrelation profile at this wavelength (Figure 6c).

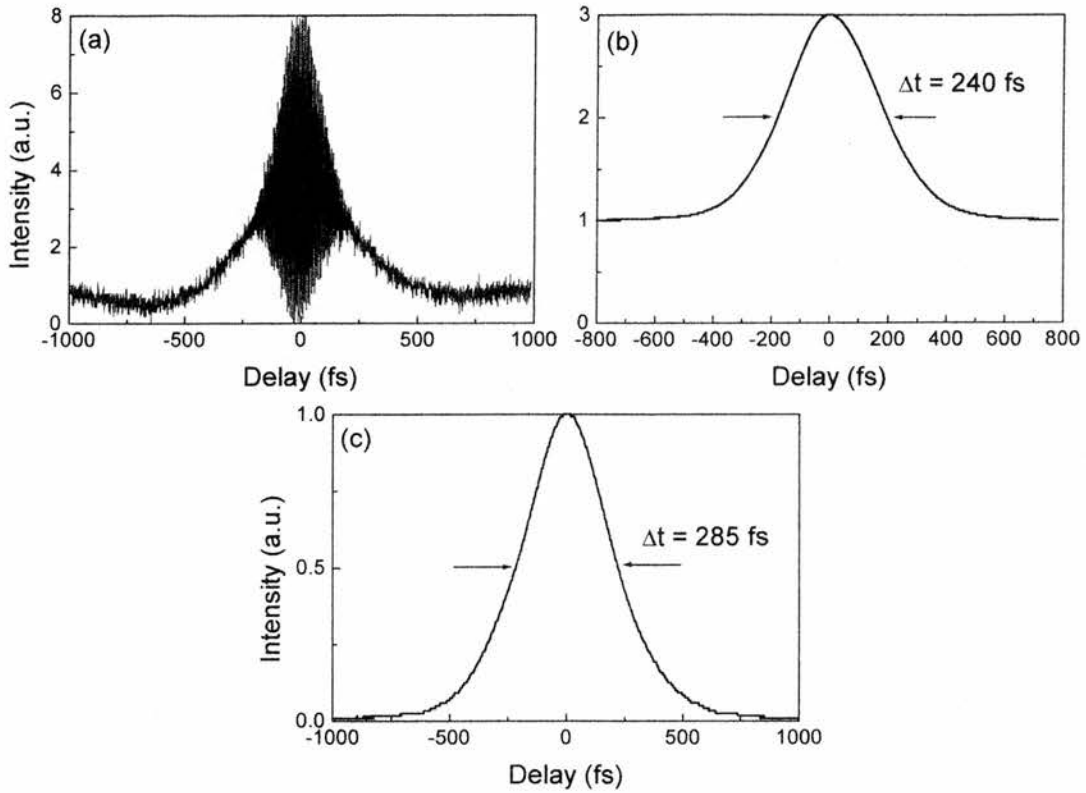


Figure 6. Autocorrelation profiles measured using the GaN laser diode at wavelengths of 425 nm (a, b) and 415 nm (c).

The performance of the laser-diode-based autocorrelator can be appreciated better when it is compared with the conventional approach using a phasematched nonlinear crystal. Broadband second-harmonic generation in the visible is problematical because of the high first-order dispersion and birefringence in all popular nonlinear crystals at these wavelengths. This means that the phasematching behaviour depends strongly on the propagation angle inside the crystal and very short crystals must be used if phasematching over an appreciable bandwidth is required. We illustrate this point with an example of the crystal BBO which can be used to frequency double light with a wavelength as short as 400 nm. Tuning from 440 - 630 nm would require a crystal

rotation of around 50° and, for the crystal bandwidth to be sufficient to frequency-double transform-limited 100 fs Gaussian pulses across this range, a thickness of 100 μm . Measurement across the same range without any angle tuning would require a crystal thickness of less than 5 μm . The useful measurement range of the laser-diode extends from ~ 415 to 780 nm, allowing it to complement the coverage provided by other two-photon devices based on AlGaAs or GaAsP which include the common Ti:sapphire operating range from $\sim 750 - 1050$ nm. The laser-diode is therefore suitable for autocorrelating low power but extremely broadband visible pulses such as those recently produced by continuum generation in photonic-bandgap fibre¹⁷. Dispersion in the waveguide structure of the diode may make it unsuitable for measurements of very short visible pulses, however simulations of pulse broadening in an AlGaInP waveguide autocorrelator have shown that even if the pulse broadens by 40% after entering the waveguide the measured autocorrelation profile is almost identical to that of the unbroadened pulse¹⁸. Further work is therefore required to establish whether significantly shorter visible pulses can be measured using the technique presented here.

3.3 Frequency-Resolved Optical Gating

The frequency and intensity properties of pulsed laser have long been used to probe and even alter properties of matter. These properties are routinely measured using (interferometric and intensity) autocorrelators and spectrometers. However, these measurements just provide qualitative information about the phase $\phi(t)$ and require *a priori* assumptions about the shape $I(t)$ of the pulses¹⁹. For many experiments, it is

important to have accurate knowledge of the temporal and phase information describing the pulse profiles. For example, the phase becomes important in interactions with matter in which optical transitions have a phase relaxation time exceeding the temporal pulse width and interpulse separations.

3.3.1 Time-frequency domain methods

There has been a lot of active research to the development of tools based on the simultaneous acquisition of the time and frequency information of the pulse (time-frequency domain methods) that have permitted the retrieval of the full complex electric field $E(t)$.

The relevant concept in the application of time-frequency methods to ultrashort pulse science is that of the *time-frequency distribution*. These are functions of two variables (time and frequency), meant to be a joint distribution representing the time-varying spectral properties of the ultrashort laser pulse. In other words, a time-frequency distribution should show what frequencies are present at a given time (and vice versa). A simple and intuitive way to represent this is using the short-time Fourier transform¹⁹,

$$SFT(f, \tau) = \int_{-\infty}^{\infty} dt E(t) g(t - \tau) \exp(i2\pi ft) \quad (3.9)$$

where $g(t)$ is some arbitrary gate function. The gate selects the part of the signal near time τ , and the Fourier transform determines the frequency content of that part of the signal.

There is a wide variety of possible time-frequency distributions, each with its own particular strengths and weaknesses. They are mathematically rigorous, and in general, they are quite visually intuitive and contain all relevant information about

the laser pulse. Amongst the most relevant include the Wigner function²⁰, the sonogram^{21,22}, and the spectrogram^{23,24}. From a practical point of view, the Wigner distribution has the severe limitation that no way has yet been found to measure the Wigner distribution of an ultrashort pulse in the laboratory, as this measurement appears to require a time-reversed replica of the pulse. On the other hand, the sonogram and the spectrogram have the useful property of being non-negative, making a laboratory measurement possible. The sonogram is generated by filtering the signal in the frequency domain and then recording the resultant output as a function of time. The spectrogram is defined similarly to the sonogram but in the time domain and it can be shown that is the formal equivalent to the sonogram, but in the time domain.

3.3.2 The frequency-resolved optical gating technique

Using optical methods to obtain a spectrogram of the pulse to be measured is the basis of the technique called frequency-resolved optical gating (FROG). The resulting spectrogram is then referred to as the FROG trace. This is formally equivalent to the spectrogram of the field $E(t)$ and mathematically it can be described as:

$$\begin{aligned}
 I_{FROG}(\omega, \tau) &= \left| \int_{-\infty}^{\infty} dt E(t) g(t - \tau) \exp(i\omega t) \right|^2 \\
 &= \left| \int_{-\infty}^{\infty} dt E_{sig}(t, \tau) \exp(i\omega t) \right|^2
 \end{aligned} \tag{3.10}$$

where $g(t - \tau)$ is a variable-delay gate function and τ is the delay.

Experimentally, the FROG technique involves splitting the pulse to be measured into two variable-delayed pulses, $E(t)$ and $g(t-\tau)$, respectively. The two pulses are then crossed in any instantaneously responding nonlinear-optical medium, generating a signal of the form $E_{sig}(t) = E(t)g(t-\tau)$. This nonlinear mechanism can result from a variety of processes, being the most widely used polarisation (Kerr) rotation (polarisation-gate, PG-FROG), three-wave mixing (self-diffraction, SD-FROG) and second-harmonic generation (SHG-FROG)²⁵. In any case, the spectrum of the generated signal is then measured as a function of the delay between the two input pulses. In the case of SHG-FROG, the corresponding mathematical spectrogram has the form²⁶:

$$I_{SHG-FROG}(\omega, \tau) = \left| \int_{-\infty}^{\infty} dt E(t) E(t-\tau) \exp(-i\omega t) \right|^2 \quad (3.11)$$

Because the optical signal $E_{sig}(t)$, has a mathematical form that depends on the particular nonlinear response used to gate the light pulse, the exact shape of the pulse spectrogram also depends on the choice of gating technique from which it was generated. Interestingly, the different types of FROG show nontrivial differences in their traces and in each case, qualitative information can be extracted from visual observation of the trace.

To completely characterise the ultrashort pulse, the resulting spectrogram has to be processed using iterative two dimensional Fourier transform algorithms that retrieve the pulse information^{27,28}. There are two fundamental algorithms and these are known as the “Basic” and “Generalised Projections” algorithms. Although these algorithms have some differences in the way they use the retrieval constrictions²⁷, they work under variations of the same general principle. An initial guess, $E(t)$, is made as to the expected shape and form of the pulse to be measured and from this

the signal electric field, $E_{sig}(t, \tau)$, is calculated. A Fourier transform of $E_{sig}(t, \tau)$, converts the signal electric field to $E_{sig}(\omega, \tau)$ in terms of frequency. The intensity of $E_{sig}(\omega, \tau)$ is then replaced with the intensity of the measured FROG trace $E'_{sig}(\omega, \tau)$ through:

$$E'_{sig}(\omega, \tau) = \frac{E_{sig}(\omega, \tau)}{|E_{sig}(\omega, \tau)|} [I_{FROG}(\omega, \tau)]^{1/2} \quad (3.12)$$

The inverse Fourier transform then converts the signal electric field to $E'_{sig}(t, \tau)$. In order to complete the cycle, a new version of $E(t)$ is generated by integrating the signal field, $E'_{sig}(t, \tau)$, with respect to τ . This results in an improved guess pulse, $E(t)$, and the algorithm continues until it has converged sufficiently and the pulse can be identified. After each iteration of the algorithm, the FROG trace of the guess pulse is calculated and compared with the actually measured FROG trace. The convergence of the algorithm is monitored by calculating the root-mean-square (rms) error G , of the difference between the experimentally generated FROG trace I_{FROG} and the squared magnitude of the signal field generated by the current guess for $E(t)$. This can be described mathematically by:

$$G = \sqrt{\frac{1}{N^2} \sum_{\omega, \tau=1}^N \left(I_{FROG}(\omega, \tau) - |E_{sig}(\omega, \tau)|^2 \right)^2} \quad (3.13)$$

where N is the number of frequency values use to describe the spectrum at each of the N delay times. The increment in delay values, $\delta\tau$ must be related to the increment in frequencies, by

$$\delta\nu = \frac{1}{N\delta\tau} \quad (3.14)$$

where a square array (*i.e.* $N \times N$) is needed because of fast Fourier transform requirements.

3.3.3. Implementation of a real-time SHG-FROG scheme

In our work, we required a convenient means of characterising femtosecond oscillators that would allow easy monitoring of pulse duration and chirp of several sources such as OPO's and frequency-doubled OPO's. An implementation of a FROG system suitable for the relatively low power signal pulses produced by synchronously pumped optical parametric oscillators (and SHG from the signal beam) had to be considered. PG-FROG and SD-FROG rely on third-order nonlinear effects, $\chi^{(3)}$, and consequently require high intensities to produce signal electric field. For this reason, FROG implementations based on SHG, were used in this work.

Although SHG-FROG is useful to our purposes, it has one main drawback: it contains a time reversal ambiguity²⁷. From Equation (3.11), it is possible to see that the signal field is invariant (except for a trivial temporal offset) with respect to a change of sign of the delay time τ , so that the SHG-FROG trace is always symmetric about τ : $I_{FROG}(\omega, \tau) = I_{FROG}(\omega, -\tau)$. This leads to an ambiguity in the retrieved electric field with respect to time such that the field $E(t)$ yields the same FROG trace as $E^*(-t)$. Practically speaking, this ambiguity is not so restrictive, and in most cases, it is possible to use some *a priori* knowledge of the pulse that can be used to remove it. For example, in a later chapter (see Chapter 5) we will take advantage of the fact that pulses will acquire positive linear chirp after propagation through normal (positive) dispersion optics.

The first experimental realization of SHG-FROG²⁹ (called spectrally resolved autocorrelation) consisted on recording the spectra of individual autocorrelations for each value of delay, constructing a spectrogram. Modern FROG systems operate by progressively recording spectra for particular delay values and building up the

FROG trace from there⁷⁻¹¹. Our FROG system is a variation of the common approach and provides a FROG trace in real-time that is constantly updated³¹. This dramatically reduces the acquisition time and allows the spectral and temporal pulse characteristics to be constantly monitored. The optical setup of our FROG system is illustrated in Figure 7.

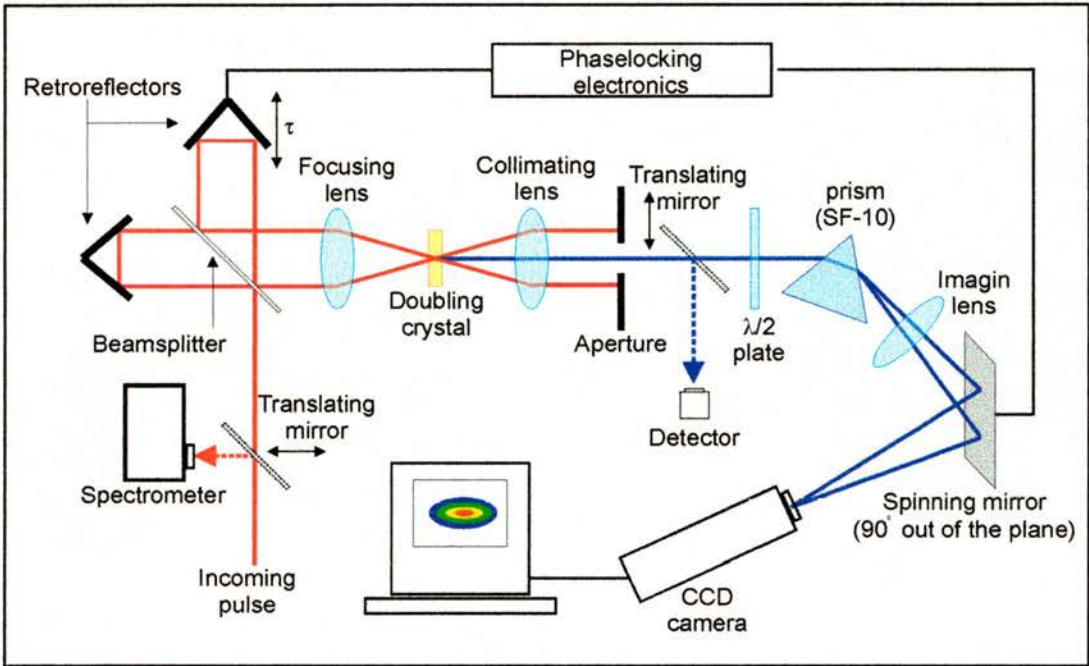


Figure 7. Realtime SHG-FROG schematic.

An input pulse is split into two replicas using the usual Michelson interferometer comprising two retroreflectors. One of the retroreflectors is mounted on a loudspeaker to provide the required delay, τ . The two beams, the probe $E(t)$ and the delayed gate $E(t-\tau)$, are then recombined into the nonlinear crystal to generate the nonlinear signal, $E_{sig}(t)$, by using type I ($e+e \rightarrow o$) noncollinear, phase matching. This configuration provides a background-free autocorrelation. Although there is some scattered fundamental light, propagating along with the SH light, the dispersion of the prism ensured that the fundamental light was directed away from

the CCD. Also, an aperture is placed to spatially filter the output from the crystal and to remove the SHG light that was due solely to either one of the pump beams. The SH signal is then collimated and directed towards the near-Brewster angled prism (SF-10) to be dispersed (in the frequency domain). To minimise reflection losses on the input facet of the prism, a $\lambda/2$ plate can be incorporated to rotate by 90^0 the polarisation of the frequency doubled beam. The frequency dispersed autocorrelation signal was then swept across the surface of a Charge Coupled Device (CCD) camera (placed at 90^0 out of the plane) by a spinning mirror, providing the dispersion in the time domain. In this way, the prism disperses the SHG signal beam in the frequency axis while the spinning mirror disperses the signal in the delay axis. These two actions combined, formed the FROG trace.

Our FROG system was designed to characterise the pulses that were used to pump our OPO's ($\lambda = 800$ nm), the OPO pulses ($\lambda = 1250$ nm) and the OPO frequency-doubled pulses ($\lambda = 625$ nm). To do this, three beam splitters were incorporated on a translation stage in the Michelson interferometer. Also, three different nonlinear crystals (also placed on translation stage) were used: BBO, KDP and KDP. The three crystals were cut for frequency-doubling each of the wavelengths at normal incidence and care was taken to select crystals with sufficient phasematching.

To ensure that the spectrogram that is being recorded by the CCD camera is complete and continuous, the spinning mirror is phase locked to the waveform that drives the autocorrelator speaker so that the frequency scan and the delay scan were always synchronous. This was achieved by using a small motor to spin the mirror freely. An error signal was then derived, by comparing the frequency of spin with the

frequency of the loudspeaker, and this signal was fed back into a loop that adjusted the loudspeaker frequency and phase to minimise the error value.

Before retrieving the pulse, the FROG trace had to be calibrated in time and frequency. To this end, the SHG signal (after being collimated and spatially filtered) is directed towards a silicon detector using a translating a mirror, at 45° , that was incorporated into the system. Two measurements have to be made. Firstly, a typical intensity autocorrelation measurement has to be performed. This measurement will calibrate the delay axis of the FROG trace by comparing the autocorrelation with its delay marginal. Secondly, the spectrum of the SHG beam has to be recorded. To this end, the autocorrelator is turned off and the SHG signal spectrum measured when the delay between the two arms is adjusted to zero. This measurement calibrates the frequency axis of the FROG trace when compared with a vertical slice of the FROG trace taken at zero delay.

The FROG trace was then digitised and displayed on a computer screen. The frame-grabber produced data arrays of 512 by 512 pixels that were processed to reduce background noise and calibrated in delay and wavelength. Finally, the retrieval algorithm was applied to the data set to obtain the pulse information. To this point, it is important to say that not all the pulses could be retrieved using a single algorithm. We found that the system worked more efficiently when a combination of two different types of algorithms were used. In this case, if the value of G had not been reduced after a certain number of iterations, the algorithm would swap to a different one, until no more reduction of the rms error can be achieved.

Example of a FROG trace and the related retrieved profiles for pulses from a Ti:sapphire laser using our FROG system can be seen in Figure 8. In this retrieval, a

Gaussian pulse was chosen as initial guess. An error of $G = 0.00295$ was achieved after 165 iterations by using two different algorithms.

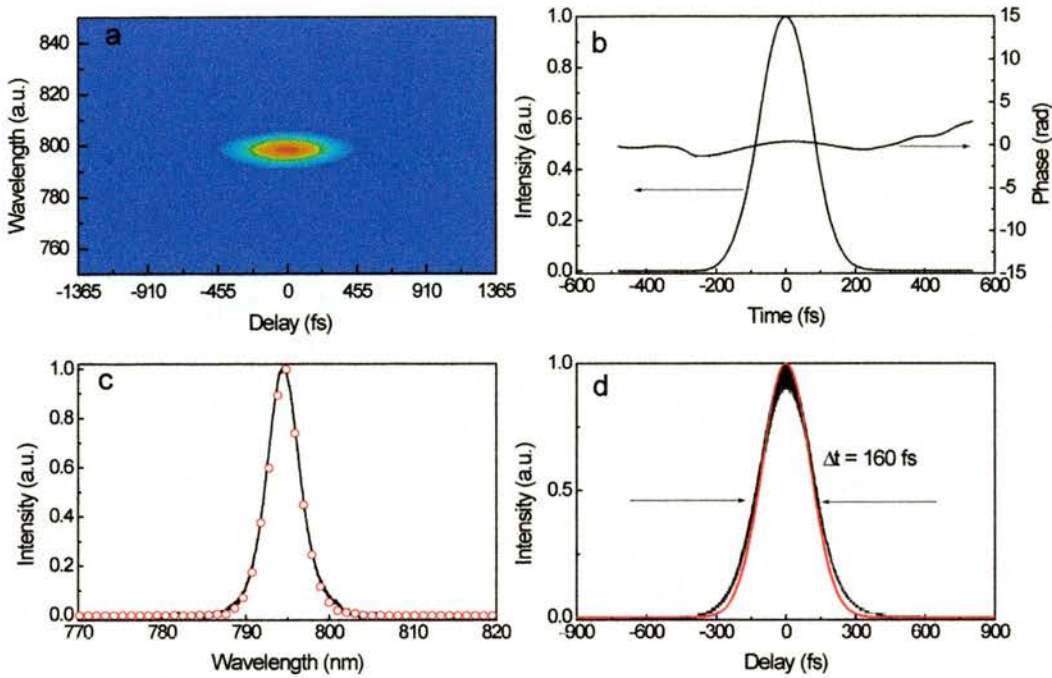


Figure 8. (a) FROG trace and (b) retrieved temporal intensity profile and phase of pulses of 160 fs. (c) Retrieved (circles) and measured (solid line) spectra, and (d) calculated (red) and measured (black) intensity autocorrelation.

Pulses of 160 fs (FWHM) were retrieved from the FROG system as shown in Fig. 8b. Figure 8c and 8d show the calculated spectrum and intensity autocorrelation compared with the corresponding experimental measurements. The good agreement confirms the accuracy of the FROG our technique.

3.3.4 The crosscorrelation-FROG technique

Implementation of a SHG-FROG method to measured mid-infrared pulses is inconvenient because the sensitivity of available silicon CCD devices is poor at the

second-harmonic frequency with wavelengths longer than $2.1 \mu\text{m}$. An alternative way to characterise pulses in the mid-infrared (mid-IR) is by an analogous technique called cross-FROG (XFROG).³¹ In this technique, the spectrogram is formed by sum-frequency mixing a mid-IR (probe) pulse with a time-delayed near-infrared (pump) pulse. This powerful technique has the advantage that it allows simultaneous retrieval of both, pump and probe pulses.

Preliminary experiments characterising the idler pulses (centred at $2.35 \mu\text{m}$) from a femtosecond OPO, using the XFROG technique, were carried out. The idler pulses were collinearly crosscorrelated with the time-delayed pump pulses (centred at 835 nm) from a self-modelocked Ti:sapphire laser. The two beams were focused into a 2 mm thick KTA sum-frequency-mixing crystal. The signal from the crystal was then spectrally resolved using a conventional monochromator (1200 lines/mm) and recorded using a 512 element linear NMOS-CCD array. Figure 9 shows the XFROG trace measured with this system and the retrieved XFROG trace and intensity profiles, after processing the data through an appropriate algorithm. The good agreement found between the measured and reconstructed intensity autocorrelation of the pump pulses (Fig. 9e) and the measured and retrieved idler spectrum (Fig. 9f) confirms the accuracy of this technique.

Due to the fact that the XFROG is based on sum-frequency mixing, it is specially suited for characterising pulses of long wavelengths. In particular, we will apply this technique to completely characterise the $5 \mu\text{m}$ (or longer) idler pulses from a PPLN-based optical parametric oscillator.³²

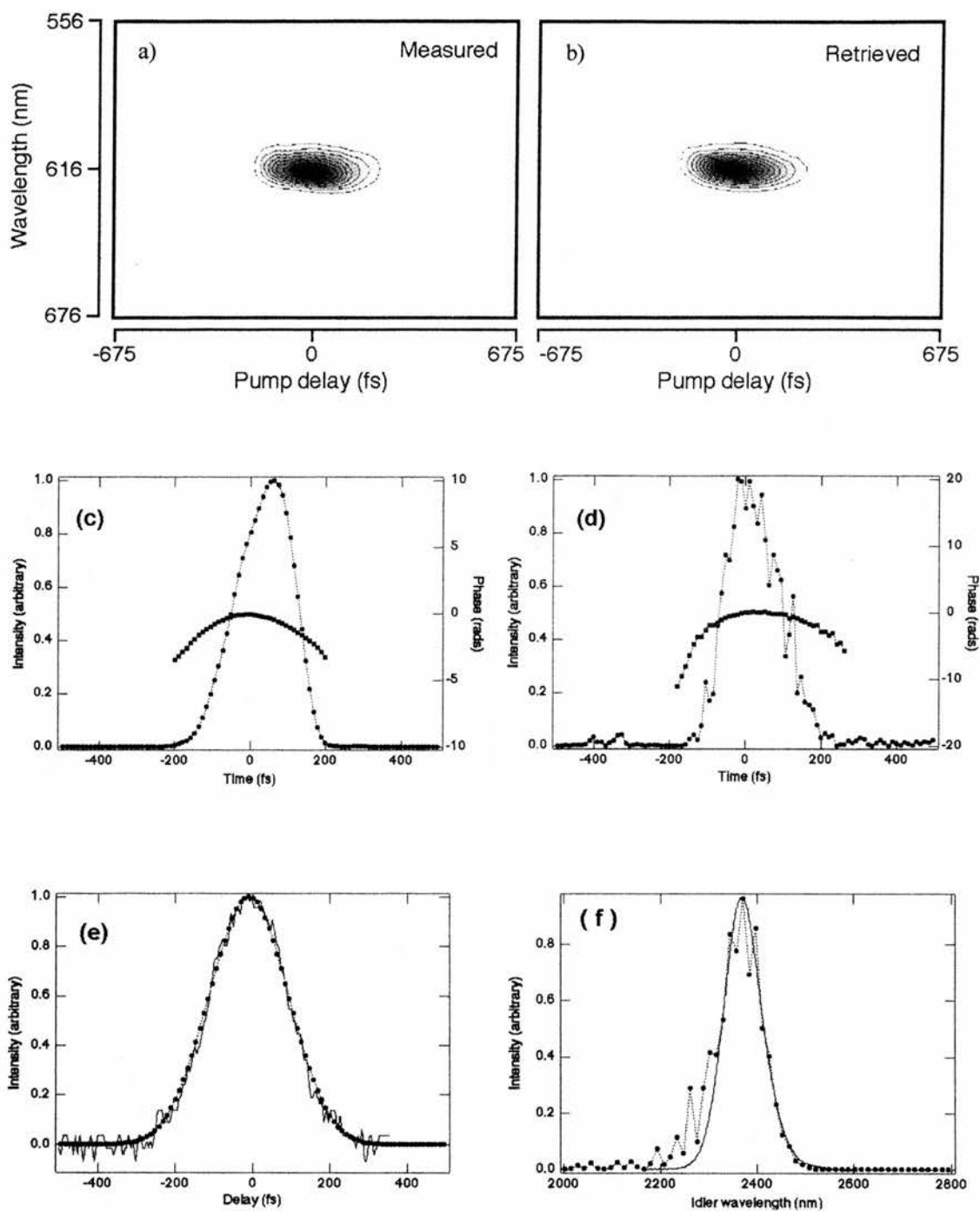


Figure 9. Measured and retrieved (b) XFROG traces; retrieved temporal intensity of the pump (c) and idler (d) pulses. Measured (solid) and calculated (symbol) intensity autocorrelation of the pump pulses (e); measured (solid) and calculated (symbols) idler spectrum.

3.4 Conclusions

In this chapter, several of the techniques and devices to characterise ultrashort pulses have been summarised and studied. We started by introducing the relevant concepts concerning to SHG-autocorrelation. This was extended to a different $\chi^{(2)}$ medium, such as two-photon absorption in semiconductors. Here, we have presented the one- and two-photon absorption response of a GaN-based laser diode. Its ability to measure visible femtosecond pulses was demonstrated by presenting interferometric and intensity autocorrelations across the wavelength range 415 - 630. We also showed that typical measurements required powers of no more than a few milliwatts.

The inability of the $\chi^{(2)}$ -based autocorrelators to accurately measure the complete electric field of femtosecond pulses was highlighted as a main limitation of these devices. Time- and frequency-domain techniques were then introduced as powerful tools that avoid this limitation. Relevant concepts of the FROG technique to measure the intensity profile and phase of ultrashort pulses were then presented. Here, details for the construction of a SHG-FROG device were given and its performance illustrated by measuring the pulses from a modelocked Ti:sapphire laser. Finally, we implemented the XFROG technique to simultaneously retrieve the complete electric field of both pump and probe pulses in the near- and mid-infrared. Because this technique is based on sum-frequency mixing, XFROG offers the advantage of retrieving pulses in the mid-IR. In the future, we will apply this technique to characterise the 5 μm idler pulses from an OPO.

3.5 References

1. H. P. Weber, "Method for pulsewidth measurement of ultrashort light pulses generated by phase-locked lasers using nonlinear optics," *J. Appl. Phys.*, **38**, 2231 – 2234 (1967).
2. See section 3.2 and references therein.
3. P. Loza-Alvarez, W. Sibbett, D. T. Reid, "Femtosecond autocorrelation measurements of CW-modelocked pulses from 415 – 630 nm using a gallium nitride laser diode" *Electron. Lett.*, **36** 631 – 633 (2000).
4. G. J. Valentine, J-M. Hopkins, P. Loza-Alvarez, G. T. Kennedy, W. Sibbett, "Ultralow-pump-threshold, femtosecond $\text{Cr}^{3+}:\text{LiSrAlF}_6$ laser pumped by a single narrow-stripe AlGaInP laser diode," *Opt. Lett.*, **22**, 1639 – 1641 (1997).
5. J.-C. Diels, J. J. fontaine, I. C. McMichael, F. Simoni, "Control and measurements of ultrashort pulse shapes (in amplitude and phase) with femtosecond accuracy," *Appl. Opt.*, **24**, 1270 – 1282 (1985).
6. A. Yariv, *Quantum Electronics*, 3rd ed. (Wiley, New York, 1989), p64.
7. D. T. Reid, M. J. Padgett, C. McGowan, W. Sleat, W. Sibbett, "Light emitting diodes as measurement devices for femtosecond laser pulses," *Opt. Lett.*, **22**, 233 – 235 (1997).
8. J. K. Ranka, A. L. Gaeta, A. Baltuska, M. S. Pshenichnikov, D. A. Wiersma, "Autocorrelation measurement of 6-fs pulses based on the two-photon-induced photocurrent in a GaAsP photodiode," *Opt. Lett.*, **22**, 1344 – 1246 (1997).
9. W. Rudolph, M. SheikBahae, A. Bernstein, L. F. Lester, "Femtosecond autocorrelation measurements based on two-photon photoconductivity in ZnSe," *Opt. Lett.*, **22**, 313 – 315 (1997).
10. L. P. Barry, P. G. Bollond, J. M. Dudley, J. D. Harvey, L. Leonhardt, "Autocorrelation of ultrashort pulses at 1.5 μm based on nonlinear response of silicon photodiodes," *Electron. Lett.*, **32**, 1922 – 1923 (1996).
11. P. Loza-Alvarez, D. T. Reid, M. Ebrahimzadeh, W. Sibbett, H. Karlsson, P. Henriksson, G. Arvidsson and F. Laurell, "Periodically-poled RbTiOAsO₄ femtosecond optical parametric oscillator tunable from 1.38 to 1.58 μm ," *Appl. Phys. B*, **68**, 177 – 180 (1999).
12. D. T. Reid, W. Sibbett, J. M. Dudley, L. P. Barry, B. Thomsen, J. D. Harvey, "Commercial semiconductor devices for two photon absorption autocorrelation of ultrashort light pulses," *Appl. Opt.*, **37**, 8142 – 8144 (1998).
13. D. T. Reid, C. McGowan, M. Ebrahimzadeh, W. Sibbett, "Characterization and Modeling of a noncollinearly phase-matched femtosecond optical parametric oscillators," *IEEE J. Quantum. Electron.*, **33**, 1 – 9 (1997).
14. K. C. Burr, C. L. Tang, M. A. Arbore, M. M. Fejer, "Broadly tunable mid-infrared femtosecond optical parametric oscillator using all-solid-state-pumped periodically poled lithium niobate," *Opt. Lett.*, **22**, 1458 – 1460 (1997).
15. A. M. Streltsov, A. L. Gaeta, P. Kung, D. Walker, M. Razeghi, "Application of GaN photodiode for autocorrelation measurements of visible femtosecond pulses," in *Conference on Lasers and Electro-Optics*, OSA Technical Digest (Optical Society of America, Washington, DC, 1999) pp 536 Paper CFG6.
16. S. Nakamura, *MRS Internet Journal of Nitride Semiconductor Research* **2**, 5.

17. J. K. Ranka, R. S. Wineler, A. J. Stentz, "Efficient visible continuum generation in air-silica microstructure optical fibers with anomalous dispersion at 800 nm," in *Conference on Lasers and Electro-Optics*, OSA Technical Digest (Optical Society of America, Washington, DC, 1999) Postdeadline paper CPD8-1.
18. D. Burns, S. T. Lee, M. D. Dawson, A. I. Ferguson, "Femtosecond autocorrelator based on AlGaInP diode laser" in *Conference on Lasers and Electro-Optics/Europe*, OSA Technical Digest (Optical Society of America, Washington, DC, 1998) pp 103 Paper CTuI66, Glasgow 1998.
19. Z. E. Penman, T. Schittkowski, W. Sleat, D. T. Reid, W. Sibbett, "Experimental comparison of conventional pulse characterisation techniques and second-harmonic-generation frequency-resolved optical gating," *Opt. Commun.*, **155**, 297 – 300 (1998).
20. K. W. DeLong, R. Trebino, D. N. Fittinghoff, C. L. Ladera, "Review of time-frequency domain concepts with application to ultrashort laser pulses," *SPIE/OE LASER* (1995).
21. J. Paye, A. Mingus, "Space-time Wigner functions and their applications to the analysis of a pulse shaper," *J. Opt. Soc. Am. B.*, **12**, 1480 – 1490 (1995).
22. E. B. Treacy, "Measurement and interpretation of dynamic spectrograms of picosecond light pulses," *J. Appl. Phys.*, **42**, 3848 – 3858 (1971).
23. J. L. A. Chilla O. E. Martinez, "Direct determination of the amplitude and the phase of femtosecond light pulses," *Opt. Lett.*, **16**, 39 – 41 (1991).
24. D. J. Kane, R. Trebino, "Single shot measurement of the intensity and phase of an arbitrary ultrashort pulse by using frequency-resolved optical gating," *Opt. Lett.*, **18**, 823 – 825 (1993).
25. D. J. Kane, R. Trebino, "Characterization of arbitrary femtosecond pulses using frequency-resolved optical gating," *IEEE, J. Quantum. Electron.*, **29**, 571 – 579 (1993).
26. K. W. DeLong, R. Trebino, D. J. Kane, "Comparison of ultrashort-pulse frequency-resolved-optical-gating traces for three common beam geometries," *J. Opt. Soc. Am. B.*, **11**, 1595 – 1608 (1994).
27. K. W. DeLong, R. Trebino, J. Hunter, W. E. White, "Frequency-resolved optical gating with the use of 2nd-harmonic generation," *J. Opt. Soc. Am. B.*, **11**, 2206 – 2215 (1994).
28. R. Trebino, D. J. Kane, "Using phase retrieval to measure the intensity and phase of ultrashort pulses: Frequency-resolved optical gating," *J. Opt. Soc. Am. A.*, **10**, 1101 – 1111 (1993).
29. K. W. DeLong, R. Trebino, "Improved ultrashort pulse-retrieval algorithm for frequency-resolved optical gating," *J. Opt. Soc. Am. A.*, **11**, 2429 – 2437 (1994).
30. J. Paye, M. Ramaswamy, J. G. Fujimoto, E. P. Ippen, "Measurement of the amplitude and phase of ultrashort light pulses from spectrally resolved autocorrelations," *Opt. Lett.*, **18**, 1946 – 1948 (1993).
31. D. T. Reid, C. McGowan, W. Sleat, M. Ebrahimzadeh, W. Sibbett, "A real-time FROG trace acquisition system for non-amplified femtosecond oscillators," *Eng. and Lab. Notes*, 2-page supplement to *Optics and Photonics News*, **8**, (May 1997).
32. D. T. Reid, P. Loza-Alvarez, C. T. A. Brown, T. Beddard, W. Sibbett, "Amplitude and phase measurement of mid-infrared femtosecond pulses using XFROG," in *Conference on Lasers and Electro-Optics*, OSA Technical Digest (Optical Society of America, Washington, DC, 2000) pp 584 paper CFE2.
33. P. Loza-Alvarez, C. T. A. Brown, D. T. Reid, W. Sibbett, M. Missey, "High-repetition-rate ultrashort-pulse optical parametric oscillator continuously tunable from 2.8 to 6.8 μm ," *Opt. Lett.*, **24**, 1523 – 1525 (1999).

CHAPTER 4

OPTICAL PARAMETRIC OSCILLATOR BASED ON PERIODICALLY-POLED CRYSTALS

In this chapter four different synchronously-pumped optical parametric oscillators, based on periodically-poled crystals of either RbTiOAsO_4 or LiNbO_3 (PPRTA and PPLN respectively), are described. These have different characteristics on their tunability ranges and pulse durations and in each case different aspects of their performance were studied.

In the following section, an OPO implementation that is based on PPRTA crystal and that is continuously tunable from 1.375 to 1.575 μm will be described.¹ Another OPO implementation (section 4.2), that is based on a modification of an earlier demonstration of femtosecond operation using a PPLN-based OPO² will then be described. This new approach, led to the construction of an all-solid-state femtosecond OPO with extended tunability.^{3,4} Using an alternative arrangement, described in section 4.3, a characterisation of an OPO, using different mirror sets, was carried out. In particular, dispersive effects arising at the extremes of the tuning range were studied. Finally, in section 4.4, I present the demonstration of the PPLN-based OPO as a source of idler wavelengths as long as 6.8 μm and with a 4 μm tunability range towards shorter wavelengths⁵.

4.1 The periodically-poled RbTiOAsO₄ OPO

Conventional sources delivering high repetition rate, high average power, femtosecond pulses that offer broad tunability in the near-infrared region are restricted mainly to either colour-centre lasers which operate under cryogenic conditions or OPOs. In most instances the OPO-source options are preferred, and as I have mentioned already, (see Chapter 1), these OPOs can be based on a variety of nonlinear birefringent and QPM materials. Broad spectral coverage can be readily achieved by tuning the pump wavelength, the OPO cavity-length and the grating period of the crystal and to cope with wide tunability it is required in practice to use several sets of cavity mirrors.

In the particular case of Ti:sapphire-pumped PPRTA-based OPO systems, much of the effort has been concentrated only on systems using ps and fs and generating radiation in the mid-IR and below 1.3 μm . Here I describe a PPRTA-based femtosecond OPO that operates at room temperature, delivers output powers up to 110mW and is cavity-length-tunable from 1.375 to 1.575 μm for the signal and from 1.845 – 2.225 μm for the idler, using only a single cavity mirror set.

The OPO was based on a PPRTA crystal⁶ of length 4.5 mm, width 1 mm and height 5 mm having a grating period of 30 μm (the faces of the crystal had antireflection coatings for a wavelength of 1.1 μm , which introduced some additional loss at the 1.5 μm operating wavelength as discussed later). Figure 1 shows the experimental setup.

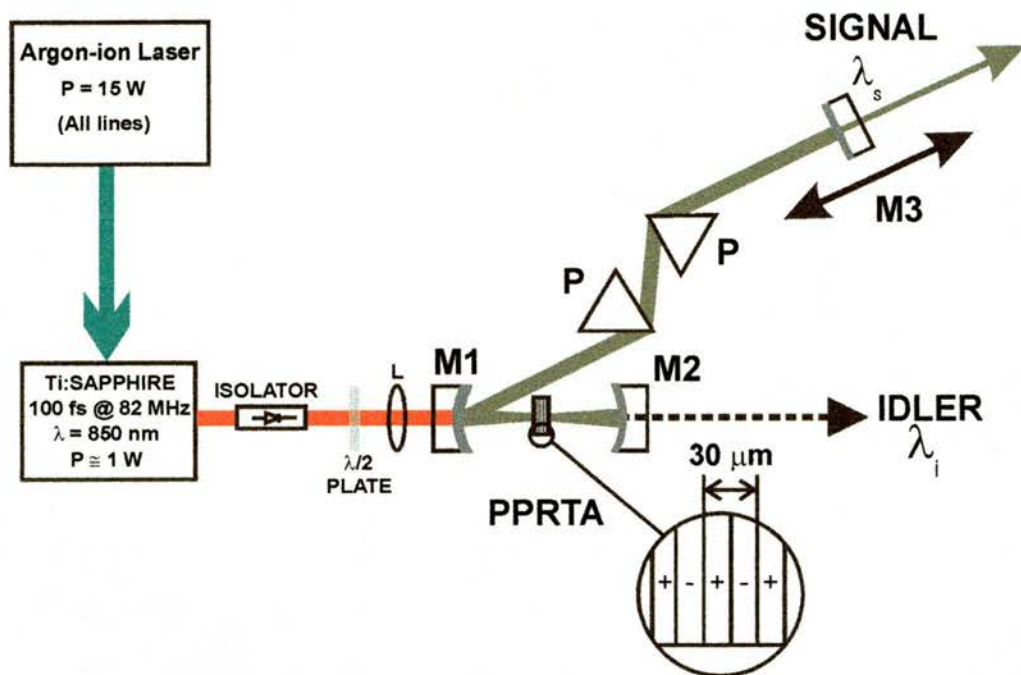


Figure 1. Cavity configuration of the PPRTA-based OPO. M1, M2, highly reflecting curved mirrors; M3, end mirror; Ps, prisms; L, lens; $\lambda/2$ plate, half-wave plate.

The OPO was synchronously pumped by a modelocked Ti:sapphire laser at a repetition rate of 84 MHz, with output pulses of 100 fs duration and a centre wavelength of 850 nm and an average output power of ~ 1 W. A 90 mm focal-length lens was used to focus the pump beam (2 mm diameter) through the cavity mirror into the PPRTA crystal. The polarisations of the pump, signal and idler beams were all horizontal in the cavity and parallel to the poling direction which lay along the crystallographic c axis (optical Z axis). The OPO cavity consisted of two highly reflecting (HR) curved mirrors M1 and M2 ($r = -100$ mm) and one flat output coupler or HR mirror, M3. With this parameters, ABCD matrix calculations have shown that the intracavity transverse mode inside the PPRTA crystal has a radius of ~ 22 μm . Initially all the mirrors used were highly reflecting at the central wavelength of 1.5 μm , having a bandwidth of 125 nm (transmittance less than 1%). The oscillator

was configured in a dispersion-compensated cavity by means of two SF14 prisms (P) with an apex separation of 30 cm. Under these conditions it was possible to continuously tune the signal from 1.375 to 1.575 μm by varying the cavity length over approximately 65 μm . The corresponding idler tuning was from 1.845 to 2.225 μm .

The phase matching behaviour of the PPRTA crystal was calculated by using the modified Sellmeier equations of Fenimore *et. al.*,⁷ where the wavevector mismatch (Eq. 2.1) is given by:

$$\Delta k = k_p - k_s - k_i - k_g \quad (4.1)$$

where the subscripts p, s and i refer to pump, signal and idler, respectively, and $k_g = 2\pi/\Lambda$ where Λ is the grating period. The variation of the normalised gain coefficient $\text{sinc}^2(\Delta kL/2)$ across the OPO tuning range, together with the experimental cavity length tuning wavelengths are plotted in Figure 2 and it can be seen that the distribution of recorded data agrees well with the predicted regions of parametric gain. Due to the high gain and broad phasematching bandwidth of the crystal and the antireflection coating used on its faces, oscillation at a wavelength of 1.1 μm (also shown in Figure 2) was also observed even though this wavelength lay well outside the high-reflectivity bandwidth of the cavity mirrors.

The output power performance of the OPO was studied by using several output couplers. By using a high-reflector the pump threshold was measured to be only 90 mW for oscillation at a signal wavelength of 1.5 μm . By using a 5% output coupler and pumping with 920 mW, the maximum signal output power was 110 mW at 1.46 μm and the slope efficiency was 15.2%. The minimum power that could be

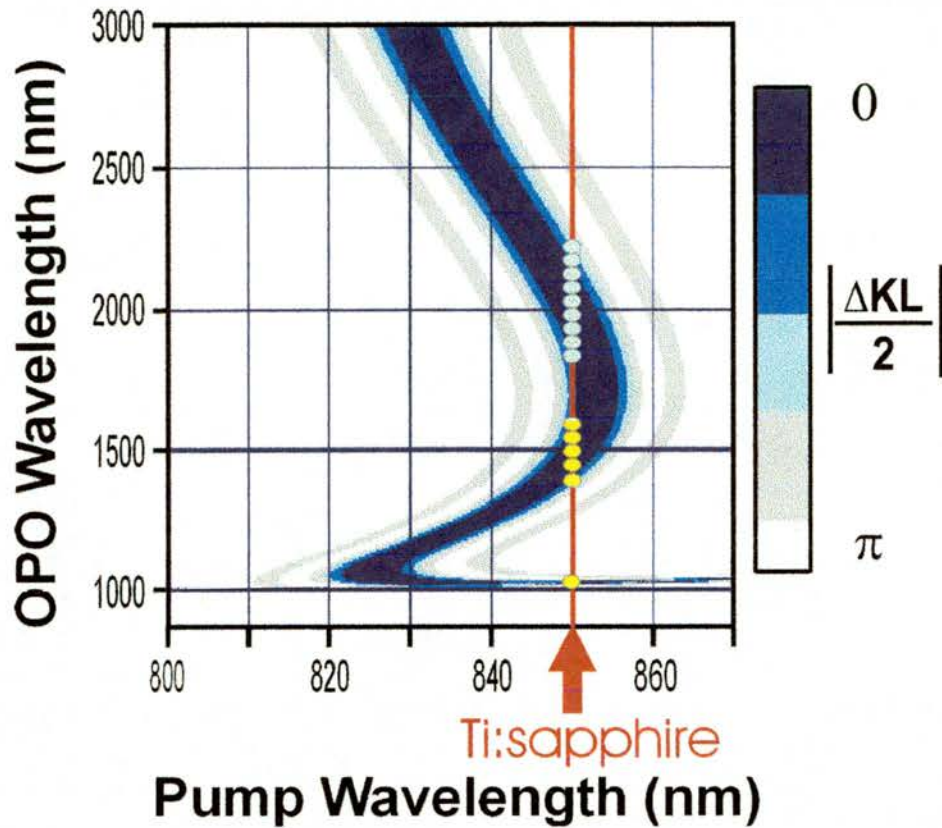


Figure 2. Pump wavelength tuning and phase matching diagram together with experimentally recorded wavelengths. Signal wavelengths are represented with filled circles and idler wavelengths with open circles.

measured reliably was of 10 mW when pumping with an average power of 280 mW. A linear fit to the obtained data indicates that the pump threshold for this wavelength was ~195 mW. For 1.55 μm , a maximum average output power of 30 mW was reached, showing a slope efficiency of 10.2%. As before, an output power of 5 mW was obtained for pump powers of 360 mW and a calculated pump threshold of 300 mW. Figure 3 (a) shows the variation of output powers of the signal wavelengths for the complete spectral range generated by varying the cavity length of the OPO resonator. It can be seen that the oscillator provided high average output powers at wavelengths that can be difficult to obtain due to atmospheric water absorption. For a 3% output coupler the slope efficiency was deduced to be of 8.6% at 1.475 μm and

the maximum output power was 45 mW. An improvement of the extraction efficiency would be expected by using a crystal with antireflection coating centred at 1.5 μm . The existing coating introduces a loss of 1.5 % per surface (6% roundtrip) at the central wavelength of 1.5 μm . From measurements taken to date, it can be estimated that an optimised crystal anti-reflection coating would enable average powers in excess of 200 mW to be produced at 1.5 μm .

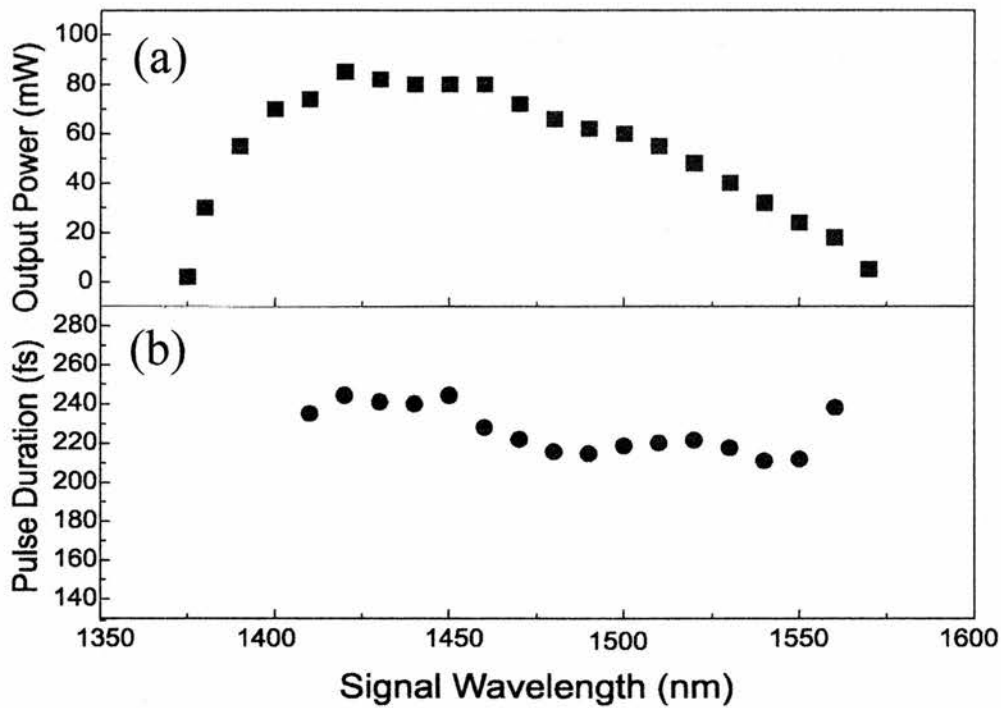


Figure 3. (a) Output power and (b) pulse durations for the PPRTA-OPO over the tuning range, 1.375 to 1.575 μm using a 5% output coupler and pumping with 850 mW of average power from the Ti:sapphire laser.

Pulse durations were also measured across the range of signal wavelengths obtained by varying the OPO cavity length. These results are depicted in 3 (b), where it can be seen that an almost constant pulse duration across the tuning range with a minimum pulse duration of 215 fs measured at a signal wavelength of 1.49 μm .

Figure 4 shows an interferometric autocorrelation and spectrum recorded at this wavelength which imply a duration-bandwidth product of $\Delta\tau\Delta\nu = 0.389$ (sech²(t) pulse intensity profile is assumed). The autocorrelation was measured using a GaAs light emitting diode⁸ and the spectrum was recorded using a scanning monochromator (resolution 0.4 nm). At this stage, the group velocity dispersion (GVD) was not adjusted for minimum pulse duration but was set at a value which enabled generation of constant duration near-transform limited pulses across the tuning range with good stability. The uncompensated GVD in this configuration, might therefore explain the large signal-pulse duration obtained, although pulse duration is also dependent on pump-signal group velocity walk-away (GVW) and pump depletion. A model (which lies outside the scope of this work) including all these factors would provide a better understanding of the signal pulse-shaping process.

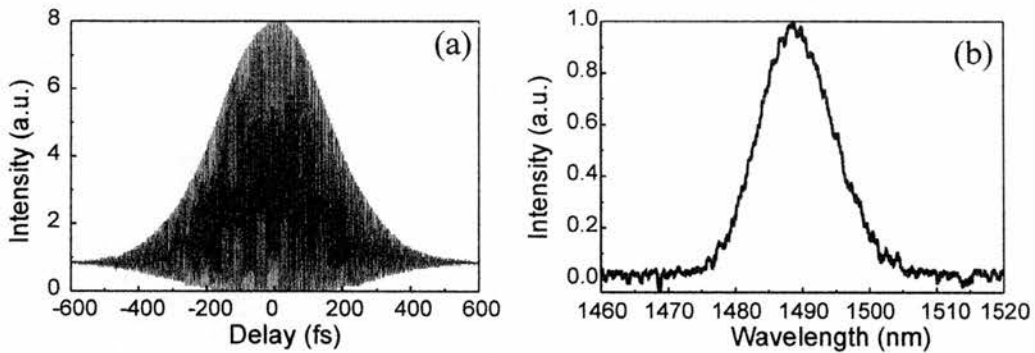


Figure 4. (a) Interferometric autocorrelation and (b) spectrum for signal pulses from the compensated-cavity OPO operating at 1.49 μm . The pulse duration is 215 fs and the spectral bandwidth is 13.4 nm giving a $\Delta\tau\Delta\nu$ product of 0.39.

By adjusting the dispersion compensation of the cavity to near zero GVD, the broad phasematching bandwidth of the crystal made simultaneous oscillation possible in two distinct spectral regions. The output spectrum (Figure 5 (a)) and its

respective interferometric autocorrelation (Figure 5 (c)) show clearly this dual-wavelength behaviour. Pulses as short as 150 fs were obtained by spectral filtering of the intracavity mode using an adjustable slit placed immediately before mirror M3. The interferometric autocorrelations of the filtered beam are shown in Figure 5 (b) and (d) which correspond to the short and long wavelength components respectively. Under the conditions of near-zero GVD, small perturbations of the system introduced a chaotic shift of the central wavelength of the pulses, thus preventing the laser from operating in a stable regime.

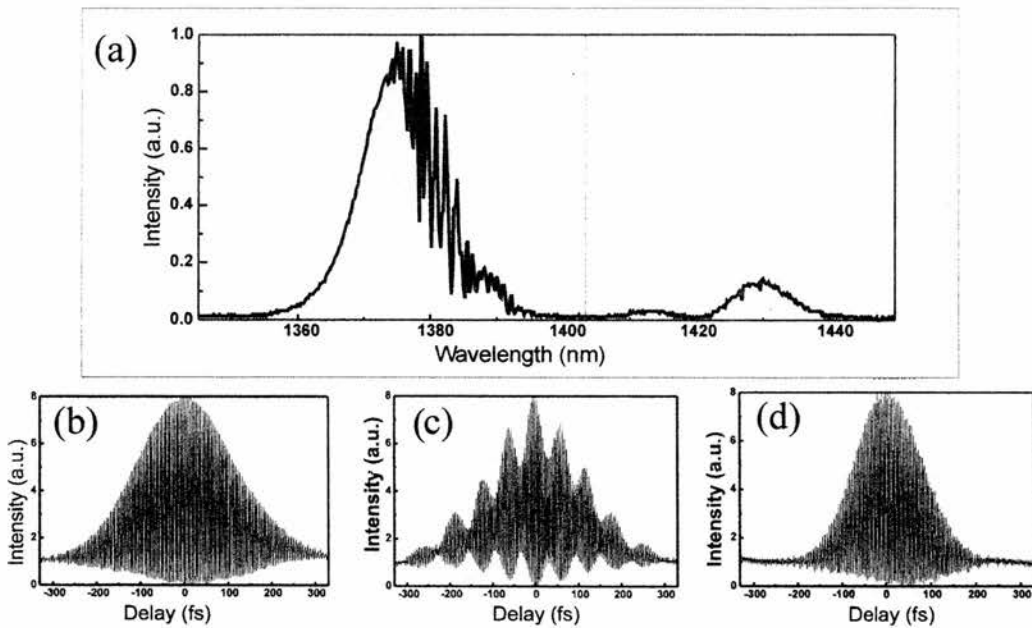


Figure 5. Spectra and interferometric autocorrelations of the signal output pulses during double pulse oscillation within the OPO cavity. Double spectrum (a) and its corresponding interferometric autocorrelation (c). Spectrally-filtered spectrum, showing an interferometric autocorrelation of a pulse of 150 fs centered at $1.375 \mu\text{m}$ (b). Spectrally-filtered spectrum showing an interferometric autocorrelation of a pulse of 150 fs centred at $1.430 \mu\text{m}$ (d).

The behaviour of the idler pulses was also studied. The average output power of the idler pulses was measured directly after the mirror M2 and the recorded data can be seen on Figure 6 (a). A maximum average output power of 65 mW was

measured after mirror M2 (in the present system, the substrate of mirror M2 does not have an optimised transmission at idler wavelengths). Figure 6 (b) shows an interferometric autocorrelation measured with a InGaAs photodiode at the central wavelength of $2.1 \mu\text{m}$ which shows that the idler pulses had durations of 133 fs. The duration of idler pulses is shorter than the signal and may be explained through the limited interaction between the pump and signal/idler pulses which results from the large value of pump-signal and pump-idler group velocity walk-away (~ 180 and 190 fs/mm respectively).

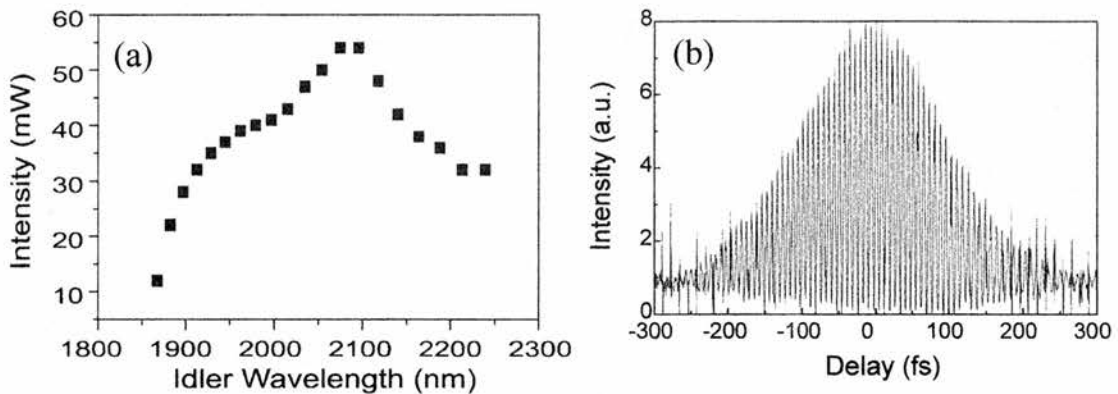


Figure 6. (a) Average output power in the idler beam for wavelengths across the available spectral range and (b) interferometric autocorrelation of idler pulses centred at $2.1 \mu\text{m}$.

4.2 All-solid-state PPLN-based optical parametric oscillator

In this section, results that show the use of an all-solid-state Ti:sapphire pump source in combination with a PPLN-based OPO are presented. This source represents a robust device of high repetition rate femtosecond pulses in the mid-infrared with tunability to $\sim 5 \mu\text{m}$.

The PPLN OPO was synchronously pumped by a Kerr-lens mode-locked Ti:sapphire laser which produced pulses of ~ 100 fs duration at a repetition rate of 82 MHz and an average output power of 800-900 mW at 830 nm. The Ti:sapphire laser was pumped by a diode-pumped, CW, frequency doubled Nd:YVO₄ laser (Spectra-Physics Millennia) which produced 5 W of output power at 532 nm. The PPLN crystal with dimensions of 1 mm long, 0.5 mm wide and 11 mm high had eight gratings having periods evenly spaced between 20.5 and 22 μm . The only grating used in the experiment was the 20.5 μm because this allowed generation of the longest possible idler wavelengths available from the OPO. The crystal was anti-reflection coated at 1.1 μm on both faces and the crystal temperature was maintained at 100 °C to avoid the effects of photorefractive damage which was apparent as a constant shifting and extensive break-up of the output beams.² It was necessary to include an optical isolator between the pump laser and the OPO to prevent feedback from the OPO disrupting the mode-locking process in the Ti:sapphire laser. Following the isolator, a half waveplate was used to obtain the horizontal polarisation state of the pump required for the $e \rightarrow e + e$ interaction, in order to access its largest, d_{33} , coefficient. The polarisation of the signal and idler waves were therefore horizontal in the cavity and were parallel to the poling direction (the experimental set up is shown in Figure 7). The pump beam was focused using a 50 mm focal length lens to optimally match the radius of the intracavity signal beam. The radius of curvature of the concave focusing mirrors M1 and M2 was 100 mm and the cavity mirrors comprised a high reflectivity mirror at 1.064 μm on a BK7 substrate (M1), one with high reflectivity at 1.1 μm on a CaF₂ substrate (M2) which was transparent to beyond 5 μm (so allowing extraction of the idler) and a high

reflector or an output coupler centred at $1.064 \mu\text{m}$ (M3). A pair of SF14 prisms, with an apex separation of 45 cm, was used to dispersion compensate the cavity. As mentioned on the previous section, ABCD matrix calculation has shown that the radius of the mode size inside the PPLN crystal is approximately $r = 19 \mu\text{m}$.

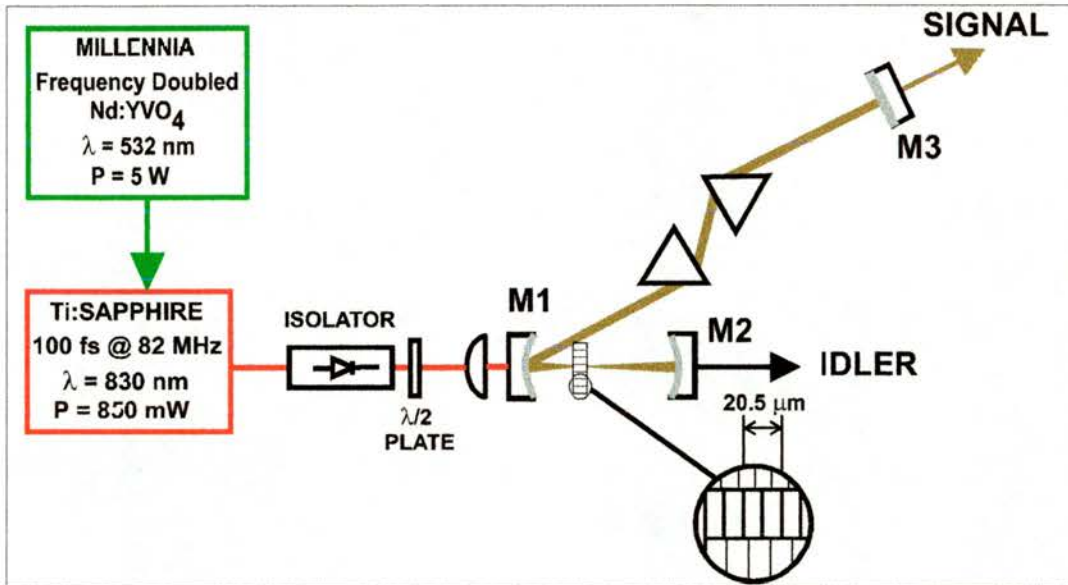


Figure 7. PPLN OPO cavity configuration. Inset illustrates the crystal poling direction.

The signal pulses generated were measured using a GaAs LED ($E_g = 980 \text{ nm}$) autocorrelator.⁸ The spectrum and the interferometric autocorrelation of the signal pulses are shown in Figure 8 (a) and (b) respectively. The pulse duration was 210 fs and the duration-bandwidth product was $\Delta\tau\Delta\nu = 0.41$. By varying the cavity length, it was possible to tune from 996 nm to $1.22 \mu\text{m}$ for the signal wavelength.

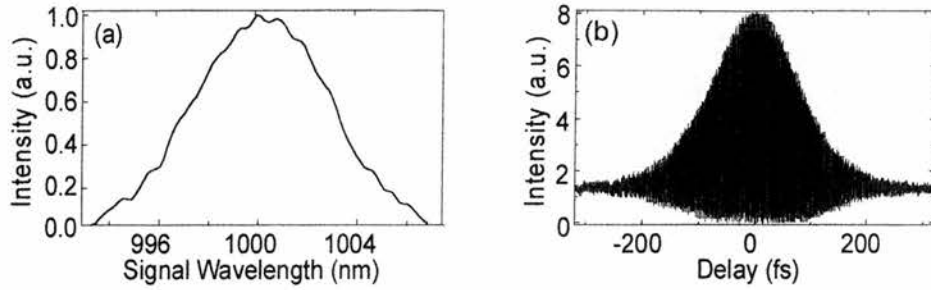


Figure 8. (a) Signal spectrum and (b) interferometric autocorrelation of the signal implying pulses of a duration of 210 fs. and a duration-bandwidth product of $\Delta\tau\Delta\nu = 0.41$.

At the idler wavelength, the pulses were autocorrelated by using an extended-sensitivity InGaAs photodetector. Autocorrelation profiles were recorded at several idler wavelengths and figure 9 shows the spectra and autocorrelation traces at a wavelength of 4.45 μm . The pulses have a duration of 200 fs and the duration-bandwidth product is $\Delta\tau\Delta\nu = 0.42$.

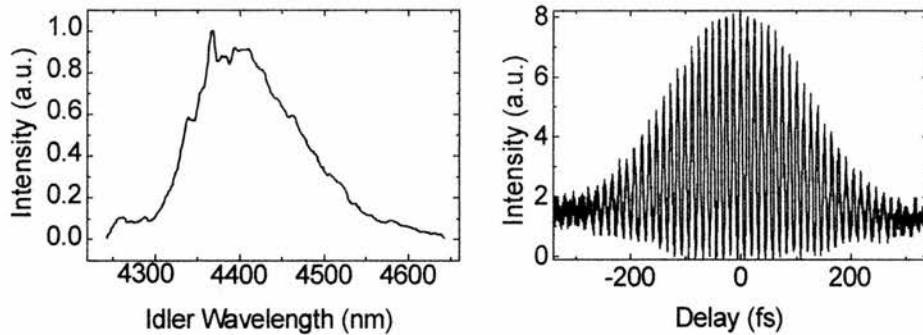


Figure 9. Typical interferometric autocorrelations and spectra of idler at 4.45 μm

Idler wavelengths ranging from 2.6 to 4.98 μm were generated from the OPO by varying the cavity length. Figure 10 shows an interferometric autocorrelation recorded at 4.88 μm , which implies a pulse duration of 190 fs. The monochromator cut-off wavelength was 4.5 μm so spectra beyond this limit could not be measured with the equipment available to me.

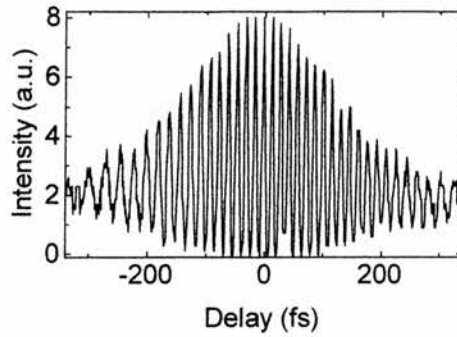


Figure 10. *Interferometric autocorrelation at 4.88 μm .*

A maximum output power of 106 mW at 2.6 μm and 25 mW at 4.88 μm was measured for the idler wavelength, when all the cavity mirrors were high-reflecting at the signal wavelengths. By using a 15 % output coupler for the signal wavelengths, a maximum average output power of 240 mW was measured at the central wavelength of 1.16 μm .

4.3 Characterisation of a PPLN-based OPO in the 1.26 to 1.58 μm range

In the previous section, an all-solid-state OPO operating at wavelengths as long as 4.98 μm was described. In this section, a characterisation of a PPLN OPO, working at the idler wavelengths between 1.8 and 2.2 μm , is presented. Furthermore, using different mirror sets, dispersion effects that arises at the extremes of the corresponding tuning range (1.06 – 1.30, 1.27 – 1.54 and 1.33 – 1.55 μm), are studied.

The PPLN-based OPO was synchronously pumped by an argon-ion pumped modelocked Ti:sapphire laser operating at a pulse repetition rate of 84 MHz, with output pulses of 100 fs duration and an average output power of ~ 1.5 W. The PPLN

crystal that was used for this work was the same as that described for the work discussed in section 4.2. The polarisation of the pump, signal and idler beams were horizontal in the cavity and parallel to the poling direction, which lay along the crystallographic c axis (optical Z axis). Figure 11 shows the experimental set up. The pump beam was focused into the crystal with a 50 mm focal length lens. The OPO was configured for collinear phasematching in an asymmetric three-mirror cavity. It consisted of two curved ($r = -100$ mm) high reflecting mirrors and a plane output coupler. Different sets of mirrors centred at 1.1, 1.4 and 1.5 μm were used in order to tune the OPO from 1.065 to 1.55 μm and from 1.65 to 3.215 μm for the signal and idler wavelengths respectively. The cavity operated with no intracavity prisms, and was not therefore dispersion compensated.

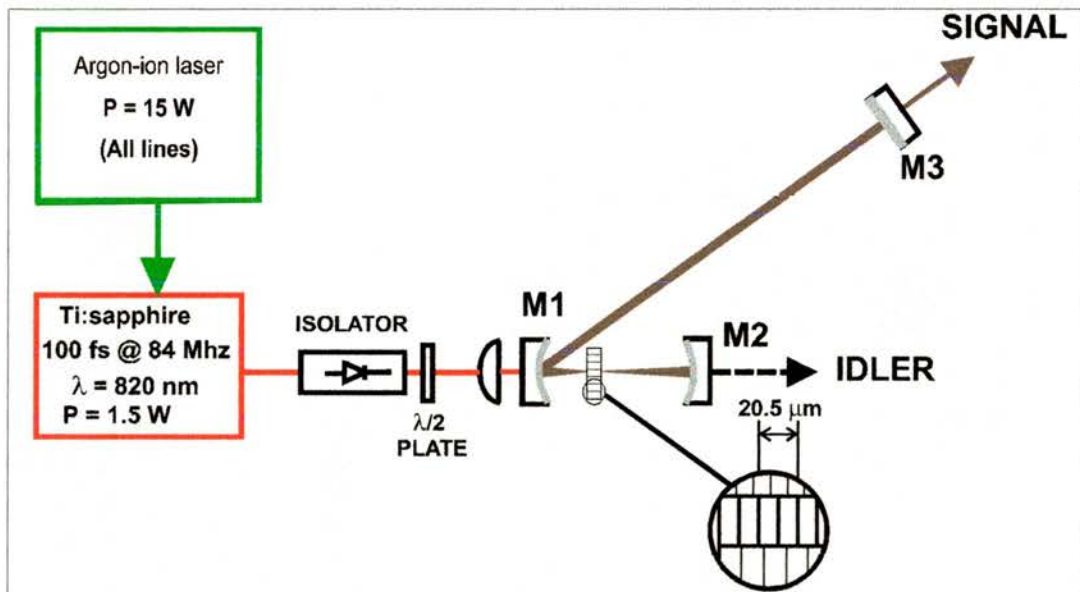


Figure 11. Experimental setup.

For the three sets of mirrors used, it was possible to produce transform-limited pulses without any dispersion compensation elements. This effect was found to apply mainly for those pulses with resonant wavelengths lying at the long-

wavelength end of the mirror bandwidth. Figure 12 shows several spectra and intensity autocorrelations taken at both edges of the mirror bandwidth.

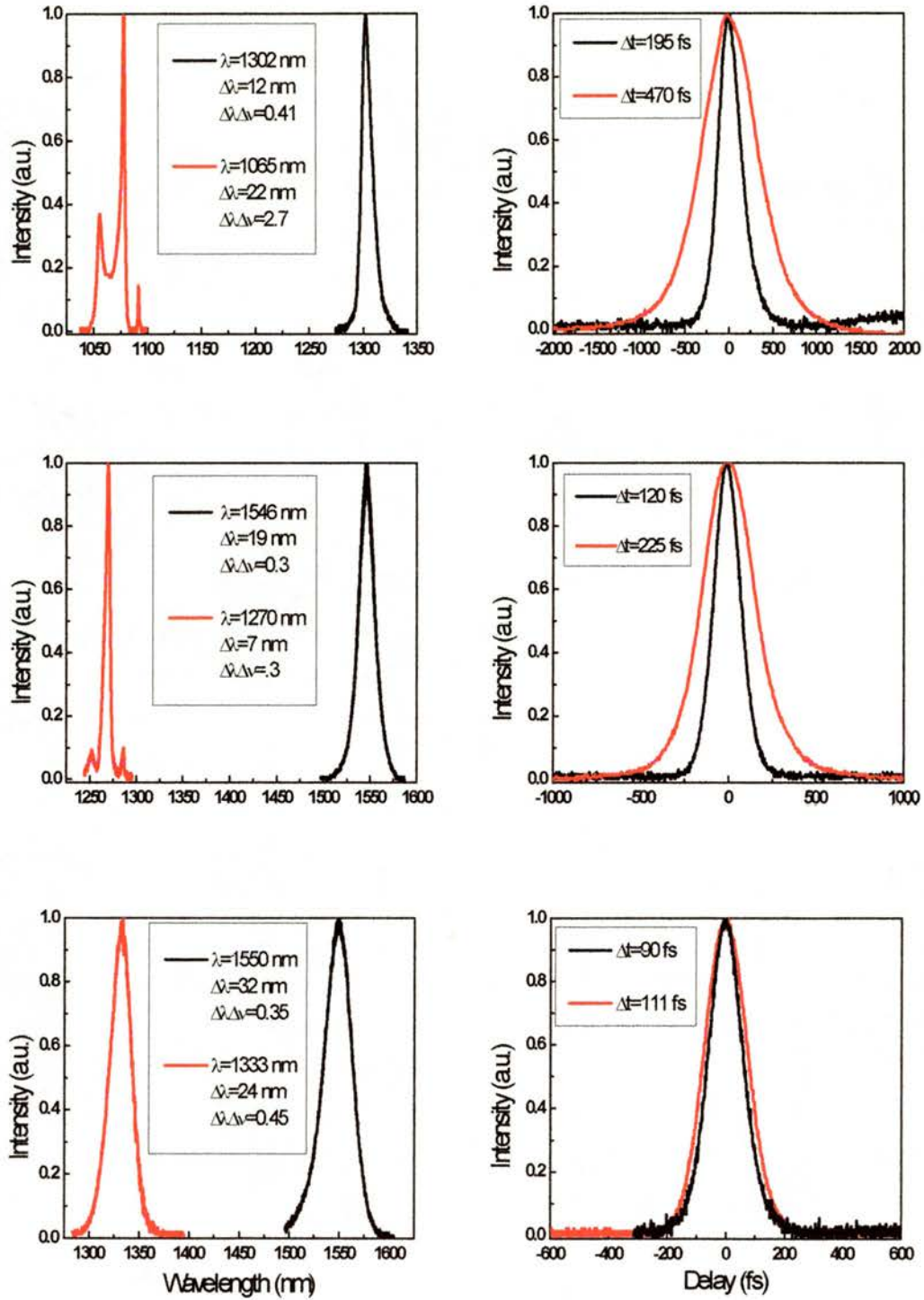


Figure 12. Signal tuning range showing transform limited pulses at the end of the mirror bandwidth reflectivity.

The results shown in figure 12 could be explained by analogy with chirped mirrors. Without any dispersion compensation the pulses are broadened by normal dispersion and self-phase modulation caused by the gain crystal. At the long edge of the reflectivity bandwidth, the longest wavelengths travel deeper into the mirror before being reflected. Consequently, these wavelengths are delayed with respect to their shorter wavelength components. These effects simulate negative group velocity dispersion, such that self-phase modulation and positive dispersion can be compensated with the result that transform-limited pulse generation can be obtained directly. Analogously, pulses tuned at the short wavelength of the tuning range and lying in the short-edge of the mirror bandwidth, penetrate further into the mirror, thereby adding positive GVD to the system. Consequently, this results in the generation of frequency-chirped pulses. A more rigorous experimental test, involving a complete GVD calibration of the used mirrors, should be carried out to confirm this explanation.

Femtosecond OPOs operating in the 1.8 to 2.2 μm range might be appropriate to study some optical properties in particular semiconductor materials.⁹ This spectral range was easily obtained with the idler wavelengths of our PPLN OPO. To produce this idler spectral range, a single set of high reflector mirrors centred at 1.4 μm was used. Cavity length and pump tunability from 820 to 840 nm was performed to cover this spectral range and only a single grating period of the PPLN crystal was required ($\Lambda = 21 \mu\text{m}$). Under these conditions, idler wavelengths from 1.79 to 2.33 μm were obtained and the corresponding signal wavelengths were in the range 1.26 to 1.58 μm . Figure 13 shows the spectra of the idler and signal wavelengths covered.

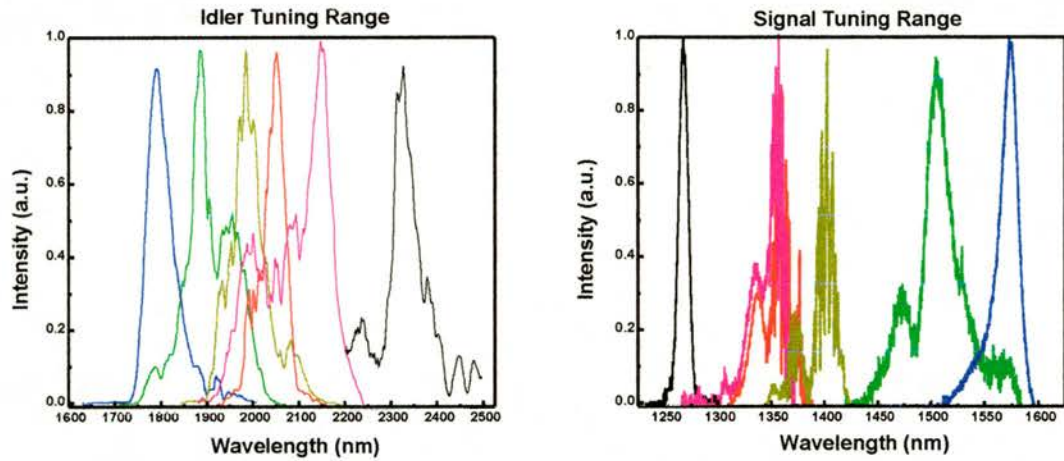


Figure 13. Idler (a) and corresponding signal (b) tuning range.

The idler beam exited the cavity through mirror M2 and then it was collimated with a 14 mm focal length lens (BK-7 substrates). Under these conditions, up to 50 mW of average output power at 1.83 μm was available. Figure 14 shows the variation of available output power for the idler spectral range studied.

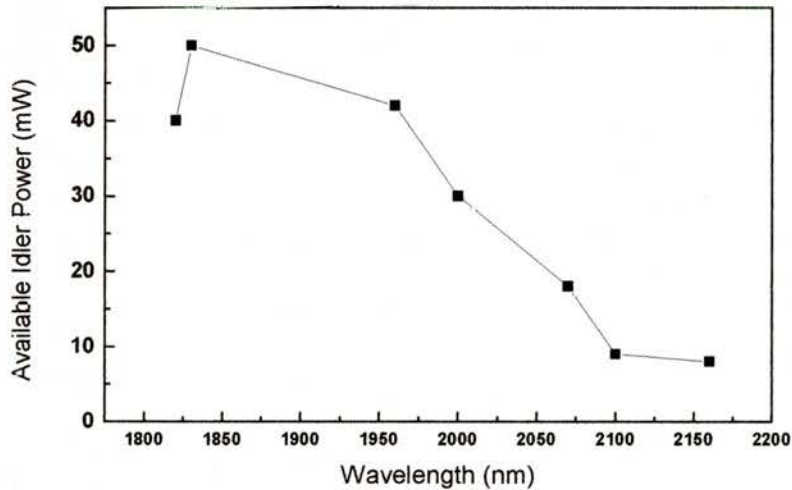


Figure 14. Available idler power for the idler spectral range.

The idler pulse durations were also studied using a silicon-photodiode-based autocorrelator. The two-photon absorption response of the silicon photodiode at 1.8 μm is shown in Figure 15.

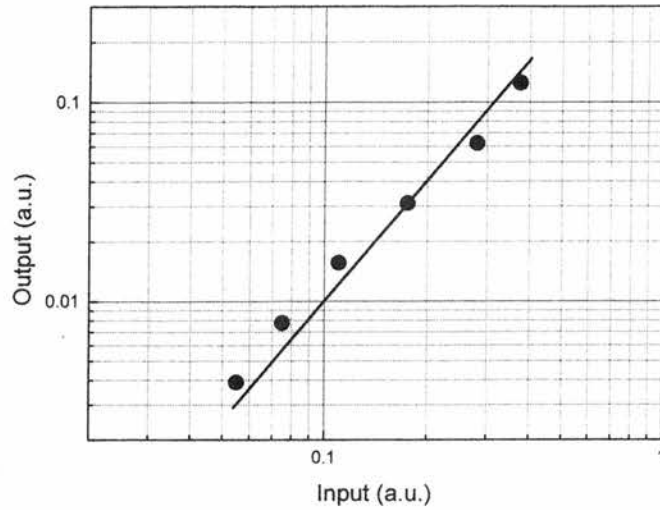


Figure 15. Two-photon absorption measurement of silicon photodiode at idler wavelengths together with a best-fit line of slope 2.

The idler pulse duration were measured to be between 100 to 200 fs depending on the wavelength. Shorter pulses were obtained for longer idler wavelengths, which implies that the idler pulse durations are limited by pump-signal walkaway. Figure 16 shows typical intensity and interferometric autocorrelations of pulses centred at 1.8 μm .

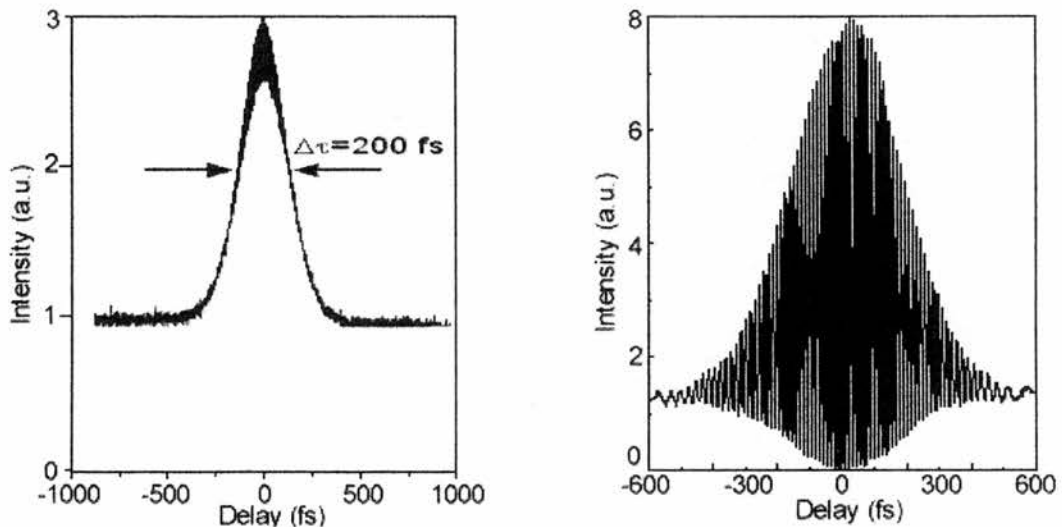


Figure 16. Typical intensity and interferometric autocorrelations of idler pulses centred at 1.8 μm with duration of 200 fs.

4.4. Optical parametric oscillator with continuous tunability from 2.8 to 6.8 μm

4.4.1 Introduction

Versatile sources of mid-infrared (mid-IR) femtosecond pulses have potential applications in trace-gas detection, time-resolved spectroscopy of semiconductors, photochemistry and detector characterisation. Tunable systems are often desirable in order to allow access to particular spectral regions such as the atmospheric transmission window around 4 μm . Conventional approaches of generating continuous-wave outputs at wavelengths throughout the mid-IR spectral region have included lead-salt diode lasers and others based on difference-frequency generation.

As previously explained, these systems have typically been limited either by their restricted tunability in any given configuration or by low average powers. OPOs offer an alternative route to producing mid-IR radiation¹⁰⁻¹⁴ and in this section I will describe the generation of broadly-tunable high-repetition-rate mid-IR femtosecond pulses using an OPO based on periodically-poled lithium niobate (PPLN).

The large nonlinearity and noncritical phase-matching capabilities of PPLN have allowed the exploitation of its high parametric gain to generate wavelengths in mid-IR region. In an OPO configuration, the largest nonlinear coefficient in PPLN (d_{33}) can be accessed by polarising the pump, signal and idler waves parallel to the z axis ($e \rightarrow e + e$). An additional advantage is that the extraordinary polarisation experiences lower absorption loss through the transmission window of the material than the corresponding ordinary polarisation. For these reasons, synchronously pumped OPOs

based on PPLN have proved to be useful tools to generate wavelengths as long as $5.3\ \mu\text{m}$.^{11,12} Recent work using picosecond pump pulses has shown that it is possible to generate wavelengths beyond the commonly recognised infrared absorption edge around $5.4\ \mu\text{m}$.¹³ In this work, evidence of idler oscillation out to $6.3\ \mu\text{m}$ was inferred from signal tuning data but no direct measurements of the idler were made beyond $5.41\ \mu\text{m}$. Demonstration of a PPLN-based picosecond OPO at the wavelengths of 6 , 6.2 and $6.6\ \mu\text{m}$ was reported shortly after that,¹⁴ but continuous tunability was not demonstrated.

In this section, I would wish to highlight the observation that a second transmission window of PPLN, extending from $6 - 7\ \mu\text{m}$ for the extraordinary polarisation, can be exploited to generate significant output powers at idler wavelengths as long as $6.8\ \mu\text{m}$.^[5]

4.4.2 The experimental setup and results

The PPLN crystal was fabricated using the standard electric-field poling technique with photoresist trenches.¹⁵ The crystal was cut to $1\ \text{mm}$ long and contained nine 1-mm wide gratings, ranging from $16.0\ \mu\text{m}$ to $20.0\ \mu\text{m}$ in $0.5\ \mu\text{m}$ increments. The sample was commercially polished and antireflection (AR) coated for pump, signal, and idler wavelengths. The length of the sample was chosen to reduce the strong material-induced absorption occurring in LiNbO_3 in the mid-IR. Figure 17 shows the measured transmission of the sample for both extraordinary and ordinary polarisations.¹⁶ It is important to note that the extraordinary polarisation of the interacting waves allows the

access to the transmission window from 6 - 7 μm , where significant output energies were measured.

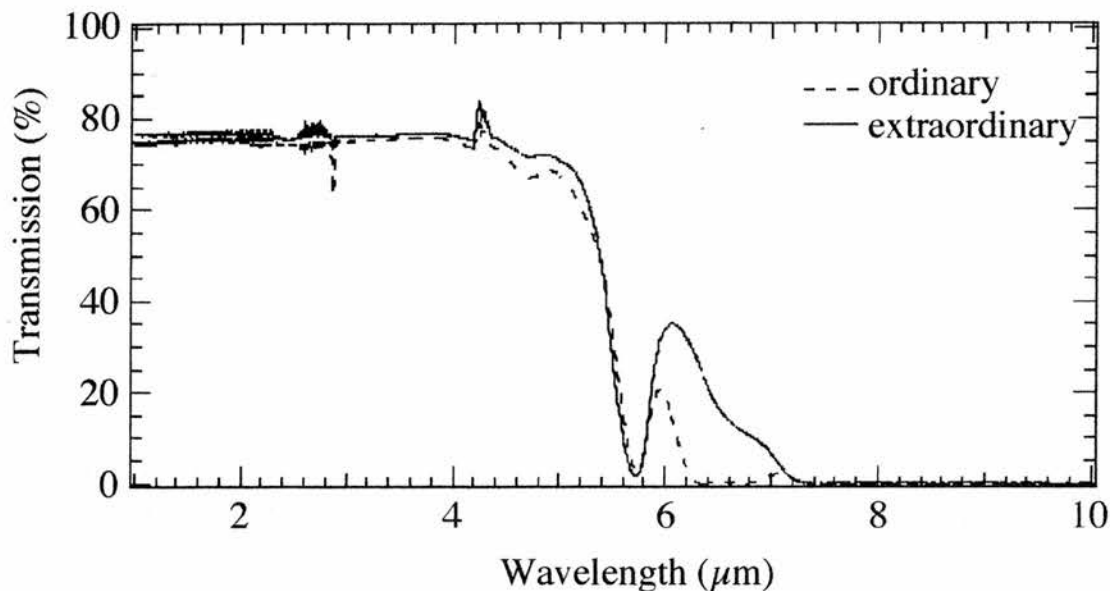


Figure 17. Measured transmission of a 1-mm long LiNbO_3 sample for incident light polarised parallel to the extraordinary (solid line) and ordinary (dashed line) crystal axes. The extraordinary wave interaction of PPLN allows OPO operation within the transmission window at wavelengths beyond 6.0 μm .

The PPLN-based OPO was synchronously pumped by a modelocked Ti:sapphire laser operating at a pulse repetition rate of 84 MHz, with output pulses of 100 fs duration and an average output power of ~ 1.5 W. The majority of the results presented here were obtained for a laser wavelength of 810 nm but shorter wavelengths were also used to extend the tuning range of the OPO to shorter idler wavelengths. The polarisation of the pump, signal and idler beams was horizontal in the cavity and parallel to the poling direction, which lay along the crystallographic c axis (optical z-axis). The OPO was configured for collinear phasematching in a symmetric four mirror X-cavity consisting of two curved mirrors ($r = -75$ mm) and two flat end mirrors. This configuration is shown in Figure 18. All the mirrors were highly reflecting (HR) for the

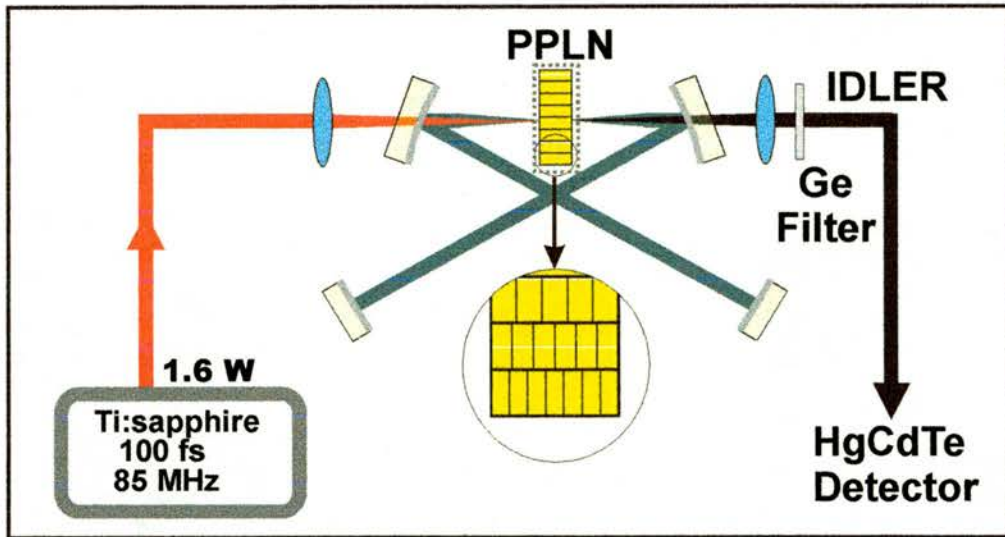


Figure 18. Experimental set up.

The idler beam was collimated with a CaF₂ 40 mm focal-length lens and directed to a scanning spectrometer. The spectrometer had a grating of 150 lines/mm with a blaze angle optimised for a wavelength of 4 μm . Idler wavelengths were measured with a liquid nitrogen cooled HgCdTe detector (EG&G J15D12-M204-S01M-60) connected to a lock-in amplifier. A germanium filter was placed in front of the input slit of the spectrometer to block any residual pump or signal light. Under these conditions it was possible to record idler spectra with central wavelengths ranging from 2.8 - 6.8 μm and good agreement was found between the idler wavelength measured in this way and that inferred from a simultaneous measurement of the residual signal and pump light leaving one of the flat cavity mirrors. Signal tunability extended across the mirror bandwidth from 910 nm to 1080 nm and figures 19 (a) and (b) show the complete OPO tunability for the idler and signal wavelengths, respectively.

spectrometer to block any residual pump or signal light. Under these conditions it was possible to record idler spectra with central wavelengths ranging from 2.8 - 6.8 μm and good agreement was found between the idler wavelength measured in this way and that inferred from a simultaneous measurement of the residual signal and pump light leaving one of the flat cavity mirrors. Signal tunability extended across the mirror bandwidth from 910 nm to 1080 nm and figures 19 (a) and (b) show the complete OPO tunability for the idler and signal wavelengths, respectively.

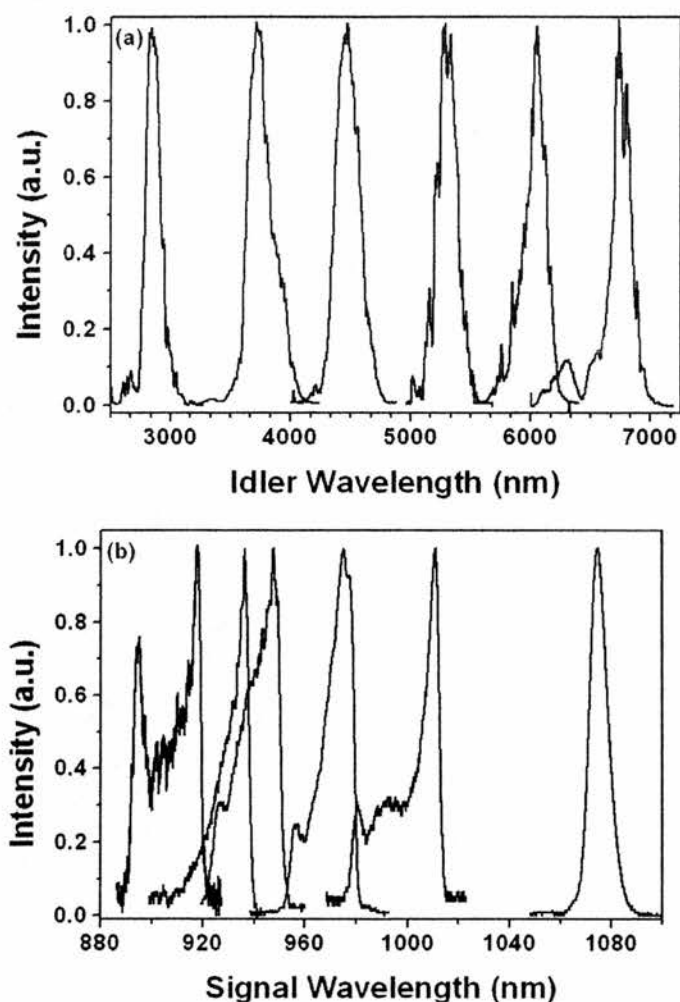


Figure 19. (a) Idler and (b) corresponding signal spectra obtained across the tuning range of the OPO. Continuous tunability was achieved by a combination of cavity length, pump wavelength and grating period tuning.

idler central wavelength was tuned from 5.2 - 6.8 μm , respectively. These results, together with the phase matching behaviour of the PPLN crystal, are shown in Figure 20.

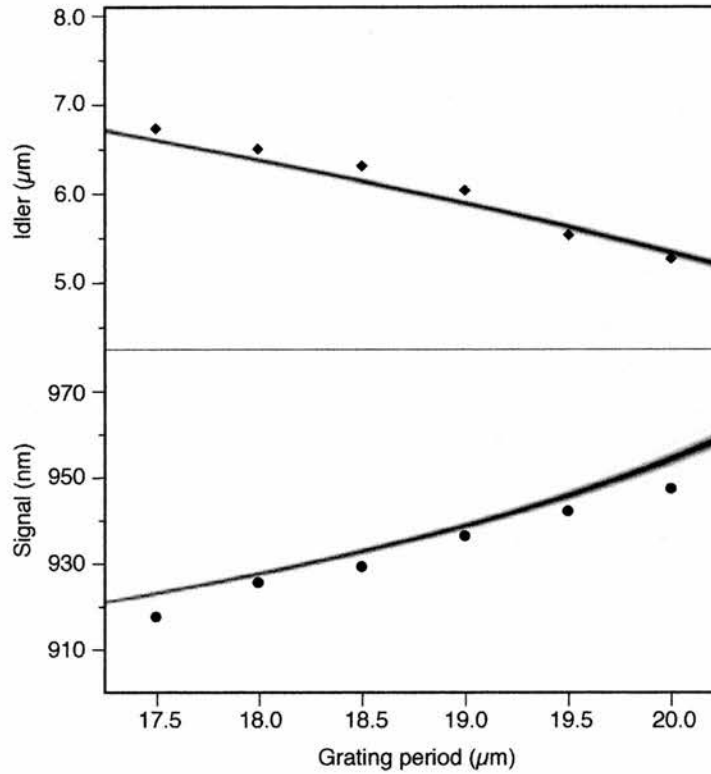


Figure 20. Signal (circles) and idler (diamonds) output wavelengths measured from the OPO operated with PPLN grating periods of 17.5, 18.0, 18.5, 19.0, 19.5 and 20.0 μm . The gain coefficient, $\text{sinc}^2(\Delta k l / 2)$, calculated using an infrared-corrected Sellmeier equation for PPLN is shown in greyscale with white representing zero and black representing unity.

The variation of the normalised gain coefficient $\text{sinc}^2(\Delta k L / 2)$ (where Δk is the wave vector mismatch and L is the crystal length) across the OPO tuning range, was calculated by using the infrared-corrected Sellmeier equation for PPLN.¹⁷ It can be seen that the distribution of recorded data agrees well with the predicted regions of parametric gain. Due to the small phasematching bandwidth, cavity length tuning in any

The variation of the normalised gain coefficient $\text{sinc}^2(\Delta kL/2)$ (where Δk is the wave vector mismatch and L is the crystal length) across the OPO tuning range, was calculated by using the infrared-corrected Sellmeier equation for PPLN.¹⁷ It can be seen that the distribution of recorded data agrees well with the predicted regions of parametric gain. Due to the small phasematching bandwidth, cavity length tuning in any individual grating was limited to a short range, but continuous idler tunability was easily achieved by pump wavelength tuning.

Average idler output powers were also investigated using an infrared sensitive power meter (Melles Griot 13PEM001) and with an antireflection-coated germanium filter placed in front of its head to block any residual pump or signal light. The output powers were observed to decrease with wavelength from a maximum of 47.7 mW at $\sim 4.64 \mu\text{m}$ to 0.2 mW at $6.5 \mu\text{m}$. Near-threshold operation and heat radiated by the germanium filter due to pump absorption prevented accurate readings of output powers being obtained at $6.8 \mu\text{m}$, and the only alternative to detect any idler was through the use of a spectrometer (as described above). As an attempt to increase idler output power, a 3 mm long crystal was also used. The results obtained with the two crystals can be seen in Figure 21.

When using the 3 mm long crystal, it was found that idler oscillation was limited to $6.4 \mu\text{m}$, and no evidence of oscillation beyond this wavelength could be found. This suggests that extraction of idler power can be limited by the crystal absorption. Furthermore, in the region between 5.5 and $6.4 \mu\text{m}$ the two crystals delivered approximately the same amount of average power. Finally, for wavelengths shorter than

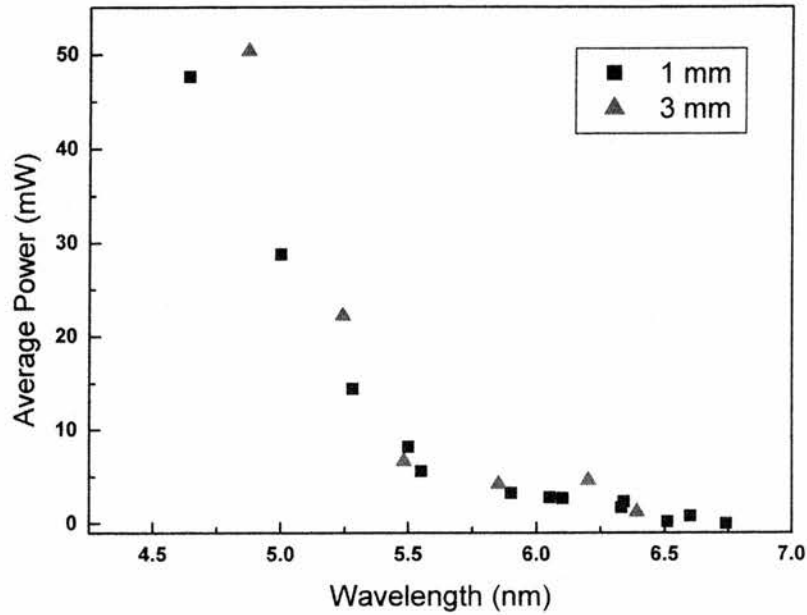


Figure 21. Idler output power as a function of wavelength (CaF_2 mirror transmission is not taken into account).

5.5 μm the longer crystals delivered more idler power. These results suggest that idler power does not depend on the crystal length but on the pump-signal group velocity walk-away (PS-GVWA). Figure 22 shows the different values of PS-GVWA as a function of idler wavelengths and for three different values of pump wavelengths. From figure 22, it is clear that for those idler wavelengths longer than 6.3 μm (that have a PS-GVWA value smaller than 100 fs/mm), parametric gain will occur in the first millimetre of the crystal. This implies that the use of longer crystal will just increase the absorption at these wavelengths. However, idler wavelengths shorter than 6.0 μm will experience more parametric gain if the crystal is longer than 1 mm.

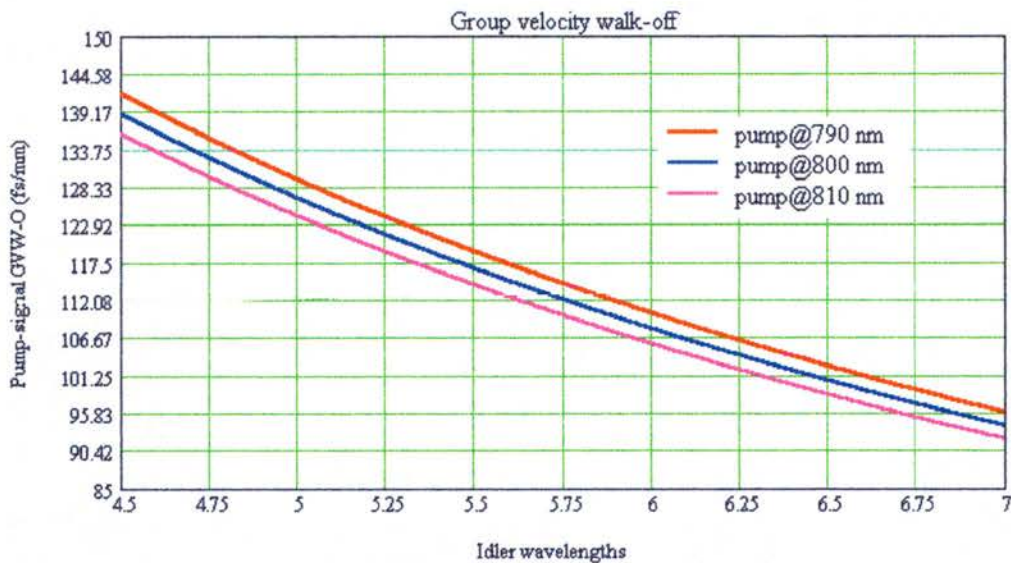


Figure 22. Pump-Signal group velocity walk-away as a function of idler wavelength.

Across the tuning range the pump oscillation threshold varied from 1.1 to 1.5 W and appeared to show a correlation with the absorption behaviour for the PPLN crystal. In particular, a local maximum in the pump threshold was observed near 5.8 μm where the crystal transmission shows a local minimum. The transmission of the crystal, together with the output power (see figure 21) that shows a gap at around 5.8 μm, are plotted in figure 23. A maximum pump depletion of ~ 35% at 5.2 μm was measured.

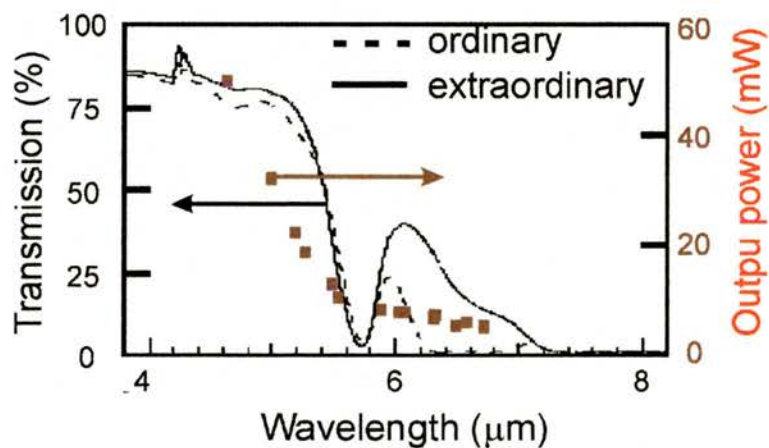


Figure 23. Idler output power and detail of the strong crystal absorption at 5.75 μm

An estimation of the idler pulse duration was made. These pulse durations were inferred from the spectral bandwidth (measured at the full width at half maximum (FWHM)) of idler pulses. According to figure 19 (a), the bandwidth of idler pulses goes from ~ 200 nm (at $5.2 \mu\text{m}$) to 150 nm (at $6.75 \mu\text{m}$). Assuming that idler pulses have a $\text{sech}^2(t)$ intensity profile, and that they are transformed limited ($\Delta\nu\Delta\tau = 0.315$), then the duration of idler pulses varies from ~ 150 to 300 fs, respectively.

To obtain shorter idler wavelengths, a $20 \mu\text{m}$ crystal grating was used and the pump central wavelength set to 780 nm. Because of the high gain and low loss of PPLN at shorter wavelengths, a small noncollinear angle between the pump and signal wavelengths was supported by the OPO. This noncollinear arrangement resulted in an effectively longer grating period. Under these conditions, a simple change in cavity length resulted in idler (signal) tuning from $2.8 \mu\text{m}$ (1070 nm) to $\sim 5.0 \mu\text{m}$ (950 nm) and in this regime, output powers in excess of 60 mW at $3.0 \mu\text{m}$ were measured with an associated pump depletion ratio of 45% .

4.5. Conclusions

In conclusion, I have described a femtosecond PPRTA-OPO which is continuously tunable in the signal-wavelength band from 1.375 to $1.575 \mu\text{m}$ with a maximum output power of 110 mW. The corresponding idler tuning was from 1.845 to $2.225 \mu\text{m}$. This OPO configuration, represents a convenient tool for generating transform-limited femtosecond pulses at useful power levels over a wide tuning range. It

also offers the additional attraction that the access to spectral regions near the atmospheric water absorption is uncompromised.

An OPO based on a crystal of PPLN with idler wavelengths operating in the 1.8 to 2.2 μm was fully characterised. In this spectral range, pulses of 200 fs with average output powers up to 50 mW were obtained and a related study of the dispersion of the system in different spectral ranges was carried out.

Extended mid-IR output generation was also demonstrated from two different OPOs systems based on PPLN crystals. The first approach led to a demonstration of a robust, all-solid-state femtosecond OPO that was tunable to $\sim 5 \mu\text{m}$. In the second system, an idler tuning range of 4 μm was demonstrated and idler pulses at wavelengths as long as 6.8 μm were produced at useful output power levels. This was made possible by exploiting a second transmission window in PPLN lying beyond the conventionally accepted infrared absorption edge of 5.4 μm . It has also been shown that my experimental results are in good agreement with the theoretical phase matching tuning range.

4.6 References

1. P. Loza-Alvarez, D. T. Reid, M. Ebrahimzadeh, W. Sibbett, H. Karlsson, P. Henriksson, G. Arvidsson, F. Laurell, "Periodically poled RbTiOAsO₄ femtosecond optical parametric oscillator tunable from 1.38 to 1.58 μm ," *Appl. Phys. B.*, **68**, 177 – 180 (1999).
2. C. McGowan, D. T. Reid, Z. Penman, M. Ebrahimzadeh, W. Sibbett, D. H. Jundt, "Femtosecond optical parametric oscillator based on periodically poled Lithium Niobate," *J. Opt. Soc. Am. B.*, **15**, 694 – 701 (1998).
3. Z. E. Penman, P. Loza-Alvarez, D. T. Reid, M. Ebrahimzadeh, W. Sibbett, D. H. Jundt, "All-solid-state mid-infrared femtosecond optical parametric oscillator based on periodically-poled lithium niobate," *Opt. Commun.*, **146**, 147 – 150 (1998).
4. Z. E. Penman, C. McGowan, P. Loza-Alvarez, D. T. Reid, M. Ebrahimzadeh, W. Sibbett, D. H. Jundt, "Femtosecond optical parametric oscillator based on periodically-poled lithium niobate," *J. Mod. Opt.*, **45**, 1285 – 1294 (1998).
5. P. Loza-Alvarez, C. T. A. Brown, D. T. Reid, W. Sibbett, M. Missey, "High repetition rate ultrashort-pulse optical parametric oscillator continuously tunable from 2.8 to 6.8 μm ," *Opt. Lett.*, **24**, 1523 – 1525 (1999).
6. H. Karlsson, F. Laurell, P. Henriksson and G. Arvidsson, "Frequency doubling in periodically poled RbTiOAsO₄," *Electron. Lett.*, **32**, 556 – 557 (1996).
7. D. L. Fenimore, K. L. Schepler, D. Zelmon, S. Kuck, U. B. Ramabadran, P. V. Richter, D. Small, "Rubidium titanyl arsenate difference-frequency generation and validation of new Sellmeier coefficients," *J. Opt. Soc. Am. B.*, **9**, 1935 – 1940 (1996).
8. D. T. Reid, M. Padgett, C. McGowan, W. E. Sleat, and W. Sibbett, "Light emitting diodes as measurement devices for femtosecond laser pulses," *Opt. Lett.*, **22**, 233 – 235 (1997).
9. M. Ebrahimzadeh, C. T. A. Brown, University of St. Andrews, Private communication (1999).
10. S. Marzenell, R. Beigang and R. Wallenstein, "Mid-infrared femtosecond AgGaSe₂ optical parametric oscillator," in *Conference on Lasers and Electro-Optics*, OSA Technical Digest (Optical Society of America, Washington DC, 1999), pp. 35, Paper CMG4
11. K. C. Burr, C. L. Tang, M. A. Arbore, M. M. Fejer, "Broadly tunable mid-infrared femtosecond optical parametric oscillator using all-solid-state-pumped periodically poled lithium niobate," *Opt. Lett.*, **22**, 1458 – 1460 (1997).
12. L. Lefort, K. Peuch, S. D. Butterworth, G.W. Ross, P. G. R. Smith, D.C. Hanna, D. H. Jundt, "Efficient, low-threshold synchronously-pumped parametric oscillation in periodically-poled lithium niobate over the 1.3 μm to 5.3 μm range," *Opt. Com.*, **152**, 55 – 58 (1998).
13. L. Lefort, K. Peuch, G.W. Ross, Y.P. Svirko and D.C. Hanna, "Optical parametric oscillation out to 6.3 μm in periodically poled lithium niobate under strong idler absorption," *Appl. Phys. Letts.*, **73**, 1610 – 1612 (1998).
14. M. Sato, T. Hatanaka, S. Izumi, T. Taniuchi, H. Ito, "Generation of 6.6- μm optical parametric oscillation with periodically poled LiNbO₃," *Appl. Opt.*, **38**, 2560 – 2563 (1999).
15. L. E. Myers, R. C. Eckardt, M. M. Fejer, R. L. Byer, W. R. Bosenberg, and J. W. Pierce, "Quasi-phase-matched optical parametric oscillators in bulk periodically poled LiNbO₃," *J. Opt. Soc. Am. B*, **12**, 2102 – 2116 (1995).

16. M. Missey, Private communication (1999).
17. D. H. Jundt, "Temperature-dependent Sellmeier equation for the index of refraction, n_e , in congruent lithium niobate," *Opt. Lett.*, **22**, 1553 – 1555 (1997).

CHAPTER 5

SIMULTANEOUS SECOND HARMONIC GENERATION AND PULSE COMPRESSION

In Chapter 4, I described some alternative sources of high repetition-rate femtosecond pulses operating in the near- and mid-infrared. I have shown that by taking advantage of the quasi-phasematching (QPM) technique to implement synchronously pumped optical parametric oscillators (OPOs), it is possible to obtain femtosecond pulse radiation in essentially any wavelength region from 0.9 to 7 μm at substantial average output powers.

To obtain femtosecond pulses in the visible, it is a common practice to frequency double the output pulses from a Ti:sapphire laser or an OPO using a birefringent nonlinear crystal (see for example Section 3.2). Femtosecond pulses produced in this way are typically not transform-limited because of group velocity mismatch, phase mismatch and linear absorption.¹ However, by using the QPM technique it is possible to overcome this problem by designing grating periods in the nonlinear crystal that are not strictly periodic.² In this way frequency doubled pulses in the femtosecond regime that have transform limited characteristics can be produced.³

5.1. Simultaneous SHG and pulse compression in AP-KTP

In this chapter I will describe the use of this technique in extracavity and intracavity configurations to simultaneously frequency double and compress the chirped output femtosecond-pulses that are produced by an RTA-based OPO. Initially a description is given of the RTA OPO source together with a frequency-resolved optical gating (FROG) characterisation of the chirp femtosecond output pulses. Then extracavity and intracavity simultaneous SHG and pulse compression using an aperiodically-poled crystal of KTP (AP-KTP) are described. My experimental results are compared with a numerical model (elaborated by Dr. P. Faller, University of St. Andrews) that calculates the temporal and spectral shape and phase of the SHG pulses. The model uses the retrieved data obtained after the FROG characterisation of the input pulses. I also used the model to predict the chirped-grating parameters of the crystal that would give optimum pulse compression. Finally, to further test these results, an aperiodically poled crystal of lithium niobate (APPLN), having eight different chirped grating period is used for systematic measurements. Experimental results are discussed and compared with those from an extended version (by Dr. D. Artigas, Universitat Politècnica de Catalunya) of our previous the numerical model.

5.1.1. The RTA-based optical parametric oscillator

The OPO was synchronously-pumped with a self-modelocked Ti:sapphire laser delivering pulses of 100 fs centred at 800 nm, at a repetition frequency of 84 MHz and with an average pump power of 1.3 W. Figure 1 shows a schematic of

the experimental setup. The OPO was based on a 3 mm long birefringently phase-matched RTA crystal. Collinear noncritical phasematching along the optical x axis was used to ensure the maximum possible gain for the type II ($o \rightarrow o+e$) parametric interaction. Collinear phasematching is commonly realised in practice by introduction of the pump light into the crystal through one of the resonator mirrors. For the short lengths (few millimeter) of the crystals used in femtosecond OPO's, this geometry can make optimal focusing technically difficult. The resonator configuration that was adopted for the RTA OPO (illustrated in Figure 1) allows independent focusing of the pump and the signal beams.

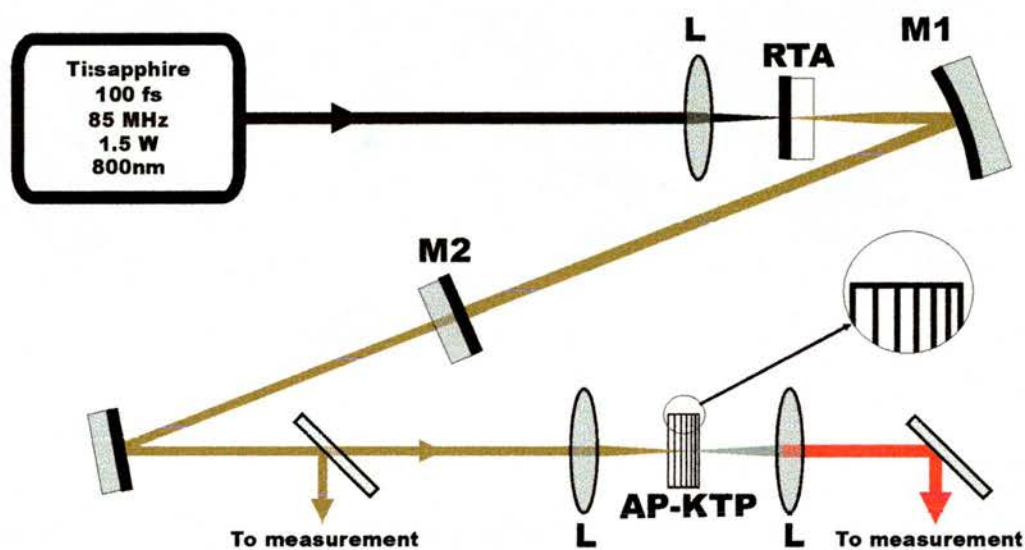


Figure 1. Experimental setup for simultaneous SHG and pulse compression for the extracavity configuration; M1, highly reflecting curved mirror; M2, end mirror; L, lens.

The RTA crystal was coated on one side with a highly reflecting mirror at the signal wavelength, and the opposite face had an antireflection coating for the same wavelength. Pump light was focused to a point inside the crystal that was close to the highly reflecting mirror face and coincident with the beam waist of the intracavity signal mode allowing independent focusing of the pump and the signal beams and therefore affording a maximum extraction of energy⁴. The intracavity signal mode

was focused with a concave highly reflecting mirror (M1) and a plane high reflector end mirror (M2) completed the cavity.

By using a 10% output coupler, the average output power from the OPO was up to 600 mW at the signal wavelength (1.25 μm) and 150 mW at the idler wavelength (2.22 μm). The pump depletion ratio was as high as 85%. The resonator configuration adopted for the RTA-OPO had no group velocity dispersion compensation. Consequently, pulses exiting the OPO are expected to be severely broadened by normal dispersion in the RTA crystal and therefore, the leading edge contains the longer wavelength components. The signal pulses generated were autocorrelated using a GaAs light emitting diode⁵ and pulses of ~ 290 fs, measured at the full width at half maximum (FWHM) and assuming $\text{sech}^2(t)$ pulse shape, were found. The pulses were centred at 1.25 μm and had a FWHM spectral width of 37 nm. The pulse duration-bandwidth product was $\Delta\nu\Delta\tau = 2.0$ (~ 6 times transform-limited). Figure 2 shows a typical intensity autocorrelation and spectrum generated by this OPO. These data served as a basis for the design of chirped-period grating in a KTP crystal.

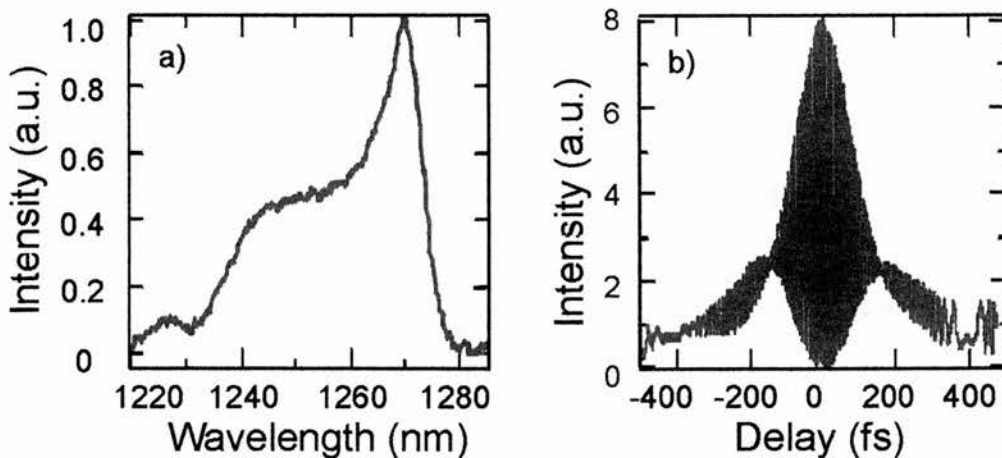


Figure 2. a) Pulse spectrum and b) interferometric autocorrelation of the signal output from the RTA-based OPO showing frequency-chirped pulses of $\Delta\tau = 286$ fs, with a spectral bandwidth of 37 nm centred at 1.25 μm . The pulse duration-bandwidth product is $\Delta\nu\Delta\tau = 2.00$.

5.1.2. Extracavity SHG and pulse compression

With the previous data and assuming a linear frequency chirp of the fundamental pulses, the calculation of the dependence of the conversion position such that the converted frequency components all emerge simultaneously from the crystal was straightforward. The pulse duration, wavelength of the leading and trailing edges of the pulse and the group-velocity dispersion at the fundamental and second harmonic wavelengths had to be taken into account.

The limited amount of frequency-chirp present in the input pulses required the use of a crystal with a short active length. The resulting aperiodically-polled KTP crystal (AP-KTP) had a total length of 630 μm , and the grating periods varied from 15.45 to 14.20 μm . It was fabricated by an electrical poling technique⁶ using a flux-grown KTP crystal having the poling direction parallel to the z-axis. To this point it is important to mention that although KTP has a lower effective nonlinear coefficient than lithium niobate ($d_{\text{eff}} \sim 8$ pm/V and 14 pm/V, respectively), the effects of photorefractive damage are less noticeable (this is an escalating problem in PPLN as the SHG wavelengths becomes shorter) and therefore can be operated at room temperature.

Experimental results and discussion

To carry out extracavity frequency doubling, the output signal beam from the RTA-based OPO was focused with a 15 mm focal length lens into the AP-KTP crystal.⁷ The generated second-harmonic output beam was collimated with a similar lens and characterised using second-harmonic autocorrelation. We measured the SHG pulses from AP-KTP crystal when it was oriented in two different directions.

When the input face of the crystal corresponded to the longest grating period, SHG pulses as short as 120 fs having a spectral bandwidth of $\Delta\lambda = 8.5$ nm were obtained. The pulse duration-bandwidth product of $\Delta\tau\Delta\nu = 0.77$ implied that the pulses were approximately twice the transform-limited value by assuming a $\text{sech}^2(t)$ intensity profile. Figure 3 shows typical autocorrelations and spectra obtained. Placing the crystal in the opposite direction (shortest grating as the input face), SHG pulses of 240 fs (blue line in Fig. 3a) with a spectral bandwidth of $\Delta\lambda = 8.5$ nm and a pulse duration-bandwidth product of $\Delta\tau\Delta\nu = 1.54$ were obtained. In each configuration, the spectra of the pulses were found to be approximately the same, implying that SHG pulse compression was due solely to the aperiodicity in the doubling crystal and not to spectral clipping or self-phase-modulation. The short active interaction length (630 μm) of our crystal resulted in a relative low peak power efficiency of $\sim 4.5\%$ and a maximum average output power of 9 mW was measured in either configuration. A theoretical estimation of the peak power efficiency (see section 5.3.4) gives a value of 6.68 % which implies that the levels of power obtained are correct.

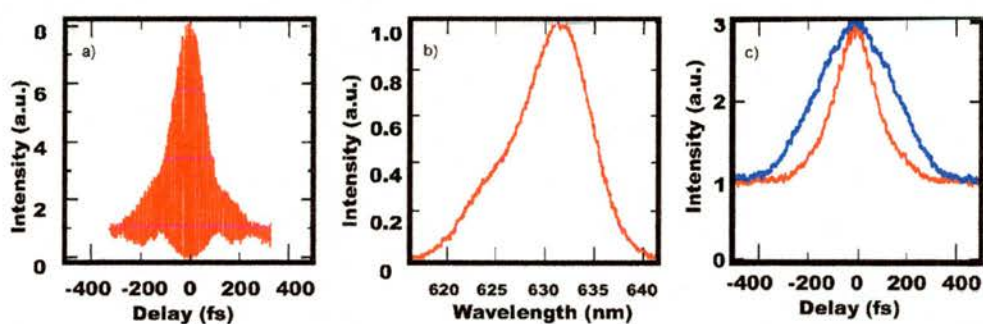


Figure 3. Pulse characterisation of the extracavity SHG pulses from AP-KTP crystal. a) Interferometric autocorrelation for pulses in the compression direction b) Spectra of the pulses (for both configurations) centred at 630 nm with a spectral bandwidth of $\Delta\lambda = 8.5$ nm. c) Intensity autocorrelations showing pulses of $\Delta\tau = 121$ fs (red line) for the compression direction and $\Delta\tau = 240$ (blue line) for the expansion direction. The pulse duration-bandwidth product obtained were $\Delta\nu\Delta\tau = 0.77$ for the compression direction and $\Delta\nu\Delta\tau = 1.54$ for the expansion direction.

5.1.3 Intracavity SHG and pulse compression

As a strategy to obtain useful output powers at the SHG wavelengths we performed intracavity frequency doubling by introducing a folding section with the AP-KTP crystal inside the OPO resonator. Figure 4 shows the variations of our experimental setup. The folding section consisted of two concave mirrors ($r = 100$ mm) and the AP-KTP crystal was placed at the waist of the intracavity-signal beam. All the mirrors were highly reflecting at the signal wavelengths. The two faces of AP-KTP crystal were antireflection coated for the signal wavelength and the orientation was such that the longest grating period faced the intracavity-signal pulse immediately after it was generated from the RTA crystal. To characterise the fundamental pulses before they reach the AP-KTP crystal, a 5% transmittance folding mirror (FM) was placed directly after mirror M1 and before AP-KTP crystal.

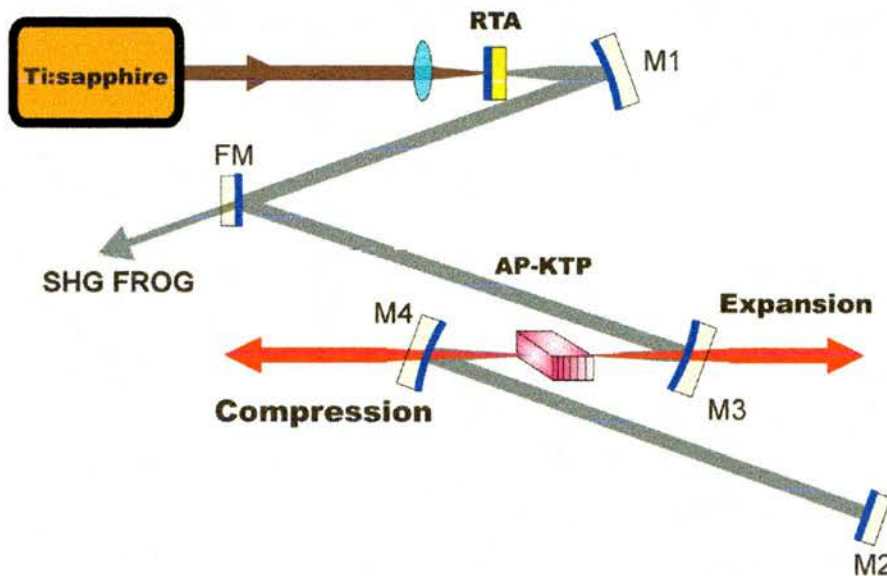


Figure 4. Experimental setup for simultaneous SHG and pulse compression for the intracavity configuration; M1, M3, M4, highly reflecting curved mirrors; FM, 5% output coupler, M2, end mirror.

An average output power of 80 mW of the signal beam that was coming directly from the RTA crystal and after the mirror FM was measured (the signal

beam coming from the opposite direction was not taken into account). Using this output the fundamental pulses were then characterised using a SHG-based frequency resolved optical gating (SHG-FROG) technique^{8,9}. The characteristic ambiguity associated with by the SHG-FROG technique ($E(t) = E^*(-t)$) was easily removed because signal pulses were propagating in normal (positive) dispersive materials. The retrieved pulses showed durations of 290 fs with positive quadratic temporal phase (leading edge containing the longer wavelength components). The intensity and phase profiles retrieved from the FROG trace of the fundamental pulses, together with the independently measured spectrum and autocorrelation are shown in figure 5.

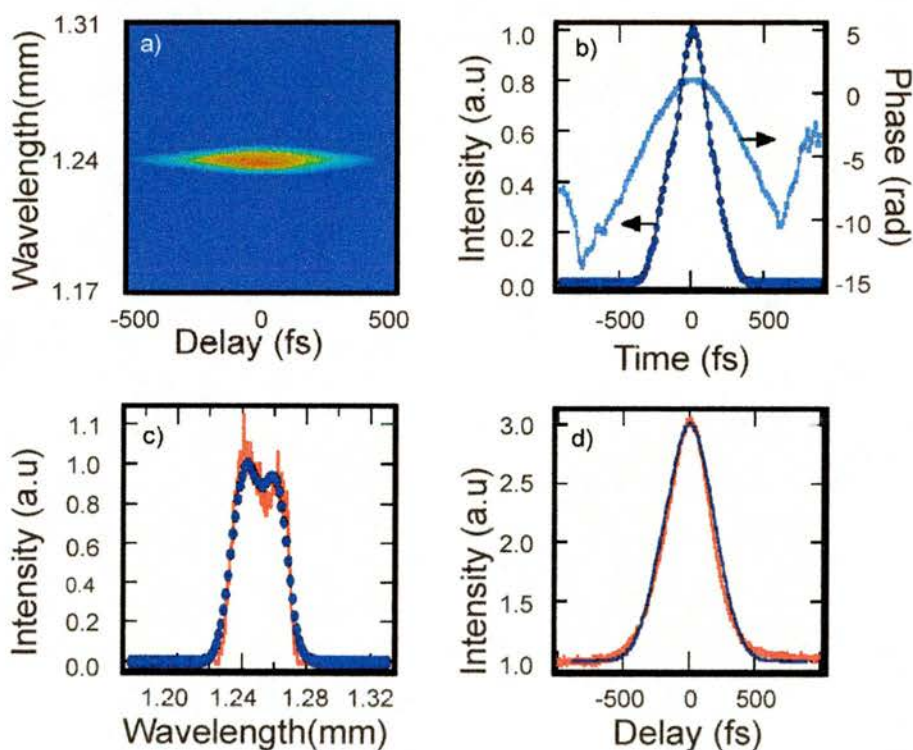


Figure 5. FROG characterisation of the signal output from the RTA-based OPO that shows pulse durations of $\Delta\tau = 290$ fs with positive quadratic phase and with pulse duration-bandwidth products of $\Delta\nu\Delta\tau = 2.0$. a) FROG trace, b) temporal intensity profile and phase of the retrieved pulses, c) measured (red line) and retrieved (blue dots) spectra of the pulses centred at $1.25 \mu\text{m}$ and with spectral bandwidth of 37 nm, d) measured (red line) and retrieved (blue line) intensity autocorrelations.

The good agreement between the spectrum and autocorrelation of the retrieved pulse and the experimental quantities confirms that the FROG measurement and retrieval are accurate.

5.1.4 The numerical model

We used the retrieved temporal intensity and phase profiles of the OPO signal output as the input pulse to a numerical model to simulate SHG in quasi-phase-matching crystals. Our model is based on that described by M. A. Arbore *et al.*,¹⁰ and consists of coupled-wave equations describing SHG by plane wave pulses propagating through an aperiodic QPM crystal. This model takes into account the group velocity mismatch between the fundamental and second harmonic pulses. We neglect the group velocity dispersion and make the assumption that the fundamental pulses are undepleted throughout the crystal. The equations are then expressed as:

$$\frac{\delta A_1(z,t)}{\delta z} + \frac{1}{v_{g1}} \frac{\delta A_1(z,t)}{\delta t} = 0 \quad (5.1)$$

$$\frac{\delta A_2(z,t)}{\delta z} + \frac{1}{v_{g2}} \frac{\delta A_2(z,t)}{\delta t} = \Gamma s(z) A_1^2(z,t) \exp(i\Delta k_0 z) \quad (5.2)$$

where $\Gamma = i\pi d_{\text{eff}}/\lambda_1 n_2$. $A(z,t)$ is the slowly varying pulse envelope, λ is the vacuum centre wavelength, n is the refractive index, v_g is the group velocity and $\Delta k_0 = 4\pi(n_2 - n_1)/\lambda_1$ is the vector mismatch which is defined for the refractive indices and evaluated at the centre of fundamental and second harmonic pulses. The indices 1 and 2 are, respectively, for the fundamental and second harmonic. The coefficient $s(z) = \pm 1$ is the sign of nonlinear coefficient which changes for each new half period. We begin by using the complex pulse amplitude determined by the FROG analysis and the equations are then solved using a basic two-variable

integration algorithm.¹¹ The crystal has a total length L and has been divided into half periods $\Lambda/2$ where $s(z)$ is constant. Their length increased linearly by Δx from $\Lambda_i/2$ to $\Lambda_f/2$ (defined as the quasi-phase-matched parameter for the input and output face), as shown in figure 6. The half pseudo-periods have been divided into slices of size δz and care has been taken for the boundaries, to ensure that we integrate over the whole length where $s(z)$ is constant. The integration steps δz and δt have also been chosen to avoid numerical aliases.

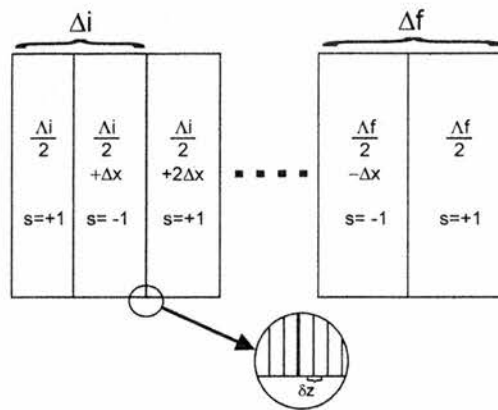


Figure 6. Schematic representation of the QPM crystal geometry used in the model.

5.1.5 Experimental results and discussion

We studied the behaviour of our SHG pulses under several conditions. Firstly, the mirrors M2, M3, and M4 (see figure 4) had high reflectivity at the SHG wavelengths. Under these circumstances, the fundamental pulses oscillating inside the OPO cavity were frequency doubled when they passed through the AP-KTP crystal travelling from mirror M3 to M4 (compression direction) and from M4 to M3 (expansion direction). This configuration delivered rather long SHG pulses due to superposition of the pulses generated in both directions, however, we were able to extract up to 220 mW of average output power coming directly after mirror FM. To

avoid any kind of pulse superposition, we used highly transmissive mirrors at the SHG wavelengths. The SHG pulses taken through mirror M4 (compression direction) and mirror M3 (expansion direction) were then collimated with an 80 mm focal length lens. We were able to obtain in a single beam an average output power of up to 120 mW, resulting in a 18.7 % peak power efficiency of SHG for the compression direction and 110 mW in the expansion direction. The SHG autocorrelations of the pulses show durations of 121 fs and 222 fs for the compression and expansion directions respectively. As in the extracavity case, the pulses generated in the compression and expansion directions differed only in their duration and the spectra were found to be similar. Figures 7 and 8 show typical spectra and autocorrelations of the pulses obtained from the expansion and compression directions respectively.

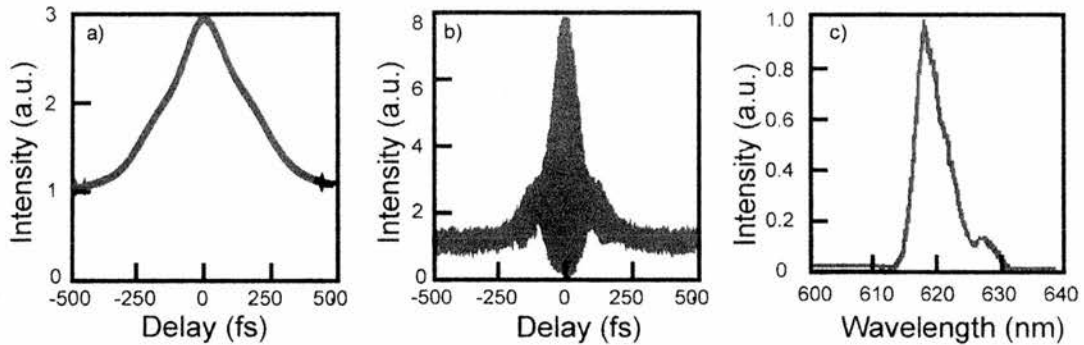


Figure 7. Autocorrelations and spectral measurements of the intracavity SHG pulses generated with the AP-KTP oriented in the expansion direction. a) Intensity and b) interferometric autocorrelations showing pulse durations of $\Delta\tau = 222$ fs. c) Spectrum of the pulses centred at 620 nm with a spectral bandwidth of $\Delta\lambda = 6$ nm. The pulse duration-bandwidth product is $\Delta\nu\Delta\tau = 1.04$

Fundamental pulses in the intracavity configuration were better matched to the crystal parameters as they generated, in the compression direction, nearly transform limited pulses. These SHG pulse had a pulse duration-bandwidth product of $\Delta\lambda\Delta\tau = 0.48$. As explained below, SHG with pulse compression depends on the

intensity profile and phase of the fundamental pulses. A change in any of these parameters will affect the compression behaviour of the SHG pulses. Introducing the AP-KTP crystal (and a folding section) inside the OPO cavity will produce a change in the phase and intensity profile of the signal (fundamental) pulses. Therefore, an extracavity configuration is expected to generate different SHG pulses compared to the intracavity configuration.

The retrieved data of the fundamental pulses from the OPO were used in our model to predict pulse compression characteristics. For modelling purposes, we considered a crystal of length 630 μm , the initial and final grating periods were of 15.45 and 14.20 μm and the temporal and spatial steps were 4 fs and 0.025 μm , respectively. The results of the numerical model compared with the experimental SHG pulses taken from the compression direction (directly after mirror M3) can be seen on figure 8.

These results indicate that the pulses are nearly chirp-free and with duration of 124 fs. Good agreement was found between the directly measured quantities and those inferred from the numerical model, thus confirming directly that this model could predict the SHG mechanism in an aperiodically-poled crystal. The small discrepancies may come by several factors such as inaccuracy of the Sellmeier equations, poling duty cycle of the crystal or self-phase-modulation. Practical limitations prevented us from doing a FROG measurement of the SHG pulses. A large crystal phasematching bandwidth is needed to frequency double the whole bandwidth of the compressed SHG pulses. This would necessitate a very thin crystal that would result in an SHG efficiency too low for our CCD camera to record because of its reduced sensitivity at 300 nm.

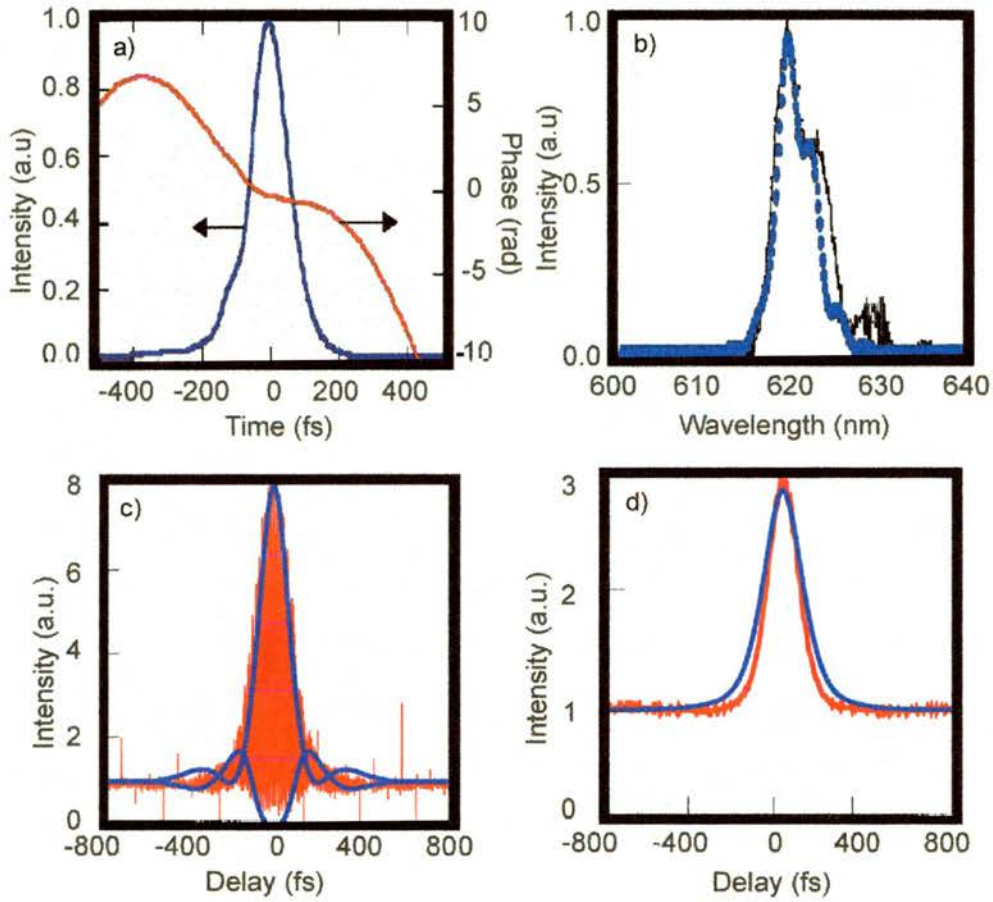


Figure 8. Pulse characterisation from the intracavity SHG using the AP-KTP crystal oriented for compression, showing pulses as short as 124 fs with nearly constant phase and pulse duration-bandwidth product of $\Delta\nu\Delta\tau = 0.48$. a) Temporal intensity profile and phase obtained with the model, b) measured (black line) and calculated spectra (blue dots) of the pulses centred at 622 nm with a spectral bandwidth of 5 nm, c) measured (red) and calculated (blue) interferometric autocorrelations, d) measured (red) and calculated (blue) intensity autocorrelations.

We studied the evolution of the SHG as it was generated inside the AP-KTP crystal with the numerical model. Figure 9 shows the evolution of the shape and phase of generated pulses and its FWHM, for propagation in each tenth of the crystal length. Although Fig. 9c suggests that shorter SH pulses are generated after the two-thirds and before the end of the crystal, the pulse shapes and their phases showed relatively more structure than the pulse generated at the end.

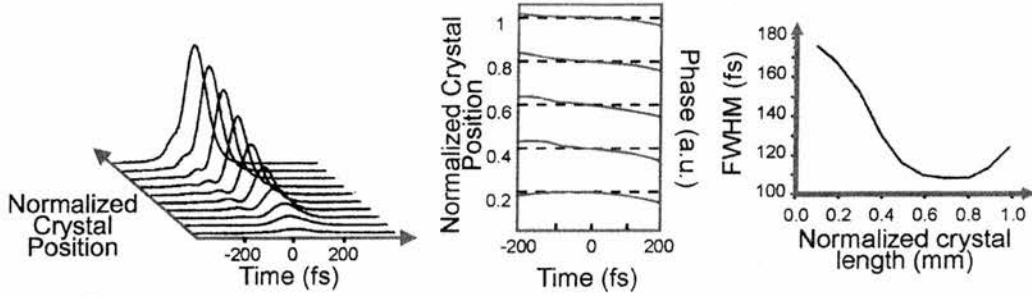


Figure 9. Theoretical evolution of the SHG pulses inside the QPM crystal. a) Temporal intensity, b) temporal phase, c) full width at half maximum.

To study the effect of the aperiodicity of the crystal domains on the temporal characteristics of the generated pulses, we made a numerical analysis by varying each time one of the quasi-phase-matching parameters: crystal length L , initial (A_i), final (A_f) and central (A_0) grating periods and crystal bandwidth ($\Delta A = A_f - A_i$). These results can be seen on figure 10. In each case, the results of the model are compared with the experimentally used crystal parameters (solid line in figure 10): $L = 630 \mu\text{m}$, $A_i = 14.20 \mu\text{m}$, $A_f = 15.45 \mu\text{m}$, $A_0 = 14.835 \mu\text{m}$, $\Delta A = 1.2 \mu\text{m}$. We evaluate the “smoothness” of the pulse shape, the temporal width (measured at the FWHM) and the “flatness” of the pulse phase. In case 1 (Fig. 10a) we varied the crystal length; in case 2 (Fig. 10 b) the initial grating period and in case 3 (Fig. 10c) the final grating period. In these three cases, shorter pulses with smoother pulse shape, showed more structure in their phases than the more distorted longer pulses. As can be seen in figures 10a – c, the experimentally used crystal parameters represented the best compromise to generate shorter pulse duration, smoother pulse shape and flatter phase. For cases 4 and 5 (see Figures 10 d and 10 e) we varied the central grating period and crystal bandwidth, respectively. In both cases we found a tendency to produce smoother pulses, and higher conversion efficiencies for longer central gratings and wider crystal bandwidths. Finally, we found that by taking a crystal bandwidth of $\Delta A = 2.95 \mu\text{m}$, pulses as short as 80 fs that were symmetric and with

almost no phase structure were produced by the model (Fig. 10f). This suggested that optimum compression required conversion of pulse frequencies lying outside the FWHM bandwidth.

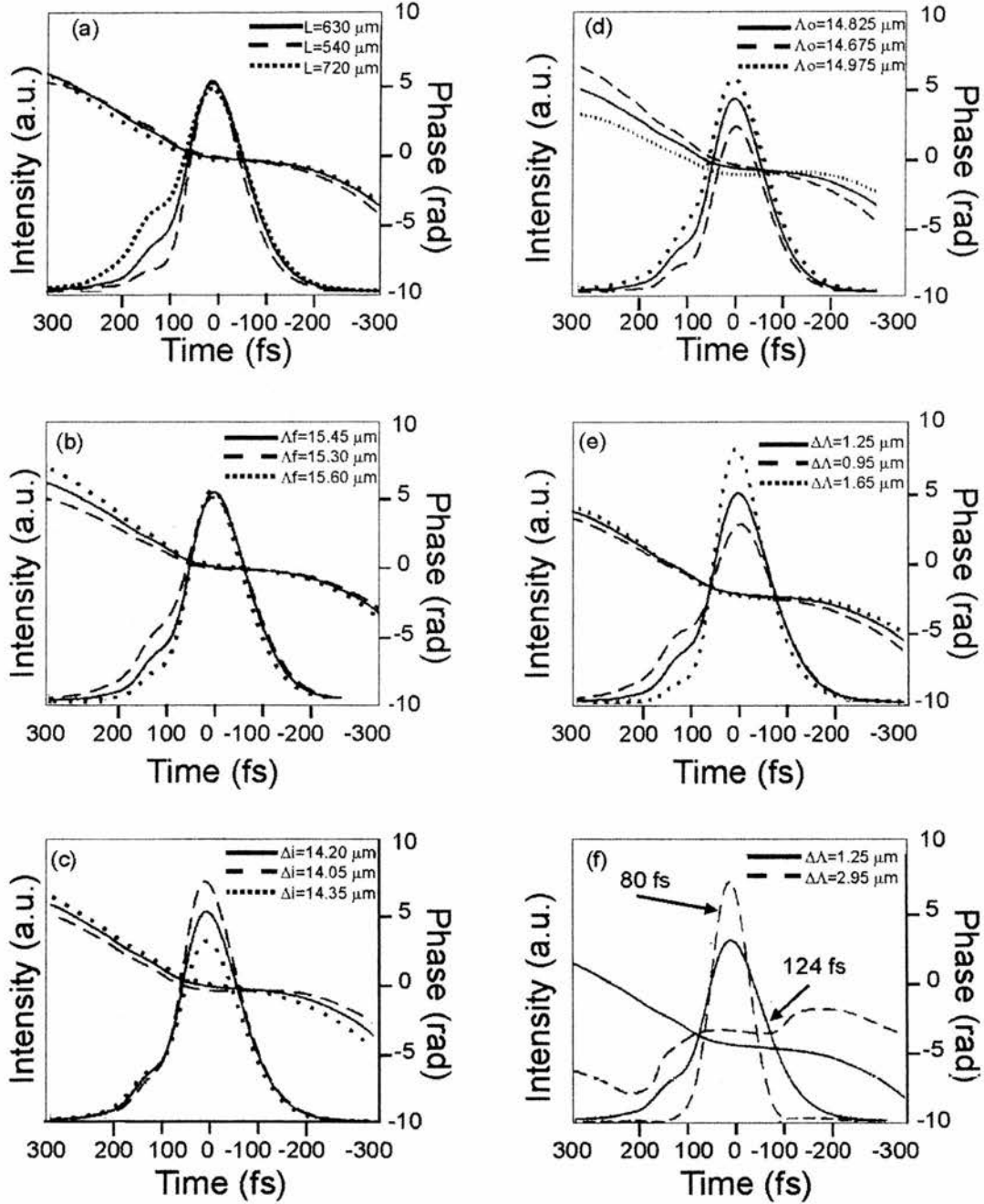


Figure 10. Second harmonic pulses predicted by the model using different QPM parameters: crystal length L , initial (Λ_i), final (Λ_f) and central (Λ_0) grating periods and crystal bandwidth $\Delta\Lambda = \Lambda_f - \Lambda_i$. One parameter was varied each time as follows: a) Λ_f , Λ_i constant and L varies, b) Λ_f , L constant and Λ_f varies, c) Λ_f , L constant and Λ_i varies, d) $\Delta\Lambda$, L constant and Λ_0 varies, e) and f) Λ_0 , L constant and $\Delta\Lambda$ varies. In each case, the results of the model are compared with the experimentally used crystal parameters (solid line): $L = 630 \mu\text{m}$, $\Lambda_i = 14.20 \mu\text{m}$, $\Lambda_f = 15.45 \mu\text{m}$, $\Lambda_0 = 14.835 \mu\text{m}$, $\Delta\Lambda = 1.2 \mu\text{m}$.

Our modelling-based analysis has thus shown that, for a given fundamental pulse, it is possible to optimise the quasi-phase-matching parameters in order to design a chirped-grating in a nonlinear crystal that would produce better pulse compression, pulse shape and phase flatness. This analysis has also proved that in our initial basic calculation of the chirped-grating period for the crystal, described in Section 5.2, we underestimated the chirping and shape of our fundamental pulse. The numerical model is, however, limited by the experimental conditions. The limited frequency-chirp on the input pulses necessitated a short KTP crystal and consequently resulted in a relatively large phase-matching bandwidth seen by each spectral component of the pulse. This meant that second harmonic generation of each frequency occurred not at an exact position in the KTP crystal but instead was delocalised over a significant length of the crystal, thereby compromising pulse compression. As an example we have calculated that for a pulse with a centre wavelength of $1.24 \mu\text{m}$, grating periods varying from $14.65 - 15 \mu\text{m}$ correspond to the $\Delta kl = \pm \pi$ phase matching condition. Frequency doubling of this component alone will therefore occur over more than 25% of the crystal length. Shorter SHG pulses might be expected if the fundamental pulse from the OPO was pre-chirped to a substantially longer duration, thus enabling a physically longer (smaller bandwidth) KTP crystal to be used. The characteristically large chirp present on pulses produced by modelocked, Q-switched or gain-switched diode lasers suggest that these devices may be more suitable sources of input pulses to aperiodically poled doubling crystals. We aim to test this in future work by using as the input chirped 40 ps pulses from a gain-switched InGaAs/GaAs diode laser operating at 980 nm and with a single-mode average output power of 100 mW.¹²

5.1.6 Efficiency calculations

An estimation of the SHG single-pass power conversion efficiency can be made using a Gaussian-wave analysis provided by Boyd and Kleinman.¹³ Expressed in *esu* units the SHG efficiency is given by:

$$\eta = \left(\frac{2}{\pi}\right)^2 \frac{128\pi^2 \omega_1^2 e^{-\alpha l}}{c^3 n_1^2 n_2} P_1 \chi^2 l k_1 h(B, \xi) \quad (5.3)$$

where

$$\chi^2 = \frac{3 \times 10^4}{4\pi} d_{eff} \quad (5.4)$$

and P_i is the power, ω_i is the frequency, λ_i is the wavelength, α is the absorption losses, l is the crystal length, k_i is wave vector, c is the speed of the lighth, n_i is the index of refraction. The subscripts $i=1, 2$, refer to the fundamental and second harmonic wavelengths respectively. The factor $(2/\pi)^2$ represents the reduction in overall second-harmonic generation power because of quasi-phase matching.¹⁴ The function $h(B, \xi)$ (or the Boyd and Kleinman factor) contains all of the dependence of the second harmonic power upon the optimisable parameters such as phase mismatch, focal position and strength of focusing. These parameters are to be optimised by fine adjustments on the crystal position and orientation to maximise P_2 . In this case (QPM), there is no walk-off between fundamental and SHG beams, therefore the term B , that refers to double refraction angle, is equal to zero. Finally, Boyd and Kleinman provide plots of $h(0, \xi)$ that depend on the focussing parameter ξ , which is defined as:

$$\xi = \frac{\lambda}{2\pi w_0^2 n(\lambda)} l \frac{1}{2} \quad (5.5)$$

where w_0 is the radius of the beam waist formed in the crystal. Figure 11 reproduces the dependence on the Boyd and Kleinman factor $h(B, \xi)$ with the focusing parameter of the fundamental beam.

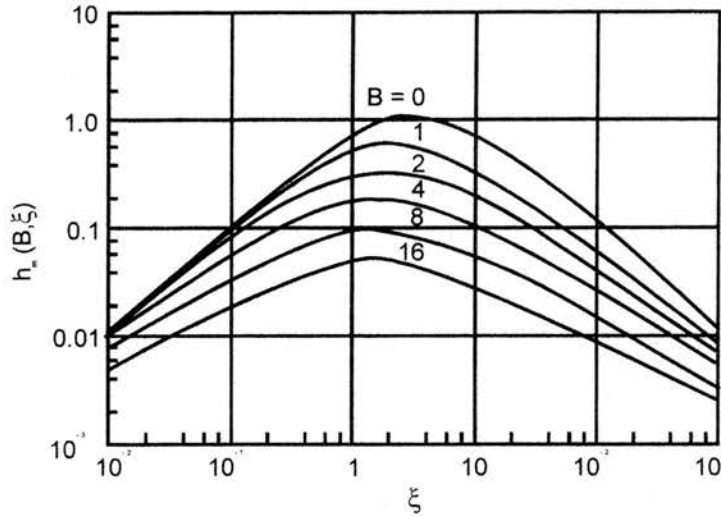


Figure 11. $h(B, \xi)$ as a function of the focusing parameter for several values of B , the double refraction angle.

An ABCD matrix calculation to obtain the spot size of the beam waist inside the crystal was performed. Once the focussing parameter has been calculated, it is possible to use Fig. 11, to obtain a value for the Boyd and Kleinman factor $h(0, \xi)$.

Considering SHG pulses of 125 fs at a repetition rate of $84 \times 10^6 \text{ s}^{-1}$, it is possible to obtain an average output power of 15 mW and 105 mW for the single pass extracavity and intracavity experiments respectively. The corresponding experimental values are 9 mW and 120 mW. Finally, a simple calculation, will lead to the peak power second harmonic efficiency generated by the crystal η . We obtained a value of $\eta = 6.68 \%$ and $\eta = 15.8 \%$ for the extracavity and intracavity experiments respectively. The corresponding experimental efficiencies are 4.5 % and 18.7 %. From the above results we can say that the agreement in the efficiency is reasonably good and that the level of powers obtained are correct.

5.2 Simultaneous SHG and pulse compression in APPLN

Introduction

In the previous section, we have tested simultaneous SHG and pulse compression using an aperiodically-poled crystal of KTP (AP-KTP) with a chirp grating that was calculated to compensate for the chirp of the OPO pulses. In this section, we use an OPO, based on a crystal of periodically-poled RTA, to produce arbitrary positive linearly chirped femtosecond pulses that would be frequency doubled and compressed using 8 different linearly varying grating periods in a crystal of lithium niobate (APPLN). As before, our experimental results will be compared with a complete numerical model that calculates the complex pulse amplitude of the SHG pulses.

5.2.1. The PPRTA-based optical parametric oscillator

The OPO was synchronously pumped with a self-modelocked Ti:sapphire laser operating at the central wavelength of 840 nm and delivering transform-limited pulses of 100 fs at a frequency of 84 MHz and with an average output power of 1.5 W. The experimental set up is shown in Figure 12. The OPO was based on a 2 mm long crystal of periodically-poled RbTiOAsO₄ which had a grating period of $\Lambda = 30 \mu\text{m}$. The crystal domains were poled parallel to the crystallographic c axis in order to access the highest nonlinear coefficient available which has a value of $d_{33} = 15.8 \text{ pm/V}$. The polarisation of the pump, signal and idler wavelengths were all horizontal in the cavity and parallel to the poling direction. Signal pulses centred at $1.25 \mu\text{m}$ were made to oscillate inside the OPO cavity which consisted of two high-

reflector curved ($r = -100$) mirrors and a flat 10 % output coupler. The PPRTA crystal was placed at the focal point of the intracavity signal beam and the cavity contained no dispersion compensation elements.

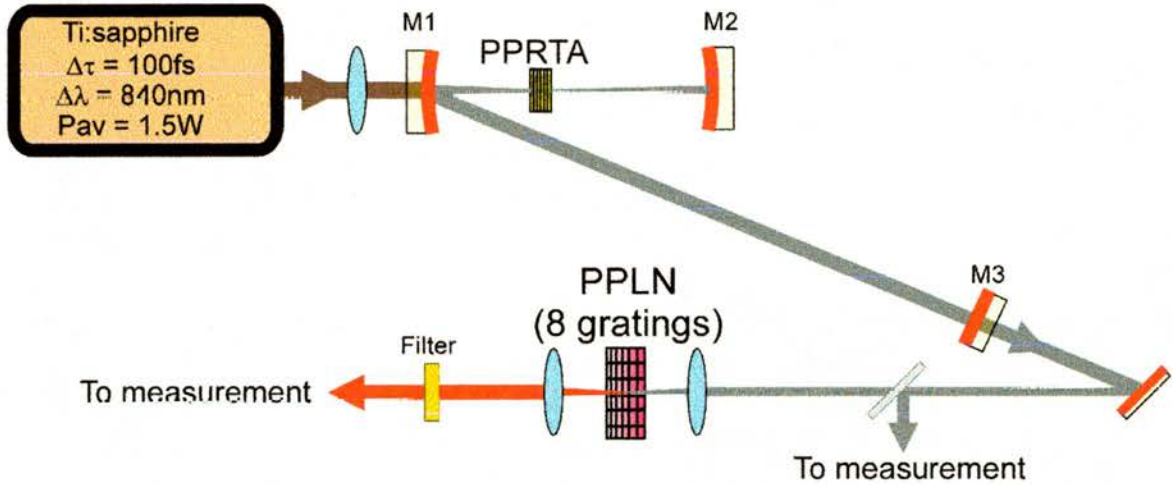


Figure 12. Experimental set up for simultaneous SHG and pulse compression using a crystal of PPLN with 8 different linearly chirped gratings.

Under these conditions, output signal pulses of 280 fs full width half maximum (FWHM) duration were measured with an average output power of 100 mW. Because of the normal dispersion in the PPRTA crystal, signal pulses were expected to be positively chirped and the exact phase profile was determined by SHG-FROG characterisation of the pulses.^{8,9} The retrieved FROG trace and intensity profile and phase of the signal pulses (and calculated spectrum and autocorrelations), together with the experimental FROG trace, and the independently measured spectrum and autocorrelations are shown in Figure 13. The usual ambiguity associated with SHG-FROG ($E(t) = E^*(-t)$) was easily removed because the signal pulses travel in normal dispersive elements. The good agreement between the retrieved and experimental data confirmed the accuracy of our measurements and the FROG retrieval.

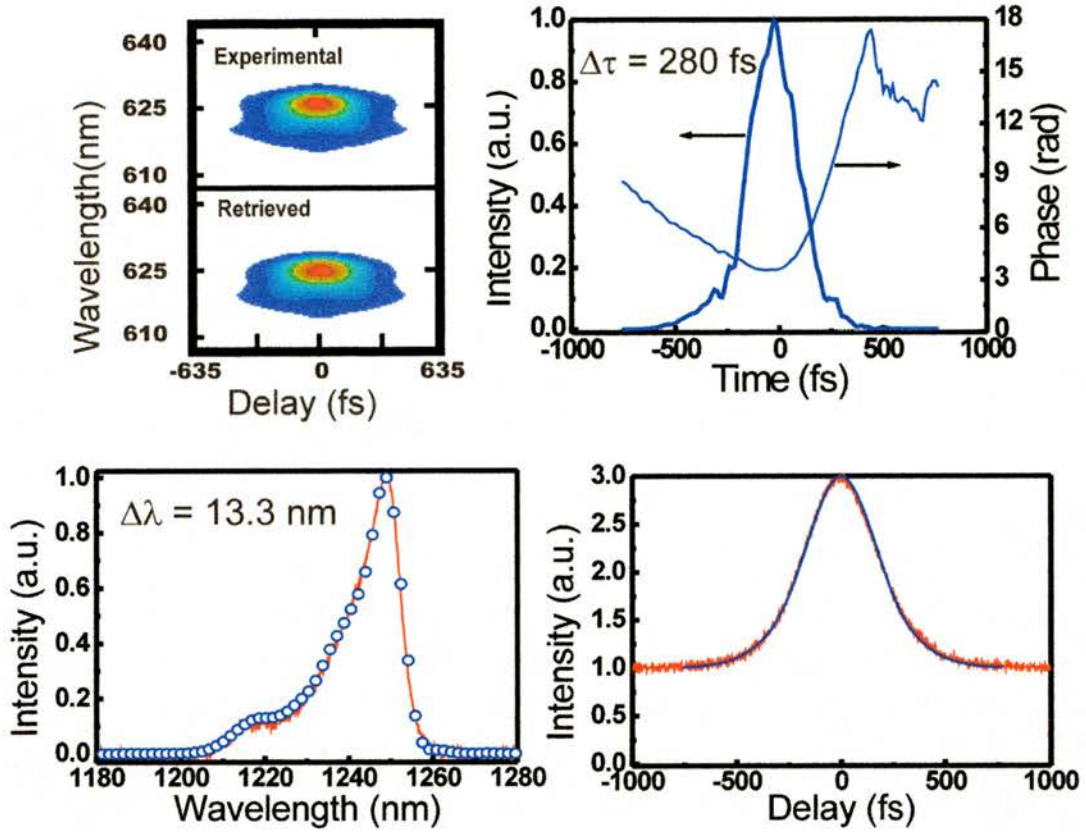


Figure 13. FROG characterisation of the signal output from the PPRTA-based OPO that shows pulse durations of $\Delta\tau = 280$ fs with positive quadratic phase. a) FROG experimental and retrieved FROG traces, b) temporal intensity profile and phase of the retrieved pulses, c) measured (red line) and retrieved (blue dots) spectra of the pulses centred at $1.25 \mu\text{m}$ and with spectral bandwidth of 13.3 nm, d) measured (red line) and retrieved (blue line) intensity autocorrelations.

5.2.2. The aperiodically poled lithium niobate crystal

To study simultaneous SHG and pulse compression, we used a single crystal of lithium niobate (LiNbO_3) with 8 different chirped periodically-poled gratings. The gratings were poled parallel to the z axis to access the largest nonlinear coefficient $d_{33} = 27$ pm/V. The crystal was cut to $700 \mu\text{m}$ long with an active (poled) region of $460 \mu\text{m}$ immersed in between unpoled regions of $200 \mu\text{m}$ and $40 \mu\text{m}$ length, respectively. Each grating had a clear aperture of 1 mm height by 0.5 mm wide and

the gratings into the crystal were separated to each other by gaps of 100 μm of unpoled material. The PPLN crystal was fabricated using the standard electric-field poling technique with photoresist trenches.¹⁶ In the gratings, the initial (Λ_i) and final periods (Λ_f) were different except for grating 1 in which $\Lambda_i = \Lambda_f = \Lambda_0$. The average (or central) grating period [$\Lambda_0 = \Lambda_{av} = (\Lambda_i + \Lambda_f)/2$] was left constant to ensure phasematching was centred at the same wavelength on every grating. We define the chirp of the crystal as

$$\Delta g = \frac{\Lambda_i - \Lambda_f}{\Lambda_0} \quad (5.6)$$

where Λ_i and Λ_f are the periods facing the input and output pulses, respectively. From Equation (5.6) we can define a positive crystal chirp if the longest period of crystal is facing the input pulses, *i.e.*, when $\Delta g > 0$. The crystal is negatively chirped when oriented with the opposite direction ($\Delta g < 0$). The different values for the initial, Λ_i , and final, Λ_f , periods and the percentage of chirping in each of the gratings are listed in Table I.

GRATING NUMBER	Λ_i (μm)	Λ_f (μm)	Δg (%)
G1	10.65	10.65	0
G2	10.9	10.4	4.7
G3	11.0	10.3	6.6
G4	11.1	10.2	8.5
G5	11.2	10.1	10.3
G6	11.3	10.0	12.2
G7	11.5	9.8	16
G8	11.7	9.6	19.7

Table I. Starting and ending periods and total crystal chirp of the different gratings of the PPLN crystal.

5.2.3. The numerical model

As explained previously (section 5.1.4) the retrieved data obtained with the FROG characterisation were used in a numerical model to calculate the complex pulse amplitude of the frequency-doubled pulses after propagation through the aperiodically-poled lithium niobate crystal. The numerical model (an extended version of that explained in section 5.1.4) consisted of the coupled-wave equations for uniform wave planes for second-harmonic generation that are obtained after assuming the slowly varying envelope amplitude (SVEA) approximation:

$$i \frac{\partial A_1(z,t)}{\partial z} + i \cdot k_1' \frac{\partial A_1(z,t)}{\partial t} - \frac{1}{2} k_1'' \frac{\partial^2 A_1(z,t)}{\partial t^2} + \sigma(z) \Gamma_1 A_1^*(z,t) A_2(z,t) \exp(i\Delta k \cdot z) = 0 \quad (5.7)$$

$$i \frac{\partial A_2(z,t)}{\partial z} + i \cdot k_2' \frac{\partial A_2(z,t)}{\partial t} - \frac{1}{2} k_2'' \frac{\partial^2 A_2(z,t)}{\partial t^2} + \sigma(z) \Gamma_2 A_1^2(z,t) \exp(-i\Delta k \cdot z) = 0 \quad (5.8)$$

where $A_i(z,t)$ is the slowly varying complex pulse amplitude, $k_i = \frac{2\pi}{\lambda_{0i}} n(\lambda_{0i})$, and primes indicate derivative with respect to the wavelength. Wave vectors were calculated using the Sellmeier equations published by D. H Jundt.¹⁵ In contrast to our model of section 5.1.4, this model does not make any approximations (such as the non-depletion approximation) and it includes group-velocity mismatch and second-order group velocity dispersion. This allowed for a finer agreement with our experiment. Our model also admits third-order group velocity dispersion and third-order nonlinear effects, but these do not play important role in this experiment. The subscripts $i = 1,2$ refer to fundamental and second-harmonic respectively and the nonlinear terms are given by $\Gamma_1 = 2\omega_{01}^2 d_{33} / k_1 c^2$ and $\Gamma_2 = \omega_{02}^2 d_{33} / k_1 c^2$. The

coefficient $\sigma(z)$ is the sign of the domain polarisations and it changes for each new half period $\lambda/2$.

We begin by using the complex pulse amplitude of the fundamental pulses, determined by the SHG-FROG characterisation of the output pulses from the OPO, and then the equations (5.7) and (5.8) are solved with the split step Fourier method using 2048 points with temporal and spatial steps of $\delta t = 3$ fs and $\delta z = 0.2$ μm , respectively. The crystal has a total length of 700 μm which was divided into three regions. Incident light travels first through a passive region (unpoled) of length $L_1 = 40$ μm , then the active (poled) region of a length of $L = 460$ μm and finally a second passive region of $L_2 = 200$ μm . The lengths of the three regions were inferred from the mask design and measurements made using an optical microscope. For the purposes of the model, the active region was divided into n periods and the length of each subsequent period increased linearly by Δx .

5.2.4. Experimental results and discussion

The signal output pulses from the PPRTA-OPO were focused into the APPLN crystal using an 8.5 mm focal length lens after passing through an IR-pass optical filter (RG-1000). The crystal was placed inside an oven maintained at 110°C to avoid any photorefractive damage. A 10 mm focal length lens was used after the APPLN crystal to collimate the second-harmonic output beam. Finally, we used an OPO high-reflector mirror after the collimating lens to block any residual fundamental light. The experimental set up is shown in Figure 12. To characterise

the SHG pulses, we performed SHG autocorrelation and the spectra of the SHG pulses were recorded using a scanning monochromator with a resolution of 0.3 nm.

We studied the effect of pulse duration and output powers of the SHG pulse by using the crystal with the $\Delta g > 0$ and $\Delta g < 0$ orientations. In the two cases, we found that an optimum conversion efficiency was obtained when the pulses were propagated through a grating with small or zero ($\Delta g \approx 0$) chirp and an average SHG power of ~ 10 mW was measured. Figure 14 shows the SHG average output powers obtained when using the different chirped gratings. As expected, for $\Delta g > 0$, the increased chirp of the gratings has the effect of reducing the effective nonlinear coefficient and therefore reducing the conversion efficiency. However, for $\Delta g < 0$, the chirp of fundamental pulses were better matched to the crystal chirp parameters for gratings G2 and G3, and the average SHG power was maintained. A similar observation has recently been reported using a diode laser-pumped aperiodically-poled crystal.¹⁷

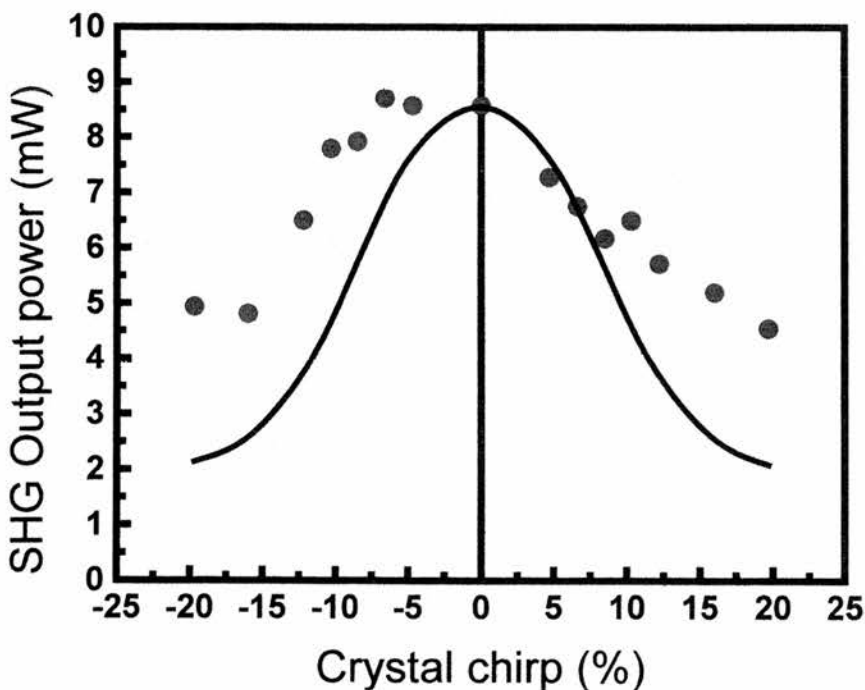


Figure 14. Measured (symbols) and calculated (line) average output power of the SHG pulses generated in each of the crystal gratings.

To compress the fundamental pulses delivered by the PPRTA-OPO, the crystal was oriented for positive crystal chirp ($\Delta g > 0$). Using the grating $G2$ ($\Delta g = 4.7\%$) a minimum in the SHG pulse duration was measured. Here transformed limited pulses with a duration of $\Delta\tau = 140$ fs and a pulse duration-bandwidth product of $\Delta\nu\Delta t = 0.44$ were recorded. Although pulse compression was also obtained for gratings $G3$ and $G4$, compression was not optimum in these gratings. The crystal chirp in the remaining gratings was too strong to adequately compress the fundamental pulses. This will be explained in detail below. Figure 15 (16) shows the measured interferometric [15a (16a)] and intensity [15b (16b)] autocorrelations and the measured spectra [15c (16c)] for the frequency doubled pulses obtained in each one of the crystal gratings when the crystal was oriented for $\Delta g > 0$ ($\Delta g < 0$).

It is interesting to note that for corresponding crystal gratings the spectra of the pulses obtained for chirp of $+\Delta g$ (Figure 15c) are very similar to the spectra obtained for a chirp of $-\Delta g$ (Figure 16c). The small discrepancies between these measurements are attributed to instabilities (noise) in the OPO. This means that for each chirped grating, the spectra of the SHG pulses does not depend on the orientation of the grating. This confirms that any compression or expansion mechanism of the SHG pulses are due solely to the chirp of the gratings and no other mechanisms such as self-phase modulation or spectral clipping are acting on them.

Figure 17 (symbols) illustrates the different measured values of the pulse durations (FWHM inferred from intensity autocorrelations) of the SHG pulses for positive and negative chirped gratings. Also in Figure 17 we show the calculated intensity autocorrelations for the pulse obtained with the numerical model considering two different situations. The unpoled regions L_1 and L_2 of the crystal and

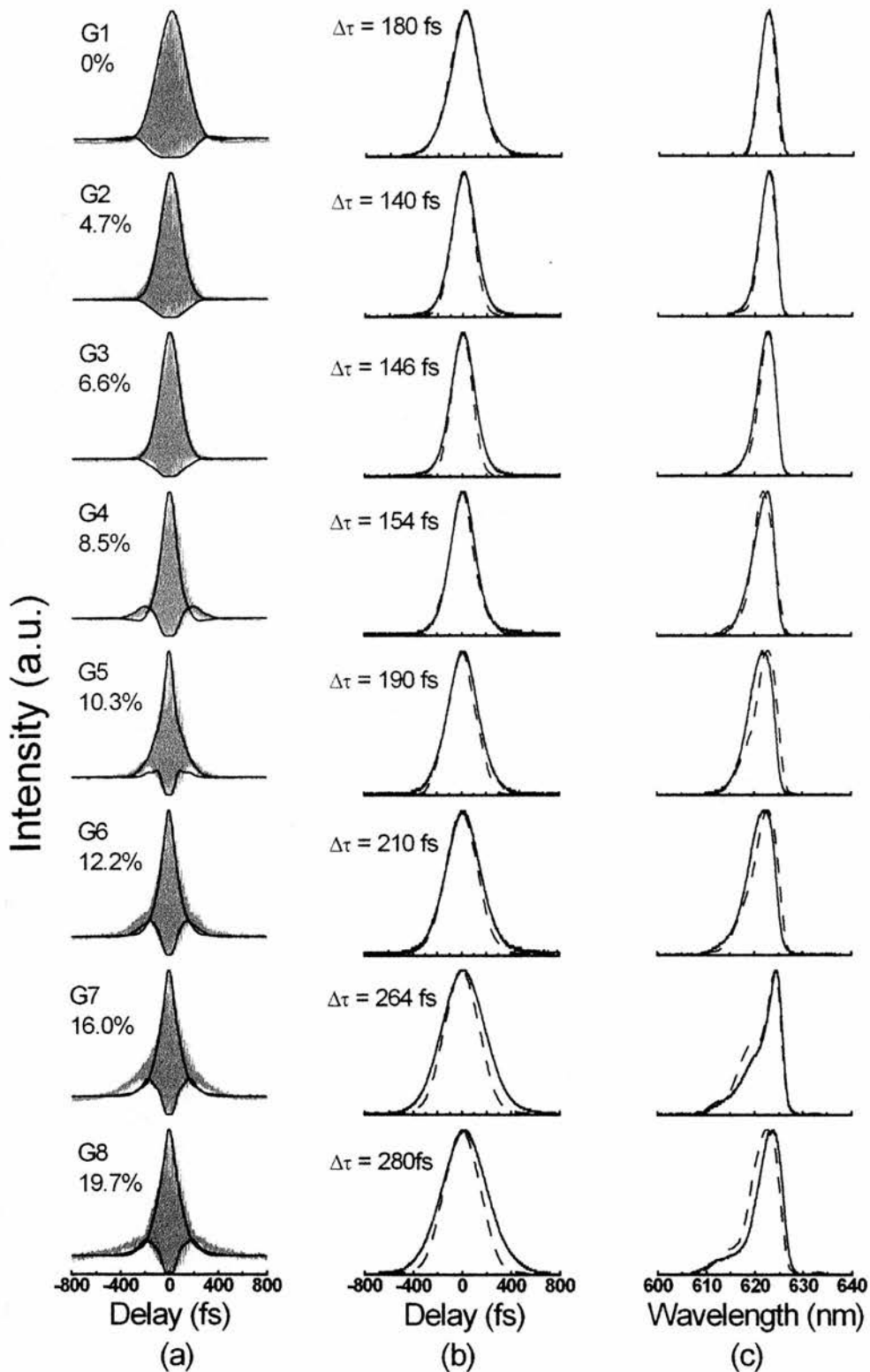


Figure 15. a) Measured (gray) and calculated (black line) interferometric autocorrelation. b) and c) Measured (solid line) and calculated (dashed line) intensity autocorrelations and spectra, respectively. The autocorrelations and spectra shown correspond to each one of the crystal gratings and when $\Delta g \geq 0$.

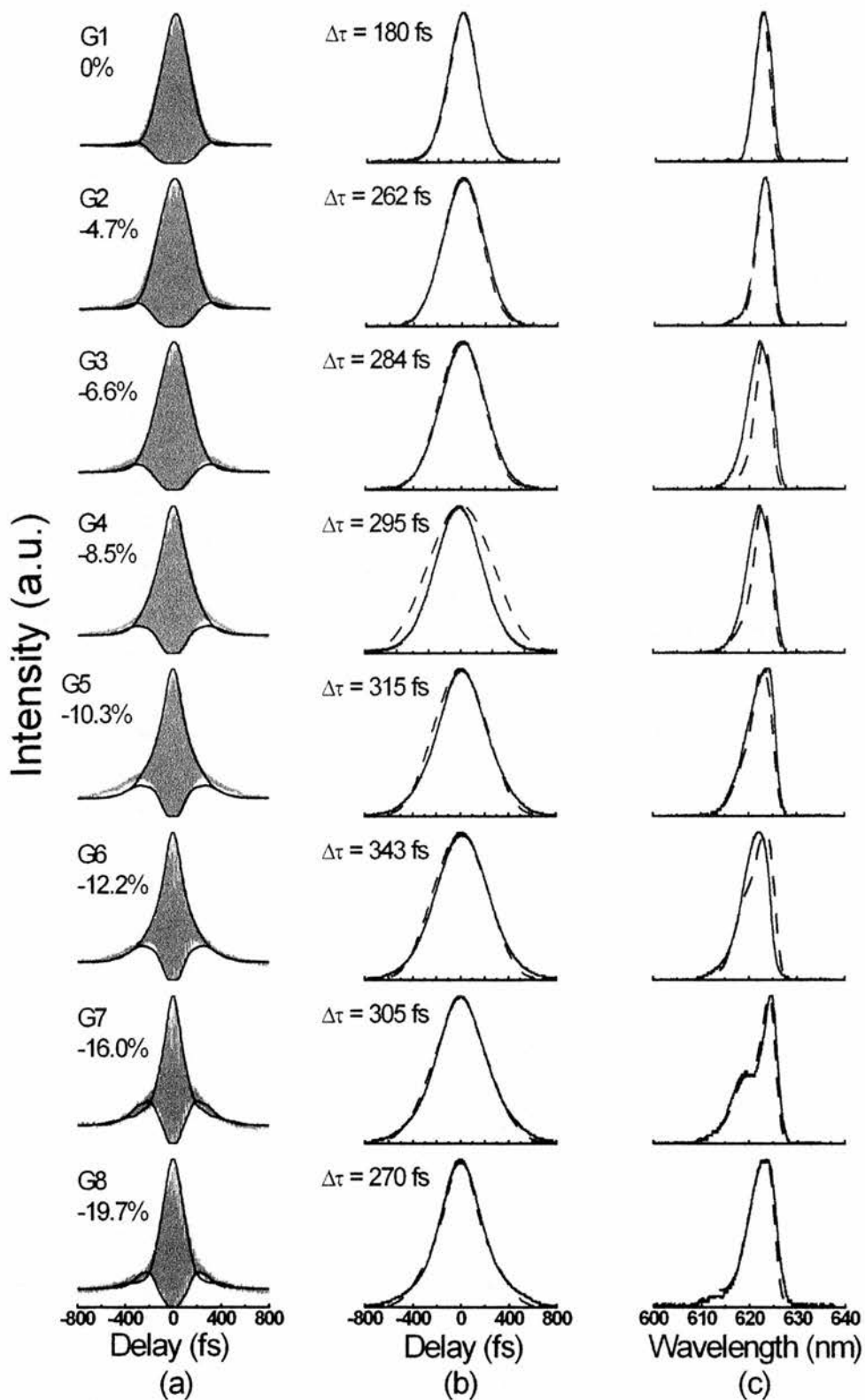


Figure 16. a) Measured (gray) and calculated (black line) interferometric autocorrelation. b), c) measured (solid line) and calculated (dashed line) intensity autocorrelations and spectra, respectively. The autocorrelations and spectra shown correspond to each one of the crystal gratings and when $\Delta g \leq 0$

the dispersion caused by the collimation optics was not considered in the first situation (light blue) but they were included in the second (dark blue). The inclusion of the unpoled regions L_1 and L_2 adds extra dispersion to the pump pulse increasing its chirp. As a consequence, the grating where the minimum compression was obtained is shifted from $G5$ to $G3$, showing a better agreement with experiments in which optimum compression is obtained in $G2$. The collimation optics includes the collimating lens and the OPO HR-mirror (6.5 mm of BK7+coating). This extra dispersion was calculated numerically to be some 1500 fs^2 by matching the obtained numerical SHG pulse duration to the experimental result when the periodically poled grating $G1$ is used. This extra dispersion added to the SHG frequency is equivalent to propagating the pulse through 3 mm of LiNbO_3 .

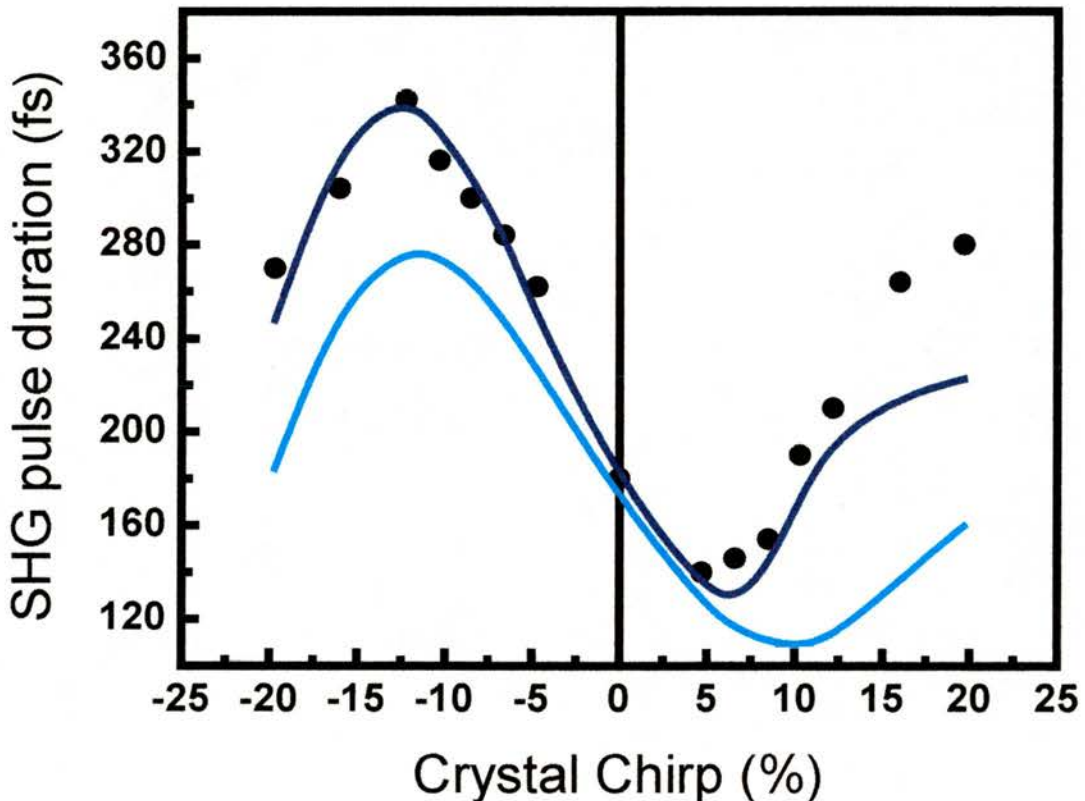


Figure 17. Measured (symbols) pulse duration inferred from SHG intensity autocorrelations of the pulses obtained for the different crystal gratings. Calculated SHG intensity autocorrelations directly after the crystal (light blue line) and assuming a dispersion from collimation optics of 1500 fs^2 (dark blue line).

The complete set of pulses calculated using our numerical model in the second situation (*i.e.*, including the unpoled regions and the dispersion of the collimation optics) was compared with our experimental results and the numerical results are shown in Figure 15a and 16a as solid lines and as dashed lines in Figures 15b,c and 16b,c. The good agreement between the numerical model and the experimental results confirms that the model is accurate and reliable. The calculated profiles of the generated frequency-doubled pulses for the different chirped gratings in the crystals are presented in Figure 18. It is interesting to note in Figure 6 that, for $\Delta g < 0$, the duration of the pulses increase with the crystal chirp up to a limit ($\Delta g = -12.2\%$) where the SHG pulses have maximum duration. After this point, the pulse duration starts to decrease (gratings G7 and G8). Our numerical model has predicted a similar behaviour of periodical “recompression” after the pulses have acquired a local maximum duration in both cases, when $\Delta g < 0$ and $\Delta g > 0$. In this last case the first local maximum recompression occurs when $\Delta g = 23\%$. We can see, using our numerical model, that the oscillatory behaviour on the pulse duration as $|\Delta g|$ increases is due to periodical power conversion between the two waves. This appears at the end of the periodically poled region of the crystal when large chirped gratings are used and, in our case ($\Delta g < 0$), the local period Λ_l is larger than $11 \mu\text{m}$. Back-conversion is maximum at $\Lambda_l = 11.3 \mu\text{m}$, *i.e.*, at the end of the grating G6, and mainly affects to the intensity peak of the pulse, obtaining a pulse with a flat top intensity (Figure 18) and resulting in the longest pulse in our experiment measurements. However, when larger chirped gratings are used, a fraction of the back-converted intensity is reinjected to the peak of the SHG pulse. The reinjection is maximum at the end of the grating G8 when $\Lambda_l = 11.7 \mu\text{m}$ and consistently, the duration obtained

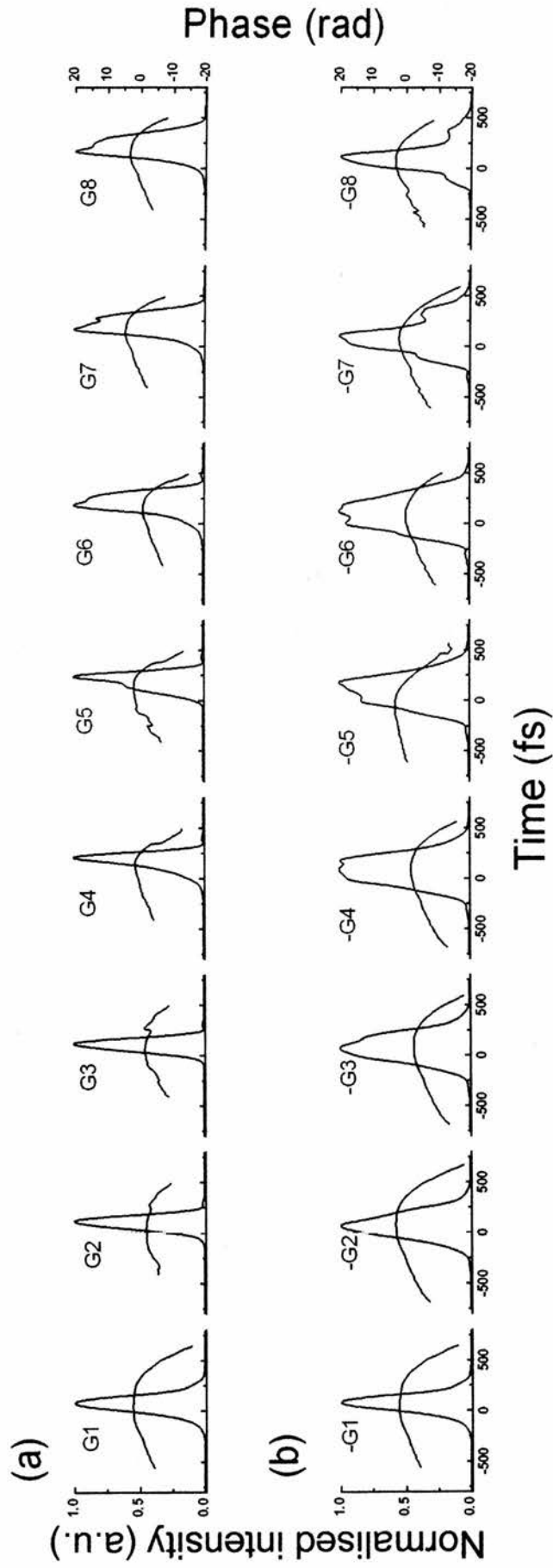


Figure 18. Calculated intensity profiles and phase of the SHG pulses. a) $\Delta g \geq 0$, b) $\Delta g \leq 0$

from the intensity autocorrelation shows a local minimum duration. This effect of oscillatory intensity conversion is also evident as a consequent reduction of the conversion efficiency (see Figure 14).

5.3 Conclusions

In the first part of the chapter, where the use of an aperiodically-poled nonlinear crystal of KTP is described, I have presented simultaneous pulse compression and SHG from a RTA-based OPO using two configurations, extracavity and intracavity. For the extracavity case, a reduction in chirp factor from six to two (assuming $\text{sech}^2(t)$ intensity profile) and SHG pulse durations of 120 fs has been achieved. For the intracavity case, nearly transform-limited pulses at 625 nm with average output power up to 120 mW (18.7% peak power efficiency) has been obtained in a single beam. The input 290 fs pulses with quadratic positive temporal phase were up-converted and compressed to 120 fs pulses with nearly-constant temporal phase across the centre of the pulse. These results were confirmed by a numerical model using the FROG measurements of the input pulses. The numerical model was used to calculate an optimised chirp grating for a crystal that would generate transform-limited pulses for our initial fundamental input pulse.

In the second part of the chapter, I have investigated simultaneous SHG and femtosecond pulse compression of an arbitrary pulse in a crystal of APPLN. It was found that a chirped grating, $\Delta g = 4.7\%$, resulted in optimum pulse compression for our fundamental pulses. Here, fundamental pulses of 280 fs duration with positive quadratic phase were frequency doubled and compressed to nearly transformed-limited pulses of 140 fs and with a pulse duration-bandwidth product of

$\Delta\nu\Delta\tau = 0.44$. It was also found that a reversal on the sign of a crystal grating did not substantially modify the pulse spectra. This confirms that any compression or expansion mechanisms are due only to a change in the phase caused by the aperiodicity of the grating, in agreement with the observation made in the first part of the chapter (section 5.1.5). We have shown both experimentally and theoretically that large (absolute) values for the crystal chirp may result in recompression of the SHG pulses due to periodical power conversion between the interacting waves. All our experimental results are in good agreement with a more complete numerical model based on FROG measurements of the input pulses. An extended version of our numerical model will be used as a basis to study idler pulse compression from an APPLN-based optical parametric oscillator.¹⁸

5.4 References

1. E. Sidick, A. Knoesen, A. Dienes, "Ultrashort-pulse second-harmonic generation in quasi-phase-matched dispersive media," *Opt. Lett.*, **19**, 266 – 268 (1994).
2. M. A. Arbore, A. Galvanauskas, D. Harter, M. H. Chou, M. M. Fejer. "Compression of ultrashort pulses using second-harmonic generation in aperiodically poled lithium niobate," Postdeadline paper CPD6-2 Tech. Digest of *Conference on Lasers and Electro-Optics*, **6**, (OSA, Baltimore, 1997).
3. M. A. Arbore, A. Galvanauskas, D. Harter, M. H. Chou, M. M. Fejer, "Engineerable compression of ultrashort pulses by use of second-harmonic generation in chirped-period-poled lithium niobate," *Opt. Lett.*, **22**, 1341 – 1343 (1997).
4. D. T. Reid, C. McGowan, W. Sleat, M. Ebrahimzadeh, W. Sibbett, "Compact, efficient 344-MHz repetition-rate femtosecond optical parametric oscillator," *Opt. Lett.*, **22**, 525 – 527 (1997).
5. D. T. Reid, M. Padgett, C. McGowan, W. Sleat, M. Ebrahimzadeh, W. Sibbett, "Light-emitting diodes as measurement devices for femtosecond laser pulses," *Opt. Lett.*, **22**, 233 – 235 (1997).
6. H. Karlsson, F. Laurell, P. Henriksson and G. Arvidsson. "Electric field poling of flux grown KTiOPO_4 ," *Appl. Phys. Lett.*, **71**, 3474 – 3476 (1997).
7. D. T. Reid, P. Loza-Alvarez, Ebrahimzadeh, E. U. Rafailov, P. Faller, D. J. L. Birkin, W. Sibbett, H. Karlsson, F. Laurell, "Femtosecond pulse compression by second-harmonic generation in aperiodically-poled KTP," In *Conference on Lasers and Electro-Optics*, OSA, Technical Digest, (Optical Society of America, Washington DC, 1998) Paper CME3.
8. K. W. Delong, R. Trebino, J. Hunter, W. E. White, "Frequency-resolved optical gating with the use of 2nd-harmonic generation," *J. Opt. Soc. Am. B*, **11**, 2206 – 2215 (1995).
9. D. T. Reid, C. McGowan, W. Sleat, M. Ebrahimzadeh, W. Sibbett, "A real-time FROG trace acquisition system for non-amplified femtosecond oscillators," *Eng. and Lab. Notes*, 2-page supplement to *Optics and Photonics News*, **8** (May 1997).
10. M. A. Arbore, O. Marco, M. M. Fejer, "Pulse compression during second-harmonic generation in aperiodic quasi-phase-matching gratings," *Opt. Lett.*, **22**, 865 – 867 (1997).
11. W. H. Press, S. A. Teukolosky, W. T. Vetterling, B. P. Flannery. "Numerical Recipes in Fortran," Cambridge University Press, 2nd edition, Chapter 19, 818 – 880 (1994).
12. E. U. Rafailov, D. J. L. Birkin, E. A. Avrutin, W. E. Sleat, W. Sibbett, "High average power short-pulse generation from single-mode InGaAs/GaAs laser diodes," *IEE Proceedings Optoelectronics*, **146**, 51 – 54 (1999).
13. G. D. Boyd and D. A. Kleinman, "Parametric interaction of focused Gaussian light beams," *J. Appl. Phys.*, **39**, 3597 – 3639 (1968).
14. M. A. Mortazavi, G. Khanarian, "Quasi-phase matched frequency doubling in bulk polymeric structures," *Opt. Lett.*, **17**, 1290 – 1292 (1994).
15. D. H. Jundt, "Temperature-dependent Sellmeier equation for the index of refraction, $n(e)$, in congruent lithium niobate," *Opt. Lett.*, **22**, 1553 – 1555 (1997).
16. L. E. Myers, R. C. Eckardt, M. M. Fejer, R. L. Byer, W. R. Bosenberg, J. W. Pierce, J., "Quasi-phase-matched optical parametric oscillators in bulk periodically poled LiNbO_3 ," *Opt. Soc. Am. B* **12**, 2102 – 2116 (1995).

17. D. J. L. Birkin, E. U. Rafailov, G. S. Sokolovskii, D. T. Reid, W. Sibbett, G. W. Ross, P. G. R. Smith, D. C. Hanna, "3.25-mW blue light by direct frequency-doubling of a 980-nm diode laser using an aperiodically poled LiNbO₃ crystal". In *Conference on Lasers and Electro-Optics*, OSA Technical Digest (Optical Society of America, Washington DC, 2000), paper CThH3.
18. T. Beddard, M. Ebrahimzadeh, D. T. Reid, W. Sibbett, "Five-optical cycle pulse generation in the mid-infrared from an optical parametric oscillator based on aperiodically poled lithium niobate," *Accepted to Opt. Lett.*, **25**, No14 (2000).

CHAPTER 6

APPLICATIONS: COHERENT CONTROL

The frequency and intensity properties of lasers have long been used to characterise and, where appropriate, to modify the properties of matter. However, the most characteristic property of laser light, namely the well-defined phase, is only rarely regarded as a control parameter. The idea of controlling optical, physical and chemical processes in matter using the coherence properties of light has captured the interest of many scientists. This is analogous to the interference of the two light beams in Young's double-slit experiment (see figure 1(a)), but it is distinctive in that one has an effective "matter interferometer", where in the case of a semiconductor it is the electrons that are being controlled.

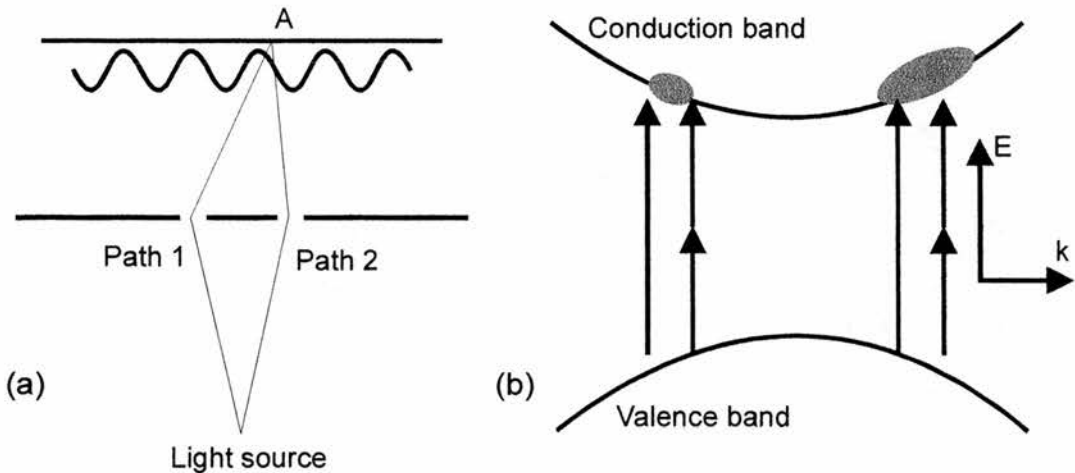


Figure 1. (a) Interference effect in a Young's double-slit experiment. (b) Conceptual diagram of interference between single and two-photon processes connecting the same valence and conducting bands in a direct bandgap semiconductor leading to asymmetrical distributions of electrons (hole distribution is not shown).

The possibility of employing laser phase was first proposed by Manykin and Alfanas'ev¹ who investigated the absorption control of an atomic medium. They considered the interference of quantum mechanical transition amplitudes for two pathways coupling the same initial and final state of an atom. In particular they suggested that simultaneous single-photon and three-photon absorption could control state populations and hence the transmission of the medium. Although ideas relating to quantum interference control, or coherent control (CC) lay virtually dormant for many years, they have been recently revived and demonstrated in a variety of atomic and molecular systems. Two essential developments revitalised the field. First, the development of practical and appropriate ultrafast lasers. Second, the introduction of technical control concepts has put the required theoretical framework on a rigorous foundation². In this section the several possibilities of CC via laser induced quantum interference will be introduced. We start with a brief review of this approach, and providing examples of the capabilities of CC in several research areas. Recent references that provide relevant advances in the field will be presented. In the next section, we will focus our attention on the use of CC to generate electric current in semiconductors. Here, relevant concepts will be summarised, the key theoretical results will be reviewed and the main experimental achievements will be presented.

6.1 Some applications using coherent control

Coherent control of excitons

P. Heberle *et al.*,³⁻⁵ have demonstrated femtosecond coherent control of excitons in quantum wells with phase-locked pairs of 100 fs infrared pulses. Copolarized pump pulses allowed coherent control of exciton density and coherent destruction of

excitons within a few hundred femtoseconds of their creation. This coherent carrier destruction generates ultrafast exciton dynamics that are not limited by the linewidth of the optical transition. This technique avoided speed penalties in devices associated with long-lived carrier populations. The authors also investigated coherent control of spin dynamics and conversion of unpolarised excitons (see also X. Marie *et al*⁶ and P. Le June *et al*⁷) into spin polarised ones, using cross-polarised pump pulses. X. D. Hu *et al*⁸, have investigated theoretically CC of optical absorption and emission (optical gain) in semiconductor double quantum wells by the use of two coherent light sources. Specifically, they showed that electron-hole pair (exciton) formation in any symmetric double well can be controlled by intensity and phase of a dc microwave field. N Garro *et al*⁹ have investigated the manipulation of the phase and amplitude of the state of a three-level exciton system by excitation with pairs of phase-locked optical pulses. They demonstrated coherent control over the phase of quantum beating between the light- and heavy-hole excitons. They showed that the amplitude of the coherent manipulation must diminish as a function of time delay between the components of the pulse pair in a way which takes into account both the dephasing of the excitons and their unphasing which arises from inhomogeneous broadening.

Coherent control of intersubband transitions in semiconductors

P. I. Tamborenea *et al*¹⁰ have performed numerical calculations to study CC of multisubband wavepackets by means of pairs of subpicosecond terahertz laser pulses in quantum well structures. They analyzed four quantum well structures and demonstrated numerically the possibility of measurable CC of the population of the excited electrons. S. M. Sadeghi *et al*¹¹, studied quantum interference and nonlinear

optical processes in the conduction band of an n-doped quantum well driven by one or two infrared fields. The fields couple a broad upper subband to a lower energy subband and the ground subband, forming a Λ configuration. By including the effect of electron-electron scattering and dynamic screening, they showed that this configuration could lead to coherent control of the intersubband transitions, such as coherent population trapping.

Coherent control of terahertz pulse generation

P. C. M. Planken, *et al*¹², used two phase locked pulses to enhance, weaken, and also phase shift terahertz (THz) radiation emitted by optically excited quantum beats in a coupled quantum well. D. S. Citrin *et al*¹³, have shown that shaped optical pulses may be used to control coherently terahertz pulse generation from a planar semiconductor microcavity biased by a dc electric field. The terahertz signal was due to optical rectification arising from the time-dependent polarization associated with mode oscillations.

Coherent control of high-speed all-optical switching

D. S. Citrin, *et al*,^{14,15} theoretically investigated coherent control of excitons in quantum wells at high repetition rates to determine the practical constraints for application in high-bit-rate optical switching. They found that there exists a trade off between optical pathlength (number of quantum wells) and excitation density that severely limits the applicability of this mechanism for implementation in 100-Gb/s optical systems. More recently,¹⁶ Citrin discussed the possibility of the use of ultrafast pulsed THz radiation to coherently control normal-mode oscillations in microcavities.

Coherent control of electrons

N. B. Baranova *et al*¹⁷ predicted, calculated and observed for the first time the polar asymmetry of the electron released by the interference of two-photon absorption at ω and one-photon absorption at frequency 2ω . The effect was observed experimentally for the simultaneous illumination of a photomultiplier by picosecond Nd-laser pulses and its second harmonic. A. D. Bandrauk *et al*,¹⁸ used coherent control to examine a molecular three-level system and demonstrated phase control of electron transfer in molecules. With this technique, the coherent superposition of electronic states was achieved. V. B. Deyirmenjian *et al*¹⁹ demonstrated that if a pump laser pulse produces a superposition of two image states, the intensity and in certain cases the direction of electrons photoemitted from this wave packet can be coherently controlled via a probe pulse. R. van Leeuwen *et al*²⁰ altered the energy and angular distribution and time of ejection of electrons of calcium Rydberg atoms by changing the relative phase and delay between the two laser pulses.

Coherent control of atomic transitions

C. Chen *et al*,²¹ investigated a two-color coherent-control process at high densities of the absorbing medium. They irradiated a vapour of atomic mercury with a coherent field, where one component was nearly resonant with the three-photon $6s\ S-1(0) \rightarrow 6p\ P-1(1)$ transition, and a second component was the third harmonic of the first. They observed interference between the two excitation pathways for this transition. V. Blanchet *et al*,²² have shown theoretically and experimentally, using a sequence of pairs of identical pulses, that temporal coherent control can produce optical and quantum interferences in the $(6s-7d)$ two-photon transition of Cs and that can be clearly distinguished.

Coherent control of atomic ionisation

T. Nakajima *et al.*,²³ presented theory and calculations for phase-dependent laser-atom interactions involving autoionizing states in Xe. They demonstrated that the simultaneous one- and three-photon excitation of one or two neighbouring autoionizing states can exhibit profound changes of the line shape, as the relative phase of the two fields is varied from 0 to π . Similarly, R. Taieb *et al.*,²⁴ presented a theoretical study of two-colour coherent control of atomic multiphoton ionization with high-order harmonics. The calculation was performed by numerical integration of the time-dependent Schrodinger equation for a (three-dimensional) hydrogen atom. N. E. Karapanagioti, *et al.*,²⁵ achieved coherent control of the ionization of Xe and Kr by employing a four-photon resonant, five-photon ionization scheme. The control occurred through the simultaneous irradiation of atoms by a laser field and its third harmonic as the relative phase of the two fields was varied. More recently, N. L. Manakov *et al.*,²⁶ demonstrated using alkali metal atoms, that a weak, static electric field enables nearly complete coherent phase control of the total ionization yield in a two-colour ionization process using fundamental and second-harmonic radiation. In their experiment the static electric field induced a dipole-forbidden resonance in the two-photon transition amplitude so that the final photoelectron states were identical to those in a single-photon transition.

Coherent control of Phonons

T. Dekorsy *et al.*,²⁷ have demonstrated experimentally the possibility of coherent control of the lattice dynamics in solid-state materials. The authors generated coherent longitudinal optical phonons via ultrafast screening of GaAs surface-space-charge fields by free carriers excited with femtosecond laser pulses. The phonons

were observed through anisotropic changes in the refractive index. By carefully adjusting the relative phase of the pulses, the authors were able to accurately control the amplitude of the coherent vibrations from resonant enhancement to total extinction. More recently M. U. Wehner *et al.*,²⁸ used sub-femtosecond timescale coherent control processes to suppress or amplify phonon oscillations in GaAs. With this technique the authors set out to explore the possibility of reversing or enhancing scattering processes (uncompleted due to the time scale used).

X. D. Hu *et al.*,²⁹ have shown an effect that may be interpreted as quantum interference between a single-phonon emission process and a single-phonon-two-photon process. Quantum interference between electron-lattice and electron-light interaction that allows coherent control of optical phonon emission rates in semiconductors was theoretically demonstrated. In their analysis, they have shown that the longitudinal-optical-phonon-mediated return rate of electrons into the lowest electron subband of a GaAs/AlGaAs heterostructure can be controlled by the phase of a microwave field which resonantly couples two upper electronic subbands of the heterostructure. For the investigated structure, they predicted a variation of the relaxation rate by a factor of 2 between 400 and 900 fs.

Coherent control of Molecular phase and vibrational dynamics

G. K. Paramonov,³⁰ used coherent superposition of infrared laser pulses for efficient control of the population dynamics in the presence of competing multiphoton transitions. This was demonstrated for the state-selective vibrational excitation of the OH bond on a femtosecond timescale. V. V. Lozovoy *et al.*³¹, have reported qualitative analysis of experimental data which shows that the phase modulation of the chirped femtosecond pump light pulse affects the degree of localisation and the

decay of the vibrational wave packet in the electronic B-state of iodine. This result suggested the possibility of controlling intramolecular dynamics by varying the phase characteristics of the pump and probe pulses. S. Lee³² has carried out analysis for molecular phase in one- and three-photon ($\Omega(1), \Omega(3)$) coherent control scheme. It was shown that the imaginary part of the three-photon transition operator, which is due to the contribution of the intermediate continua, can give different phase factors for the one- and three-photon transition amplitudes, yielding very important effects of molecular phase in ($\Omega(1), \Omega(3)$) coherent control. He also showed that the interactions between the final continuum states can result in nonzero molecular phase, when the intermediate states are discrete.

Coherent control of spontaneous emission

T. Quang *et al.*,³³ have demonstrated coherent control of spontaneous emission from a three-level atom with one resonant frequency near the edge of a photonic band gap. As a result of quantum interference and photon localization, spontaneous emission can be totally suppressed or strongly enhanced depending on the relative phase between the control and pump laser fields.

Coherent control of chemical reactions

M. Shapiro *et al.*,³⁴ have used coherent control to provide a quantum-interference based method for controlling chemical reactions such as branching photodissociation reactions (in IBr, DOH and Na-2) and symmetry breaking (in H₂O). B. N. Jagatap *et al.*,³⁵ studied the control of an excited state molecular population, using two lasers and competitions involving different laser excitation pathways and different excitation mechanisms of the same photonicity. One of the mechanisms required a

non-zero permanent dipole difference between the initial and final states, the other required a virtual state. They demonstrated control of the final state population via changes in the relative phase, or in the angle between the polarisation vectors of the two lasers.

6.2 Coherent control of electrical currents in semiconductors

Controlling the magnitude and polarity of the current flowing through a semiconductor is essential to modern electronic technology. Normally this is achieved by applying a bias voltage for a given concentration and spatial distribution of charges carriers. The role of this voltage is to give thermodynamic preference to the flow of photoelectrons in one direction. One can optically control the magnitude of the current via optical pumping, but in most applications, the direction of the electron photoemission can not be selected optically because, in symmetric structures, positive and negative propagating electronic waves are excited equally by the electromagnetic field. However, in recent years, a variety of schemes have been suggested for generating and controlling photocurrents in semiconductors by exploiting the coherence properties of the illuminating source. In a semiconductor it is possible to excite an electron of the valence band to the conduction band by two different mechanisms, direct single-photon absorption and two-photon absorption. When either one of these mechanisms occurs in a semiconductor, the electrons generated in the conduction band have the same probability of being generated with momentum \mathbf{k} or momentum $-\mathbf{k}$. If the two mechanisms occur at the same time and the phases of the optical exciting fields are related, it is possible to favour the

generation of electrons having a particular momentum direction. This imbalance in the momentum can be used to generate an electrical current on a transmission line. In this section, we will review the advances that have been made towards achieving this goal.

6.2.1 Coherent control of photocurrents. Review

The idea of exploiting CC to induce photocurrents in semiconductors was first proposed by G. Kurizki *et al*³⁶. In this work, the authors suggested preparing a coherent superposition of two donor $|s\rangle$ and $|p\rangle$ states and, from there, to excite a free state using two laser beams tuned at the energy separation between the levels. They predicted that the direction of the photocurrent would depend directly on the relative phase between the two beams without any need for applying an external voltage. The first experimental demonstration of coherent control of currents was carried out using superlattices and was presented by E. Dupont *et al*³⁷. In this work, the direction of emission of photoexcited electrons in AlGaAs/GaAs quantum well superlattices was controlled by adjusting the relative phase difference between mid-infrared radiation (from a TEA CO₂ laser) and its second harmonic. A classic photoconductive model led to an expression for the current density that is directly proportional to $\sin(2\phi_\omega - \phi_{2\omega})$, where ϕ_ω and $\phi_{2\omega}$ are the phases of the fundamental (10.6 μm) and SHG (5.3 μm) beams, respectively. The relative phase between the two collinear beams was controlled by a dispersive NaCl crystal mounted on a rotating stage. By rotating the salt crystal from $\theta = 12.8^\circ$ to 13.7° a phase shift of π was imposed and the authors were able to invert the direction of emission of the photocarriers. Electrical currents of $\sim 15 \mu\text{A}$ ($-15 \mu\text{A}$ for the next relative phase shift

of π) were reported using incident pulse energies of $\sim 10 \mu\text{J}$ at $10.6 \mu\text{m}$ and $\sim 50 \mu\text{J}$ at $5.3 \mu\text{m}$.

An extra step was then carried out by R. Atanasov and co-workers by extending the theoretical³⁸ and experimental^{39,40} investigation of CC of electrical currents to bulk, undoped semiconductors. In their theoretical work (ref. 38), they consider subjecting a semiconductor to two coherent beams ω and 2ω thereby satisfying $E_g/2 < \hbar\omega < E_g$ where E_g is the fundamental bandgap. The one- and two-photon interband transitions lead, using the Fermi's golden rule, to an electron (e) and hole (h) injection current process. The subsequent transport is then calculated with a hydrodynamic model of electron hole plasma. The rate of current injection $J_{e,h}^I$ of electron and hole is related to the optical electric fields $E^\omega, E^{2\omega}$ by

$$J_{e,h}^I = \vec{\eta}_{e,h} : E^\omega E^\omega E^{-2\omega} + c.c. \quad (6.1)$$

where $\vec{\eta}_{e,h}$ is a fourth-rank purely imaginary tensor, which for GaAs has four independent components, the largest being $(\vec{\eta}_{e,h})_{xxxx}$. The fact that the period of the optical beams is short compared with the current relaxation time, allows, in equation (6.1), for decay effects to be treated separately. The dynamic equation for the evolution of the current density is then

$$\dot{J}_{e,h} = J_{e,h}^I - J_{e,h} / \tau_{e,h} \quad (6.2)$$

where $\tau_{e,h}$ is the current relaxation time. For both beams polarised along the crystalline x axis, the rate of change of current can be expressed explicitly as:

$$\left(\dot{J}_{e,h}\right)_x = 2 \left[(\eta_{e,h})_{xxxx} \left| E_x^\omega E_x^\omega E_x^{-2\omega} \sin(2\phi_\omega - \phi_{2\omega}) \right. - \frac{(J_{e,h})_x}{\tau_{e,h}} \right] \quad (6.3)$$

where ϕ_ω and $\phi_{2\omega}$ are the phases of the two optical beams. Equation (6.3) shows that the relative phase difference $\Delta\phi = 2\phi_\omega - \phi_{2\omega}$ can be used to control the current direction and magnitude. Because the effective mass of holes is much greater than that of the electrons, holes therefore make a much smaller contribution to the electrical current than electrons and indeed $|\eta_h| \ll |\eta_e|$.

The 2ω and ω pulses also give rise to linear and two-photon optical absorption respectively, which inject an electron-hole density N . The macroscopic speed of the injected electron is also estimated by using

$$v = \frac{J}{eN} \quad (6.4)$$

For GaAs, the maximum macroscopic speed of injected electrons is $v_{max} = 500 \text{ km}\cdot\text{s}^{-1}$ which is close to the $850 \text{ km}\cdot\text{s}^{-1}$ speed of each individual electron. Assuming incident irradiances of $I_0^\omega = 90 \text{ MW}\cdot\text{cm}^{-2}$ and $I_0^{2\omega} = 15 \text{ KW}\cdot\text{cm}^{-2}$ for the two beams, with gaussian pulse widths of $\tau_\omega = \tau_{2\omega} = \tau_e = 100 \text{ fs}$, a peak current of $\sim 1 \text{ KA}\cdot\text{cm}^{-2}$ for a carrier of 10^{14} cm^{-3} is obtained. The carriers obtain their speed in femtosecond timescale, with the current rise time dictated by the optical pulse rise time. In the case of normal current production, where existing carriers are accelerated by an electric field, a carrier density of 10^{15} cm^{-3} is required to produce $J=1 \text{ KA}\cdot\text{cm}^{-2}$. This current would occur $\sim 300 \text{ fs}$ after the field is “instantaneously” turned on.

In their experiments, several sources have been used. In one experiment (ref. 39), they used an optical parametric generator (OPG) which provides 175 fs pulses at 250 kHz, with average powers up to 30 mW (peak power, $P_p = 685 \text{ KW}$). This source was used near $1.55 \mu\text{m}$ and had a pulse duration-bandwidth of $\Delta\nu\Delta t = 0.66$. The second source was a KTP based optical parametric oscillator (OPO) that

produced 1 ps pulses at 82 MHz, tunable near 1.55 μm ($\Delta\nu\Delta t = 0.48$) and average powers up to 150 mW ($P_p = 1.83$ KW). In both cases, up to 20 μW of collinearly generated second-harmonic average power could be obtained ($P_p = 460$ W and 0.25 W, respectively). As explained before, a 1 mm thick BK7 glass was used to vary the relative phase of the beams. For current generation samples of GaAs and low-temperature-grown GaAs (LT-GaAs) were used. Time-integrated currents were measured via charge collection in an unbiased metal-semiconductor-metal (MSM) electrode structure. When both beams, coming from the OPG, were incident the MSM sample, a modulation in the induced voltage was observed with rotation of the BK7 glass. However, phase-related current control from the OPO could not be achieved. This is possibly because the recombination time for the low-density carriers is much longer than the pulse period. In this case, the steady-state carrier density is larger than the injected carrier density per pulse.

In a second experiment (ref. 40), a synchronously pumped OPO delivering near-transform-limited pulses of 1 ps at 82 MHz with an average output power of 100 mW (peak power of 1.2 kW) and tunable from 1.4 to 1.6 μm was used. Also, an OPA producing pulses of ~ 150 fs at 250 kHz with $P \sim 50$ mW ($P_p = 1.3$ MW) in the 1.1 to 1.8 μm and with a pulse duration-bandwidth product of $\Delta\nu\Delta t = 0.48$ was used. In both cases, up to 2 mW of collinearly generated second-harmonic average power could be generated ($P_p = 24$ W and 53 KW, respectively). The relative phase, $\Delta\phi$, between the two collinear beams, which could be varied by half a cycle, was controlled in two different ways. One was based on a rotating BK7 plate, as described before, whereas in the second method, a Michelson interferometer with a dichroic mirror to separate the two beams was incorporated. In this interferometer, the length of one of the arms was controlled by a piezoelectric transducer (PZT).

This technique allowed for background-free measurements of CC current with rapid phase scan. A displacement amplitude of $\lambda/4$ was applied to the PZT to alter the phase, $\Delta\phi$, to allow the signal to be measured in a single sweep. For current generation, samples of GaAs and LT-GaAs were used. CC currents were observed in both GaAs and LT-GaAs. However, as before, the GaAs MSM structures only gave evidence of CC effects with the OPA. For picosecond pulse excitation with peak irradiance of only $30 \text{ MW}\cdot\text{cm}^{-2}$ (@ $1.55 \text{ }\mu\text{m}$) and $9 \text{ kW}\cdot\text{cm}^{-2}$ (@ $0.775 \text{ }\mu\text{m}$), peak current densities of similar to $10 \text{ A}\cdot\text{cm}^{-2}$ at peak carrier densities of 10^{15} cm^{-3} are inferred from the steady-state signals.

More recently, the same authors have extended the theory and carried out experiments that have shown evidence of CC of current in LT-GaAs using three beams derived from an optical parametric process⁴¹. This offers an additional degree of freedom to enhance coherent control of currents. This enhancement can occur as the energy of the parametrically generated source beams approach an intermediate resonance such as an impurity level or the band gap. In their experiment, a regenerative amplified Ti:sapphire laser ($0.8 \text{ }\mu\text{m}$) operating at a repetition rate of 250 KHz was used to pump an optical parametric amplifier to produce pulses of 150 fs at $1.8 \text{ }\mu\text{m}$ and $1.2 \text{ }\mu\text{m}$. The three colours were separated into independent delay lines for individual control of two pulse delay. As before, one delay line is mounted on a PZT to allow fine control of $\Delta\phi = \phi_p - \phi_s - \phi_i$, where $\phi_{p,s,i}$ refers to the phases of the pump ($0.8 \text{ }\mu\text{m}$), signal ($1.2 \text{ }\mu\text{m}$) and idler ($1.8 \text{ }\mu\text{m}$) beams, respectively. In this case, current injection occurs as a result of the interference of single-photon absorption with nondegenerate two-photon absorption pathways.

Coherence control of electron populations and excitons in semiconductors represents a promising and exploitable close-related mechanism to generate phase-

controlled currents. Ultrafast carrier coherent control has been investigated by several groups (see previous section on “Coherent control of excitons”). In particular J. J. Baumberg, *et al*^{5,42} have reported the coherent control of exciton dynamics with a phase-locked femtosecond-pulse pair in quantum well samples of GaAs. In their experiment, a Michelson interferometer generates two pump pulses that are temporally separated in order to create an interference pattern. These pump pulses are focused on to the sample, creating excitons. A translation of one of the arms of the interferometer of $\lambda/2$ ($\Delta\tau_{12} = 1.34$ fs) reverses the interference pattern which destroy the excitons that had been created. This exciton dynamics induce a change in the reflectivity of the sample, ΔR , which is monitored by a third probe pulse at a time delay τ_x . Coherent control of the exciton density is then evident by interferograms of the pump-induced reflectivity changes ΔR versus $\Delta\tau_{12}$. Time-resolved measurements of the evolution of the population at a fixed time-delay, $\Delta\tau_{12}$, demonstrate that a large intermediate exciton population is excited. It is then demonstrated that the first pulse creates excitons, which are subsequently enhanced or destroyed by the second pulse (for constructive or destructive interference respectively). This destructive process permits creation of ultrafast exciton pulses limited in speed only by the pulse duration

6.3. Electrical pulse generation by coherent control.

My approach

We have seen that the scientific and technological possibilities that are opened up by coherent control processes are impressive. The manipulation of carrier populations in semiconductors has attracted our attention because it promises to

remove some of the main obstacles towards ultrafast and coherent optoelectronics. It is of particular interest, to exploit coherent control for the manipulation (generation / removal) of carrier populations on a femtosecond timescale. Understanding the physics that underlie these processes will open the possibility of optically controlled electrical currents and of generating and controlling ultrafast electrical pulses.

In the previous section we established the relevant concepts and recognised the ongoing work in the field of ultrafast coherent control of electrical currents. Analogously, in the previous chapters, we have demonstrated a number of ultrafast source devices and ultrashort pulse characterisation techniques. We are now in position to propose an experimental implementation to merge these two topics and perform preliminary tests relative to the generation of electrical pulses by implementing coherent control procedures.

6.3.1 The OPO source

The experimental realisation will involve the construction of a coherent source producing at least two phase-related ultrashort pulses. One will be centred on a frequency, ω for which the photon energy is high enough to excite direct transition in the semiconductor with bandgap energy E_g . The other will be centred on a frequency, $\omega/2$ and a photon energy that is close to one half of the bandgap energy, E_g . One effective way to achieve this is to use an optical parametric oscillator (OPO) because this source produces simultaneously more than two phase-related beams: pump, signal and idler. A source of this type offers several advantages. Firstly, there is the possibility to tune the $\omega/2$ pulses (signal beam, in this case) around some

central wavelength [$1.5 \mu\text{m}$ ($E_p \sim 0.83 \text{ eV}$), for example], which relates to energies close to half of the bandgap energy associated with a semiconductor. Furthermore, if operated near degeneracy, the idler beam can provide an extra degree of freedom. The signal beam can be frequency doubled in either, an extracavity or an intracavity configuration (similar to those described in Chapter 5 section 5.1) to produce ω pulses.

Our typical pump source for the OPO is a self-modelocked Ti:sapphire laser. This, when operated at around 820 nm ($E_p \sim 1.52 \text{ eV}$), can provide the ω pulses⁴¹ (in which case current injection occurs as a result of the interference of single-photon absorption with a "nondegenerate" two-photon absorption pathway). By way of illustration, figure 1 shows the OPO tuning curve as a function of the pump wavelength for a 1 mm long PPLN nonlinear crystal having a grating period of $\Lambda = 21 \mu\text{m}$.

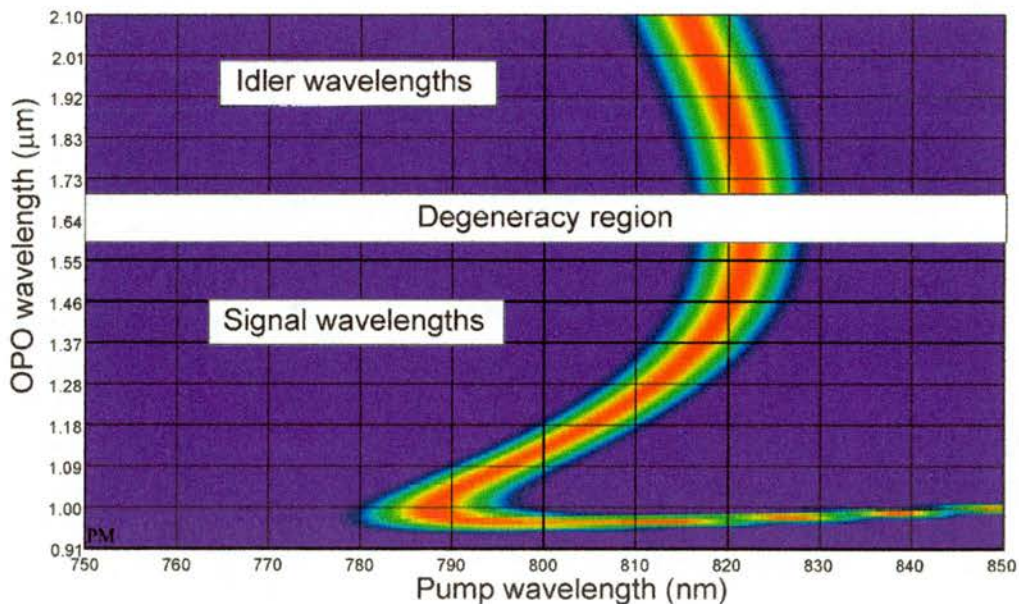


Figure 1. OPO tuning range of a PPLN crystal with a grating period of $21 \mu\text{m}$.

As shown in figure 1, it is possible to obtain signal wavelengths from 1.4 to $\sim 1.62 \mu\text{m}$ (or E_p from 0.88 to 0.766 eV) and idler wavelengths from ~ 1.66 to $2.0 \mu\text{m}$

(E_p from 0.74 to 0.62 eV), if pumped at ~ 820 nm ($E_p \sim 1.52$ eV). The range of wavelengths thus obtained can be used to stimulate the one-photon and two-photon transitions in a variety of semiconductors such as Si ($E_g = 1.11$ eV), GaAs ($E_g = 1.43$ eV), InP ($E_g = 1.28$ eV), etc⁴³.

To date, we have presented experimental evidence that femtosecond OPOs, based on PPLN or PPRTA crystals, can be operated reliably around the signal wavelengths of 1.55 μm . For the specific application required here, these two systems would be greatly improved if we replaced the existing AR crystal coatings (presently at a central wavelength of 1.1 μm) with more suitable coatings centred at 1.5 μm . The existing coatings limit the delivered output power. For example, in the case of the PPRTA crystal, the existing AR coatings introduce intracavity losses of 1.5% per surface (6% per round trip) at the central wavelength of 1.5 μm . Despite these deleterious losses, typical average output powers near 30 mW have been obtained.

The OPO cavity includes a pair of prisms to dispersion compensate the signal beam and produce transform-limited pulses. The introduction of a pair of prisms (SF-14) with an apex separation of 300 mm, allowed us to demonstrate (in the PPRTA OPO) pulses of duration of 200 fs that could be obtained over the entire tuning range. Similar results were obtained using the PPLN OPO. This implies that the typical peak powers were of ~ 2 kW. This peak power value for the $\omega/2$ beam would be two orders of magnitude larger than the value previously reported using analogous systems^{39,40}.

In a second stage of the experiment, the possibility of using pulses with controlled negative and positive chirp to shape the ultrafast electrical pulses will be considered.

6.3.2 The experimental setup

The basic experimental set up to generate and measure ultrafast electric currents is illustrated in figure 2 and described below.

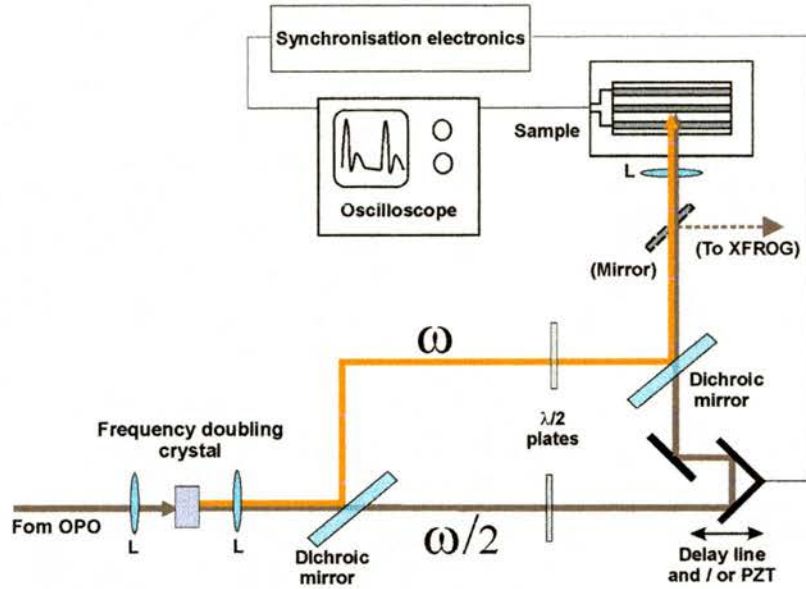


Figure 2. Diagram of the proposed experimental setup for the coherent control of photocurrent using a pair of phase related beams.

The signal (or idler) beam, will provide the $\omega/2$ pulses by directing them to a delay line. This beam will be frequency doubled using a nonlinear crystal (such as type I ($\sigma+\sigma\rightarrow e$) β BBO or PPLN ($\Lambda = 17 \mu\text{m}$)) to provide the ω pulses. The ω and $\omega/2$ pulses will be separated using a dichroic mirror (HR @ 750 nm and HT @ 1.5 μm) to allow independent delay of the two beams. The two beams will be collinearly recombined using a second dichroic mirror. Both pulses are then focused on the gap area of the semiconductor, between the two electrodes (or sent to a sum-frequency mixing crystal for X-FROG characterisation). Initially sample materials such as semi-insulating GaAs and low-temperature-grown GaAs (LT-GaAs) will be tested. Finally, the cavity of the OPO would be stabilised in order to generate low jitter pulses in synchronisation with the Ti:sapphire laser pulses.

The relative phase shift between the ω and $\omega/2$ pulses could be controlled by several mechanisms. Our first approach would be to drive the delay line across the position of zero delay using a suitable piezoelectric translation (PZT) stage. A sinusoidal voltage would be applied to the piezocontroller using a function generator to give a displacement amplitude of at least $\lambda/2$ (or a total of $\lambda/4$ path change for the $\omega/2$ beam). The displacement of the PZT would vary the phase by at least, a cycle and thus produce a change in the direction of the current generated. This will allow the signal extrema to be measured in a single sweep. The reversal on the current direction would be monitored as a change of voltage, V , on an oscilloscope. In this case, measurement would be assisted by lock-in amplification.

Two $\lambda/2$ plates will be introduced to control the polarisation of the beams. The beam polarisations should be across the crystalline x axis to take advantage of the largest fourth-rank tensor element, η_{xxxx} of GaAs. This dictates that the gaps between the electrodes should be oriented along the crystal (100) direction. Although it has been shown that the response of the sample is reduced up to one order of magnitude using cross-polarised beams^{38,40}, the effect of crossing different linear polarisation (from parallel to perpendicular) of the two beams enables the electrical pulses to be shaped and studied in detail.

The flexibility afforded by the independent control of the polarisations of the two beams can be used later to aid in pulse characterisation. In fact, with perpendicularly polarised beams we can perform birefringent sum-frequency mixing for a cross-FROG (X-FROG) procedure. In order to perform this characterisation, a 300 μm thick, type II sum-frequency phasematching (o+e \rightarrow e) βBBO crystal will be used. As described previously (see chapter 3, section 3.3.4), the X-FROG technique

will allow us to simultaneously retrieve the phase and intensity profile of the two beams involved.

The two beams will be focused in the gap space between the electrodes. Here, different illumination conditions (incident average power and spot sizes) will be tested. In addition, several gap sizes that range from a few to several tens of micrometers should be considered. The amount of generated current, and therefore the voltage, V , would be expected to vary with the irradiance and with the gap size.

6.3.3 The Collaboration with NPL

As explained before, the main propose would be to generate ultrafast photocurrents with the ω and $\omega/2$ pulses. These photocurrents would be monitored in an interdigitated device structure and then propagated to a coplanar waveguide for subsequent characterisation. The electric pulse signal will be measured using the electrooptic sampling (EOS) technique⁴⁴. In this EOS technique the pump beam is modulated to allow phase sensitive detection and to perform this task, the laser beam is split in two components where one is acoustooptically modulated and directed to the sample to generate the electrical signal to be measured. The other beam is sent via a delay line to the sample, passing first through a polariser, a compensator and an electrooptic probe. The polarisation of the laser beam reflected off the probe is rotated by the application of an electric field across the electrooptic tip caused by the generated electrical pulse. An analyser is then used to convert any changes of polarisation in intensity changes, which are then detected with a photodiode in phase with the acoustooptic modulation. The resolution of the modulator interaction geometry is then determined by the convolution time of the optical probe pulse and the travelling electrical signal as they propagate through the electrooptical material.

A specially-made electrooptic probe⁴⁵ (LiTaO₃) will be used to minimise invasiveness and enhance the temporal resolution of the proposed measurement system⁴⁶. To achieve this, research will be undertaken in collaboration with the Centre for Electromagnetic and Time Metrology at the National Physical Laboratory (NPL). Thus, a second part of the experiment would involve the construction of similar OPO system at the NPL facilities and perform there the relevant measurements concerning the duration and profile of the generated electric pulse.

6.4 Conclusions

In conclusion, in this chapter I have presented a general outline of some of the possibilities that optical coherent control offers. In particular, I have reviewed the physical processes and presented the most important results of electric pulse generation using coherent control. With this background as a basis, it have been possible to describe an experimental setup that will be used to perform preliminary experiments and to study the relevant physics involved in this field. The experimental setup will involve the construction and characterisation of a synchronously pumped OPO to excite carriers in semiconductor samples using at least two phase-related beams. In this way, it is feasible to excite electrons from the valence band to the conduction band by two different quantum mechanical routes. The interference between these distinct quantum mechanical pathways will favour the generation of electrons having a particular momentum direction. The study of this generated signal should provide evidence of ultrafast photocurrents that can be generated in the semiconductor. This photocurrent will be characterised in detail using the NPL facilities.

6.5 References

1. A. Manykin and A. M. Afanas'ev, "On the possibility of making a medium transparent by multi-quantum resonance," *Sov. Phys JETP*, **25**, 828-830 (1967).
2. W. S. Warren, H. Rabitz, M. Dahleh, "Coherent control of quantum dynamics - the dream is alive," *Science*, **259**, 1581 - 1589 (1993).
3. A. P. Heberle, J. J. Baumberg, K. Kohler, "Ultrafast coherent control and destruction of excitons in quantum-wells," *Phys. Rev. Lett.*, **75**, 2598 - 2601 (1995).
4. A. P. Heberle, J. J. Baumberg, E. Binder, T. Kuhn, K. Kohler, K. H. Ploog, "Coherent control of exciton density and spin" *IEEE J. Sel. Top. Quantum Electron.*, **2**, 769 - 775 (1996).
5. J. J. Baumberg, A. P. Heberle, K. Kohler, K. Ploog, "Ultrafast coherent carrier control in quantum-wells," *J. Opt. Soc. Am. B*, **13**, 1246 - 1250 (1996).
6. X. Marie, P. Renucci, S. Dubourg, T. Amand, P. Le Jeune, J. Barrau, J. Bloch, R. Planel, "Coherent control of exciton polaritons in a semiconductor microcavity," *Phys. Rev. B-Condens Matter*, **59**, R2494 - R2497 (1999).
7. P. Le Jeune, X. Marie, T. Amand, M. Brousseau, J. Barrau, "Coherence of excitons in quantum wells," **164**, *Phys. Status Solidi A-Appl. Res.*, 527 - 533 (1997).
8. X. D. Hu, W. Potz, "Coherent control of intersubband transitions in semiconductor nanostructures," *Phys. Status Solidi B-Basic Res.*, **204**, 350 - 353 (1997).
9. N. Garro, M. J. Snelling, S. P. Kennedy, R. T. Phillips, K. H. Ploog, "Coherent control of resonant quantum well emission," *J. Phys.-Condes. Matter*, **11**, 6061-6067, (1999).
10. P. I. Tamborenea, H. Metiu, "Coherent control of multisubband wavepackets with terahertz (Thz) pulses," *J. Chem. Phys.*, **110**, 9202 - 9213 (1999).
11. S. M. Sadeghi, S. R. Leffler, J. Meyer, "Quantum interference and nonlinear optical processes in the conduction bands of infrared-coupled quantum wells," *Phys. Rev. B*, **59**, 15388 - 15394 (1999).
12. P. C. M. Planken, I. Brener, M. C. Nuss, M. S. C. Luo, S. L. Chuang, "Coherent control of terahertz charge oscillations in a coupled-quantum-well using phase-locked optical pulses," *Phys. Rev. B*, **48**, 4903 - 4906 (1993).
13. D. S. Citrin, M. Yamanishi, Y. Kadoya, "Coherent control of terahertz generation in a DC-biased semiconductor microcavity," *IEEE J. Sel. Top. Quantum Electron.*, **2**, 720 - 723 (1996).
14. D. S. Citrin, T. B. Norris, "Coherent control of quantum-well excitons in a resonant semiconductor microcavity for high-speed all-optical switching," *IEEE J. Sel. Top. Quantum Electron.*, **2**, 401 - 409 (1996).
15. D. S. Citrin, T. B. Norris, "Constraints on coherent control of quantum-well excitons for high-speed all-optical switching," *IEEE J. Quantum Electron.*, **33**, 404 - 407 (1997).
16. D. S. Citrin, "Terahertz sideband generation and coherent control in semiconductor microcavities," *Phys. Rev. Lett.*, **82**, 3172 - 3175 (1999).
17. N. B. Baranova, A. N. Chudinov, B. Ya. Zel'dovich, "Polar asymmetry of photoionization by a field with $\langle E^3 \rangle \neq 0$. Theory and experiment," *Opt. Commun.*, **79**, 116 - 120 (1990).

18. A. D. Bandrauk, H. T. Yu, E. E. Aubanel, "Coherent control of electrons in molecules," *Can. J. Chem.-Rev. Can. Chim.*, **74**, 988 - 994 (1996).
19. V. B. Deyirmenjian, J. E. Sipe, "Coherent control of the angular distribution of electrons photoemitted from metal surfaces," *Phys. Rev. Lett.*, **82**, 4942-4945 (1999).
20. R. van Leeuwen, M. L. Bajema, R. R. Jones, "Coherent control of the energy and angular distribution of autoionized electrons. *Phys. Rev. Lett.*, **82**, 2852 - 2855 (1999).
21. C. Chen, D. S. Elliott, "Propagation effects in two-color coherent-control processes," *Phys. Rev. A*, **53**, 272 - 279 (1996).
22. V. Blanchet, C. Nicole, M. A. Bouchene, B. Girard, "Temporal coherent control in two-photon transitions: From optical interferences to quantum interferences," *Phys. Rev. Lett.*, **78**, 2716 - 2719 (1997).
23. T. Nakajima, P. Lambropoulos, "Effects of the phase of a laser field on autoionization," *Phys Rev A*, **50**, 595 - 610 (1994).
24. R. Taieb, V. Veniard, A. Maquet, "Two-color coherent control of atomic multiphoton ionization with high-order harmonics: Time-dependent Schrodinger equation treatment," *J. Opt. Soc. Am. B.*, **13**, 363 - 370 (1996).
25. N. E. Karapanagioti, D. Xenakis, D. Charalambidis, C. Fotakis, "Coherent control through atomic interference at a virtual level," *Instit Phys Confer Ser.*, **154**, 248 - 253 (1997).
26. N. L. Manakov, V. D. Ovsianikov, A. F. Starace, "DC field-induced, phase and polarization control of interference between one- and two-photon ionization amplitudes," *Phys. Rev. Lett.*, **82**, 4791-4794 (1999).
27. T. Dekorsy, W. Kutt, T. Pfeifer, H. Kurz, "Coherent control of lo-phonon dynamics in opaque semiconductors by femtosecond laser-pulses," *Europhys. Lett.*, **23**, 223 - 228 (1993).
28. M. U. Wehner, M. H. Ulm, D. S. Chemla, M. Wegener. "Coherent dynamics in semiconductors on a 10 fs timescale: Coherent control of scattering processes," *Phys. Status Solidi B-Basic Res.*, **206**, 281 - 291 (1998).
29. X. D. Hu, W. Potz. "Coherent manipulation of phonon emission rates in semiconductor heterostructures," *Phys. Rev. Lett.*, **82**, 3116 - 3119 (1999).
30. G. K. Paramonov. "Coherent control of linear and nonlinear multiphoton excitation of molecular vibrations," *Chem. Phys.*, **177**, 169 - 180 (1993).
31. V. V. Lozovoy, S. A. Antipin, F. E. Gostev, A. A. Titov, D. G. Tovbin, O. M. Sarkisov, A. S. Vetchinkin, S. Y. Umanskii. "Experimental demonstration of the coherent control of the molecular iodine vibrational dynamics by chirped femtosecond light pulses," *Chem. Phys. Lett.* **284**, 221 - 229 (1998).
32. S. Lee. "On the molecular phase in coherent control" *J. Chem. Phys.*, **107**, 2734 - 2737 (1997).
33. T. Quang, M. Woldeyohannes, S. John, G. S. Agarwal, "Coherent control of spontaneous emission near a photonic band edge: A single-atom optical memory device," *Phys. Rev. Lett.*, **79**, 5238 - 5241 (1997).
34. M. Shapiro, P. Brumer, "Quantum control of chemical reactions," *J. Chem. Soc.-Faraday Trans.* **93**, 1263 - 1277 (1997).
35. B. N. Jagatap, W. J. Meath, "On the competition between permanent dipole and virtual state two-photon excitation mechanisms, and two-photon optical excitation pathways, in molecular excitation," *Chem. Phys. Lett.*, **258**, 293 - 300 (1996).

36. G. Kurizki, M. Shapiro, P. Brumer. "Phase-coherent control of photocurrent directionality in semiconductors," *Phys. Rev. B*, **39**, 3435 – 3437 (1989).
37. E. Dupont, P. B. Corkum, H. C. Liu, M. Buchanan, Z. R. Wasilewski, "Phase-controlled currents in semiconductors," *Phys. Rev. Lett.*, **74**, 3596 – 3599 (1995).
38. R. Atanasov, A. Hache, J. L. P. Hughes, H. M. vanDriel, J. E. Sipe, "Coherent control of photocurrent generation in bulk semiconductors," *Phys. Rev. Lett.*, **76**, 1703 – 1706 (1996).
39. A. Hache, Y. Kostoulas, R. Atanasov, J. L. P. Hughes, J. E. Sipe, H. M. vanDriel, "Observation of coherently controlled photocurrent in unbiased bulk GaAs," *Phys. Rev. Lett.*, **78**, 306 – 309 (1997).
40. A. Hache, J. E. Sipe, H. M. van Driel, "Quantum interference control of electrical currents in GaAs" *IEEE J. Quantum Electron.*, **34**, 1144 – 1154 (1998).
41. J. M. Fraser, A. Hache, A. I. Shkrebti, J. E. Sipe, H. M. vanDriel, "Three color coherent generation and control of current in low-temperature-grown GaAs," *Phys. Rev. Lett.*, **74**, 2014 – 2016 (1999).
42. A. P. Heberle, J. J. Baumberg, K. Kohler, "Ultrafast coherent control and destruction of excitons in quantum-wells," *Phys. Rev. Lett.*, **75**, 2598 – 2601 (1995).
43. J. I. Pankove, *Optical processes in semiconductors*. 1st ed. (Prentice-Hall, Englewood Cliffs, New Jersey, 1971) Chapter 1.
44. J. A. Valdmanis, G. A. Mourou, "Subpicosecond Electrooptic Sampling – Principles and Applications," *IEEE J. Quantum Electron.*, **22**, 69 – 78 (1986).
45. A. J. A. Smith, A. G. Roddie, D. Henderson, "Electrooptic sampling of low temperature GaAs pulse generators for oscilloscope calibration," *Opt. Quantum Electron.*, **28**, 933 – 943 (1996).
46. M. Y. Frankel, S. Gupta, J. A. Valdmanis, G. A. Mourou, "Terahertz Attenuation and Dispersion Characteristics of Coplanar Transmission-Lines," *IEEE Trans. Microwave Theory and Techniques*, **39**, 910 – 916 (1991).

CHAPTER 7

GENERAL CONCLUSIONS

Review

In this thesis I have demonstrated optical parametric oscillators (OPOs) having a range of cavity configurations and using a variety of crystals such as periodically poled RbTiOAsO₄ (PPRTA), and periodically poled lithium niobate (PPLN). The different characteristics of the OPO cavities and/or crystals were considered with specific characteristics in mind. These included extended tunability (Chapters 3, 4), transform-limited pulse operation (Chapter 4), maximum extraction of energy (Chapter 4, 5) and chirped femtosecond pulse operation (Chapter 5). Also, I have presented detailed studies of the pulse compression techniques during second-harmonic generation (SHG) using aperiodically-poled crystals such as KTiOPO₄ (APP-KTP) and APPLN (Chapter 5).

On the ultrashort pulse characterisation side, novel techniques such as SHG frequency-resolved optical gating (SHG-FROG) and cross-correlation-based FROG (or X-FROG) were implemented and novel devices for two-photon absorption based autocorrelators for the visible spectral range were investigated (Chapter 3).

Finally, in Chapter 6 several of the techniques were applied to outline a system that could be implemented for the study coherent control of electrical currents in bulk semiconductor materials. In what follows I will summarise the most

significant observations for each chapter, together with the implications and suggested future directions of research of these fascinating topics.

Conclusions and future directions

In Chapter 1, synchronously pumped optical parametric oscillators are presented as alternative and versatile sources of high-repetition rate, high optical average output power and capable of delivering femtosecond pulses with broad tunability. Conventional sources of femtosecond pulses were discussed, and the potential of OPOs was made evident by reviewing some emerging applications. Also, in the first part of this chapter I described a complete review of synchronously pumped femtosecond OPOs based on periodically-poled materials. The section concluded with an overview of the current state-of-the-art of these sources.

In the second part of the chapter, the self-modelocked Ti:sapphire laser was presented as a pump source for the OPOs, where a brief review of the concepts of modelocking and some of the techniques necessary to maintain stable operation were described. Conditions for linear and nonlinear pulse propagation were described at the end of this chapter.

A review of nonlinear optical theory was given in Chapter 2. The coupled amplitude wave equations were presented in the general form of three-wave mixing interactions, and the relevant concepts of phasematching in birefringent nonlinear crystals were described. Quasi-phasematching (QPM) in periodically poled ferroelectric materials was then studied. I have reviewed relevant concepts to QPM and presented the procedures that are especially appropriate to periodically-poled ferroelectric materials. Finally, the physical linear and nonlinear properties of the

nonlinear materials used in this work, which were lithium niobate, KTiOPO_4 and RbTiOAsO_4 , were discussed.

Implementations of several pulse characterisation techniques were described in Chapter 3. Firstly, I reviewed the principles of second-order autocorrelation. These principles were applied to pulse measurements based on two-photon absorption using a $\chi^{(2)}$ medium based on semiconductor devices. In particular, a GaN-based laser diode was characterised by presenting the single- and two-photon response of the device at several wavelengths in the visible spectral range. With this device, interferometric and intensity autocorrelations in the 415 – 630 nm wavelength range were then performed. Autocorrelation of ultrashort pulse in this optical range using the GaN-based diode laser is proving to be much more efficient than SHG-autocorrelation, where a collection of thin crystals and angles to phasematch the same spectral range is normally needed. However, in either case, SHG- or two-photon absorption autocorrelations, emphasis was made to the fact that with these techniques, the pulse intensity profile has to be assumed and that no accurate information on the phase of the pulses can be obtained. To address this, the frequency-resolved optical gating (FROG) technique was described and implemented as a procedure for complete characterisation of ultrashort pulses. Detailed information for implementing a SHG-FROG set up was given and its performance illustrated by measuring the pulses from a modelocked Ti:sapphire laser and by characterising the fundamental (signal) pulses from the OPOs described in Chapter 5. In the last section, the cross-correlation-based FROG (X-FROG) technique was implemented. Because this technique is based on sum-frequency mixing, XFROG is promising to be a very suitable technique to characterise

ultrashort pulses in the near- and mid-infrared¹ and for experiments of the pump-probe type, as it can retrieve simultaneously the two pulses involved.

Implementations and subsequent characterisation of novel synchronously pumped OPO systems is the purpose of Chapter 4. With these systems, and using a few nonlinear crystals (PPRTA and PPLN), I have demonstrated that it is possible to extend the wavelength range of conventional high-repetition rate, and high average output power femtosecond sources. Thus, I have highlighted several systems that, when used in conjunction, have an exceptional tunability range that extends from 900 nm to 6.8 μm . These sources deliver ultrashort pulses of durations between 100 to 400 fs and with average output powers from $\sim 200 \mu\text{W}$ to 600 mW.

I presented a femtosecond OPO based on a crystal of PPRTA that was continuously tunable from 1.375 to 1.575 μm using a single set of mirrors. I showed that by adjusting the dispersion inside the cavity, it was possible to produce transform-limited pulses across the whole spectral range. This OPO represented an alternative source to produce femtosecond pulses in a region where operation of more conventional femtosecond sources may be compromised due to the strong water absorption present in this spectral region.

I also demonstrated a very practical and simple femtosecond OPO system that uses a single crystal of PPLN to obtain idler wavelengths in an optical range that goes from 2.8 μm and up to 6.8 μm . To the best of my knowledge, this system produced the longest idler wavelength obtained from any PPLN-OPO. This OPO exploited the transmission window in lithium niobate lying beyond the conventional cut-off transmission window of 5.8 μm and extending up to 7 μm . The high thresholds and low output powers obtained at the longer wavelengths produced with

this OPO can be overcome if a better primary pump source were to be used. In particular, high-pump thresholds have prevented the operation of a similar system using a 10 W, all-solid-state pumping schemes based on diode-pumped, CW, frequency-doubled Nd:YVO₄ laser (Spectra-Physics Millennia). Such a system will improve the stability and the efficiency of the system, as proved to be the case on the first stage of the experiment (see section 4.2) where a 5 W Millennia was used as a primary pump source. To obtain higher average output powers, an alternative setup and materials might have to be considered. In this respect, semiconductors are interesting materials because of their high nonlinear coefficients and large transmission in the mid-infrared spectral region. Unfortunately they have high absorption losses at the wavelengths typically available from self-modelocked Ti:sapphire lasers and therefore, high-repetition-rate devices using these materials are limited to be used as single-pass, difference-frequency generators or in OPOs to be pumped using a secondary source. For example, recent work has demonstrated high repetition rate, femtosecond pulse oscillation up to 8 μm in the idler wavelengths using two cascaded OPO where a CsTiOAsO₄ (CTA) based OPO was used to pump another OPO based on a crystal of AgGaSe₂.² This configuration, although more complicated, has an optical pump threshold of less than 0.5 W and can deliver average output powers of several milliwatts between 6 and 8 μm .

The principles of simultaneous SHG and pulse compression are the subject matters of Chapter 5, where two different experiments are studied. Firstly, by using a crystal of APP-KTP, I showed that it was possible to obtain femtosecond pulse compression by placing the frequency-doubling crystal extracavity and intracavity. In the extracavity case, a reduction in chirp factor of the fundamental pulse to the

SHG pulses from six to two (assuming $\text{sech}^2(t)$ intensity profile) was obtained. Due to the limited chirp of our fundamental pulses, short crystal lengths had to be used. This represented a limiting factor which prevented us from obtaining higher optical powers in the frequency-doubled output and consequently a peak power efficiency of 4.5% was obtained. This implied that longer chirped fundamental pulses should be used, and in fact earlier work showed a 150-fold compression relative to the input pulses and with single pass efficiencies of 40 % for a 50 mm crystal.³ Nevertheless, in the second half of the experiment, intracavity frequency doubling proved to be an efficient technique to increase the output powers available while, at the same time, maintaining or even increasing the compression ratio. Thus, transform-limited pulses with durations of 120 fs and having SHG output powers as high as 120 mW were obtained.

In the second experiment, I demonstrated effective SHG and pulse compression using an APPLN crystal with 8 different chirped gratings. Here, arbitrary pulses from an uncompensated OPO cavity were successfully frequency doubled and compressed. I showed that any compression or expansion mechanism was due to the chirp of the gratings, and no spectral clipping or self-phase modulation was acting on the pulses which confirmed our previous observation in the first part of the chapter where only one grating was used. It was also shown that optimum pulse compression took place for one of the chirped gratings (G_2), where transform-limited pulses were measured, and that increasing or decreasing the grating chirp, produced longer pulses. The excess chirp on the crystal grating was then shown to produce periodic back-conversion of optical power between the interacting waves, which resulted in recompression of the SHG pulses. This fact was also evident as a reduction of the conversion efficiency.

Our corresponding numerical model was in good agreement with the experimental results. This confirmed that the FROG system described in Chapter 3 is reliable and the retrieval was accurate. Our model can equally be used to design novel (for example, nonlinearly chirped) crystal gratings that would produce optimum compression for input fundamental pulses with arbitrary frequency chirp. The success of this experiment, opens up new research lines and currently, interest exists in implementing the model to study more elaborate phenomena such as optical parametric oscillation with idler pulse compression.⁴ In this case, it has been shown that by using crystals with chirped grating as the active medium in OPOs, pulses having only 5 optical cycles (FWHM) at the idler wavelength of 3 μm with bandwidths in excess of 700 μm have been produced.

In Chapter 6, several of the techniques and systems described in this work were combined as a proposed scheme to study coherent control of electrical currents in bulk semiconductors. A brief review of the several possible applications using coherent control was presented. Also, I have analysed the physical processes relevant to the generation and control coherent of electrical currents and a resume of preliminary works in the field were presented. With this background I have proposed an optical system based on an OPO and a frequency doubling crystal to deliver two phase-related beams, fundamental and second-harmonic, to excite a semiconductor bulk material. The simultaneous single- and two-photon absorption mechanisms will excite carriers into the conduction band by two different quantum mechanical routes which will interfere. This results in the generation of electrons with a particular momentum direction and generating an ultrashort pulse of electrical current. These electrical pulses will be sampled and used to perform calibration of ultrafast

oscilloscopes at the National Physics Laboratories. It is also of interest to perform a complete study of the influence of the optical pulse parameters, such as intensity, polarisation, pulse profiles and chirping, on the electrical pulses being generated. As mentioned before, this study will be assisted by performing the X-FROG characterisation technique. This will allow suitable control of the parameters of the two optical pulses.

Finally, I would like to claim that the generation and study of ultrashort optical pulses and sources have now achieved a level of understanding and reliability that opens up a range of new and very interesting applications (such as the one described above). I would even venture to say that these systems are now ready for new and even more exciting application ideas to emerge. However, there is still room for improvements and further work has to be done; the way is long but is this never ending process which keeps fascinating all the people that have ever explored the world of nonlinear optics and ultrafast science in general.

7.1 References

1. D. T. Reid, P. Loza-Alvarez, C. T. A. Brown, T. Beddard and W. Sibbett, "Amplitude and phase measurement of mid-ir femtosecond pulses using XFROG," *submitted to Opt. Lett.*
2. S. Marzenell, R. Beigang and R. Wallenstein, "Synchronously pumped femtosecond optical parametric oscillator based on AgGaSe₂ tunable from 2 μm to 8 μm ," *Appl. Phys. B*, **60**, 423 – 428 (1999).
3. M. A. Arbore, A. Galvanauskas, D. Harter, M. H. Chou, M. M. Fejer, "Engineerable compression of ultrashort pulses by use of second-harmonic generation in chirped-period-poled lithium niobate," *Opt. Lett.*, **22**, 1341 – 1343 (1997).
4. T. Beddard, M. Ebrahimzadeh, D. T. Reid, W. Sibbett, "Five-optical cycle pulse generation in the mid-infrared from an optical parametric oscillator based on aperiodically poled lithium niobate," *Accepted to Opt. Lett.*, **25**, No14 (2000).

Publications

Journal publications

P. Loza-Alvarez, D. T. Reid, M. Ebrahimzadeh, W. Sibbett, D. Artigas, M. Missey, "Femtosecond second-harmonic pulse compression in aperiodically-poled lithium niobate – a systematic comparison of experiment and theory," *Submitted to JOSA B*, (2000).

D. T. Reid, P. Loza-Alvarez, C. T. A. Brown, T. Beddard, W. Sibbett, "Amplitude and phase measurement of mid-IR femtosecond pulses using XFROG," *To be published, Opt. Lett.*, (2000).

P. Loza-Alvarez, W. Sibbett D. T. Reid, "Femtosecond autocorrelation measurements of CW-modelocked pulses from 415 – 630 nm using a gallium nitride laser diode," *Electron. Lett.*, **36**, 631 – 633 (2000).

P. Loza-Alvarez, C. T. A. Brown, D. T. Reid, W. Sibbett, M. Missey, "High repetition rate ultrashort-pulse optical parametric oscillator continuously tunable from 2.8 to 6.8 μm ," *Opt. Lett.*, **24**, 1523 – 1525 (1999).

P. Loza-Alvarez, D. T. Reid, P. Faller, M. Ebrahimzadeh, W. Sibbett, "Simultaneous second harmonic generation and femtosecond-pulse compression in aperiodically-poled KTiOPO_4 using an RbTiOAsO_4 -based optical parametric oscillator," *J. Opt. Soc. Am. B.*, **16**, 1553 – 1560 (1999).

P. Loza-Alvarez, D. T. Reid, P. Faller, M. Ebrahimzadeh, W. Sibbett, H. Karlsson, F. Laurell, "Simultaneous femtosecond-pulse compression and second harmonic generation in aperiodically-poled KTiOPO_4 ," *Opt. Lett.*, **24**, 1071 – 1073 (1999).

P. Loza-Alvarez, D. T. Reid, M. Ebrahimzadeh, W. Sibbett; H: Karlsson; P: Henriksson; G: Arvidsson F. Laurell, "Periodically poled RbTiOAsO_4 femtosecond

optical parametric oscillator tunable from 1.38 to 1.58 μm ,” *Appl. Phys. B*, **68**, 177 – 180 (1999).

Z. E. Penman, C. McGowan, P. Loza-Alvarez, D. T. Reid, M. Ebrahimzadeh, W. Sibbett, D. H. Jundt, “Femtosecond optical parametric oscillator based on periodically-poled lithium niobate,” *J. Mod. Opt.*, **45**, 1285 – 1294 (1998).

Z. E. Penman, P. Loza-Alvarez, D. T. Reid, M. Ebrahimzadeh, W. Sibbet, D. H. Jundt, “All-solid-state mid-infrared femtosecond optical parametric oscillator based on periodically-poled lithium niobate,” *Opt. Commun.*, **146** 147 – 150 (1998).

G. J. Valentine, J-M. Hopkins, P. Loza-Alvarez, G. T. Kennedy, W. Sibbett, D. Burns., A. Valster. “Ultra-low pump threshold, femtosecond $\text{Cr}^{3+}:\text{LiSrAlF}_6$ laser pumped by a single, narrow-stripe AlGaInP laser diode,” *Opt. Lett.*, **22**, 1639 – 1641 (1997).

Conference publications

P. Loza-Alvarez, D. T. Reid, W. Sibbett; “Autocorrelation of femtosecond pulses from 415-630 nm using a GaN laser diode,” In *Conference on Lasers and Electro-Optics/Europe*, OSA Technical Digest (Optical Society of America, Washington DC, 2000), pp. 137, paper CTUK101.

D. T. Reid, P. Loza-Alvarez, C. T. A. Brown, T. Beddard, W. Sibbett; “Amplitude and phase measurements of mid-infrared femtosecond pulses using X-FROG,” In *Conference on Lasers and Electro-Optics/Europe*, OSA Technical Digest (Optical Society of America, Washington DC, 2000), pp. 77, paper CTUH2.

D. T. Reid, P. Loza-Alvarez, C. T. A. Brown, T. Beddard, W. Sibbett; “Complete characterisation of mid-infrared femtosecond pulses using XFROG,” In *The twelfth International Conference on Ultrafast Phenomena*, OSA Technical Digest (Optical Society of America, Washington DC, 2000), pp. 173, paper MF28.

P. Loza-Alvarez, D. T. Reid, P. Faller, M. Ebrahimzadeh, W. Sibbett; D. Artigas, M. Missey, "Frequency-doubling and compression of chirped femtosecond pulses using aperiodically-poled lithium niobate," In *Conference on Lasers and Electro-Optics*, OSA Technical Digest (Optical Society of America, Washington DC, 2000), pp 476 paper CThM38.

D. T. Reid, P. Loza-Alvarez, W. Sibbett; "Femtosecond autocorrelation of CW-modelocked pulses from 415-630 nm using a GaN laser diode," In *Conference on Lasers and Electro-Optics*, OSA Technical Digest (Optical Society of America, Washington DC, 2000), pp. 584, paper CFE2.

D. T. Reid, P. Loza-Alvarez, C. T. A. Brown, T. Beddard, W. Sibbett; "Amplitude and phase measurements of mid-infrared femtosecond pulses using X-FROG," In *Conference on Lasers and Electro-Optics*, OSA Technical Digest (Optical Society of America, Washington DC, 2000), pp. 618, paper CFL2.

Loza-Alvarez, C. T. A. Brown, D. T. Reid, W. Sibbett. "Generation of femtosecond pulses tunable to beyond 6 μm ," In *National Quantum Electronics Conference* (QE14 September 1999). Manchester. UK (1999), pp. 49, paper 4-1.

P. Loza-Alvarez, D. T. Reid, M. Ebrahimzadeh, W. Sibbett; H: Karlsson; P: Henriksson; G: Arvidsson, F. Laurell, "Periodically Poled RbTiOAsO₄ femtosecond optical parametric oscillator tunable from 1.38 to 1.58 μm ." In *Conference on Lasers and Electro-Optics*, OSA Technical Digest (Optical Society of America, Washington DC, 1998), pp. 488, paper CThCC2.

D. T. Reid, P. Loza-Alvarez, M. Ebrahimzadeh, W. Sibbett; H: Karlsson and F. Laurell "Femtosecond Pulse compression by second-harmonic generation in aperiodically-poled KTP" In *Conference on Lasers and Electro-Optics*, OSA Technical Digest (Optical Society of America, Washington DC, 1998), pp. 17, paper CME3.

P. Loza-Alvarez, D. T. Reid, M. Ebrahimzadeh, W. Sibbett; H: Karlsson; P: Henriksson; G: Arvidsson and F. Laurell. "Periodically Poled RbTiOAsO₄ femtosecond optical parametric oscillator tunable from 1.38 to 1.58 μm ." In *Conference on Lasers and Electro-Optics/Europe*, OSA Technical Digest (Optical Society of America, Washington DC, 1998), pp. 213, paper CWH4.

D. T. Reid, P. Loza-Alvarez, M. Ebrahimzadeh, W. Sibbett; H: Karlsson and F. Laurell "Femtosecond Pulse compression by second-harmonic generation in aperiodically-poled KTP" In *Conference on Lasers and Electro-Optics/Europe*, OSA Technical Digest (Optical Society of America, Washington DC, 1998), pp. 214, paper CWH5.

G. J. Valentine, M. P. Critten, G. T. Kennedy, J-M. Hopkins, P. Loza-Alvarez, W. Sibbett. "Novel Resonator Designs for Low Threshold Self-Mode-Locking". In *Conference on Lasers and Electro-Optics*, OSA Technical Digest (Optical Society of America, Washington DC, 1997), paper CMI1.

P. Loza-Alvarez, J-M. Hopkins, G. J. Valentine, M. P. Critten, D. Burns, W. Sibbett, "Ultralow-Threshold KLM Cr³⁺:LiSrGaF₆ Laser Pumped by a Self-Injection Locked AlGaInP Diode Laser," In *National Quantum Electronics Conference (QE-13 September 1997)*. Cardiff. UK (1997), paper PVIII-1.

J-M. Hopkins, P. Loza-Alvarez, G. J. Valentine, D. Burns, and W. Sibbett. "Femtosecond Pulse Generation from a Cr³⁺:LiSrAlF₆ Laser Pumped by a Low-power Single-stripe AlGaInP Diode Laser". In *National Quantum Electronics Conference (QE-13 September 1997)*. Cardiff. UK. (1997), paper PVIII-5.

Acknowledgements

First of all, I would like to thank my supervisor Professor Wilson Sibbett for giving me the great opportunity to work in his group and test what science is, and for always providing excellent guidance and support during this work.

I will eternally be in debt to Dr. Derrick T. Reid for his invaluable help, endless patience and for having unconditionally shared with me a little part of his vast knowledge.

Thanks go to Dr. Majid Ebrahimzadeh for his advice and for giving me continual encouragement in this work.

Thanks also go to Dr. Roberto Ortega-Martinez for his assistance, for always being in contact with me and without whose opportune help I would not be writing this work.

I acknowledge all the W-squad group: Bill Sleat, for knowing everything about electronics, Gordon Kennedy, Mathew Critten, Edmond Williams, Gregori Sokolovski, for transmitting their knowledge to the w-squad group. Paul Faller, for all the computing programs. Gareth Valentine (the arabic bandit) and John-Mark Hopkins, for sharing with me the secrets of the “Noches Mexicanas” and for being my “ángeles de la guarda” during my first year. Cate McGowan, and Zoe Penman, for the works with the OPOs. Edick Rafailov, Tom Brown, Alan Kemp, David Birkin, Tom Beddard, Iain Cormack and Ben Agate, for helping me with so many things that could not possibly be written here, for their friendship during the past years and especially for being tolerant with me in the last three weeks before completing my thesis.

To all the staff and technicians in the School of Physics and Astronomy.

To Rosa for her support and giving me encouragement to finish this work, for her understanding in the difficult moments, and for the special way in which she relieves me from any stress.

To David Artigas, for developing the pulse compression program, writing so many e-mails and having introduced me into the homebrew world.

To all my friends that discovered and/or enjoyed with me all the fantastic traditions of this and remote but fascinating island in the North Sea.

To the Centro de Instrumentos and the Dirección General de Asuntos del Personal Académico de la Universidad Nacional Autónoma de México (DGAPA-UNAM) for the full scholarship to complete this degree.

To the British Council for the British Chevening scholarship during the first year of this work.

To all of you, thank you very much!.